RHEOLOGY OF LARGE GAS FRACTION LIQUID FOAMS

by

Saad Akhtar Khan

B.S.E., Princeton University, 1980

Submitted to the Department of
Chemical Engineering
in Partial Fulfillment of the
Requirements of the Degree of

DOCTOR OF PHILOSOPHY

at the

MASSACHUSETTS INSTITUTE OF TECHNOLOGY

January 1985

Signature of Author______________________________________
Department of Chemical Engineering

Certified by____
Robert C. Armstrong
Thesis Supervisor

Accepted by____
Chairman, Departmental
Committee on Graduate Studies

RHEOLOGY OF LARGE GAS FRACTION LIQUID FOAMS

by

Saad Akhtar Khan

Submitted to the Department of Chemical Engineering
in January, 1985 in partial fulfillment of the requirements
for the Doctor of Philosophy in Chemical Engineering

ABSTRACT

The rheology of foam was studied through structural modelling and experiments. A formalism was developed to calculate the total stress tensor in terms of the foam microstructure by embedding basis vectors along the foam film edges. This enabled us to calculate stresses for any arbitrary foam cell orientation and arbitrary homogeneous deformation for high gas fraction two-dimensional foam cell models. An experimental technique was developed which eliminated all previous problems associated with wall slippage in foam flow and allowed us to do experiments without resorting to any empiricisms for the wall region.

Modelling work revealed foam to behave like a Bingham plastic with its viscosity having contributions from the yield stress and dissipation in the liquid films. The yield stress, which increased with gas fraction, was proportional to the interfacial tension σ and inversely proportional to cell size. For deformations below the yield point, foam behaved like an elastic solid with the stress showing the same proportionality as before, and the liquid films undergoing an extensional motion. It is this elongational flow of the films that causes viscous dissipation in steady flows. We also found the yield stress to be unaffected by a bimodal cell size distribution indicating it to be not an important rheological parameter. For low shear rates, the foam cell structure satisifes geometric equilibrium; however, for higher shear rates the structure is determined from a force balance of the viscous and interfacial forces at each Plateau border. For large deformations, periodicity in the stress-strain behavior was observed for certain initial cell orientations and shear rates. For foams having finite liquid content, certain orientations were unstable beyond a specific strain suggesting possiblities of preferential cell orientations in foam. Finally, we observed the liquid film thickness not to be an important parameter affecting rheological properties.

Experimental work also supports the theoretical findings. We observed foam to have a Bingham fluid behavior with its viscosity, η, having a slope inversely proportional to shear rate indicating the presence of a yield stress. Further measurements showed this yield stress to increase with gas fraction. Elastic behavior of foam for small deformations was indicated by its frequency independent moduli, very small phase shift between strain input and stress output, and the ealstic modulus (G') being much larger than the loss modulus (G''). Further proof of this also came for the invariance of the normalized transient viscosity (η^+) versus strain plots for different shear rates.

Thesis Supervisor: Robert C. Armstrong
Title: Associate Professor of Chemical Engineering

ACKNOWLEDGEMENTS

I am very grateful to my advisor, Professor Robert C. Armstrong, for his help and support during the course of this work. It was a real pleasure working for him. I would like to thank the members of my thesis committee: Profs. Allen, Brenner, Brown and Hatton, for their constructive suggestions. Although meetings were rather infrequent, some of the ideas discussed really helped a lot.

This research was financially supported by Marin Marietta Aerospace through the Polymer Processing Program at MIT. I am thankful to both these organisations for their support. On a personal level, I enjoyed the company of all those associated with P^3. Special mention should however be made of Mike Demareee and Fred Cote for their help in building my equipment. I would also like to thank Saul Locke, Don Hauser and Jeff Corbin of Martin Marietta for their help in this project.

Many friends, both from inside and out of MIT helped me in this thesis. To all of them I owe my deepest gratitude. Carol worked with me on all the experiments. Her help was pivotal for this research. People from the Rheology Research Center: Antony, John, Miguel and Susan, helped me on numerous occasions with their ideas and computer/graphics ability. Outside of MIT, Sarosh and Naheed put in long hours to help me with the figures. Without their help this thesis would never had been ready on time.

During my entire stay at MIT, I always received encouragement from my parents. And, Rumana was always there to help and inspire me throughout the course of this work.

TABLE OF CONTENTS

LIST OF FIGURES

I. INTRODUCTION

A uniform dispersion of gas bubbles in a given amount of liquid in which the separation between bubbles is no more than the bubble diameter is termed a foam. Two extreme structural situations, depending on the gas to liquid volume ratio, are noticed in foams. The first type consists of spherical bubbles separated by rather thick liquid films. Such foams are termed "wet" because of their low gas content. The second type contains mostly gas. Bubbles are polyhedral in shape separated from each other by very thin liquid films between the faces (Figure I-1a). These plane parallel films are called the lamella of the foam [Bickerman, 1973; Kitchener and Cooper, 1959; Kitchener, 1964]. Most common foams fall in the second category, and our study is therefore confined only to such systems where the gas volume fraction ranges from .74 for the hexagonally close packed system to unity.

In order for foam cells to exist in mechanical equilibrium, certain geometrical conditions have to be satisfied. The first constraint, which follows from Plateau's law, requires the structure be such that the surface energy is at a local minimum. This implies that only three lamella can meet at an edge to form a border or line (Figure I-2) called the Plateau border [Rosen, 1978; Adamson, 1976; Shaw, 1970; Ross, 1969; Ross, 1983]. The coplanar angles are equal and 120 degrees each. Further, only four Plateau borders can meet at a point forming mutually equal tetrahedral angles.

The second constraint which is an outcome of Young and Laplace's equation [Rosen, 1978] states that the radius of curvature of the cells

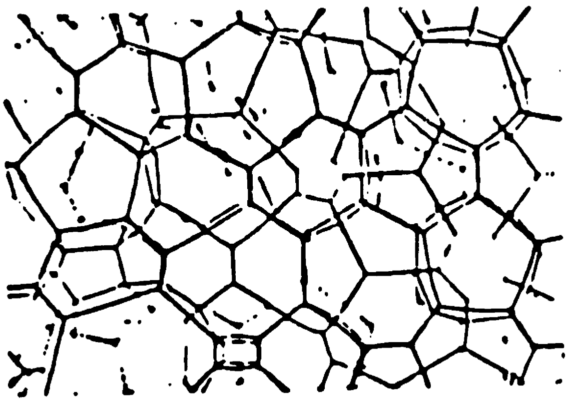

A. PHOTOGRAPH

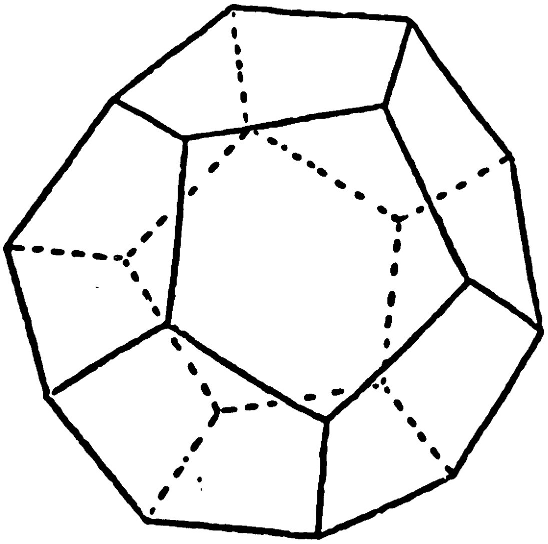

B. DODECAHEDRON

Figure I-1 Polyhedral foam cells showing very thin Plateau borders. a) Real foam [Kitchener, et al., 1959] b) Schematic representation

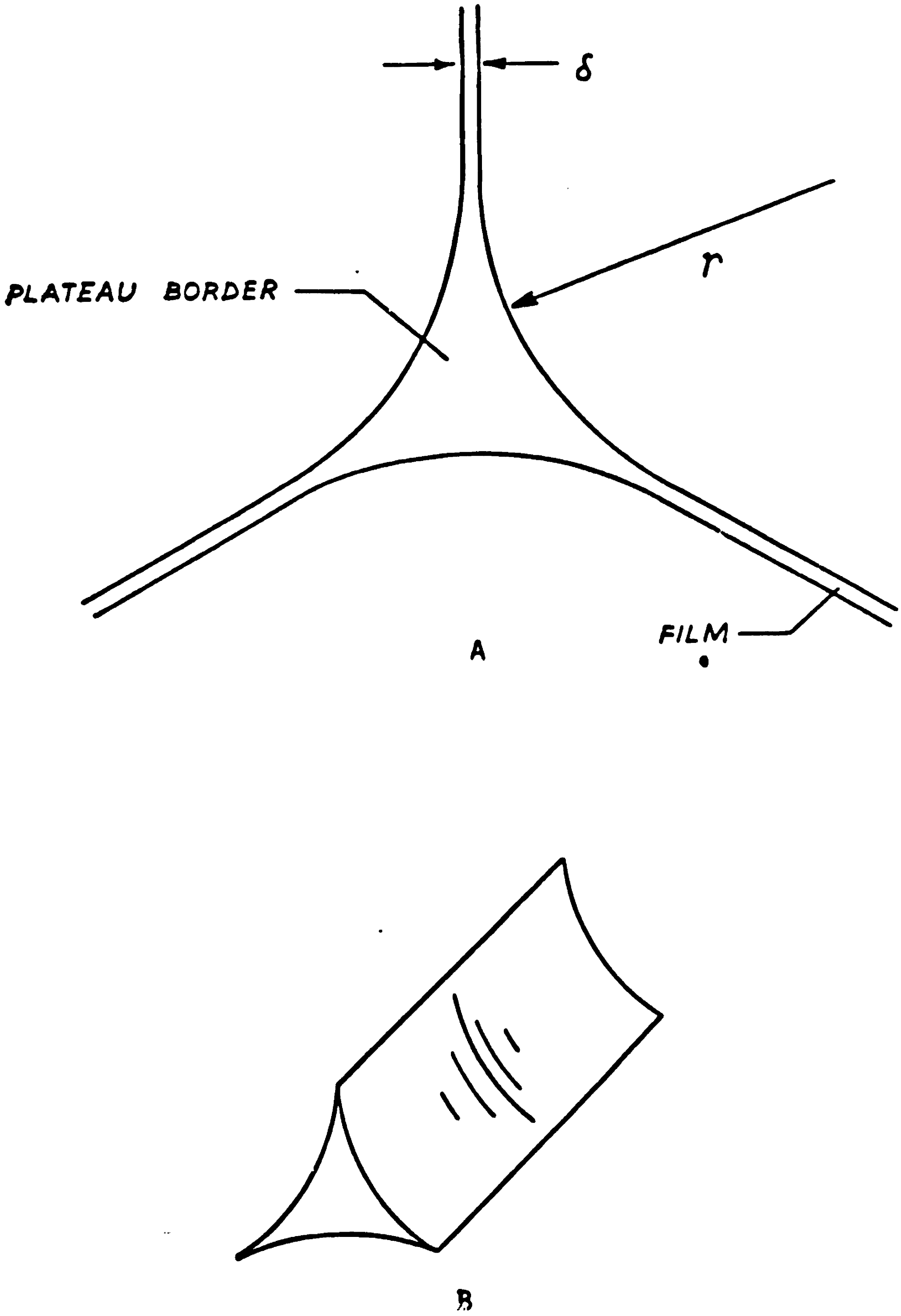

Figure I-2 Schematic of Plateau border and lamella in foam. a) Cross section through Plateau border showing 120 degree angles between films. b) Side view of Plateau border be same. Young and Laplace's law states that the pressure drop across an interface is inversely proportional to the radius of curvature. At equilibrium, the pressure difference at all points across the gas-liquid interfaces has to be same. This means that in adjoining cells the jump in pressure at a point on going from the gas phase to the liquid film should be equal. Thus at the Plateau border, where the three liquid films meet and curve concave to the gas cells, the radii of curvature have to be equal. The planar liquid walls also meet this criteria. In terms of closed cell structures, only the dodecahedron (Fig. I-1b) satisfies both equilibrium constraints. Real foam cells (Figure I-1b) are close approximations of this [Bickerman, 1973; Matzke, 1946; Matzke and Nestler, 1946; Princen, 1979; Princen, Aronson and Moser, 1980]

Like most dispersed systems, foams are unstable in a thermodynamic sense. This is because the formation of gas bubbles results in a concomitant increase in surface energy, and the system tends to reduce the excess free energy by phase separation. Nevertheless, some foams can persist for a sufficiently long time to be put to useful purposes. Articles made of solid foams are examples of this. Here the liquid films undergo cross linking reactions before the foam had time to collapse.

Pure liquids do not foam. Generally, a surfactant which can considerably lower the surface tension of the liquid to be foamed has to be added in order to produce persistent ("metastable") foams. The formation of foam is followed by liquid drainage and cell collapse. Capillary pressure, present due to the different radii of curvature at the gas-liquid interface because of polydispersity, and van der Waals attractive forces in the liquid films cause the lamella to become thinner with time. For the foam to be stable the liquid film must have some surface elasticity opposing this localised thinning. The most important source of this is the Gibbs-Marangoni surface elastic effect [Shaw, 1970; Akers ed., 1976]. Here the change in liquid film area with drainage changes the equilibrium interfacial tension (Gibbs) as well as sets up a surface tension gradient (Marangoni), both of which provide a restoring force. In addition, surface viscosity and electric double layers [Kitchener and Cooper, 1959; Kitchener, 1964; Rosen, 1978; Matijevic ed., 1971] resist drainage. A balance between all these forces determines the lifetime of a foam. Details of these along with the kinetics of bubble collapse have been investigated by several researchers [Lemlich ed., 1972; Lemlich, 1978; Nishioka and Ross, 1981; Hartland and Barber, 1974, 1975; Steiner, Hunkeler and Hartland, 1977; Kumar et al., 1982; New, 1967; Akers ed., 1976; Desai et al., 1983; Ross, 1983; Kraynik, 1983]. Our study, however, is restricted to the rheology of foams only. We focus on foams which are stable compared to the process time so that stability effects can be justifiably ignored.

A. RATIONALE FOR RESEARCH

Foam represents an important class of engineering materials. Its low density and favorable mechanical and thermal properties makes it useful in a wide range of applications. For instance, heavy and light weight metallic components of automobiles are being replaced by foams. Foam is used as a protective covering for cables. Foam cups are used for their good thermal properties. However, one of its most important current usage and which primarily motivated us to undertake this research lies in the space shuttle program. Here, polyurethane foam is used as an ablative material to make components of the external fuel tank. For certain parts foam (molded or sprayed) is used directly on metal substrates; for others, foam is used on top of a granular composite material glued onto the substrate. Foams are also used in nuclear plants as safeguards for attenuation of explosively driven shock waves.

All these represent solid foams. However, to get these final products liquid foams are used in processes, such as in some mold filling operation, where rheology becomes important. For instance, because of its unusual nature, conventional processing techniques often do not lead to desirable products. An understanding of the rheology is essential here to optimize processing conditions and study the feasibility of new products. For example, a lack of understanding of the flow behavior of the polyurethane foam used in the space shuttle ablator results in skin formation in the molded product, poor mold filling, non uniform density and elongated cell structures. Removal of this skin and other processing problems involves a trial and error procedure and is very cost intensive.

Foams are also used in fluid form. Two rather unusual yet important examples of this are the foams used to cover explosives planted by terrorists before detonating them so as to absorb shock and thereby minimize damage, and also to cover explosives with very sticky foam during transportation to prevent them from being stolen by terrorists. Commonly, foams are used universally at airports for emergency landing of aircrafts. Other examples include fire fighting foams and shaving foams. An important property governing the behavior of all such foams is their high viscosity.

Another area where foam is being used increasingly is in transport of particulates. In the oil industry, foams are used as a drilling fluid to transport propant and to remove drilling debris out of oil wells [Mitchell, 1971; Beyer, Millhone and Foote, 1972]. In making paper by the Radfoam process [Akers ed., 1976] aqueous foams are used to transport pulp and coat it onto a web. Without foaming the water carrier, roughly ten times as much water must be added in order to obtain a uniform paper sheet.

In all these processes, rheology plays a very important part. For instance, an understanding of the structure-property relation in foams will enable us to determine a priori how long different particulates can be suspended in a foam. Unfortunately, despite the diverse uses of foam, studies on its rheology are incomplete. Many critical questions still remain to be answered. The potential benefits make understanding these issues important.

B. LITERATURE REVIEW

Although work on foam morphology and stability has been going on for a long time, it is only recently that studies on its rheology have been undertaken. To the best of our knowledge, the only extensive work on "wet" foam was done by Prud'homme [1978]. He devised a technique to produce low gas fraction foams and the studied its different rheological properties. The experimental work was accompanied by some theoretical studies [Prud'homme and Bird, 1978] where expressions for different material functions were derived. This work however, is restricted to very low gas fraction foams and cannot be applied here.

Most of the studies on large gas fraction foam rheology dates back only as far as two decades and falls broadly into two categories: i) The early work, which includes several independent studies done in the late sixties and early seventies. These work however left a lot of unresolved issues and led to renewed interest in this area in the eighties. ii) The recent studies, which started almost concurrently with our work and are still in progress. Although started at the same time, most of these studies along with ours have been complementary. Any overlap whatsoever has merely served to verify the results. Both the early and recent studies are discussed here.

1. Early Studies

Most of the major studies in this area are summarized in Table I-1. This table includes the name of the researchers, the date and kind of work done and some of the major findings. One exception has been made in this section to include the recent work of Patton and coworkers [1981] here. This is because although new, their work parallels the earlier ones.

David [1968; 1969] was one of the first researchers to do a systematic study on foams. He used a capillary viscometer for his studies and observed considerable wall slippage in foam flow. Using Mooney's [1931] correction factor, he determined the viscosity of foam and found it to be shear thinning. Similar experiments done separately by Wenzel and coworkers [1967] and Patton et al [1981] reported the same findings. Power law behavior was also observed by Wenzel's group [1970] when he repeated the experiments using a vaned cone and plate apparatus. All four studies [David, 1968; David and Marsden, 1969; Wenzel, Stelson and Brungraber, 1967; Patton et al., 1981] using the tube flow experiments showed that

TABLE I-1

SUMMARY OF EARLY FOAM WORK

PARAMETERS PROPERTILS	SHEAR RATE $\dot{\gamma}$	GAS VOLUME FRACTION ϕ	BUBBLE DIAMETER d_b	TUBE DIAMETER d_t TUBE LENGTH L
VISCOSITY η	David(C) 1969 Wenzel(CP) 1970 Patton(C) $\eta \ \alpha \ 1/\dot{\gamma}$	David(C) 1969 Wenzel(CP) 1970 $\eta \neq f(\phi)$ Beyer(C) 1972 Patton(C) 1981 $\eta \ \alpha \ \phi^n$ $(n>1)$	Wenzel(CP) 1970 $\eta \neq f(d_b)$ Wenzel(C) 1967 $\eta \ \alpha \ 1/d_b$ David(C) 1969 $\eta = f(d_b)$	David(C) $\eta \ \alpha \ d_t$ Patton(C) $\eta \ \alpha \ d_t/L$
YIELD STRESS τ_y		David(C) 1969 Beyer(C) 1972 $\tau_y \ \alpha \ \phi^n$ $(n \geq 1)$ Wenzel(CP) 1970 $\tau_y \neq f(\phi)$	Wenzel(CP) 1970 $\tau_y \ \alpha \ 1/d_b$	

C: CAPILLARY FLOW EXPERIMENTS
CP: CONE & PLATE EXPERIMENTS
T: THEORY

TABLE I-1 (continued)

SUMMARY OF EARLY FOAM WORK

PARAMETERS PROPERTIES	SHEAR RATE $\dot{\gamma}$	GAS VOLUME FRACTION ϕ	BUBBLE DIAMETER d_b	TUBE DIAMETER d_t TUBE LENGTH L
SLIP VELOCITY V_s	low $\dot{\gamma}$ David(C) 1969 Beyer(C) 1972 Wenzel(CP) 1970 Surati(T) 1975 $V_s \alpha \dot{\gamma}$ high $\dot{\gamma}$ Wenzel(CP) 1970 Surati(T) 1975 $V_s \ast f(\dot{\gamma})$	David(C) 1969 Beyer(C) 1972 $V_s \alpha 1/\phi$		
SLIP LAYER THICKNESS δ	Wenzel(CP) 1970 Surati(T) 1975 $\delta \alpha \dot{\gamma}$ (low $\dot{\gamma}$) $\delta \ast f(\dot{\gamma})$ (high $\dot{\gamma}$)	Wenzel(C) 1970 $\delta \ast f(\phi)$ David(C) 1968 $\delta \alpha 1/\phi$	Wenzel(C) 1970 $\delta \alpha d_b$	

tube diameter affected viscosity. Further Patton and David found viscosity to be proportional to the tube diameter. Patton also found viscosity to be inversely proportional to tube length. This tube length dependence clearly indicates that Patton's experiments did not involve fully developed flow. Another problem with these experiments was that the tube diameter was almost commensurate with the bubble diameter. Further, the small diameter led to considerable pressure drop and hence to compressibilty effects. On the other hand, the big vanes in Wenzel's cone and plate experiments gave a very non-homogeneous flow field. This, coupled with the fact that wall slippage at the cone surface (which had no vanes) was not taken into account, makes Wenzel's data useful only in a semi-quantitative sense.

Conflicting reports exist on the dependence of viscosity on gas volume fraction (ϕ). Wenzel [1970], using a cone and plate geometry, and David [1968; 1969] found no influence of ϕ on viscosity. However, anotner study by Beyer and co-workers [1972] found viscosity to increase with increasing gas volume fraction. Wenzel [1967; 1970] also found contradictory results when trying to measure the effect of bubble diameter (d_b) on viscosity. The cone and plate experiments showed viscosity to be independent of d_b, but the tube flow experiments showed a $1/d_b$ dependence of viscosity. David also found viscosity to be influenced by bubble size but did not derive any correlation for it.

Although all studies mentioned thus far indicate the presence of a yield stress in foam, only two have attempted to measure it. Wenzel [1970] arrived at a yield stress value by fitting his stress data to a Herschel-Bulkley model. David used a "Stormer" viscometer to obtain yield stress. Wenzel's study showed τ_y to be inversely proportional to d_b^n where $n \cong .65$. Further, he did not observe any meaningful correlation between yield stress and gas fraction. David, on the other hand, found τ_y to be proportional to ϕ. Beyer and coworkers [1972] did some indirect measurements on yield stress by studying particle lifting ability of foam. They found this to increase with gas volume fraction.

Wenzel [1967] and co-workers looked at wall slip velocities for flow of foam through a tube. By using a transparent pipe, they employed flow visualization technique to time the movement of the foam at the tube wall. They found this slip velocity, V_s, to increase intially with average velocity or flow rate and then level off at higher flowrates. Later, they did more careful experiments to actually measure this slip layer. They used a vaned couette geometry where the inner cylinder had vanes to prevent slip while the outer one could be rotated by an external motor. Torque on the inner cylinder was measured. Since Wenzel already knew the yield stress from previous experiments, he focussed on the stress region below it. Then, essentially all the shearing was going on in the slip layer. For a Newtonian film undergoing laminar shearing flow, $\tau_w = \mu V_s/\delta$ where V_s is the slip velocity (velocity of cylinder), τ_w is the wall shear stress and δ the film thickness. Correlating this with experiments, he found δ to be of the same order of magnitude as the thickness of the bubble film and increasing with shear rate. He found no correlation between δ and ϕ or bubble size leading him to believe that δ is independent of foam structure. In his experiments, he also observed that the thin film seemed to have a very small yield stress of its own. Quantitative experiments were not done to measure it.

David and Marsden [1969] did not measure slip velocities directly. Rather, by using Mooney's approach [1933], they defined a slip coefficient (β) given by $V_s = \beta\tau_w$. Cappillary flow experiments revealed β (which is directly related to δ) to increase with lower gas fraction and larger wall stress. Beyer et al. [1972] also used Mooney's approach to define a slip coefficient. However, their coefficient was the inverse of David's coefficient. Using experimental results from pie flow, they developed an empirical relation between V_s, ϕ and τ_w. They found V_s to increase with wall stress and decrease with gas fraction.

Very little work has been done in developing a constitutive model for foam in terms of its structural properties. Most of the theoretical analyses [David et al., 1969; Beyer et al., 1972] was done using Mooney's approach only to obtain material functions from tube flow experimental data. Alternately, researchers fitted their data to some version of the Bingham model [Wenzel et al., 1970; Patton et al., 1981]. Mahalingam and co-workers [1975] went a step further. Using the Casson and Herschel-Bulkley models and literature data, they developed the entire foam velocity profile for pipe flow. Figure I-3 shows the velocity as a function of radial distance. At low average velocities, the flow is essentially a plug. As average velocity increases, the plug radius decreases and all three regions (skimming, intermediate, and plug) become quite distinct. Further, the slip velocity asymptotes to a constant value. However, none of these represented a structural model.

Clearly, the rheological study of foams were still in its infancy. No structure-property models existed. Contradictions and defficiencies existed in the experiments. Recently, therefore, a few groups including

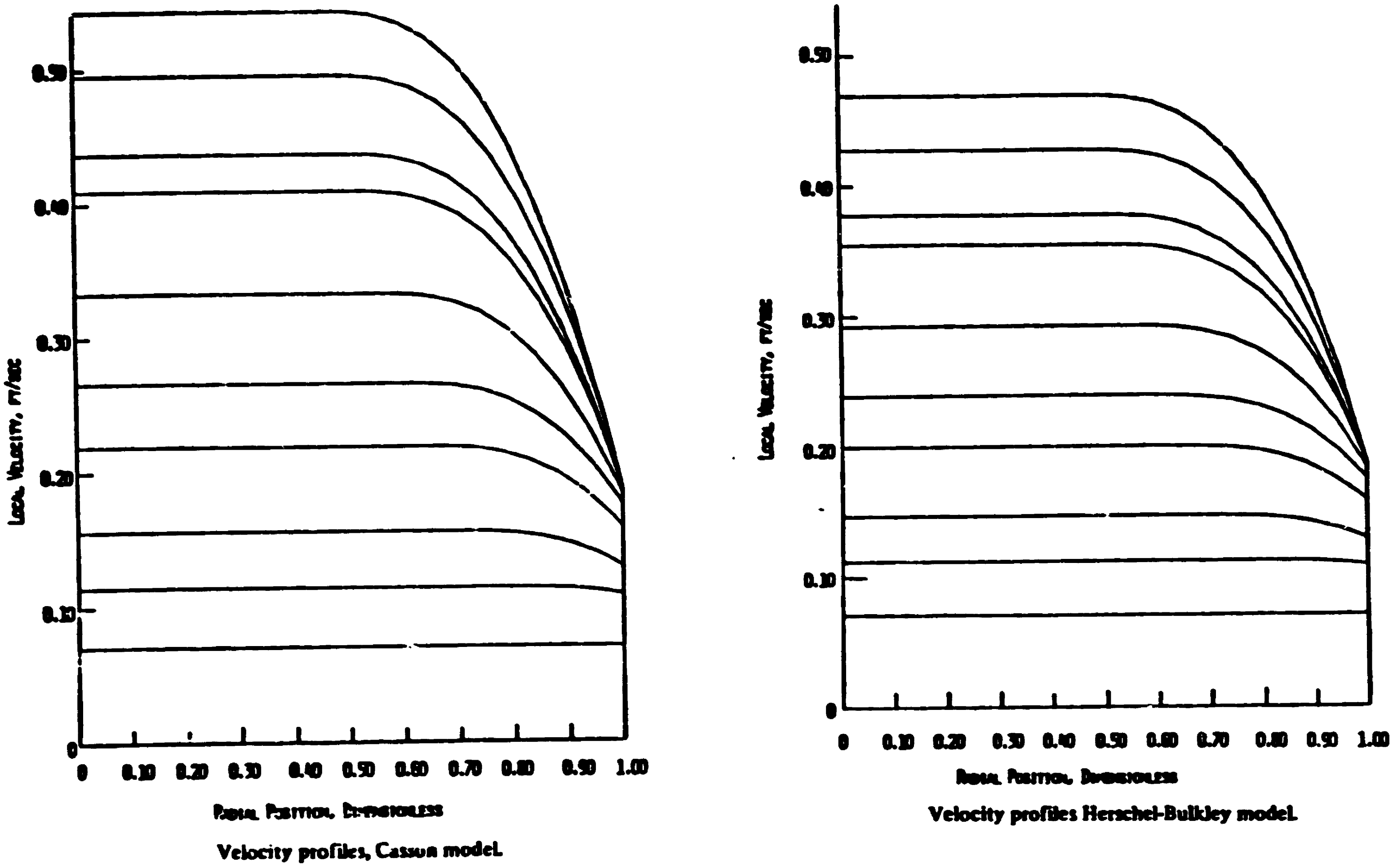

Velocity profiles, Casson model.

Velocity profiles Herschel-Bulkley model.

Figure I-3 Foam velocity profiles in a tube flow calculated by using Casson and Herschel-Bulkley models [Surati, et al., 1975].

ours undertook some further studies. A report on the findings of these groups form the subject matter of the next section.

2. Recent Work

Princen [1983] was one of the first (Prud'homme being the other) to develop a structural model for foams. He used a two dimensional hexagonal cell geometry for foam and derived stress-strain relations for shearing deformation up to the yield point. He extended his model to incorporate finite liquid volume fraction, the lower limit being determined by the hexagonally close packed sphere system (Figure I-4). His range of gas volume fraction coincides with most of the recent studies being done. Results obtained showed the stress (and also the yield stress) to be some function of ϕ, directly proportional to the surface tension (σ) and inversely proportional to the hexagonal cell side length. This inverse dependency with cell size is in agreement with Wenzel's tube flow experiments [1967].

In his model, Princen focussed on only one specific initial cell orientation (Figure I-4b) namely that where the vertices pointed upward. Further, he considered interfacial forces to be dominant, and they were assumed to act along the liquid films. Thus, the shear stress could be determined from the projection of all intersecting films on a horizontal shearing plane. In order to get the orientation of the films as functions of strain, he used an iterative technique and found the stress response to be non-linear in strain.

To verify the theory, Princen [1984] has recently focussed on experiments with oil in water emulsions. The aim of this study was to evaluate the effect of gas volume fraction, surface tension, and cell diameter on

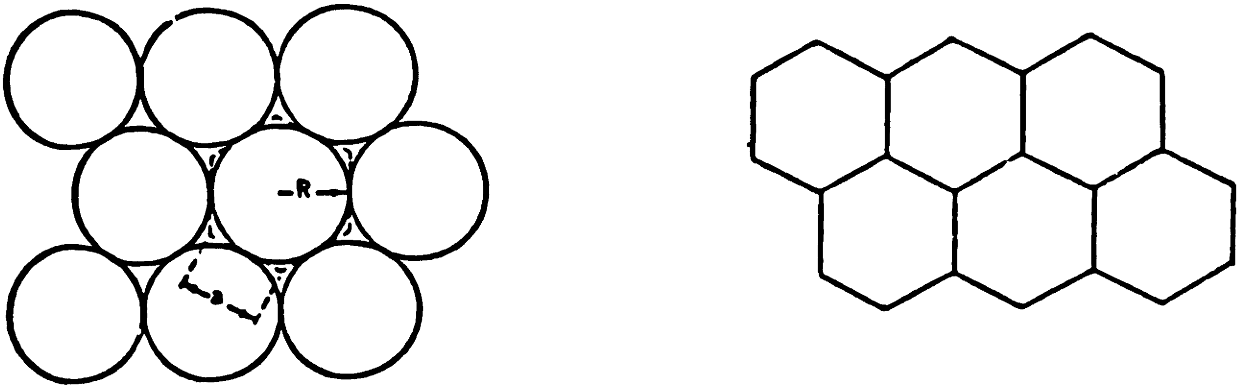

CLOSE-PACKED SPHERES

HEXAGONAL CELLS

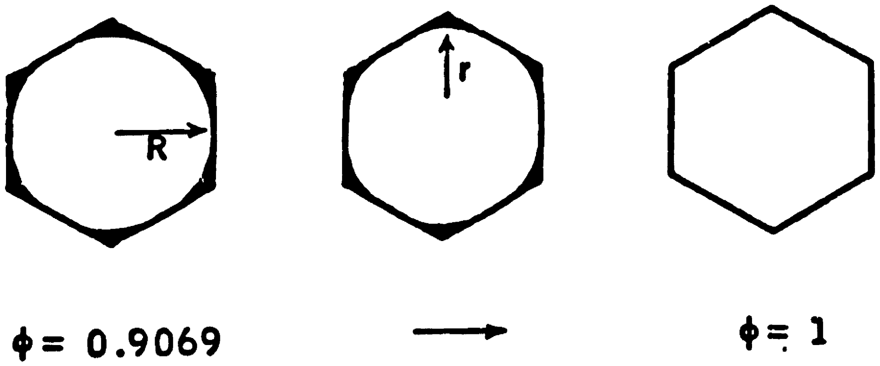

INCREASING GAS VOLUME FRACTION

Figure I-4 Two dimensional foam cell models. a) Hexagonally close-packed spheres b) Hexagonal cells having $\phi = 1$. c) Changing cell structure with increasing gas volume fraction.

the yield stress and look at boundary (wall slip) layer properties. He used a Couette device for his experiments where the outer cylinder (radius R_2) was rotated and the torque measured at the inner one. He characterized the slip layer between the emulsion and cylinder wall in terms of the "fluidity" of that layer which he defined as $\Phi_w(\tau_w) = h/\eta$. Here, Φ is a function of stress only and h, η denote the effective thickness and viscosity of the boundary layer. Thus, for flows where $\tau<\tau_y$, the emulsion moves like a plug with a rigid angular velocity (ω_E). The stresses can then be related by [Princen, 1984]:

$$\tau_1=\Phi_{w1}\ \omega_E\ R_1 \qquad \tau_2=\Phi_{w2}\ (\omega_2-\omega_E)\ R_2$$

and, $\tau_1 R_1^2=\tau_2 R_2^2$ (neglecting end effects)

Here 1 and 2 refer to the inner and outer cylinders respectively. ω_E was obtained by measuring the angular velocity of a pigmented radial line on the emulsion. By plotting Φ_{w1} vs τ_1 or τ_1 vs ω, Princen obseved a break in his curve which corresponded to the τ_y of the emulsion (Figure I-5). Thus he was able to obtain τ_y indirectly from his experiments. He found τ_y to be proportional to σ and increasing with ϕ but not to follow the 1/r dependence. He attributes the discrepancy to polydispersity, finite film thickness and contact angles.

In addition to measuring τ_y, Princen analysed the slip layer. Extrapolating the fluidity plots to zero stress and assuming a liquid viscosity, he found the effective boundary layer to be approximately 45nm. He then determined f, the fraction of the wall area occupied by thin aqueous films between the wall and adjacent flattened droplets theoretically. In this way, the corresponding film thickness was found to be around 20nm. Princen further noticed that the slip layer itself had a small

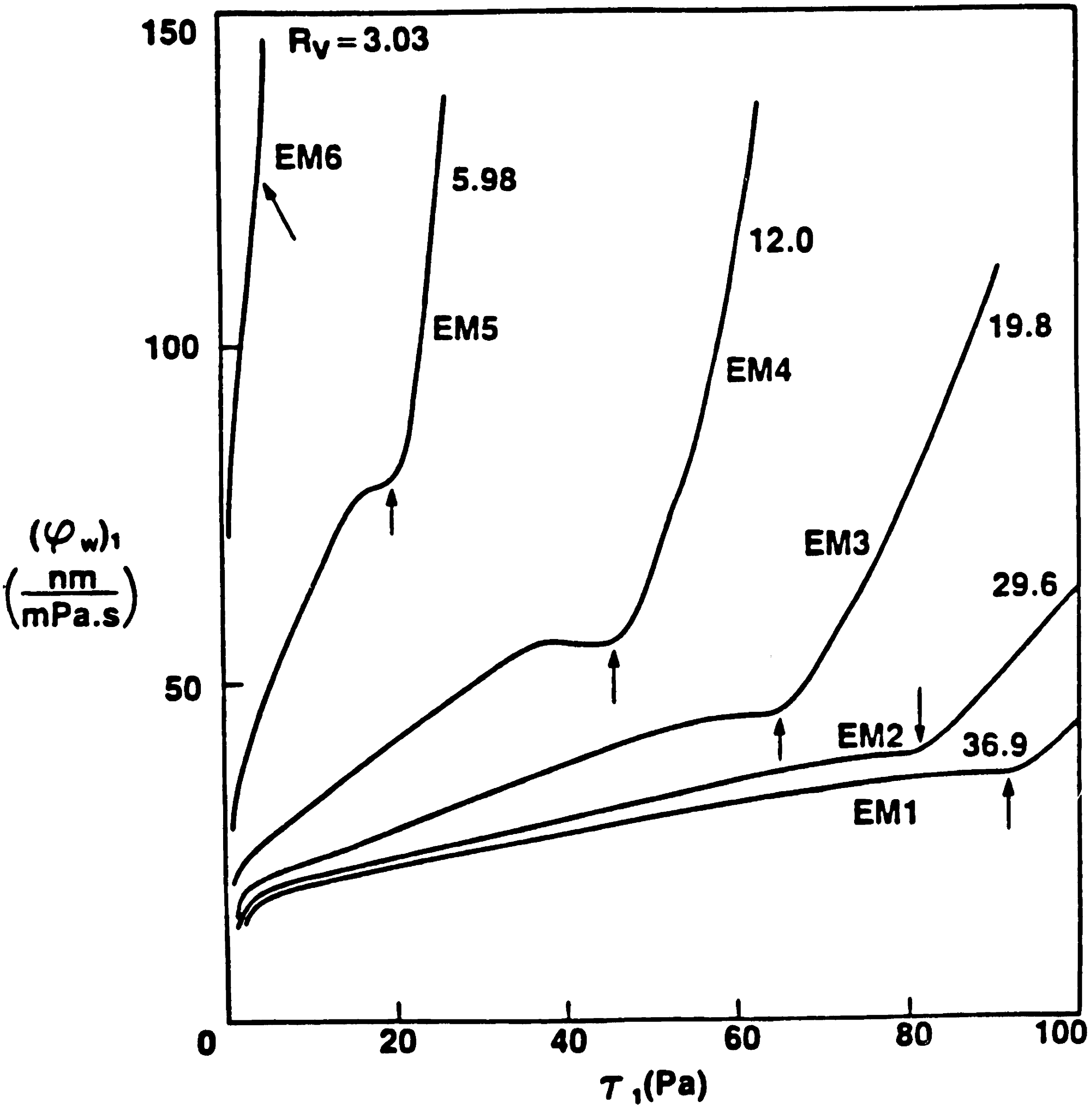

Figure I-5 Fluidity of wall layer vs. wall stress for emulsions (EM 1-6) of variable dispersed/continuous phase volume ratio, R_V. Arrows indicate yield stress [Princen, 1984].

yield stress which he attributed to surface roughness. Similar observations were also made by Wenzel in 1967.

Although Prud'homme did some intial modelling work based on a hexagonal cell geometry [1981], the emphasis of his studies has been experimental. He and Yoshimura [1984] have developed a "slip layer model", some what similar to Mooney's, where they define Φ and h to be functions of stress only. Their analyses shows that the slip layer problem in experiments can be avoided by running the same experiments twice at the same stress level in viscometers of two different sizes (capillaries with two radii, parallel plates with different gaps, etc). Thus for a parallel plate device, the true bulk shear rate $\dot{\gamma}$ is given by:

$$\dot{\gamma}=(\dot{\gamma}_2H_2-H_1\dot{\gamma}_1)/(H_2-H_1)$$

where $\dot{\gamma}_i$, H_i are the apparent shear rate and gap size respectively for the two runs.

The viscosity can therefore be obtained using the Rabinowitz correction. Figure I-6 shows stress versus shear rate curves for different runs along with the corrected result. It is clear from the plot that the material (oil in water emulsion) exhibits a yield stress.

In a second set of experiments, Prud'homme and Yoshimura [1984] measured yield stress directly by using a stress rheometer and an eight bladed vane device like Boger's apparatus [1983]. The stress rheometer was used to apply a constant torque to the vane device (a Couette apparatus with the inner cylinder having vanes) and monitor its position. The shear stress at the cylindrical surface which encompasses the blade edges could be calculated from the known torque, and the lowest stress at which the vane position changed continuously with time was taken as the yield

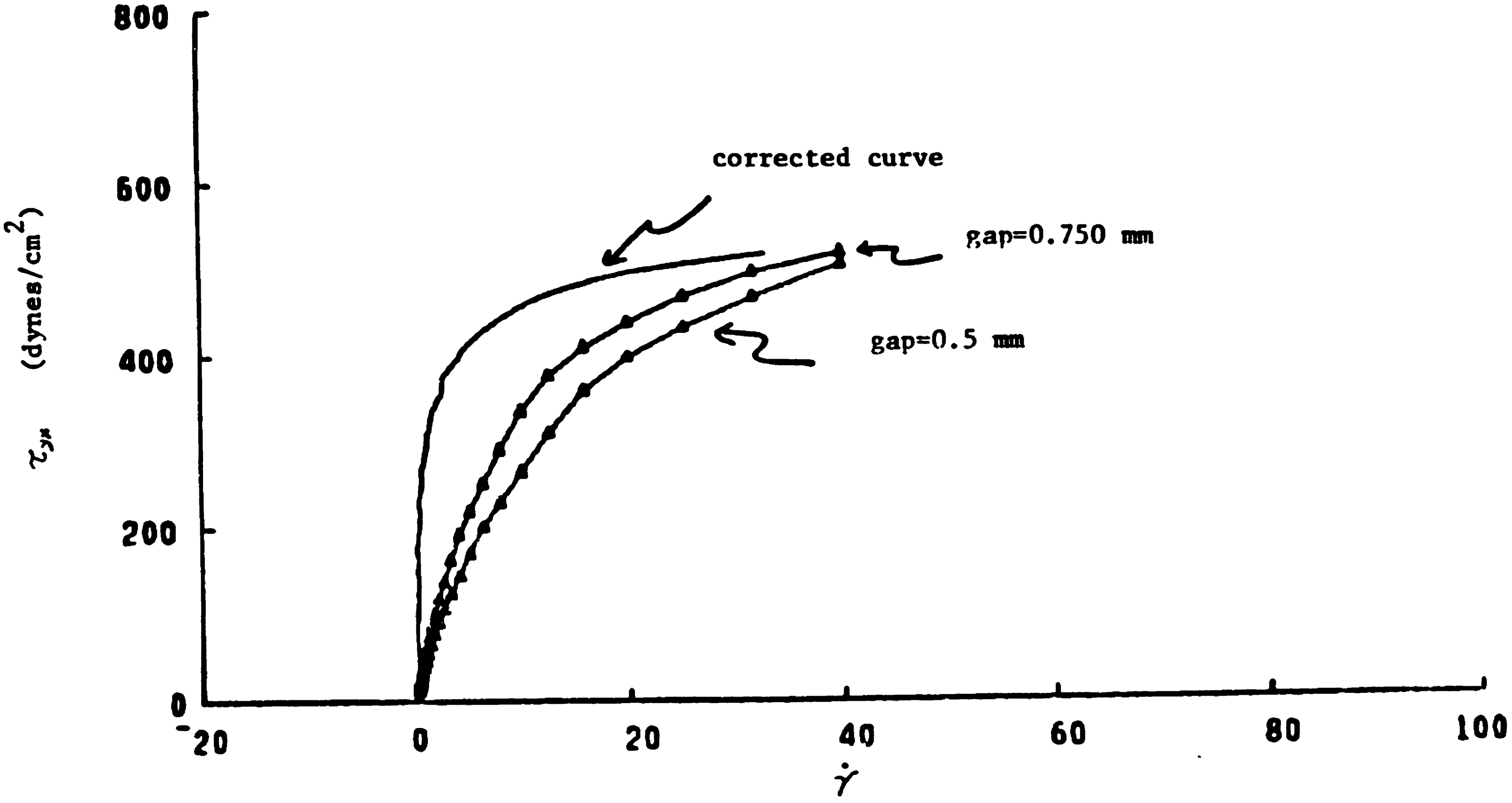

Figure I-6 Shear stress vs. shear rate curves of emulsions at two different tube radii [Prud'homme and Yoshimura, 1984]. Note that corrected curve predicts a yield stress of 450 dynes/cm^2. Here, ϕ=.92 and average bubble diameter equals 24μm.

stress. Figure I-7 shows a typical experimental plot for the same emulsion. Note from the two plots (Figure I-6, 7) that the yield stress values are different.

The final set of experiments dealt with observing the dynamic behavior of emulsions at large strains. Using a forced oscillation technique, they observed non-sinusoidal stresses on applying sinusoidal strains. They used their slip layer theory along with the assumption that the bulk fluid behaved like a Voight element to simulate such flows and found very good qualitative agreement with experimental results.

Kraynik's work involves both experiments and modelling. For his experimental study [1982] he used a capillary viscometer to measure the viscosity of foam (the other two studies have been with emulsions) and corrected for wall slip in his analyses. He used long tubes with large diameters (1 inch) to avoid the problems of compressibility and cell size effects. He also developed a new technique to measure yield stresses. In his method, a large gas bubble (~1cm diameter) is injected into the foam near the tube wall (Figure I-8). For each run the stress is measured, while from the relative motion between this bubble and a foam cell near the wall one determines whether the stress in foam is below or above the yield point. For stress smaller than the yield stress, there is no relative motion between the bubbles as the foam flows like a plug with all shearing going on in the thin wall films. For $\tau > \tau_y$, the large gas bubble being close to the center line is dragged faster. One can thus pinpoint the yield point from a few set of experiments. Figure I-9 shows such a yield stress plot for different gas volume fraction. A point to note here is that film formation is an important component

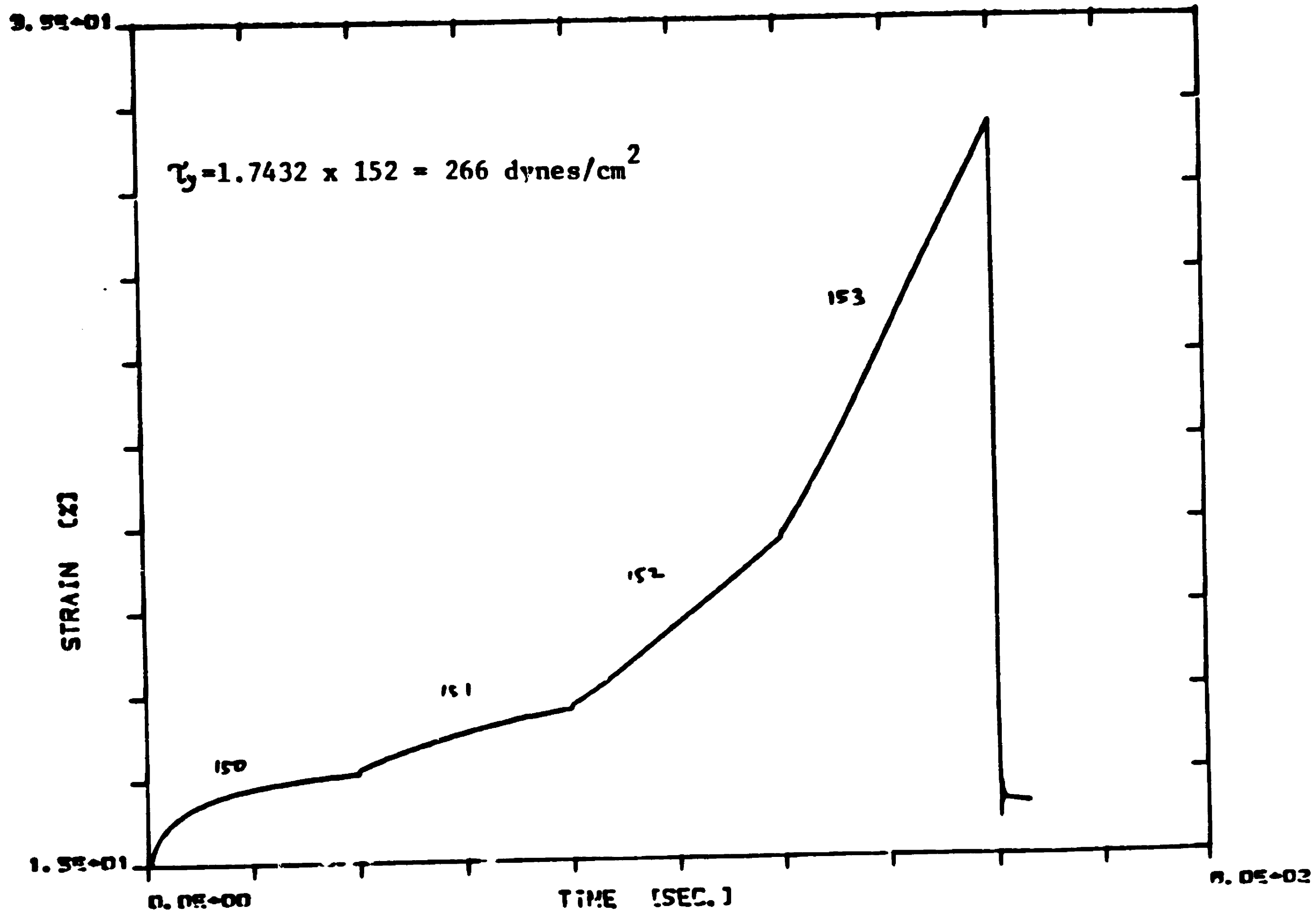

Figure I-7 Yield stress measurement of an emulsion (ϕ=.92) using the stress rheometer. The numbers are proportional to the constant torque applied during each time interval [Yoshimura and Prud'homme, 1984].

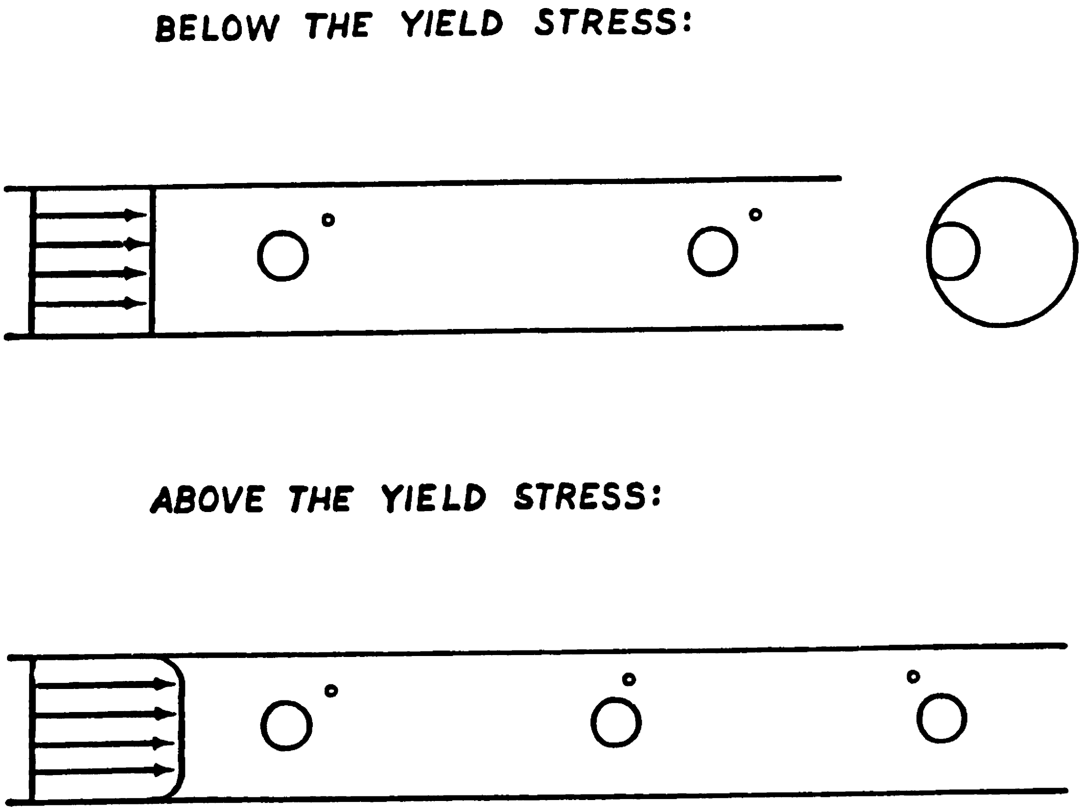

Figure I-8 Flow visualization technique used to measure yield stress in foam. Relative movement between bubbles is indicative of stresses above yield point [Kraynik, 1982].

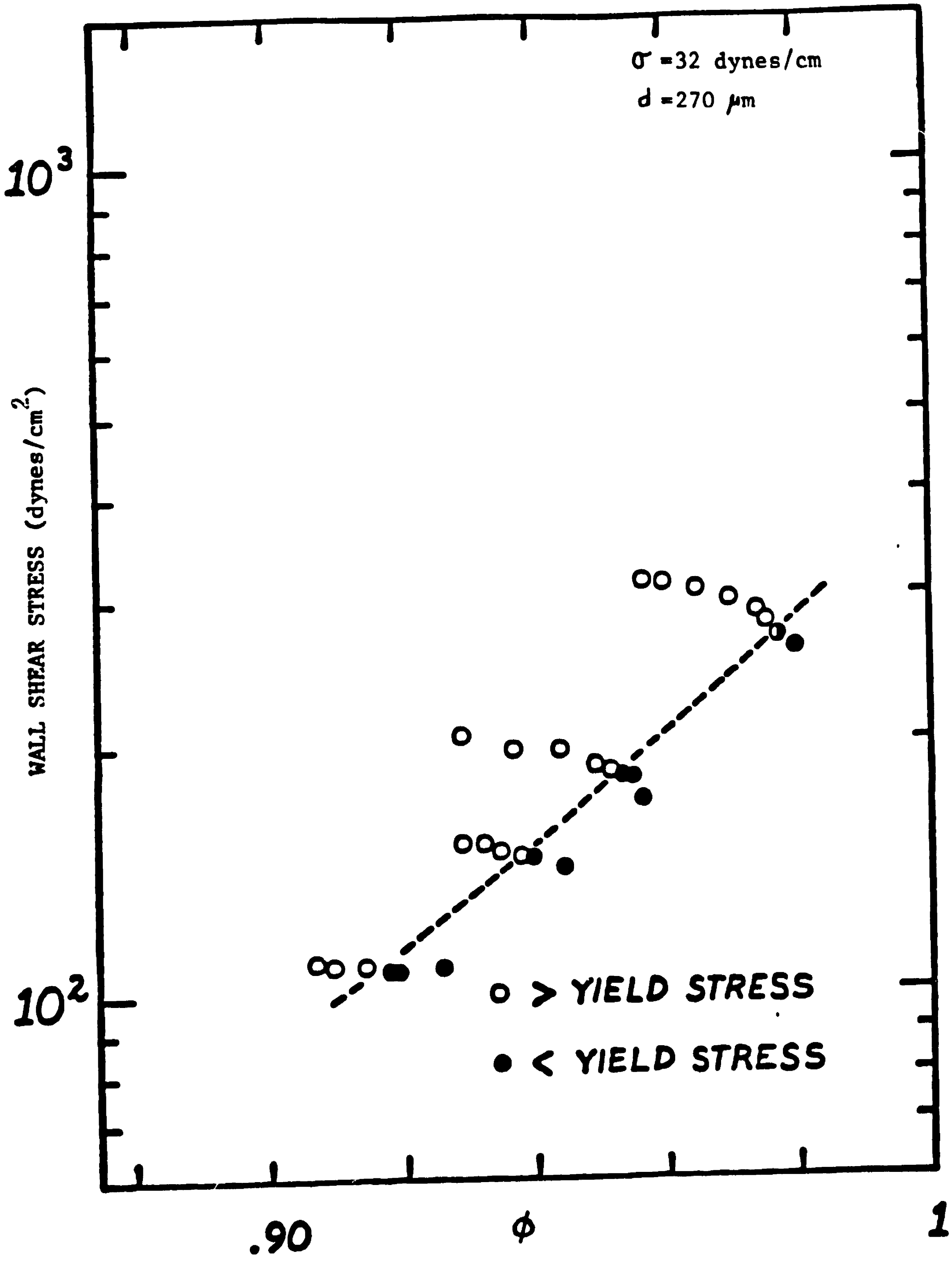

Figure I-9 Yield stress measurement using Bubble Injection Flow Visualization technique [Kraynik, 1982]. σ and d represent interfacial tension and average bubble diameter respectively.

in this technique. One has to be a little careful for stresses slightly larger than τ_y because the drag on the large bubble distorts the flow around it and may affect the motion (accelerate) of the foam cell. This may decrease or prevent relative motion between the two leading one to mistake the stress as lower than τ_y. Recently, Kraynik is engaged in modelling large deformations of foam.

C. SCOPE OF WORK

The object of this study is to examine and understand the rheological behavior of foam. We have primarily focussed on studying the shear flow properties of foam since these are most important in engineering and processing applicatons and since they are most amenable to experimental verification. In this research, two general areas have been considered:

1) Rheological model describing structure-property relationship in foam

2) Experimental Characterization of foams

The first part of this study involves developing a rheological model for foam in terms of its intrinsic properties: bubble size, gas volume fraction, liquid surface tension, liquid film viscosity. The modelling work presented in this thesis parallels its evolution with each successive model adding more complexity to the initial simplified, analytic model.

In the experimental phase of the research, experiments were designed to study systematically the dependence of the different shear flow properties of foam on shear rate. Time dependent experiments were also done. We developed methods to directly check the existence of as well as measure the value of the yield stress in foam. The influence of gas volume fraction in foam on these material functions were also be examined. Finally, the predictive ability of the model was checked against experimental data.

In Chapter II of this thesis, we develop a simple analytic model for foam rheology relating macroscopic material functions to the microstructure. We consider two-dimensional, monodisperse, hexagonal foam cells of any arbitrary initial cell orientation, and interfacial tension along the films to be the only dominant force. However, we restrict ourselves to gas volume fractions approaching unity and to low shear rates so that equilbrium conditions are preserved at any deformed state.

In Chapter III, we relax some of the restrictions of the first model by looking at polydispersity. Calculations are done here for a bimodal cell size distribution and for cells having irregular structures. We also look at higher deformation rates where equilibrium conditions may no longer prevail as viscous forces in films become finite. As before, this chapter also deals with gas volume fraction approaching unity.

In Chapter IV, the effect of gas volme fraction on rheology is studied. We confine our 2-D model to gas fractions ranging from 0.9069 for the hexagonally close packed systems to unity. The cells are therefore made of curved Plateau borders joined by straight line edges. Two cases are studied here. In the first, we consider negligible film (straight line portion) thickness with all liquid confined in the Plateau borders. In the second case, we consider films of finite thickness and use liquid film theory to relate the thickness to the radius of the Plateau border.

In the final phase of the modelling work (Chapter VII), we study large deformations of foam for both, very small (equilibrium conditions) and finite deformation rates.

Chapters V and VI cover all the experimental details of this research. We focussed on steady and dynamic shear flow experiments to evaluate the viscoelastic properties of foam. In Chapter V, we discuss a method to generate stable, reproducible foam along with techniques to measure its material properties. Because of the nature of foam, commercially available rheological equipments are inadequate to measure its properties. In Chapter VI, results of all experiments are presented and compared with model predictions.

II. MODEL FOR DRY FOAM

The goal of this chapter is to develop a rheological model for foam in terms of some of its intrinsic porperties i.e. cell size, liquid film viscosity, and interfacial tension. We restrict ourselves to gas volume fraction (ϕ) approaching unity and to very low shear rates. In this model we assume monodisperse, hexagonal foam cells of any arbitrary initial orientation and derive analytic expressions for stresses for small shearing and elongational deformation (up to the yield point) as well as for steady shear flow. For strains below the yield point, we look at the influence of initial cell orientation on the stress-strain relation for shear, normal and elongational stresses. In steady shear flow, unlike any previous models we take into account the influence of liquid film viscosity and derive a simple analytic expression for the foam viscosity.

Our approach to this problem is: i) to first determine the "micromechanics" or the actual cell structure for any arbitrary applied deformation based on the kinematics, ii) relate this information to the macroscopic variables i.e. the stresses, and finally, iii) to derive explicit material functions for certain specific flows mentioned earlier. The first two calculations form the subject matter for next section while the last one is derived in the following one.

A. MODEL AND GOVERNING EQUATIONS

1. Assumptions

In order to derive a stress-strain relation for foam, we make the following assumptions:

1. The foam cells are monodisperse, two dimensional hexagons (Figure II-1). Thus, one can visualize foam as a collection of infinitely long cylinders with hexagonal faces. The choice for hexagonal cells in two dimension is obvious because it is the only structure that meets all equilibrium criteria i.e. satisfy the force balance along the liquid films and have minimum surface energy.

2. There is negligible liquid hold up in the liquid films, i.e. the gas volume fraction, ϕ, is unity.

3. Film drainage and mass transfer are negligible while heat transfer is infinitely fast. Negligible drainage assures no wall thinning, and hence no cell rupture or coalescence. Further, with no mass transfer, bubble sizes remain constant with time as there is no diffusion of gas between bubbles. Fast heat transfer ensures isothermal conditions.

4. Since the foam cells are spatially periodic, for any deformation, the mid-points or the centroid of the hexagonal cells move affinely with the bulk. Because of geometric symmetry, this also ensures that the midpoint of each liquid film moves affinely. Further, in any deformation, the gas-liquid interfaces always remain planar. This follows from Young and Laplace's equation [Rosen, 1978; Hiemenz, 1977].

5. Total cell volume is always conserved, that is, we consider only constant volume deformations. For the two dimensional case, this means that the area of the hexagons remain constant.

6. At equilibrium, the only force acting on the cells is the interfacial tension, 2σ, along each liquid film. Effect of gravity is thus neglected. However, as the system undergoes deformation, there will be viscous forces acting along the films too. We assume the deformation to be slow

enough so that these viscous forces, which depend on deformation rate, will be very small and will not affect the structure of the cells in any way. The system can therefore be considered to be always at equilibrium.

7. In order for the foam to be stable, only three liquid films can meet at a point with an angle of 120 degrees between adjacent films [Bickerman, 1973]. This 120 degree criterion, which follows from a force balance at the Plateau border and ensures minimum surface energy, is preserved in any deformation. Loss of this leads to instability.

2. Cell Deformation and Micromechanics

From the assumptions that the midpoint of the liquid films move affinely with the bulk and that the 120 degree angle between films are always preserved, we can determine the cell deformation for any applied deformation based on kinematics only.. Let us, for modelling purposes, define a 'unit cell' as the smallest repeat structure possible in foam. This is the dashed parallelogram in Figure II-1. If we consider the undeformed hexagonal foam cells to have sides of length 'a', the area of this unit cell is $3\sqrt{3}a^2/4$. Since we are working with 2-D structures all equations in this chapter will be in terms of unit length in the infinite direction.

Let us consider hexagonal foam cells confined between two parallel plates under an applied deformation. To derive the microstructure we choose a triangular subcell within the unit cell (Figure II-1b) formed by joining the midpoints of three adjacent liquid films. Such a choice has been found to simplify calculations. Further, the rest of the unit cell contains no liquid film and can be ignored. Let us consider ΔABC

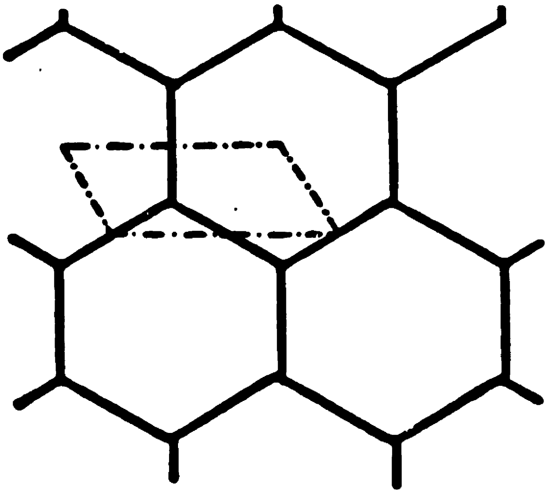

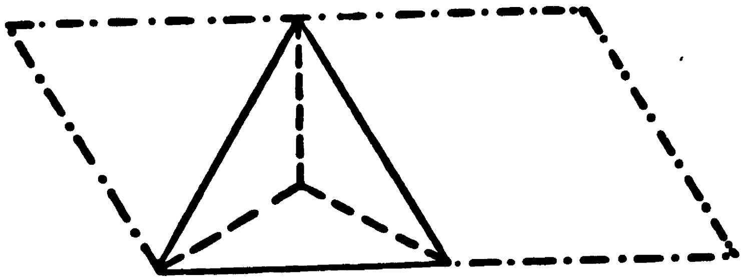

UNIT CELL WITH TRIANGULAR SUB-CELL

Figure II-1 Schematic of foam cells and unit cell. The parallelogram represents the unit cell and the dashed lines the liquid films.

in Figures II-2, 3 to be the subcell with OA, OB, OC denoting the liquid films. Thus L, the total length of the three films are given by L = OA + OB + OC . In these two figures, which show the subcell deformation for shear and elongational flows respectively, structures 2a and 3a as drawn represent a specific initial orientation of foam, namely that of Figure II-1a with no strain applied. We will refer to this orientation as the 0° orientation. Our goal here is to obtain the cell structure for any initial orientation and deformation. In order to do so, we embed two vectors $\underline{b}_1^{o}$ and $\underline{b}_2^{o}$ along sides AB and AC of ΔABC in Figures II-2a, 3a. We choose A to be the origin in our x-y coordinate system and initially have OA=OB=OC=a/2. Defining β^{o} as the matrix representation for the two vectors, we have:

$$\underline{\underline{\beta}}^{o} = (\underline{b}_1^{o}, \underline{b}_2^{o})^{\dagger} \qquad \text{II-1}$$

Since A, B, C are mid-point of nodes, they move affinely. Continuum fluid mechanics can therefore be applied on these points. Thus, A, B, C, or equivalently the vectors $\underline{b}_1$, $\underline{b}_2$ for any orientation and deformation can be found by rotating ΔABC counterclockwise by an angle θ (Figures II-2b, 3b) around point A and then applying an arbitrary deformation defined tensorially by E (Figures II-2c, 3c). Mathematically this is equivalent to

$$\underline{\underline{\beta}} = \underline{\underline{E}}\cdot\underline{\underline{\Omega}}\cdot\underline{\underline{\beta}}^{o} \qquad \text{II-2}$$

where $\underline{\underline{E}}$, $\underline{\underline{\Omega}}$ are respectively the displacement gradient and rotation tensors given by [Bird, Armstrong and Hassager, 1977]:

$$E_{ij} = \frac{dx_i}{dx_j}, \qquad \text{II-3}$$

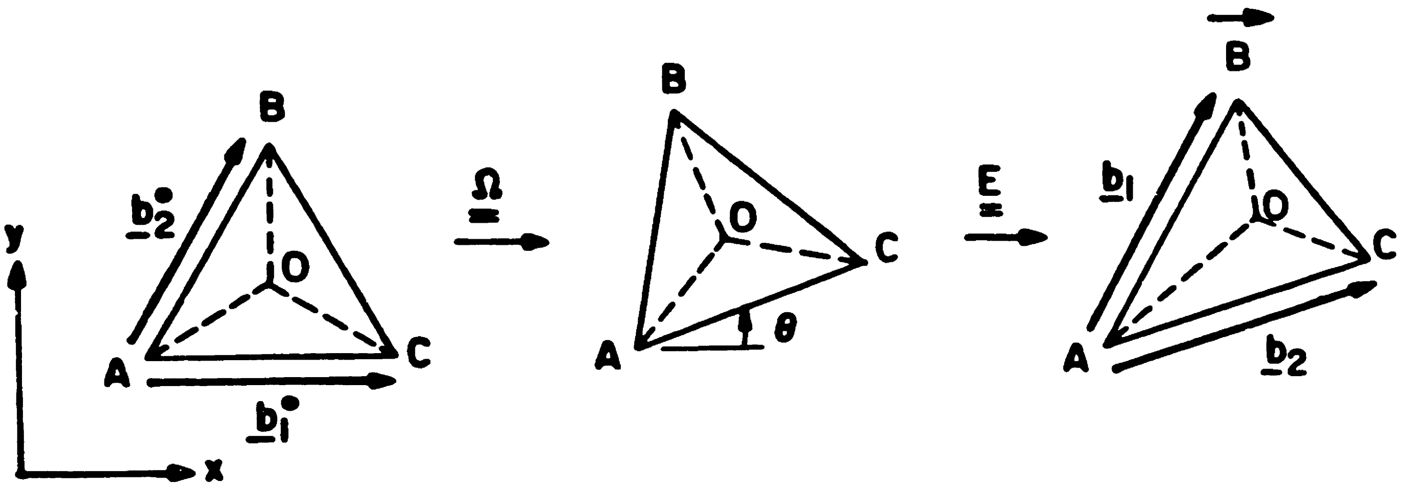

$$L = |OA| + |OB| + |OC|$$

Figure II-2 Triangular subcell used to calculate stress-strain relation in shear flow. Dashed lines represent liquid films. Ω, E are the rotation and deformation gradient tensors. Points A, B, C move affinely with the bulk.

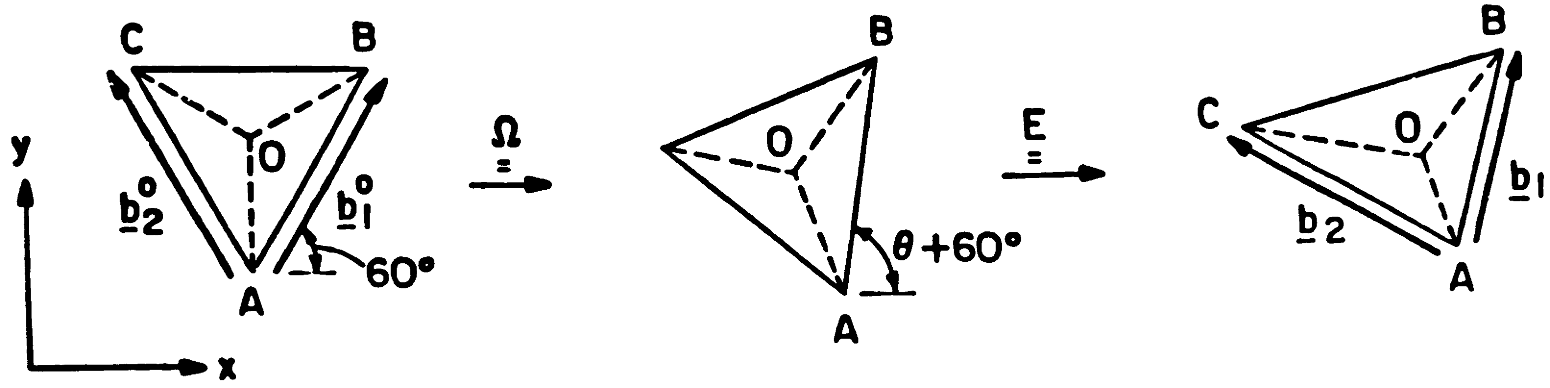

Figure II-3 Calculation of microstructure for elongational deformation given by $x = x_o e^{\varepsilon}$, $y = y_o e^{-\varepsilon}$. Note that the inital cell orientation is the same as in Figure II-2.

$$\underline{\underline{\Omega}} = \begin{vmatrix} \cos\theta & -\sin\theta \\ \sin\theta & \cos\theta \end{vmatrix} \qquad \text{II-4}$$

β is the matrix representation of $\underline{b}_1$, $\underline{b}_2$ for any orientation and strain. x_j', x_i denote Cartesian components of a particle position at present time t and past time t'.

Thus, as will be seen later, once the deformation is specified and E is known we can get β explicitly.

Thus far the coordinates of A, B and C have been found as functions of orientation and deformation using the affine motion assumption. In order to obtain the cell structure, we still need to know the coordinates of the node O. Let this have coordinates x, y given by the position vector $\underline{X}$. Therefore, embedding three vectors $\underline{g}_1$, $\underline{g}_2$ and $\underline{g}_3$ along OA, OB and OC respectively, we have:

$$\begin{aligned} \underline{\underline{G}} &= (\underline{g}_1, \underline{g}_2, \underline{g}_3)^{\dagger} \\ &= (-\underline{X}, \underline{b}_1-\underline{X}, \underline{b}_2-\underline{X})^{\dagger} \end{aligned} \qquad \text{II-5}$$

Since $\underline{g}_1$, $\underline{g}_2$, $\underline{g}_3$ always make 120 degrees with each other, we use the following relations to get the coordinates of O.

$$\frac{\underline{g}_1 \times \underline{g}_2}{\underline{g}_1 \cdot \underline{g}_2} = \frac{\underline{g}_3 \times \underline{g}_1}{\underline{g}_3 \cdot \underline{g}_1} = \sqrt{3}\ \underline{\delta}_z \qquad \text{II-6}$$

From these, we get two quadratic relations between x and y which when solved specifies point O in terms of components of $\underline{\underline{\Omega}}$ and $\underline{\underline{E}}$. Thus, we are able to completely describe the microstructural motion once the deformation is specified.

3. Derivation of Stresses

The goal of this section is to relate the microstructural deformation to the applied stresses. Two independent methods are used to derive the stresses: the work-energy concept and the force projection approach.

i) WORK-ENERGY CONCEPT

Our analysis is based on the fact that the work required to deform the foam cells is equal to the change in free energy of the foam microstructure. Consider the foam unit cell in Figure II-1b with the three liquid films, and also a continuum enclosed by this unit cell. To the latter let us apply an arbitrary, infinitesimal, homogeneous deformation such that the position vector of a typical particle in the macroscopic continuum changes from $\underline{r}$ to $\underline{r}'$, where $\underline{r}' = \underline{r} + d\underline{r}$ and

$$d\underline{r} = \underline{\underline{\alpha}} \cdot \underline{r} \qquad \text{II-7}$$

$\underline{\underline{\alpha}}$ is therefore the deformation gradient tensor. Thus, once we specify the kind of deformation, say for example shear, we can determine $\underline{r}$ and $d\underline{r}$ and hence obtain α explicitly.

The work done per unit length on applying this deformation to the continuum takes the more generalized form [Bird, et al., 1977]:

$$dW = (\underline{\underline{\tau}} : \underline{\underline{\alpha}})\, S \qquad \text{II-8}$$

where,

dW = differential work

$\underline{\underline{\tau}}$ = stress tensor

$\underline{r}$ = position vector

S = area of unit cell

This work done also equals the change in free energy of the foam microscruture in the unit cell, and is given by the product of the force along each liquid film and the change in area over which it is acting, summed over all three films. For our 2-D case, area corresponds to the length of the liquid films in a unit cell. Thus, dA, the change in energy/unit length is given by:

$$dA = \Sigma F_i \, dl_i \qquad \text{II-9}$$

where,

l_i is the length of the ith film and F_i the force along this film. The summation is over the three films in the unit cell.

There are two parts to the force term: the interfacial tension, 2σ, which is same for all films and a viscous force term $F_{\mu i}$. Correspondingly, there are two modes of energy change in foams, one arising from surface forces and the other from the viscous dissipation in the films. One can thus rewrite Equation II-9 as

$$dA = 2\sigma \, dL + F_{\mu i} \, dl_i \qquad \text{II-10}$$

where,

L is the total liquid film length in a unit cell, and, repeated indices denote summation over the films.

We will not delve into the exact form for the viscous stress term here. Suffice it to say though that since the liquid films undergo an extensional motion for any macroscopic deformation, this stress will be proportional to the Hencky elongation rate of the films [Bird, Armstrong and Hassager, 1977]. This in turn is related to the invariant of the rate of strain tensor. Since most of the chapter deals with very small deformation rates where equilibrium conditions prevail, this term can be justifiably ignored. We will, however, take this viscous stress term into account when we extend our model to derive expressions for the steady shear viscosity.

For an isothermal deformation, dA=dW [Treolar, 1967]. This gives:

$$(\underline{\underline{\tau}}:\underline{\underline{\alpha}})\, S = 2\sigma\, dL + F_{\mu i}\, dl_i \qquad \text{II-11}$$

Thus, once the deformation is specified, we can get α explicitly from Equation II-7 as well as information about the films from the micromechanics. The stresses can then be obtained from the above relation.

ii) FORCE PROJECTION APPROACH

Since work and energy are scalar quantities, the approach used in the last section cannot in general supply information about the total stress tensor. In this section, therefore, we use vectors i.e. forces along the liquid films, to obtain the stress tensor. A similar approach has been used by Kraynik [1984] in his foam model. Our work is built on some of the ideas from polymer kinetic theory of Hookean Dumbbell models [Bird, Hassager, Armstrong and Curtiss, 1977].

Consider a surface with a unit normal vector $\underline{n}$ and tangential vector $\underline{t}$. Center around this surface a square cell having the same area as the unit foam cell. Such a square area ensures that it encloses foam films having the same gas fraction as the foam, on the average. Let $\sqrt{S}$ denote the sides of the square in the $\underline{n}$ and $\underline{t}$ directions respectively. The probability that film $\underline{g}_i$ cuts the plane ($\underline{n}$) is [Bird, Hassager, Armstrong and Curtiss, 1977]:

$$\frac{(\underline{n}\cdot\underline{g}_i)}{\sqrt{S}} \qquad \text{II-12}$$

where,

$\underline{g}_i$ is the vector representation of the ith film.

The associated force in the film is $F_i\ \underline{g}_i/g_i$ and the area over which the force is applied is $\sqrt{S}$. So the contribution to the stress tensor from film i is:

$$\underline{\underline{\tau}}\cdot\underline{n} = \frac{F_i\ \underline{g}_i(\ \underline{n}\cdot\underline{g}_i)}{g_i\ S} \qquad \text{II-13}$$

It should be noted that we could have used a rectangle instead of a square because the actual lengths of the sides do not matter as long as the area is that of the unit foam cell. Thus, on rearrangement, we get the following expression for the stress tensor:

$$\underline{\underline{\tau}} = \sum \frac{F_i}{S}\,\frac{\underline{g}_i\ \underline{g}_i}{g_i} \qquad \text{II-14}$$

Since all g's are known from the kinematics, the stress can be easily calculated.

B. SMALL DEFORMATIONS BELOW THE YIELD POINT

1. Shear, Normal and Yield stresses

Stress-strain relations for small shearing deformations applied to foam are developed here. We consider the deformation of hexagonal foam cells confined between two parallel plates under an applied shear strain γ. For such a deformation, the micromechanics can be easily determined from the equations of the previous section. For shearing flows,

$$\underline{\underline{E}} = \begin{vmatrix} 1 & \gamma \\ 0 & 1 \end{vmatrix} \qquad \text{II-15}$$

From Figure II-2a, and Equation II-1, we get $\underline{\underline{\beta}}^o$ to be:

$$\underline{\underline{\beta}}^o = (\underline{b}_1{}^o, \underline{b}_2{}^o)^\dagger$$

$$= a \begin{vmatrix} \sqrt{3}/4 & \sqrt{3}/2 \\ 3/4 & 0 \end{vmatrix} \qquad \text{II-16}$$

Thus using Equation II-2, we get $\underline{b}_1$, $\underline{b}_2$ for any orientation and strain:

$$\underline{b}_1 = a\sqrt{3}/2 \{ [\cos(\theta+60) + \gamma \sin(\theta+60)] \underline{\delta}_x + \sin(\theta+60) \underline{\delta}_y \}$$

$$\text{II-17}$$

$$\underline{b}_2 = a\sqrt{3}/2 \{ [\cos\theta + \gamma \sin\theta] \underline{\delta}_x + \sin\theta \underline{\delta}_y \}$$

where $\underline{\delta}_x$ and $\underline{\delta}_y$ are the unit vectors in the x and y directions respectively.

Thus far the coordinates of A, B and C have been found as functions of θ and γ using the affine motion assumption. In order to find the cell structure, we still need to know the coordinates of the node O. Using Equation II-6, we get the following quadratic relations between x and y, the coordinates of O:

$$x^2 + y^2 - a/2 [\sqrt{3} \cos\theta + \gamma\sqrt{3} \sin\theta + \sin\theta] x$$

$$- a/2 [\sqrt{3} \sin\theta - \cos\theta - \gamma \sin\theta] y = 0 \qquad \text{II-18a, b}$$

$$x^2 + y^2 - a/2\ [\ \sqrt{3}\cos(\theta+60) - \sin(\theta+60) + \gamma\sqrt{3}\sin(60+\theta)\ ]\ x$$
$$-\ a/2\ [\ \cos(60+\theta) + \sqrt{3}\sin(60+\theta) + \gamma\sin(60+\theta)\ ]\ y = 0$$

Solving the above equations, we get for point O, the coordinates

$$x:\quad a\ [\gamma\sin(\theta+30) + 2\cos(\theta+30)]\ K\ /\ [4 + \gamma^2]$$
$$y:\quad a\ [2\sin(\theta+30) - \gamma\cos(\theta+30)]\ K\ /\ [4 + \gamma^2] \qquad \text{II-19}$$

where, $K = \{\ 1 + \gamma\sin(2\theta+60) + \gamma^2\ [1 - 2\cos(2\theta+60)]/4\ \}$

The vectors $\underline{g_i}$ are obtained from Equation II-5 and the lengths of $\underline{g_1}$, $\underline{g_2}$ and $\underline{g_3}$ are then found after considerable algebraic manipulation to be:

$$g_1 = a\ K\ /\ \sqrt{(4 + \gamma^2)} \qquad \text{II-20a, b, c}$$

$$g_2 = a\ [1 - \gamma\sin(2\theta) + \gamma^2\sin(60+\theta)\cos(\theta+30)]/\sqrt{(4 + \gamma^2)}$$

$$g_3 = a\ [1 - \gamma\cos(2\theta+30) - \gamma^2\sin(\theta)\cos(\theta+30)]/\sqrt{(4 + \gamma^2)}$$

Since we have all the structural information now, let us look at the actual cell deformatiom. Figure II-4 shows such a deformation for initial orientation $\theta=0^{\circ}$. Initially, each side has length "a" (Figure II-4a). Let us label three sides as 'a', 'b' and 'c'. As the cells deform, the three liquid films still meet at 120 degrees. Moreover, the mid-point between nodes move affinely. Under these conditions, side 'a' shrinks while 'b', 'c' elongate (Figure II-4b). With increasing strain a critical point is reached at which side 'a' reduces to zero

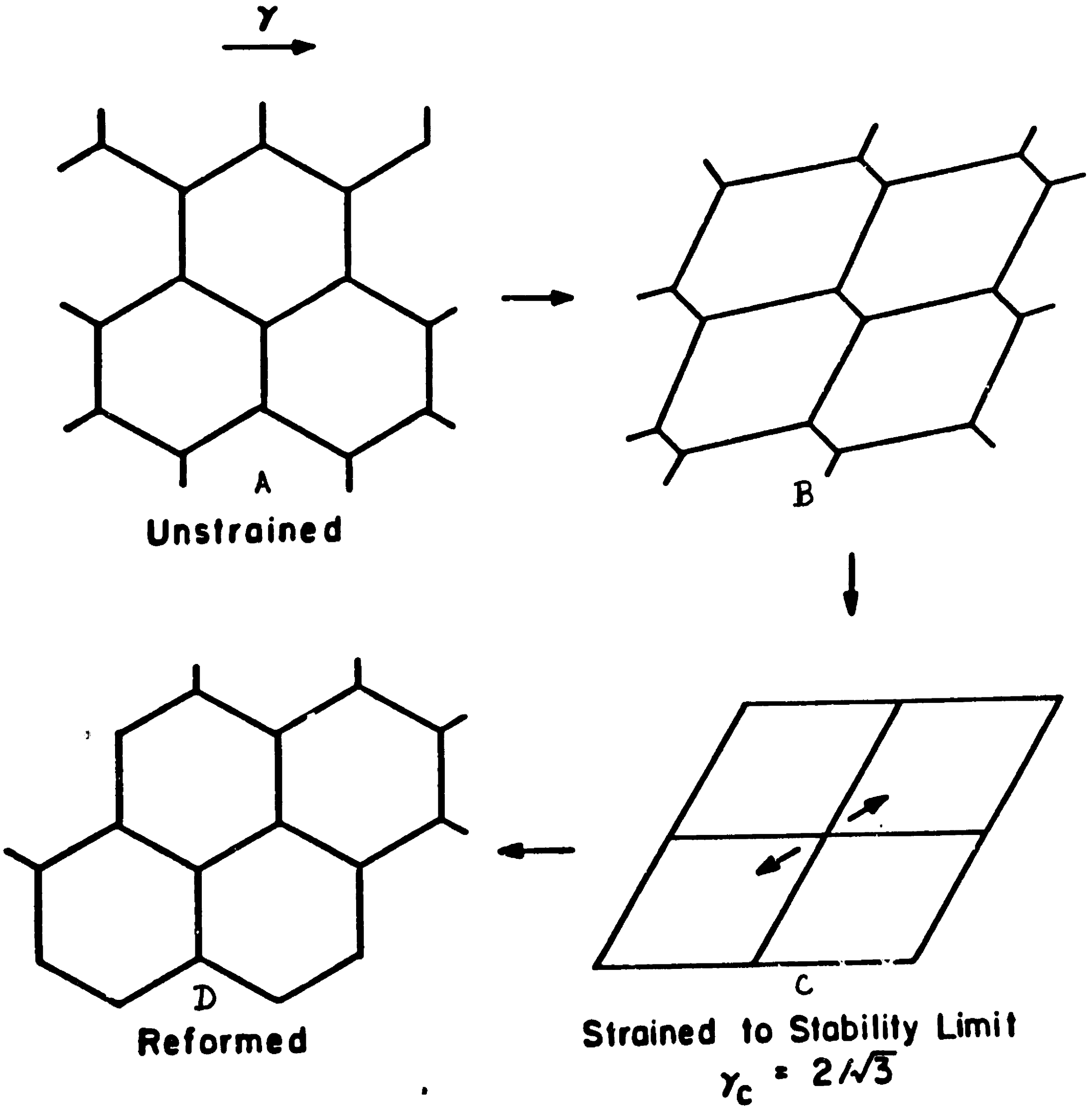

Figure II-4 Shear deformation in foam cells. Increasing strain in clockwise direction. Initial cell orientation $\theta = 0^\circ$.

length (Figure II-4c). The 120 degree angle criterion can no longer be preserved and the bubbles have reached their stable limit; they then reform (Figure II-4d). The stress corresponding to this critical strain is the yield stress. Figure II-5 shows foam deformation for a different initial cell orientation. The same criteria hold as before and the yield point is reached when side 'a' reduces to a point. The figure also reveals that deformed cells look quite different depending on their initial orientation. Comparison of the two figures indicates that the critical strain is a function of orientation.

In order to have a stress-strain equation describing this motion up to the critical point, we first use the work-energy equation derived in the previous section.

In a simple shear, $\underline{\underline{\alpha}}$ assumes the form:

$$\underline{\underline{\alpha}} = \begin{vmatrix} 0 & d\gamma \\ 0 & 0 \end{vmatrix} \qquad \text{II-21}$$

Equation II-10 in this case becomes:

$$\tau_{yx} = \frac{2\sigma}{a} \; \frac{4}{a3\sqrt{3}} \; \frac{dL}{d\gamma} \qquad \text{II-22}$$

where we assumed $F_{\mu i}$ to be negligible. From the kinematics we have found the lengths of the liquid films as functions of strain (Equation II-20). Thus,

$$\frac{dL}{d\gamma} = \frac{3}{4}a \; \frac{\gamma}{\sqrt{(\gamma 2 + 4)}} \qquad \text{II-23}$$

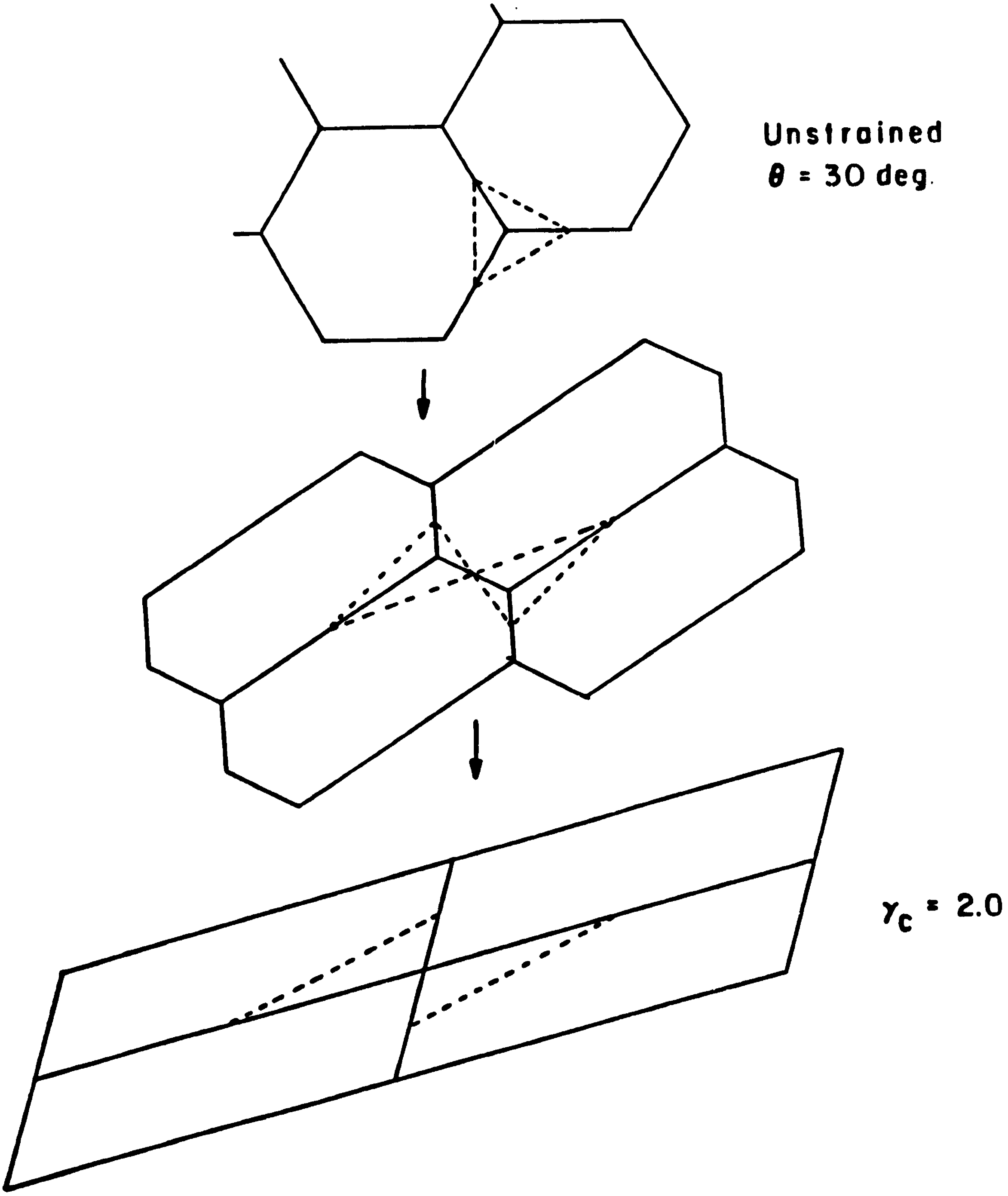

Figure II-5 Effect of initial orientation on critical strain and cell structure in a shearing deformation. $\theta = 30^\circ$ in this case.

and,

$$\tau_{yx} = \frac{2\sigma}{a} \frac{\gamma}{\sqrt{(3\gamma^2 + 12)}} \qquad \text{II-24}$$

This is the equation of state that describes the shear deformation of foam up to the critical point. An important thing to realize here is that the work-energy approach enabled us to calculate only the shear stress. Because of the scalar nature of the method, we lost all information on the normal stresses.

Using the force projection approach, however, we can get the entire stress tensor simultaneously. Equation II-14 reveals that the only information we need to calculate the stresses are the orientations and lengths of the three liquid films in a unit cell. Using them in Equation II-14 we obtain the same expression for the shear stress. For the normal stresses, however, we get:

$$\tau_{xx} - \tau_{yy} = \frac{2\sigma}{S} \Sigma \left[\frac{g_{ix}^2 - g_{iy}^2}{g_i} \right] \qquad \text{II-25}$$

which reduces tc,

$$\tau_{xx} - \tau_{yy} = \frac{2\sigma}{a} \left[\frac{\gamma^2}{\sqrt{(3\ \gamma^2 + 12)}} \right] \qquad \text{II-26}$$

Here, g_{ix} and g_{iy} represent the x and y components of the vector $\underline{g_i}$. S is the unit cell area.

As can be seen, the stress in foam is independent of the initial orientation of the cell. In Figure II-6 are plotted the shear stress and the normal stress difference (N_1) as a function of strain. As can be seen, the shear stress rises faster initially while N_1 does so at a higher strain. The cross over point is at $\gamma=1$. An interesting thing to note from the stress equations is that the ratio τ_{yx}/N_1 equals γ.

In order to get the yield stress, τ_y, we just substitute the critical strain into the shear stress expression. It must be noted here that although the stress-strain relation is independent of cell orientation, the critical strain is a function of orientation; hence, so is τ_y. The critical strain is the smallest value of γ that causes one of the g_i's in Equation II-20 to equal zero. In Figure II-7, which shows plots of critical strain and yield stress as function of initial orientation, we observe a discontinuity at $\theta = 45$ degrees. This can be explained from the fact that for $0^\circ < \theta < 45^\circ$, side OC (Figures II-2, 4, 5) reduces to zero length, whereas for $45^\circ < \theta < 60^\circ$, side OB goes to zero at the critical strain. It must be noted here that $\theta = 0$ and 60 degrees correspond to the same orientation because of the sixfold symmetry in hexagonal cells.

2. Extensional Deformation

Let us consider an extensional deformation in the x direction governed by the Hencky elongation strain ε. When such an extension is applied to the foam cells, the motion of the mid-side nodes is given by [Bird, Armstrong and Hassager, 1977],

$$x = x_o\, e^{\varepsilon} \quad , \; y = y_o\, e^{-\varepsilon} \qquad \text{II-27}$$

where, x, are the positions of a mid-point after an extension, and, x_o,

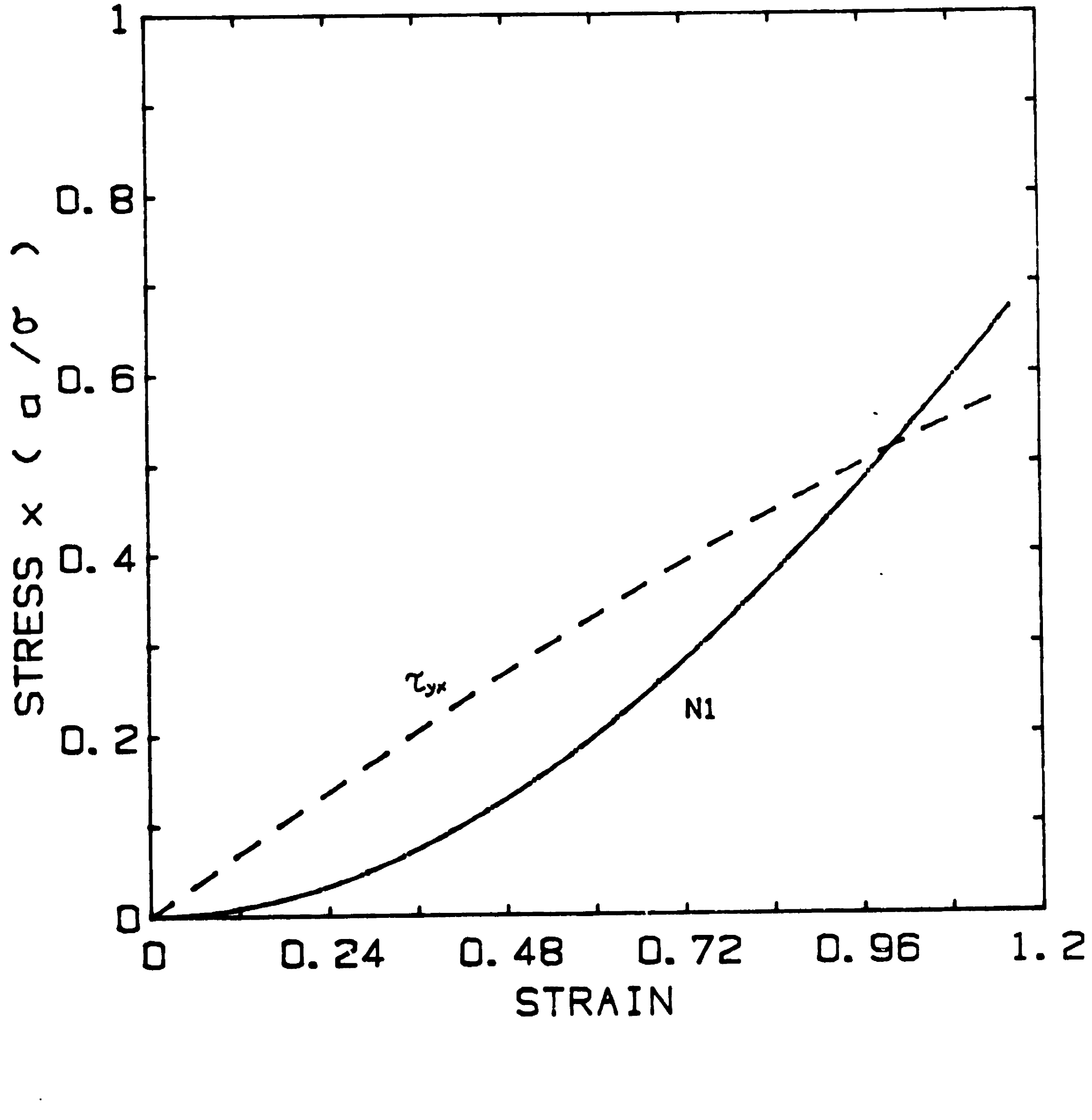

Figure II-6 Shear stress(τ_{yx}) and Normal stress difference(N_1) as a function of strain. γ=1 at the cross over point.

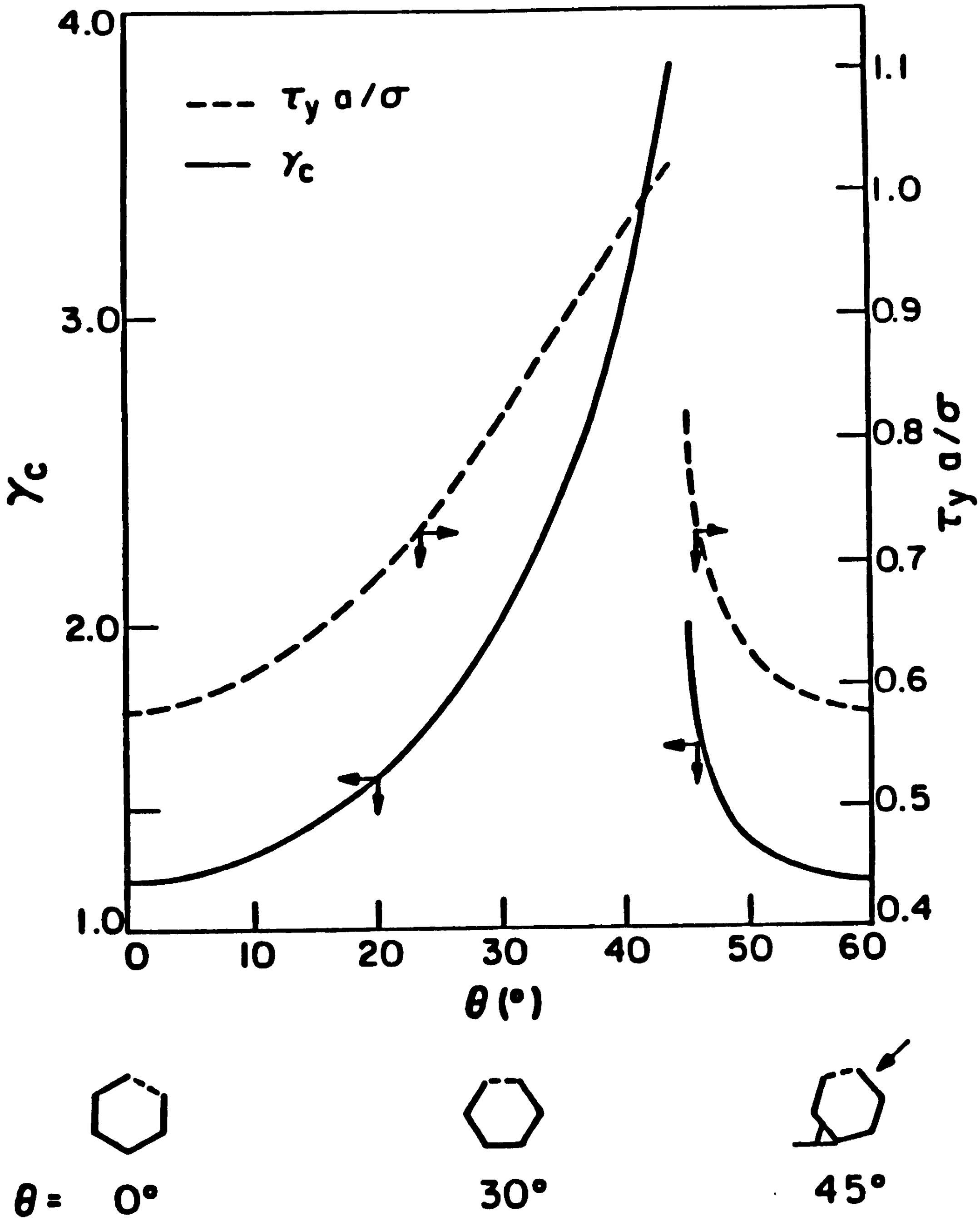

Figure II-7 Critical strain(γ_c) and yield stress(τ_y) as a function of orientation(θ). The stress has been non-dimensionalised by the surface tension(σ) and undeformed cell side length(a).

y_o are the initial coordinates of the mid-point. Further, as the cells deform, the liquid films still meet at 120 degrees. Figure II-8 shows the deformation of foam cells for a specific initial orientation ($\theta = 0^o$) using these two conditions. Initially (Figure II-8a) all cells have sides of equal length. On applying an elongation deformation, one side shrinks while the other two increase in length at the same rate (Figure II-8b). At a critical strain ε_c, one side reaches zero length and the foam has reached its stability limit. The stress corresponding to this point is the elongation yield stress τ_c. In Figure II-9 we see the effect of applying an elongational deformation to a foam for a different initial orientation, $\theta = 30^o$. In this case, one side increases in length with increasing strain and other two sides become shorter (Figure II-9b). However, the latter two sides never reach zero length because of the volume constraint. So, for this orientation, there is no yield stress or critical strain.

In order to describe the elongation deformation of foam, we use Equations II-2 and 3. Here, $\underline{\underline{\beta}}^o$ in Figure II-3 is given by:

$$\underline{\underline{\beta}}^o = (\underline{b}_1 , \underline{b}_2)^{\dagger}$$

$$= a \begin{vmatrix} \sqrt{3}/4 & -\sqrt{3}/4 \\ 3/4 & 3/4 \end{vmatrix} \qquad \text{II-28}$$

On applying a strain ε (Figure II-3c) to ΔABC for any arbritrary initial orientation θ (Figure II-3b), $\underline{\underline{E}}$ is given by:

$$\underline{\underline{E}} = \begin{vmatrix} e^{\varepsilon} & 0 \\ 0 & e^{-\varepsilon} \end{vmatrix} \qquad \text{II-29}$$

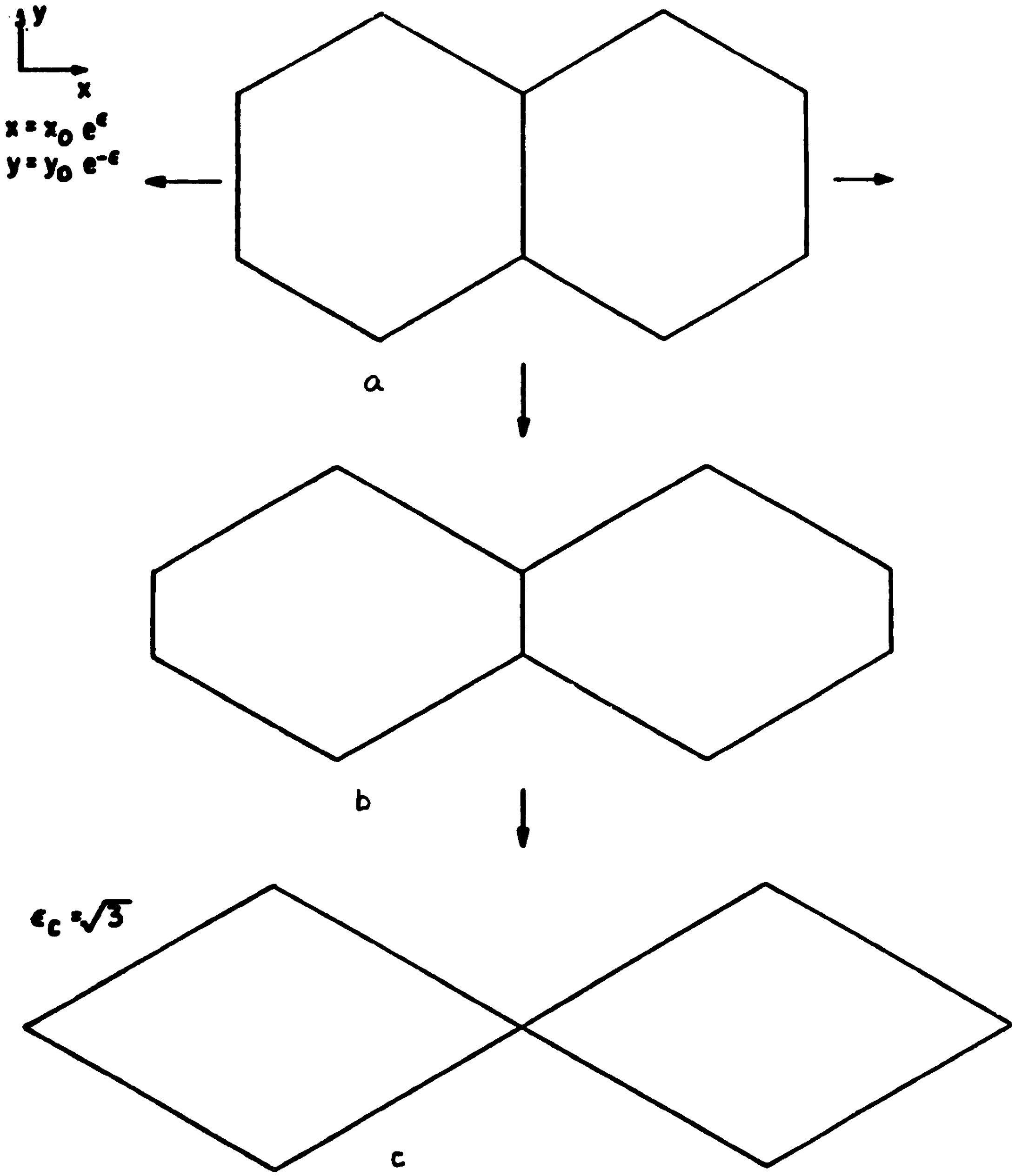

Figure II-8 Cell structure as a function of elongational deformation defined by $x = x_o e^{\varepsilon}$, $y = y_o e^{-\varepsilon}$. ε_c is the critical strain. Initial orientaion, $\theta = 0^o$.

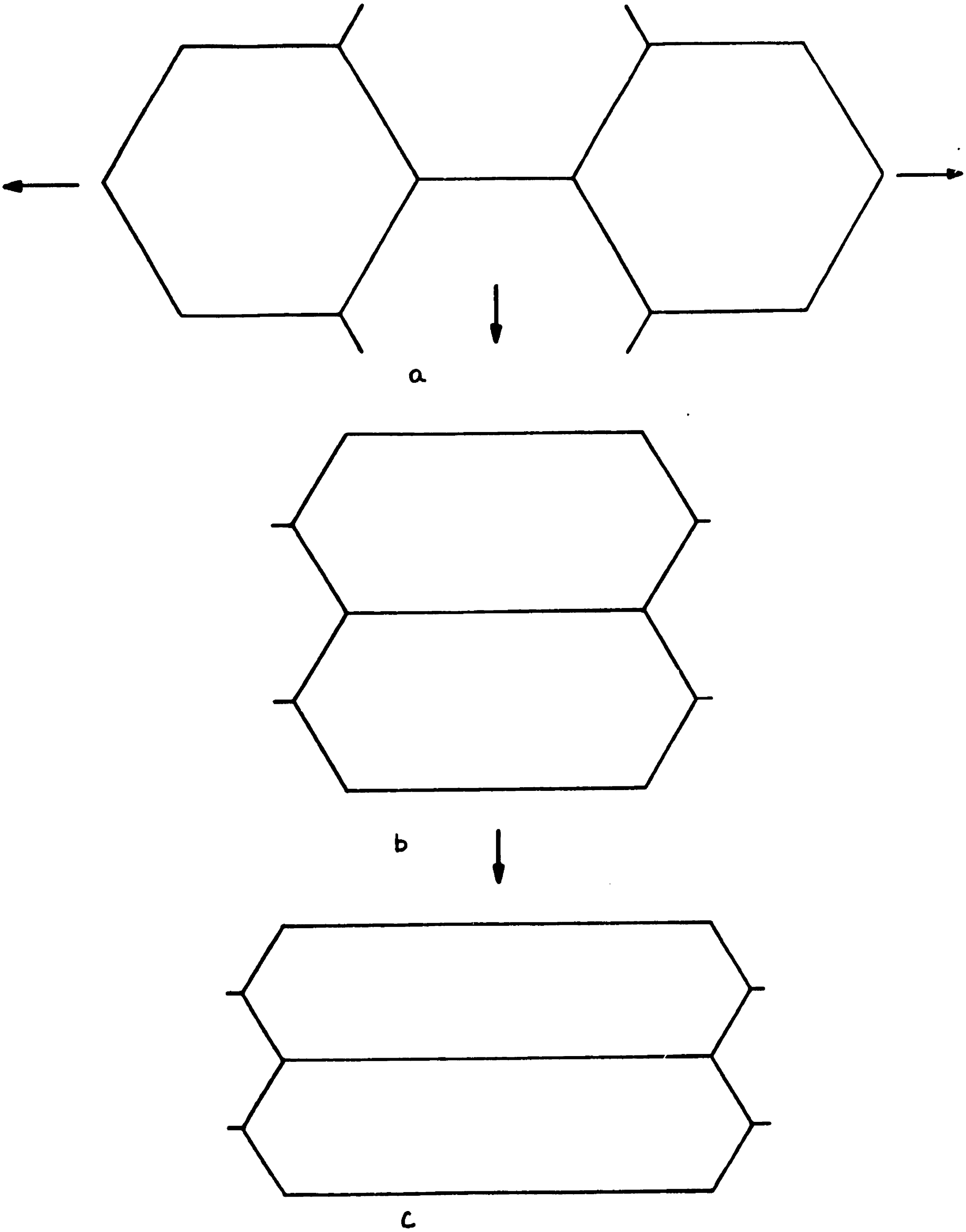

Figure II-9 Effect of initial orientation in elongational deformation. No critical strain is observed in this case of $\theta = 30^{\circ}$.

Therefore, $\underline{\underline{\beta}} = \underline{\underline{E}} \cdot \underline{\underline{\Omega}} \cdot \underline{\underline{\beta}}^{o}$

$$= a\sqrt{3}/2 \begin{vmatrix} \cos(\theta+60)\, e^{\varepsilon} & -\cos(60-\theta)\, e^{\varepsilon} \\ \sin(\theta+60)\, e^{-\varepsilon} & \sin(60-\theta)\, e^{\varepsilon} \end{vmatrix} \qquad \text{II-30}$$

We now know the coordinates of A, B, C as functions of ε and θ. In order to describe the foam structure analytically, we need to know the coordinates of O in addition. Using Equation II-6 as before, we get the coordinates of O to be:

$$x = -a \sin\theta \left[e^{-\varepsilon}(3 \cos^2\theta - \sin^2\theta) - e^{\varepsilon}(\cos^2\theta - 3 \sin^2\theta)\right]/4$$

$$\text{II-31}$$

$$y = a \cos\theta \left[e^{-\varepsilon}(3 \cos^2\theta - \sin^2\theta) - e^{\varepsilon}(\cos^2\theta - 3 \sin^2\theta)\right]/4$$

The lengths of the liquid films, as functions of θ and ε, are then found to be:

$$\begin{aligned} OA &= a\left[e^{-\varepsilon} \sin(\theta+60) \sin(60-\theta) - e^{\varepsilon} \cos(60+\theta) \cos(60-\theta)\right] \\ OB &= a\left[e^{-\varepsilon} \sin\theta \sin(60+\theta) + e^{\varepsilon} \cos\theta \cos(\theta+60)\right] \qquad \text{II-32a,b,c} \\ OC &= a\left[e^{\varepsilon} \cos\theta \cos(60-\theta) - e^{-\varepsilon} \sin\theta \sin(60-\theta)\right] \end{aligned}$$

We now have all the information to calculate the stresses using the force approach. In order to use the energy approach, we however need $\underline{\underline{\alpha}}$. For an extensional deformation, $\underline{\underline{\alpha}}$ is given by:

$$\underline{\underline{\alpha}} = \begin{vmatrix} d\varepsilon & 0 \\ 0 & -d\varepsilon \end{vmatrix} \qquad \text{II-33}$$

and,

$$\frac{dL}{d\varepsilon} = 3a/4\ [e^{\varepsilon} - e^{-\varepsilon}] \qquad \text{II-34}$$

Hence using either Equation II-11 or II-14, we get the same expression for the stresses, i.e.

$$\tau_{xx} - \tau_{yy} = \frac{2\sigma}{a\sqrt{3}} [e^{\varepsilon} - e^{-\varepsilon}] \qquad \text{II-35}$$

The force balance approach further reveals that $\tau_{yx}=0$ in this case.

From this relationship, we observe that the stress in elongational deformation is independent of orientation. However, as in the shearing case, the critical strain, ε_c, and therefore the yield stress is dependent on initial cell orientation. This critical point is found by seeing which of the Equations II-32 a,b,c go to zero for the smallest ε. Figure II-10 shows the elongational yield stress and the critical strain as a function of orientation. As we mentioned before, we observe no yield point for $\theta=30^{o}$.

C. STEADY SHEAR FLOWS

So far, we have looked at the stress-strain behavior of foam for deformations only up to the critical point. For calculations up to this point we have neglected the viscous dissipation in the liquid films. This is because the deformation was slow enough to make $\dot{\gamma}$ or $\dot{\varepsilon}$ effectively zero. In this section, we extend our model to steady shear flows and derive an expression for the viscosity of foam. From our calculations,

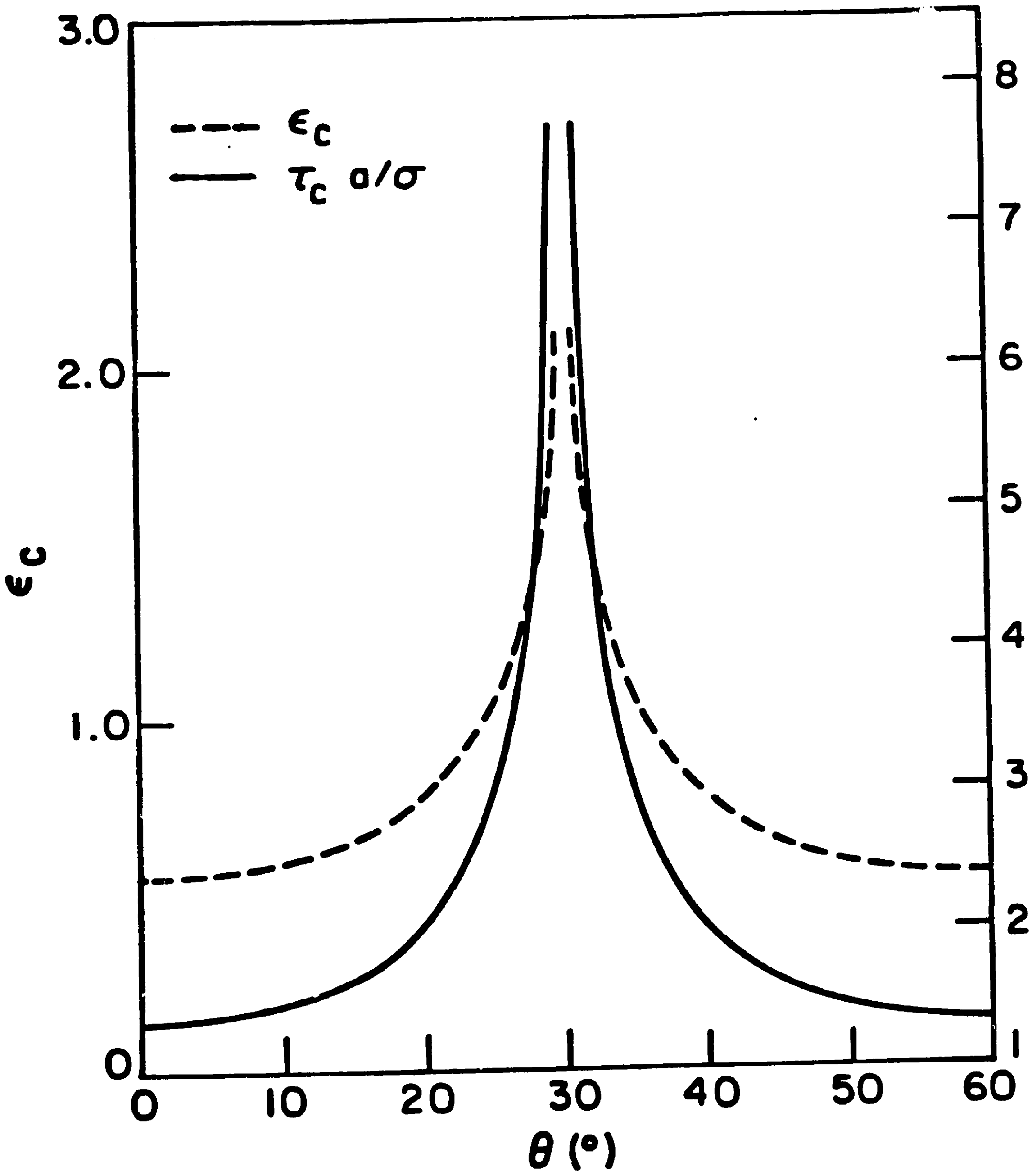

Figure II-10 Critical strain(ϵ_c) and stress(τ_c) in elongational deformation as a function of orientation. Note absence of critical point for θ=30°.

we know that one component of the shear stress for steady flows will be the yield stress term. Further, in a steady flow with shear rate $\dot{\gamma}$ the viscous force cannot be neglected. Our goal here is to derive this viscous force, $F_{\mu i}$, in terms of known variables.

From the previous section, we know that in a shear deformation the liquid films in a foam undergo planar extension or contraction. This in turn gives rise to viscous forces in them. The velocity of a thin liquid film for such an extensional flow is given by [Bird, Armstrong and Hassager, 1977]:

$$v_x = \dot{\varepsilon} x \; , \quad v_y = -\dot{\varepsilon} y \qquad \text{II-36}$$

where $\dot{\varepsilon}$, the Hencky elongation rate is given by

$$\dot{\varepsilon} = \frac{d\ln (l)}{dt} \qquad \text{II-37}$$

and l is the length of the liquid film.

In a unit cell, each liguid film has a different $\dot{\varepsilon}$ given by:

$$\dot{\varepsilon}_i = \frac{d \ln (l_i)}{d\gamma} \dot{\gamma} = A_i \dot{\gamma} \qquad \text{II-38}$$

where $\dot{\gamma}$ is the bulk shear rate and $i = 1,2,3$ in l_i represents lengths of sides OA ,OB , OC respectively, and in $\dot{\varepsilon}_i$, the corresponding elongation rate.

Thus the viscous stress, which is really the elongation stress in a film, is given by:

$$\tau_{\mu i} = \mu_L \dot{\varepsilon} \qquad \text{II-39}$$

In order to ge the corresponding force, we will assume ϕ to be slightly less than unity so that the liquid films have a nonzero thickness. Therefore,

$$F_{\mu i} = \mu_L \dot{\varepsilon} \delta_i \qquad \text{II-40}$$

where δ_i is the film thickness.

We will considor the foam cells to be still hexagonal. Then, based on geometry, the film thickness at any instant is given by:

$$\delta_i = C(\phi) a^2 / l_i \qquad \text{II-41}$$

$C(\phi)$ has been derived in Appendix A and is given by:

$$C(\phi) = \sqrt{3} (1-\sqrt{\phi}) \sqrt{\phi}/2 \qquad \text{II-42}$$

Therefore ,

$$F_i = 2\sigma + \mu_L a^2 \frac{C(\phi) \dot{\gamma}}{l_i^2} \frac{dl_i}{d\gamma} \qquad \text{II-43}$$

We can use this force expression along with our stress tensor expression (Equation II-14) to directly obtain all material functions, or use the work equation. Either way, we get the following expression for the shear stress in steady flow:

$$\tau_{yx} = \tau_y + C_1 \mu_L \dot{\gamma} \qquad \text{II-44}$$

where,

$$C_1 = C(\phi) \sum \left(\frac{dl_i}{l_i \, d\gamma} \right)^2 \qquad \text{II-45}$$

Here, the squared term represents the average value over one cycle, and τ_y the yield stress.

Hence, the foam viscosity is given by:

$$\eta = \tau_y/\dot{\gamma} + C_1 \mu_L \qquad \text{II-46}$$

For $\theta=0^o$, C_1 has a value of 0.043 assuming $\phi=0.99$

Therefore, in a steady shear flow, foam will behave like a Bingham plastic with its viscosity being the sum of two different components: the first contribution comes from its yield stress and is proportional to σ/a ; the second contribution comes from the liquid viscosity. From the form of Equation II-45, one can clearly see that this is essentially a viscous dissipation contribution. Thus, the shape of the viscosity versus shear rate curve will depend on the relative values of the two terms. At very low shear rates, the viscosity will vary as $1/\dot{\gamma}$. At high shear rates, the second term will dominate and the viscosity will become independent of $\dot{\gamma}$. However, in cases where $\tau_y >> \mu_L$ we may not observe the levelling off effect within the experimental regime.

D. DISCUSSION

In this chapter, a simplified analytical model for foam rheology has been developed. This model differs considerably from the existing foam model by Princen [1983]. Previous models developed by Prud'homme [1981] and Princen [1983] are restricted to a specific initial foam cell orientation. Real systems however have all possible orientation. Princen's stress-strain relationship however has the same σ/a dependence as ours for small deformation as it must because of dimensional consideration, and is a specific case ($\theta=0^{o}$) of our model. In his derivation, Princen does not get an analytical result describing the foam cell microstructure. Consequently, he fails to get an analytic stress-strain equation of state and uses an iterative technique to obtain stress for a specified strain. His approach is a simplified version of the force projection method. He looks at a shearing plane and the liquid films cutting that plane. The component of the interfacial tension of these liquid films in the shearing direction is then taken as the stress. Although Princen has not looked at normal stresses, steady shear viscosities, elongational deformation and the effect of liquid viscosities, he has however looked at cases where the contact-angle between gas and liquid is not zero. This is something which wil not be addressed in this thesis. Despite some of its limitations, this model had been the first one to to provide a good insight into the physics of foam deformation.

Prud'homme's calculations are in disagreement with both models although he uses the same cell geometry. In fact, he uses the hexagonal cells to derive two different expressions for viscosity, one of which is applicable to tube flows only.

In deriving the stresses in our model, we have used two different techniques: the work argument and the force projection method. It is clear from our study that the latter is a better approach since it gives the total stress tensor just from the orientation and lengths of the liquid films. In the work-energy approach, we have to know how these film lengths vary with strain. Further, we cannot get the total stress tensor. An advantage of the energy approach, however, is that it is foolproof and therefore serves as a verifying tool for other techniques.

In formulating our problem and deriving the cell structure, we assumed 120° angle between films. The entire problem can be done in a generalized way without making any such assumption by using an energy minimisation approach. In this method, we consider the system to have the minimum energy for any deformed state. It so happens that the 120° criterion ensures this [Beris, 1984].

In Figure II-11, we show a typical viscosity versus shear rate profile as predicted by the model. As mentioned before, at low shear rates the yield stress is dominating and η goes down with a slope of -1. At some shear rate, $\dot{\gamma}_t$, the liquid contribution will become important and the curve will start to level off. This transition value will depend on the ratio $\sigma/a\mu_L$.

It should be mentioned here that the viscous term in the viscosity expression could also have been derived from viscous dissipation arguments. In this approach, we assume dissipation in foam to occur predominantly in the liquid films. One can then compute this by considering foam as a continuum and equating the macroscopic dissipation in the equivalent continuum undergoing shearing flow to the energy dissipated in the extensional flow of the liquid films (microstructure).

Finally we would like to comment on some of the restrictions of the model. This model is restricted to gas fractions of unity. We feel that incorporation of liquid into it will shift the viscosity curve down. Further, real foam is polydisperse amd three dimensional. We have not

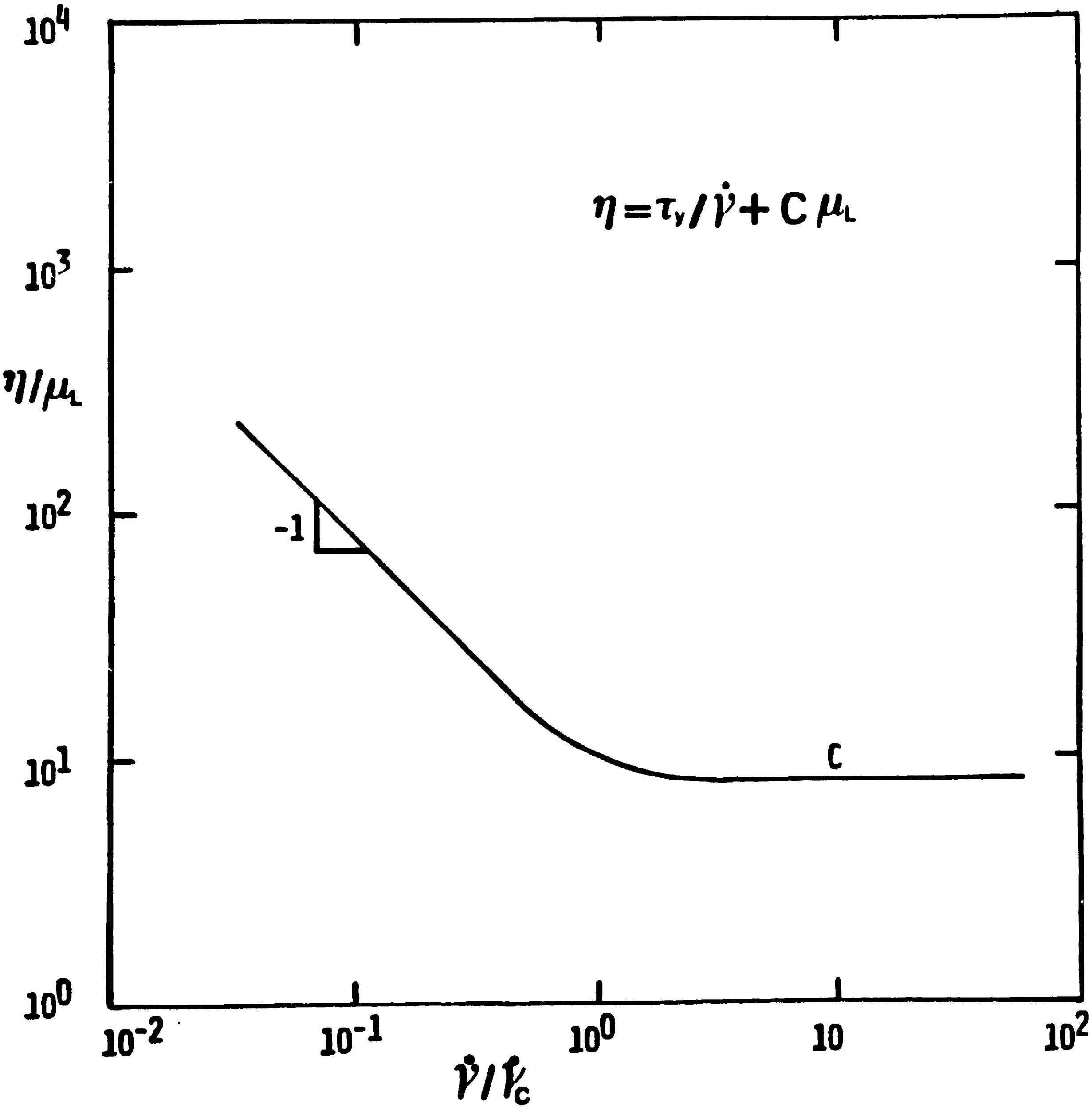

Figure II-11 Schematic of dimensionless foam viscosity versus shear rate as predicted by model. μ_L is the liquid viscosity and $\dot{\gamma}_c$ corresponds to the shear rate at which viscosity starts asymptoting to a constant value.

taken them into account here. Some of these effects are considered in later chapters. Besides these, the model has one major weakness. This is the assumption that the cells reform back to the original configuration when strained past the yield point. Although this is obvious for $\Theta=0^o$, it is not so for other orientations. In fact, this is why we did our viscosity calculation for this orientation only. We will comment further on this later on. One may also argue that equilibrium conditions (120^o angles betweeen films) may not prevail at all times. This is because with the films undergoing stretching motion, the extensional forces may become important in the force balance at the Plateau border and thereby affect the microstructure. This is the subject of the next chapter.

E. CONCLUSIONS

In this chapter, we have developed a generalized model for foam having gas volume fraction approaching unity by assuming monodisperse, two dimensional hexagonal cells. Despite its restrictions, this has been the first succesful attempt in deriving a simple, analytic interpretative model for foam flow. From the model we found that the flow behavior of foam can be described by a simple analytic expression. In steady shear flow, foam behaves like a Bingham plastic with its viscosity being dominated by the yield stress at low shear rates and the liquid viscosity at high shear rates. The yield stress, in turn, is directly proportional to the liquid film interfacial tension and inversely proportional to the cell size.

For small deformations up to the yield point, foam behaves like an elastic material with the stress strain relation independent of cell orientation. However, the critical strain is dependent on the initial cell orientation, and hence so is the yield stress.

III. POLYDISPERSITY AND VISCOUS EFFECTS ON DRY FOAM RHEOLOGY

Real foams have a distribution of cell sizes with cells having sides of different lengths. The monodisperse, dry foam model developed earlier is deficient in this respect. In this chapter, we have tried to take some of the cell size effects into account by looking at a bimodal cell size distribution i.e. a "bidisperse" foam system (Figure III-1a), and at irregular cell structures (Figure III-1b). Furthermore, in the dry foam case, all forces except interfacial tension were ignored in determining cell shape. It seems apparent that in addition to the interfacial tension, there are viscous forces in the liquid films opposing their extensional motion. The effect of such forces on cell deformation and rheology have also been looked into here separately. In all cases only shear deformation up to the yield point has been considered.

A. POLYDISPERSITY

Two ways of introducing polydispersity have been studied here. Although both are crude they provide useful indication of the sensitivity of the rheology to inclusion of cells of more than one size. In the first case, cells having initial sides of three different lengths are considered. For hexagonal cells with internal angles of 120 degrees this is the maximum number of sides possible. In the second case, repeat units of alternate layers of same size cells are considered. The first layer of this bilayered system has regular hexagonal cells; the second layer has cells with the vertical films differing in length from the other sides of the hexagon so that the resulting cells are either elongated or flattened (Figure

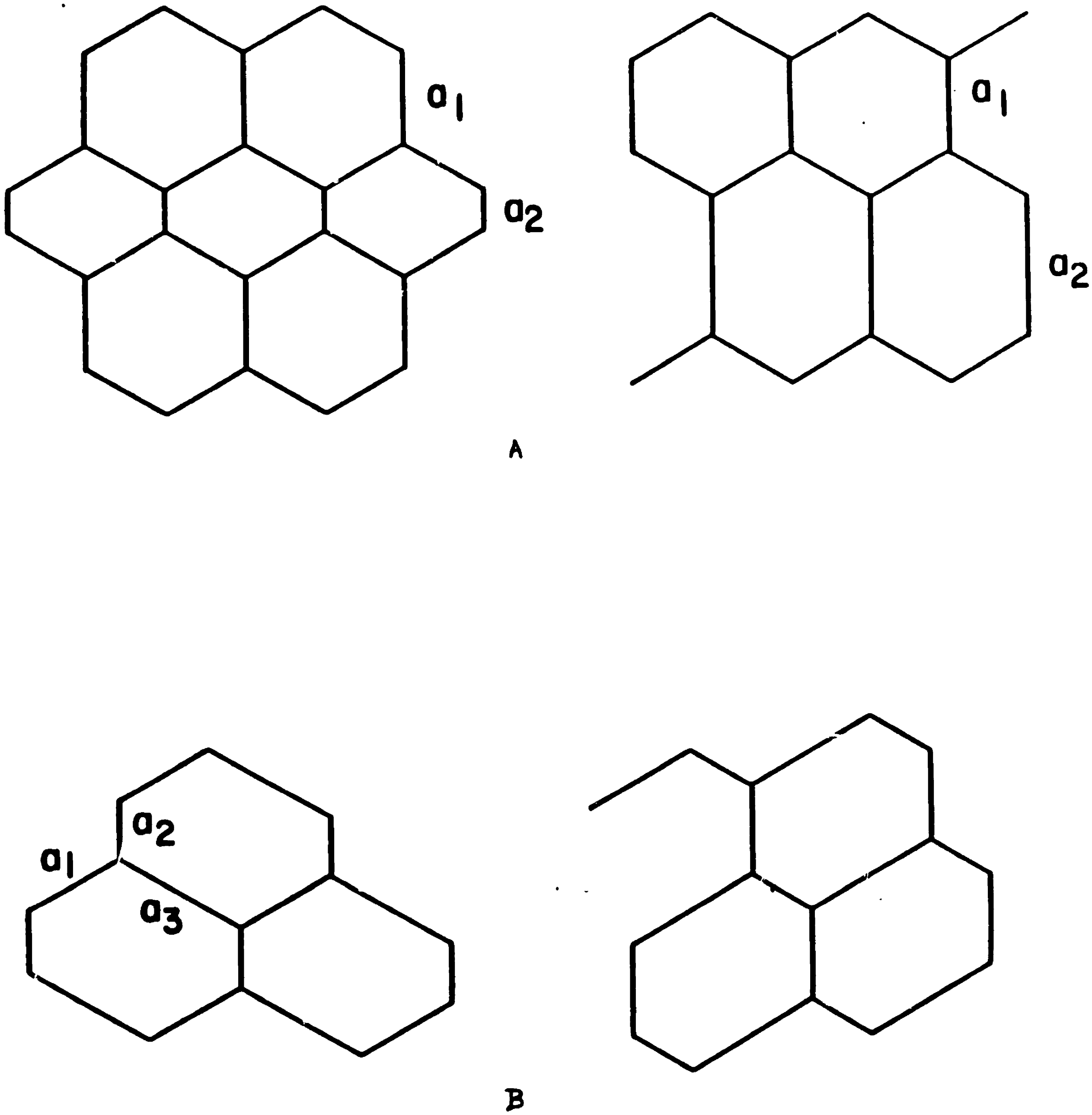

Figure III-1 Schematic diagram of Bidisperse and Irregular cell structures. a) Bimodal cell size distribution with a_1 representing side length of regular hexagons. b) Irregular cells with sides of three different lengths a_1, a_2, a_3.

III-1a). For both cases we have restricted our study to the initial orientation shown in the first figure, and to low deformation rates so that viscous forces are unimportant.

1. Irregular Cells

Although only one orientation where two sides of the hexagons point vertically have been considered here, our approach is general enough to be used for any arbitrary initial orientation. All calculations are done in terms of ratios of side lengths using 'a_1', the length of the vertical side, as reference. Further, the concepts and approach of the last chapter have been used extensively here.

As before, we will assume the liquid films to have mutual angles of 120 degrees and their mid points to have affine motion. Figure III-2 shows a unit cell along with the triangular subcell formed by joining the mid points of three adjacent films. Unlike the regular hexagon case, this triangle is scalene. OA, OB, and OC, the three liquid films, have lengths given by $a_1/2$, $a_2/2$, and $a_3/2$ respectively at zero strain. Let us define two ratios:

$$c_2=a_2/a_1 \qquad c3=a_3/a_1$$

The vectors $\underline{b_1}$ and $\underline{b_2}$ along AB and AC of ΔABC for any arbitrary strain are then given by (Section II-A.2):

$$\underline{b_1}=a_1 \left\{ [\sqrt{3}/2+\gamma(c_2+1/2)]\, \underline{\delta_x} + [c_2+1/2]\, \underline{\delta_y} \right\}$$
$$\underline{b_2}=a_1 \left\{ [\sqrt{3}/2(1+c_3)+\gamma/2(1-c_3)]\, \underline{\delta_x} + 1/2[1-c_3]\, \underline{\delta_y} \right\} \qquad \text{III-1}$$

In order to get the stress strain relation, we first need to know the lengths and orientations of the liquid films as functions of strain.

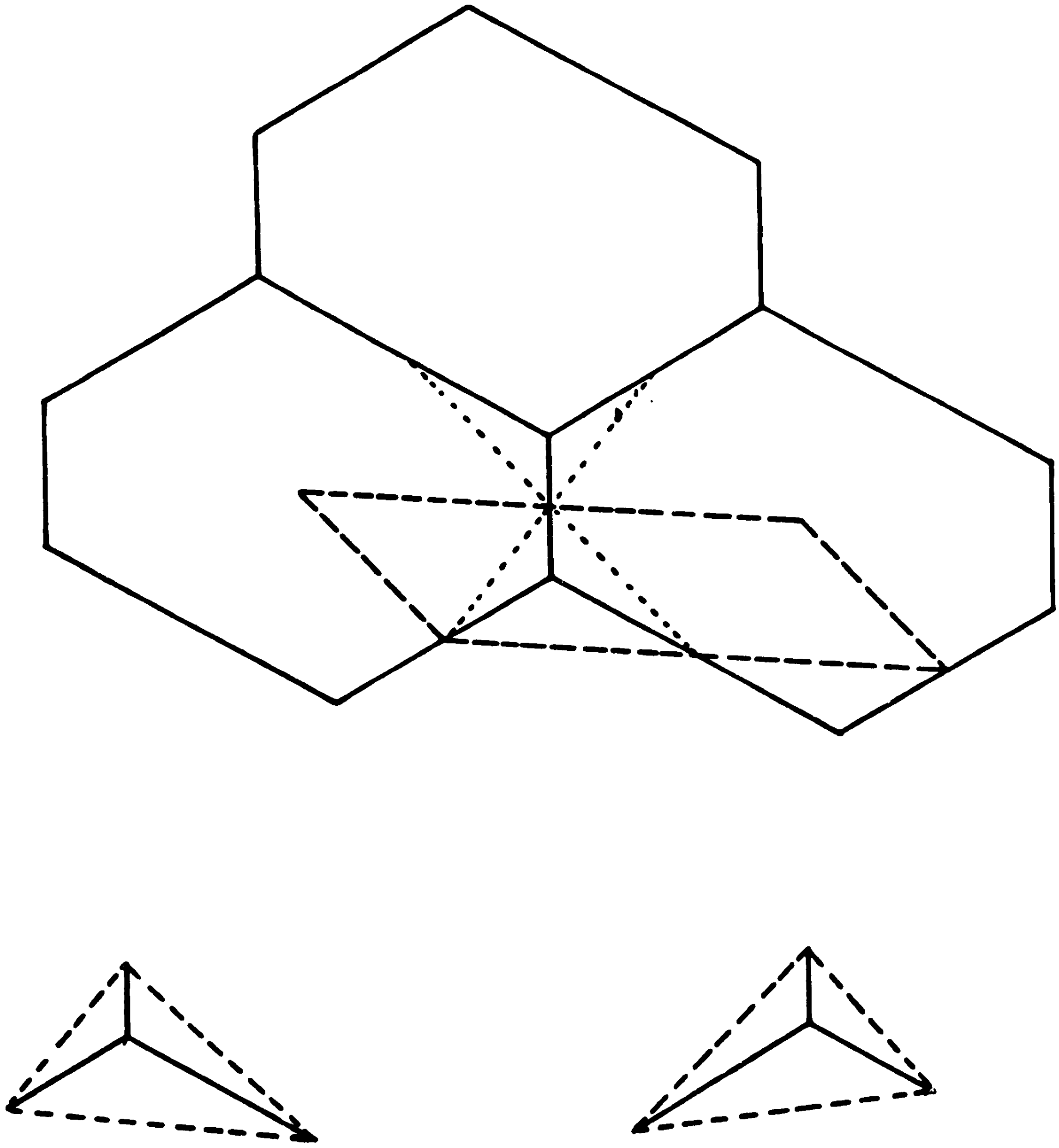

Figure III-2 Unit cell and possible subcells in an irregular cell system. Parallelogram and triangles represent unit cell and subcell respectively.

The information missing is the coordinates of point O. Let these be x, y. Then by using Equations II-6, which is an outcome of the 120 degree criterion, we get the following relations between x and y:

$$x^2 + y^2 - a_1 y \left[(1+c_2) + \gamma/\sqrt{3}\,(1/2+c_2) \right]$$
$$- a_1 x \left[1/\sqrt{3}\,(1-c_2) + \gamma\,(1/2+c_2) \right] = 0$$

$$x^2 + y^2 - a_1 x \left[\gamma/2\,(1-c_3) + 1/\sqrt{3}\,(2+c_3) \right] \tag{III-2}$$
$$+ a_1 y \left[c_3 + \gamma\,(1-c_3)\,/2\sqrt{3} \right] = 0$$

Solving these equations, we get the coordinates of point O as:

$$x = a_1 \left[(1+c_2+c_3) + \gamma/\sqrt{3}\,(1+c_2-c_3/2)\right] \times N1/D1$$
$$y = a_1 \left[(1+c_2+c_3)/\sqrt{3} - \gamma\,(c_2+c_3/2)\right] \times N1/D1 \tag{III-3}$$

where,

$$N1 = \left[2(1+c_2+c_3)/\sqrt{3} + \gamma(1+c_2+c_3) + \gamma^2(1/2+c_2)(1-c_3)/\sqrt{3}\right]$$
$$D1 = \left[4(1+c_2+c_3)^2/3 + 2\gamma(1+c_2+c_3)(1-c_3)\right.$$
$$\left. + \gamma^2\{(1+c_2-c_3/2)^2/3 + (c_2+c_3/2)^2\} \right]$$

The lengths of the liquid films can now be calculated. Thus,

$$OA = a_1 \times N1 / \sqrt{D1}$$
$$OB = a_1 \left[2\,c_2\,(1+c_2+c_3)/\sqrt{3} + \gamma\,(1-c_3)\,c_2\right.$$
$$\left. + 2\,\gamma^2\,(1/2+c_2)\,(c_2+c_3/2)/\sqrt{3} \right] / \sqrt{D1} \tag{III-4}$$
$$OC = a_1 \left[2\,c_3\,(1+c_2+c_3)/\sqrt{3} - \gamma\,(c_3{}^2+c_2c_3+c_2)\right.$$
$$\left. - \gamma^2\,(1-c_3)\,(c_2+c_3/2)/\sqrt{3} \right] / \sqrt{D1}$$

From the work-energy arguments of Section II-A.2, we know that

$$\tau_{yx} S = 2\sigma \frac{dL}{d\gamma}$$

S, the area of the unit cell, is four times the area of ΔABC and is given by:

$$S = \sqrt{3}\, a_1{}^2 \,(c_2 + c_3 + c_2c_3) \,/\, 4$$

We thus get the following stress-strain relation.

$$\tau_{yx} = \frac{2\sigma}{S\sqrt{D1}}\left[(1-c_3)(1+c_2+c_3)+\sqrt{3}\gamma \;\{\tfrac{1}{3}(1+c_2-c_3/2)^2+(c_2+c_3/2)^2\}\right]a_1 \qquad \text{III-5}$$

As before, we do not get the normal stresses from the energy arguments. Using the force approach, however, we get the normal stresses from the g's since,

$$\tau_{xx} - \tau_{yy} = 2\sigma/S \sum (\, g_{ix}{}^2 - g_{iy}{}^2 \,)/g_i$$

2. "Bidisperse System"

Certain important differences exist here from the monodisperse case. Let us focus on Figure III-3 which shows a collection of bidisperse foam cells. The centers of these cells move affinely with the bulk. The horizontal lines drawn through these points always intersect the vertical foam films at their midpoints. Consequently, from symmetry, these represent points of affine motion. However, unlike the previous cases the midpoints of the other films do not move affinely. This becomes clear from the triangular subcells formed by joining midpoints of adjacent vertical films. Because of two different cell sizes, we now deal with a pair of subcells. Figure III-3 shows the unit cell with the subcells ABC and AB'C'. It is clear from the similar triangles OAB and O'A'B' that

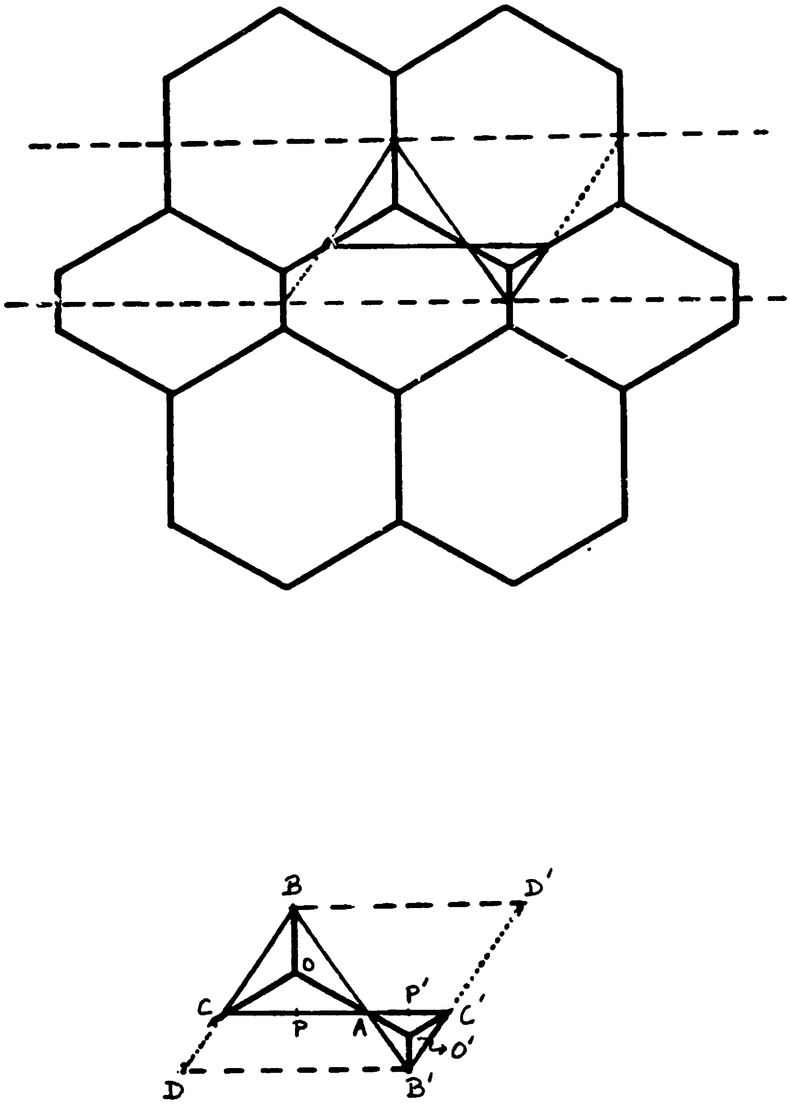

Figure III-3 Unit cell DBD'B' and triangular subcells ABC, A'B'C' in a bidisperse system. The horizontal lines through the center represent lines of affine motion.

A, C, C', which move affinely with the bulk, are not the mid points of the respective films but divide them in the ratio of the vertical sides OB and O'B'. Let OB = $a_1/2$ and O'B' = $a_2/2$. Then, the following relations at zero strain must hold:

$O'A/OA = a_2/a_1 = c$

$OA = a_1/(1+c)$ $\qquad$ $O'A = c\,OA$

$AC = \sqrt{3}a_1/(1+c)$ $\qquad$ $AC' = c\,AC$

$BP = a_1(2+c)/2(1+c)$ $\qquad$ $B'P' = c\,BP$

Let us choose A as our frame of reference for calculational purposes, and $a_1 = a$. Then, on applying a shear strain the coordinates of the vertices of the two triangles are given by:

For ΔAB'C',

A: $(0,0)$

B': $(\sqrt{3}/2\; ac/(1+c) - ac\gamma/2\; (2+c)/(1+c),\; -ac/2\; (2+c)/(1+c))$

C': $(\sqrt{3}\; ac/(1+c),\; 0)$

For ΔABC, $\qquad$ III-7

B: $(-\sqrt{3}/2\; a/(1+c) + a\gamma/2\; (2+c)/(1+c),\; a/2\; (2+c)/(1+c))$

C: $(-\sqrt{3}\; a/(1+c),\; 0)$

To get the stress, we have to find O, O' as functions of strain. For the moment, let us consider ΔABC only. Using the 120° criterion and the approach of the last section, we obtained the coordinates of O. Thus,

$$O_x: \quad \frac{a\,[(c+5) - \sqrt{3}(c+2)\gamma]\,[\sqrt{3}(5+c) - (2+c)\gamma]}{2\,(1+c)\,[\,(c+5)^2 + (c+2)^2\,\gamma^2\,]}$$

III-8

$$O_y: \quad \frac{a\,[\,(c+5)^2 - 3\,(c+2)^2\,\gamma^2\,]}{2\,(1+c)\,[\,(c+5)^2 + (c+2)^2\,\gamma^2\,]}$$

From these, we could get the following expressions for the liquid films.

$$OA = a\,[(c+5) - \sqrt{3}\,(2+c)\,\gamma] \,/\, D2$$

$$OB = a/2\,[(c+1)\,(c+5) + \gamma^2\,(c+2)^2] \,/\, D2 \qquad \text{III-9}$$

$$OC = a\,[(c+5) + \sqrt{3}\,(c+2)\,\gamma] \,/\, D2$$

where,

$$D2 = (1+c)\,\sqrt{[\,(c+5)^2 + (c+2)^2\,\gamma^2\,]}$$

Consider now the subcell AB'C'. Since the three films in the undeformed state have the lengths of the films in ΔABC scaled by c, we would anticipate this to hold for any arbitrary homogeneous deformation. Rigorous calculations showed this to be valid i.e. O'A=cOA, O'B=cOB, O'C=cOC. From the previous section, we know that the energy approach gives

$$\tau_{yx}\,S = 2\sigma\,\frac{d\,(L_1 + L_2)}{d\gamma}$$

where L_1=OA+OB+OC and L_2=O'A+O'B'+O'C'. S in this case is given by four times the areas of ΔABC and ΔAB'C' in the undeformed state. Thus,

$$S = CC' \times (BP+B'P') = \sqrt{3}\,a^2\,(c+2)$$

Substituting all these information, we get the required relation.

$$\tau_{yx} = \frac{2\sigma}{a}\;\frac{\gamma\,(c+2)}{\sqrt{\{3\,[(c+5)^2 + (c+2)^2\,\gamma^2]\}}} \qquad \text{III-10}$$

The critical strain here corresponds to the strain at which sides OA or O'A become zero. For c=1, this stress strain relation reduces to the familiar dry foam Equation II-24.

3. Results and Discussion

Several conclusions can be drawn from our study of the irregular cell system. From Equation III-5, it is clear that except for the case where c_3=1 this equation gives a non zero stress at $\gamma=0$. This means that when cell structures with three different lengths are formed they would instantaneously reform to that strained state where the stress would become zero. Such instantaneous reformation becomes apparent if one looks at a horizontal shearing plane drawn through the cells (Figure III-4). As can be seen there is no symmetry across this plane; different films are intersected at different angles with no apparent repeat units. Since shear stress is proportional to the horizontal component of the intersecting films, lack of symmetry leads to a net resultant force. In the case where c_3=1, we have cells with two different side lengths. The structure is symmetric across the x axis and the net force across any horizontal plane is zero. In Figure III-5 strain values are shown as functions of cell side ratios. These values correspond to the strains at which the shear stress (Equation III-5) would be zero for the given c's i.e. it is the strained state the cells would reform to. These strains can be negative or positive depending on the cell side ratios.

In Figure III-6 are shown the yield stress and critical strains for the c_3=1 case. In this case $\gamma=0$ does correspond to the stress free state. An important observation from the figure is the fact that although the critical strain varies with c, the yield stress remains constant. This implies that in a nonuniform shearing flow such as a pressure driven flow, the plug flow region will not be affected by the irregular structures. In the figure, we also observe the critical strain to decrease with increasing c_2. However, the horizontal displacement between cell centers of adjacent rows is more for a higher cell side ratio i.e for more elongated structures. In Figure III-7, the stress-strain plots

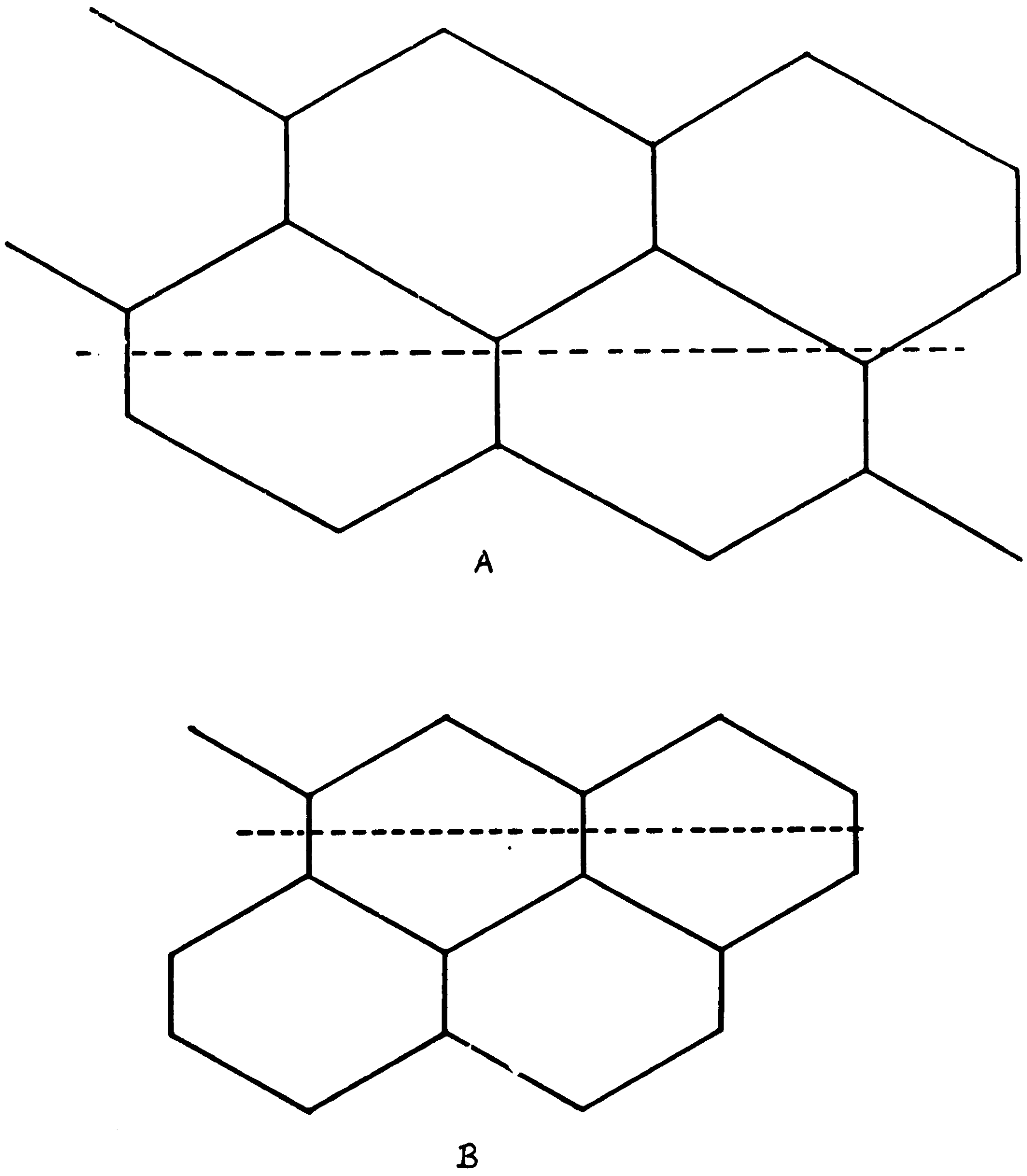

Figure III-4 Instantaneous reformation in irregular cells can be observed from the lack of symmetry across a horizontal shearing plane. a) No symmetry is observed across horizontal shearing plane for irregular cells. b) Cells with $c_3=a_3/a_1=1$ showing symmetry across horizontal plane.

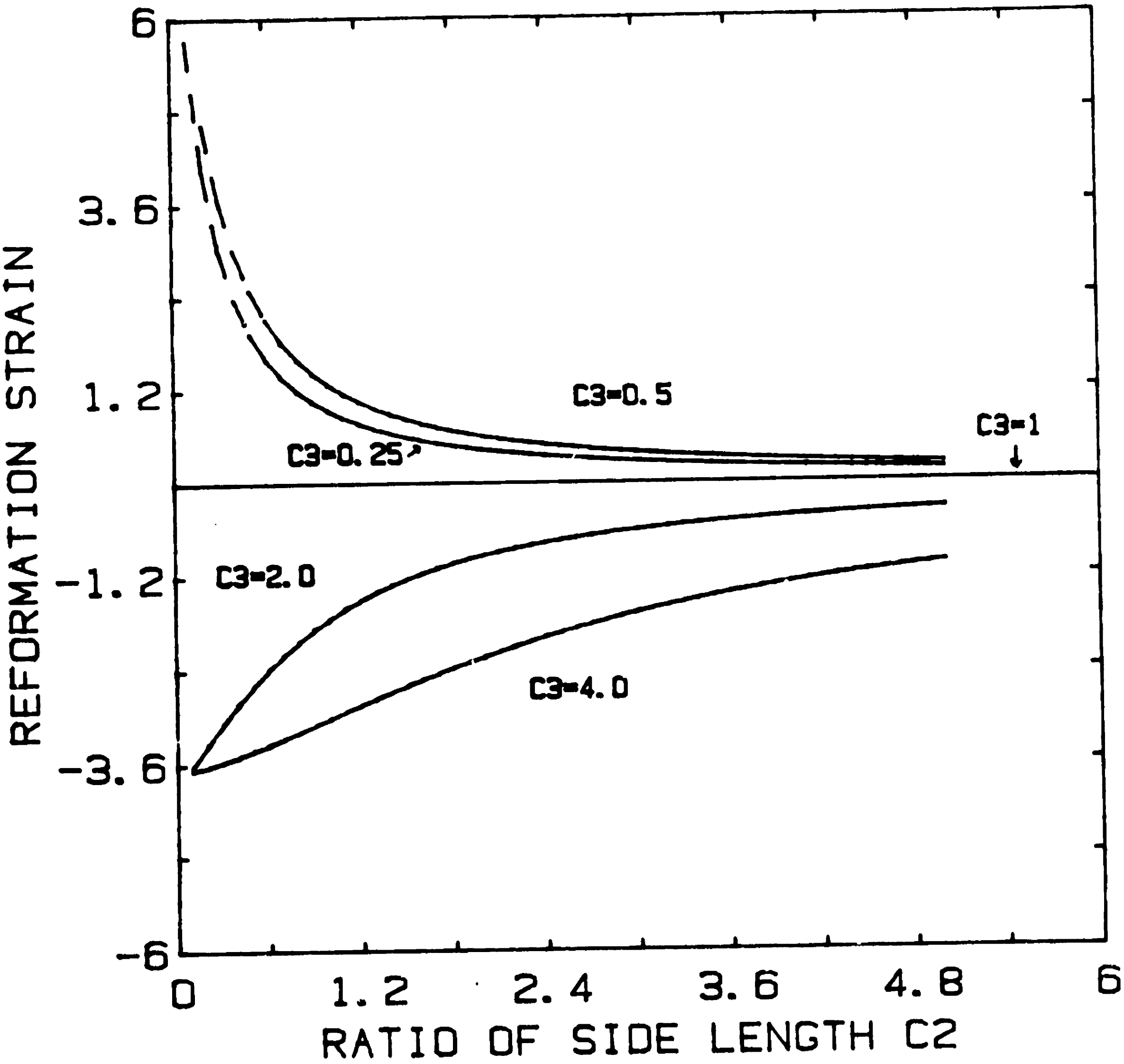

Figure III-5 Strains corresponding to a shear stress free state in an irregular cell system. These strains represent the state the irregular system will reform to as soon as they are generated. Here, $c_2=a_2/a_1$ and $c_3=a_3/a_1$ as in Figure III-1.

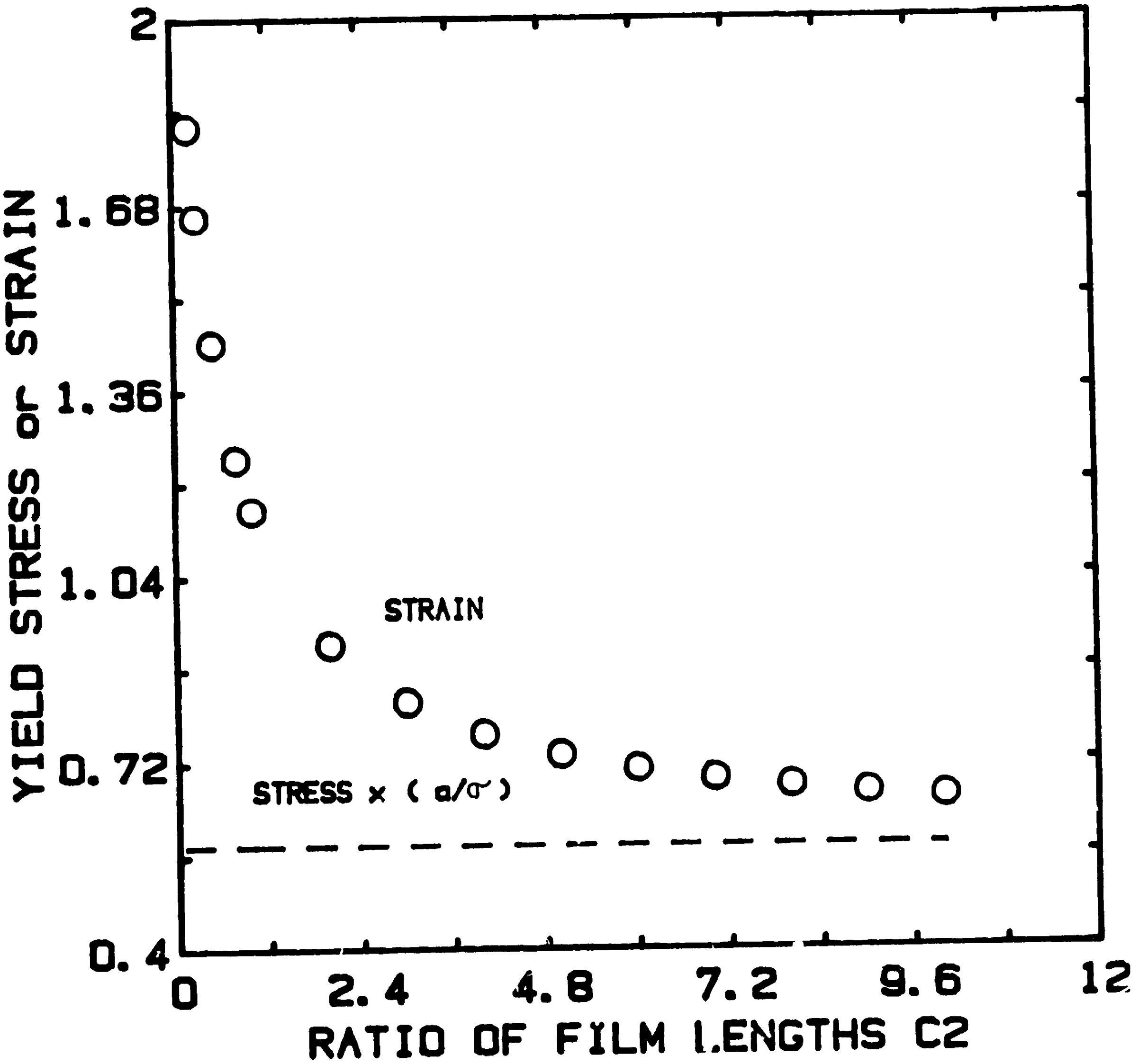

Figure III-6 Yield stresses and strains as functions of sidelength ratio c_2 for an irregular cell system. $c_3=1$ so that cells have only two different side lengths, and $c_2=a_2/a_1$ (cf. Figure III-1).

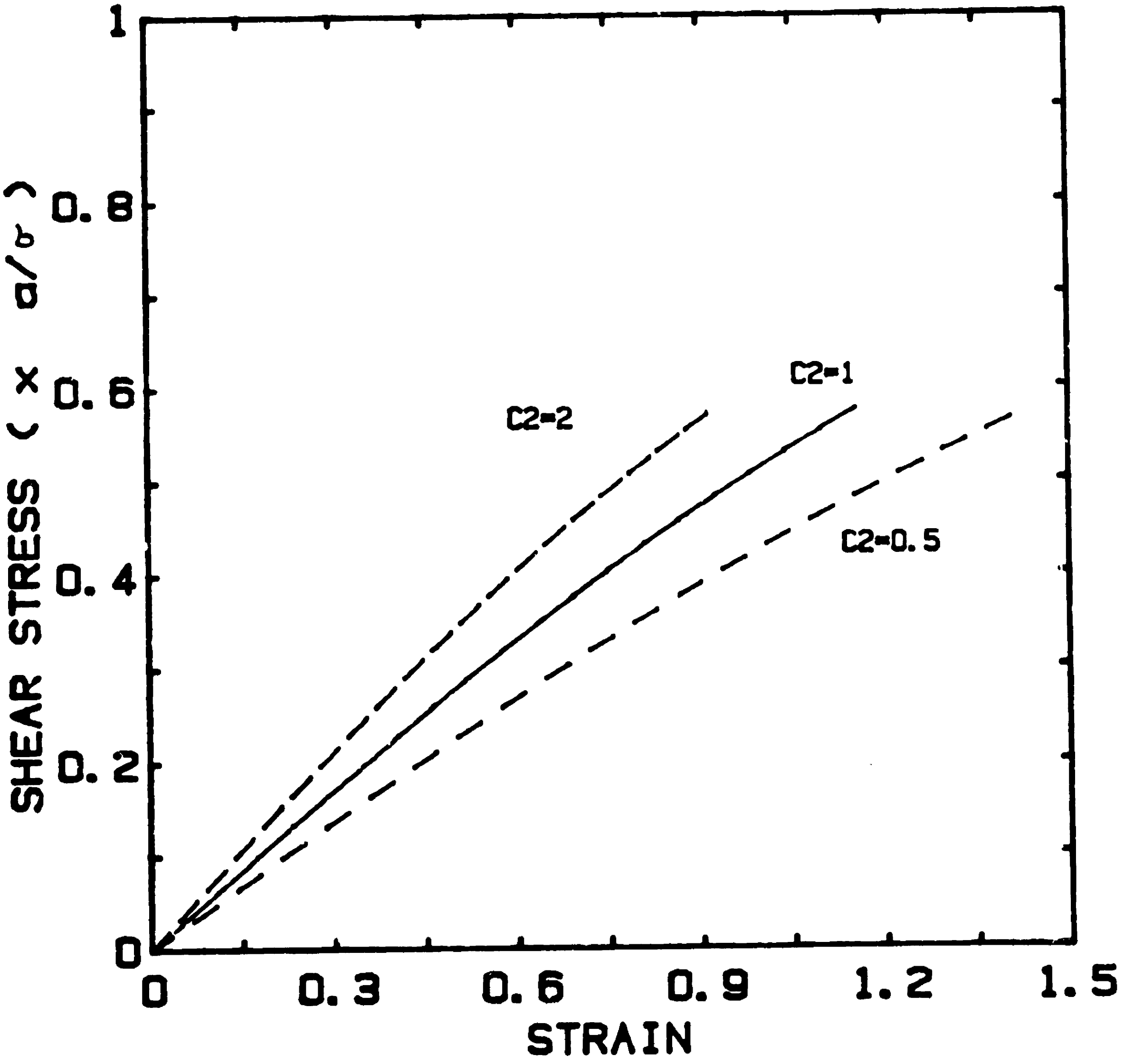

Figure III-7 Stress versus strain for an irregular cell system. Here cells have only two different side lengths ($c_3=1$) and c_2 represent ratio of the unequal sides (Figure III-1). $c_2=1$ corresponds to regular hexagons; $c_2<1$ and $c_2>1$ to squashed and elongated cells respectively.

for elongated ($c_2=2$) and flattened cells ($c_2=0.5$) are compared with the regular hexagon data. We find that for a larger c, a larger stress is needed to reach the same strain. In other words, for a given stress the more elongated cells are strained the least. Calculations reveal that the horizontal displacement between cell centers of adjacent rows, however, is larger in this case.

Central to all our calculations for the "bidisperse" system is a very general assumption that was never used directly before. In all our previous calculations, we assumed the mid points of the liquid films to move affinely with the bulk. This is no longer true for a bidisperse system. The reason for this difference can be understood from the general assumption which states that the midpoint of the cells, and not necessarily the mid points of the films, move affinely. For a monodisperse, regular system the latter is an outcome of the general assumption of affine motion of the geometric center of the cell.

In a bidisperse system, stresses are zero at $\gamma=0$. This is apparent from the symmetry observed along any plane parallel to the x axis. Figures III-8, 9 show stress-strain and critical point data for different cell size ratios. As before, we find τ_y to be invariant with c, indicating that the plug flow regime in foam flow is unaffected by "bidispersity". The critical strains are larger for smaller c's although the horizontal displacement between cell centers is smaller. The stress-strain also show the same trends as before i.e. stresses increase faster with strain for larger cell size ratios. Comparing Figures III-7 and 9, we find c to influence the stress-strain curves more for an irregular structure than a bidisperse system. This is evident from the smaller deviation of the curve from

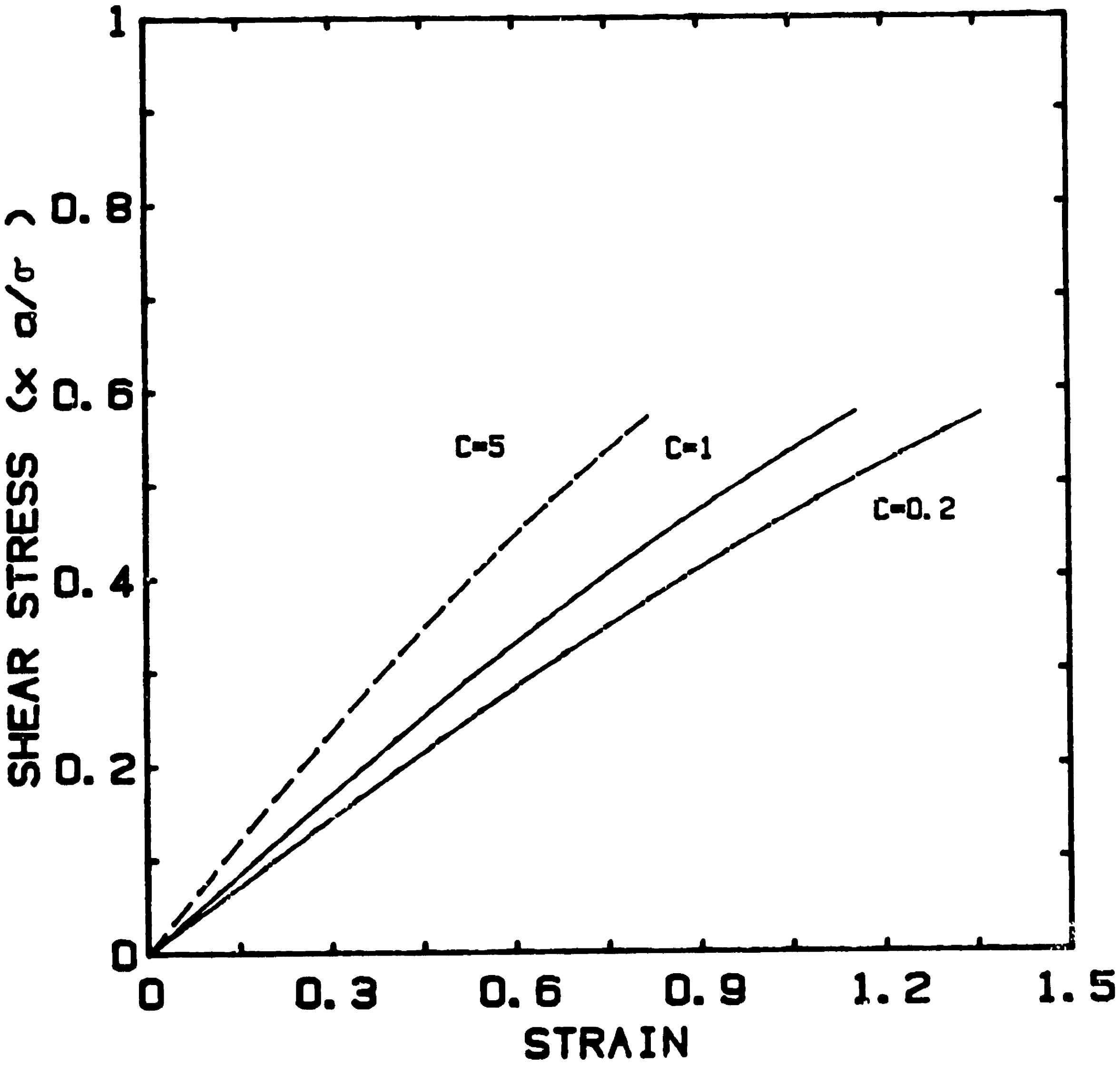

Figure III-8 Stress versus strain for different cell size ratio in a bidisperse foam system. c is the ratio of the vertical sides of the undeformed cells (cf. Figure III-1).

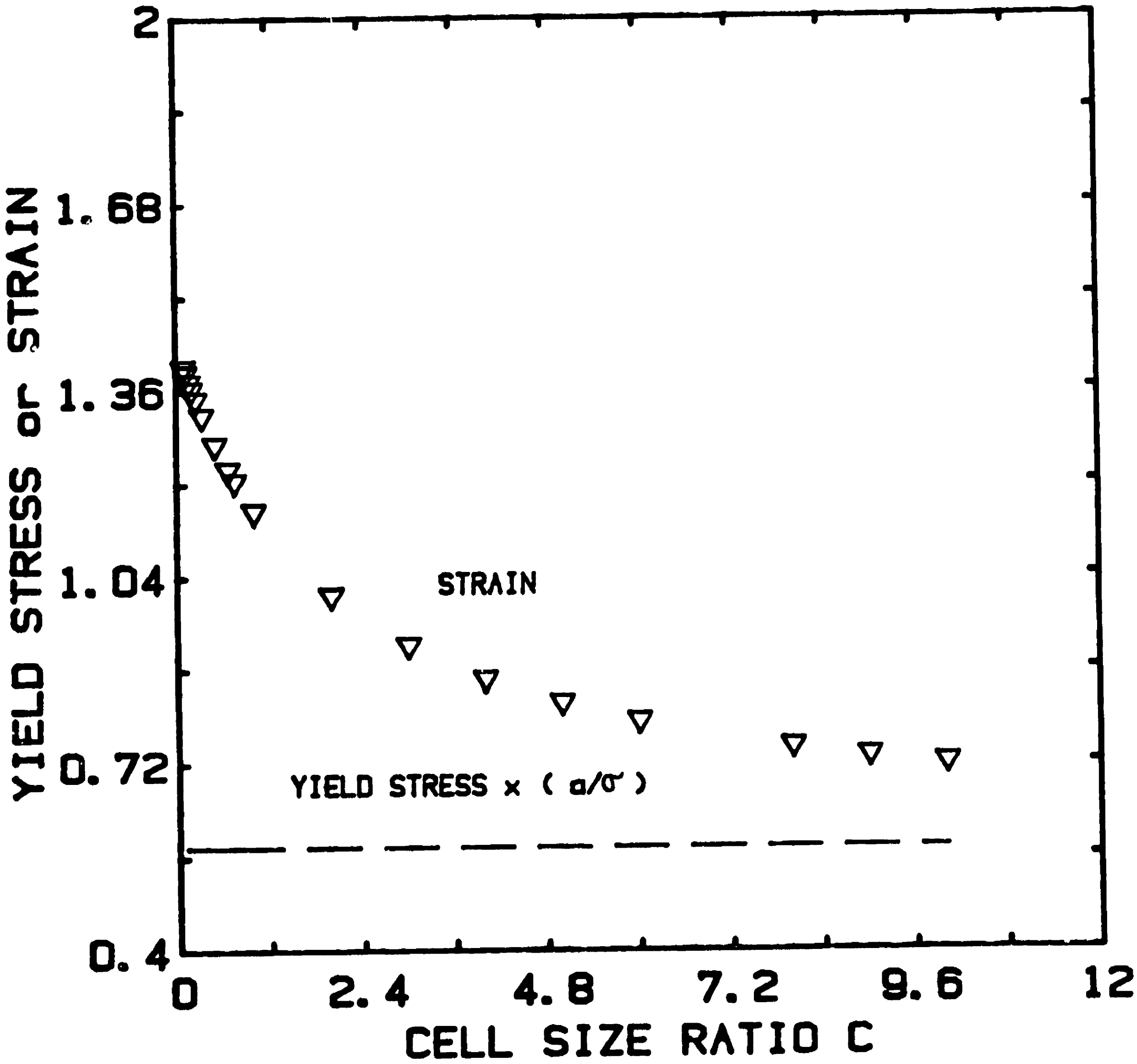

Figure III-9 Effect of cell size on the yield stress and critical strain in a bidisperse system. c is the ratio of the vertical sides of the undeformed cells.

the c=1 curve in the latter case.

B. EFFECT OF VISCOUS FORCES ON FOAM DEFORMATION

All our calculations so far has been based on equilibrium conditions. We assumed interfacial tension to be the only force in the liquid films, resulting in angles of 120° between them. In a real process, however, there is a finite shear rate. Consequently, with the onset of deformation, viscous forces are set up in the liquid films opposing their extensional motion. The angles between films are then determined from a balance of these viscous and surface tension forces at the Plateau border (Figure III-10). In this section, we study the importance of these viscous forces on cell deformation and stresses. Deformations at varying shear rates and up to the critical strain are considered here.

1. Formulation of Equations

All possible initial cell orientations are taken into account here. We restrict ourselves to monodisperse, hexagonal cells and assume the midpoints of the films to move affinely with the bulk. As will become evident later, in order for viscous forces to exist in the liquid films, these films must have a finite thickness. Thus, although we are dealing with a dry foam system, we will assume the gas volume fraction, ϕ, to be approaching, but not exactly, unity. In that case, finite films are possible and we will let this thickness be δ. This thickness is a function of gas fraction and strain. The unit cell and the triangular subcell, shown in Figure III-10, are the same as in the dry foam case.

The energy as well as the force projection approach will be used here to determine the stresses. Initially, we will however focus on

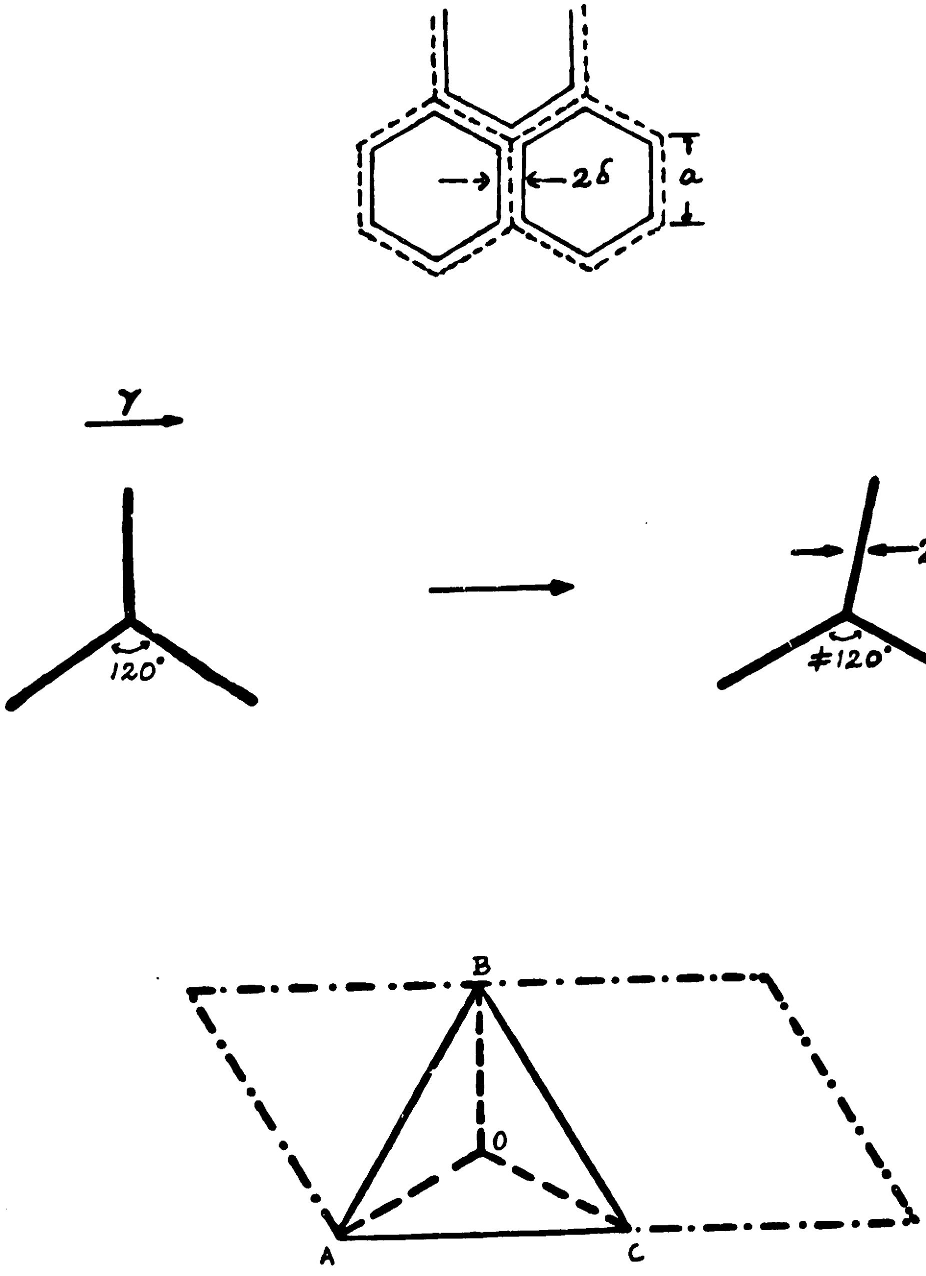

Figure III-10 Structures of foam cells and unit cell when viscous forces are present.

the former. From the work energy equivalence, we know

$$\tau_{yx} S = \underline{F} \cdot d\underline{L}$$

$$= \sum F_i \, dl_i \qquad \text{III-11}$$

Here, L = total length of films in a unit cell

$S = 3\sqrt{3}/4 \; a^2$, the area of the unit cell

F_i = the force along the film l_i and is given by, $F_i = F_\sigma + F_{\mu i}$, with $F_\sigma = 2\sigma$, and the summation is over the three films in the unit cell.

$F_{\mu i}$ is the viscous force and is different on each film, their values depending on the length and orientation of the respective films. To find $F_{\mu i}$, we use some of the concepts of elongational flow from Section II-C. As the cells deform, the films undergo a stretching and compressive motion. For such extensional flows in thin films, the viscous force is the elongation stress multiplied by the film thickness.

Thus, $F_{\mu i} = \mu_L \, \dot{\varepsilon}_i \, \delta_i$

Here μ_L is the liquid viscosity, and $\dot{\varepsilon}_i$ is the elongation rate given by:

$$\dot{\varepsilon}_i = \frac{d \ln l_i}{d\gamma} \, \dot{\gamma}$$

and δ_i is the film thickness.

Since film thickness enters our calculation, we assume ϕ to be slightly less than unity and all films to have uniform thickness initially. Thus the structure is hexagonal (Figure III-10). Some approximation is involved here since in the actual case the Plateau borders are curved. However, this does not affect the final results. Further, we will assume that liquid does not flow in and out of each film. Both these points have been discussed later. Based on geometric arguments, the thickness of a film at any instant is given by:

$$\delta_i = C(\phi)\, a^2 / l_i \qquad \text{III-12}$$

$C(\phi)$, which has been derived in Appendix A, is given by:

$$C(\phi) = \sqrt{3}/2\, (1-\sqrt{\phi})\, \sqrt{\phi}$$

In this way, we get

$$F_i = 2\sigma + \mu_L\, a^2 \frac{C(\phi)}{l_i^2} \frac{\dot{\gamma}\, dl_i}{d\gamma} \qquad \text{III-14}$$

Let $\underline{g}_1$, $\underline{g}_2$ and $\underline{g}_3$ represent three non dimensional vectors along OA, OB and OC of the triangular subcell i.e. $\underline{g}_1 = \underline{OA}/\underline{a}$ etc.

Then $g_i = l_i/a$. We now define a non dimensional number, N_{ca}, given by:

$$N_{ca} = \mu_L\, C(\phi)\, \dot{\gamma}\, a / 2\sigma \qquad \text{III-15}$$

This number, which can be thought of as a modified Capillary number, gives the relative importance of viscous and suface tension forces. In terms of N_{ca}, we get

$$F_i = 2\sigma \left(1 + \frac{N_{ca}}{g_i^2} \frac{dg_i}{d\gamma}\right) \qquad \text{III-16}$$

Substituting this into the stress expression yields:

$$\tau_{yx} = \frac{8\sigma}{a\, 3\sqrt{3}} \sum \left[\frac{dg_i}{d\gamma} + N_{ca} \frac{1}{g_i^2} \left(\frac{dg_i}{d\gamma} \right)^2 \right] \qquad \text{III-17}$$

For zero shear rate the second term in the equation drops out and the expression reduces to that of the equilibrium dry foam case. The stress tensor using the force approach was already worked out in the last chapter and is given by:

$$\underline{\underline{\tau}} = \sum \frac{F_i}{S} \frac{\underline{l}_i \, \underline{l}_i}{l_i} \qquad \text{II-14}$$

We can therefore determine the stresses from both expressions once the lengths and orientations of the liquid films g_i and their derivatives are known as functions of γ. Let us focus on ΔABC of Figure III-10 and choose A as the origin of a Cartesian coordinate system. Then from Equation II-17, the vectors $\underline{b}_1$, $\underline{b}_2$ along AB, AC are given by:

$$\underline{b}_1 = a\sqrt{3}/2 \; \{[\cos(\theta+60)+\gamma\sin(\theta+60)] \; \underline{\delta}_x + \sin(\theta+60) \; \delta_y\}$$

$$\underline{b}_2 = a\sqrt{3}/2 \; \{[\cos\theta + \gamma\sin\theta] \; \underline{\delta}_x + \sin\theta \; \underline{\delta}_y\}$$

Thus far the coordinates of A, B, C are known. To get the lengths of the liquid films we still need to know the coordinates of node O. Let this be x, y. Unlike previous cases, we cannot use the 120° degree criterion (Equation II-6) here to get x and y. However, we can use a force balance at point O. The force along each film is given by Equation III-16. At the Plateau border O, the sum of the components of the three forces in the x and y direction vanish independently. Thus,

$$\sum F_{ix} = \sum F_{iy} = 0 \qquad \text{III-18}$$

From this force balance we obtain two coupled differential equations of the form

$$R_j \, (x',y',x,y,\gamma) = 0 \qquad \text{III-19}$$

where,

$j=1, 2$ and ' denote derivatives with respect to γ. R_j is a function.

On simplification this leads to:

$$x' = (A_2B_3 - B_2A_3)/(A_1B_2 - A_2^2) \qquad y' = (A_2A_3 - B_3A_1)/(A_1B_2 - A_2^2)$$

in which A_i and B_i are given by

$$A_1 = N_{ca}\left[\frac{g_{1x}^2}{g_1^4} + \frac{g_{2x}^2}{g_2^4} + \frac{g_{3x}^2}{g_3^4}\right]$$

$$A_2 = N_{ca}\left[\frac{g_{1x}g_{1y}}{g_1^4} + \frac{g_{2x}g_{2y}}{g_2^4} + \frac{g_{3x}g_{3y}}{g_3^4}\right]$$

$$B_2 = N_{ca}\left[\frac{g_{1y}^2}{g_1^4} + \frac{g_{2y}^2}{g_2^4} + \frac{g_{3y}^2}{g_3^4}\right]$$

$$A_3 = -\left[\frac{g_{1x}}{g_1} + \frac{g_{2x}}{g_2} + \frac{g_{3x}}{g_3}\right] - N_{ca}\frac{a\sqrt{3}}{2}\left[\frac{g_{2x}^2}{g_2^4}\sin(\theta+60) - \frac{g_{3x}^2}{g_3^4}\sin\theta\right]$$

$$B_3 = -\left[\frac{g_{1y}}{g_1} + \frac{g_{2y}}{g_2} + \frac{g_{3y}}{g_3}\right]$$

$$- N_{ca}\frac{a\sqrt{3}}{2}\left[\frac{g_{2x}g_{2y}}{g_2^4}\sin(\theta+60) - \frac{g_{3x}g_{3y}}{g_3^4}\sin\theta\right]$$

g_{ix} and g_{iy} are the magnitudes of the x and y components respectively of the liquid film l_i.

These coupled ordinary differential equations were solved using a sixth order Runge-Kutta method to obtain x and y as functions of γ. With knowledge of the coordinates of point O, all necessary information such as film lengths, angles between films and stresses could be calculated.

2. Discussion of Results

In all our calculations, ϕ=0.99 were used. This resulted in a value of 4.32×10^{-3} for $C(\phi)$. Deformations only up to the yield point were calculated. However, it should be realized here that at this critical strain the length of the shrinking film never goes to zero. This is because each film has a finite liquid content determined by ϕ, and this volume is conserved at all times. Thus, the strain beyond which further shrinkage of the film leads to violation of the liquid volume conservation is characterized as the critical strain, γ_c, here. For a film with initial length a and thickness δ_o, γ_c roughly corresponds to the point l_i becomes $\sqrt{a\delta_o}$. Calculations carried out in Appendix A for $\phi=0.99$ show the length of this film to be approximately 7% of its original length at this point. The improbability of l_i going to zero value can also be seen from a different perspective. In the stress equation (III-16), one of the terms has g_i in the denominator. Thus for g_i to go to zero we would require an infinite stress.

One other thing should be noted in terms of our calculations here. Although we used a value of 0.99 for ϕ, our results for a specified Capillary number, N_{ca}, would not have changed had we used a different gas fraction to approximate a dry foam. The critical strain however would be slightly different since δ_o, which affects γ_c, is a function of ϕ. Also, it is evident from the definition of N_{ca} (Equation III-15) that for a given N_{ca} the shear rate would be different in this case.

In formulating our equations, we assumed a hexagonal foam cell and ignored the curvature of the Plateau border. In reality, the Plateau borders are curved with its radius of curvature proportional to δ^n. Introducing such curvature does affect $C(\phi)$. However, all such effects are embedded in the dimensionless Capillary number, N_{ca} and our results for a specific N_{ca} do not change. The shear rate corresponding to this

N_{ca} and the critical strain would however be different in this case. Also, inherent in our calculation is the assumption that the liquid volume of each film remain constant i.e. there is no flow into or out of it to the Plateau border. We feel this to be reasonable because with a finite shear rate the system does not have time to equilibrate and there can be only localised thinning or thickening of films. Clearly in the equilibrium situation, all δ_is should be same as predicted by liquid film theory and Young Laplace's equation (See Chapter IV).

The equations developed in the last section were solved as increasing functions of strain for different values of N_{ca} and θ. In Figure III-11, cell deformations for $\theta=0^o$ and $N_{ca}=.001$ has been compared with the equilibrium ($N_{ca}=0$) case. In all cell structures shown in this section the thin line represents the equilibrium structures and the bold one the $N_{ca}=0$ case. In this figure, which shows cell structures with increasing strain in a clockwise direction, we observe very good overlap with the $N_{ca}=0$ case. Only in structure D do we observe a very slight difference. For the equilibrium case this corresponds to the yield point with film OC having zero length. For $N_{ca}=0.001$, the films can never be zero. We are thus bound to observe some differences near the γ_c of the equilibrium case. This deviation is also reflected in the stress-strain plots of the two Capillary numbers (Figure III-12). We observe very good agreement between the two upto γ~1 (Figure III-11c). Beyond this, close to γ_c, g_3 starts to get very small, the $1/g_3$ term dominates and we see a corresponding increase in stress. Overall, however, the equilibrium model approximates the $N_{ca}=0.001$ case very well.

As we go to higher capillary numbers, we observe a gradual predominance

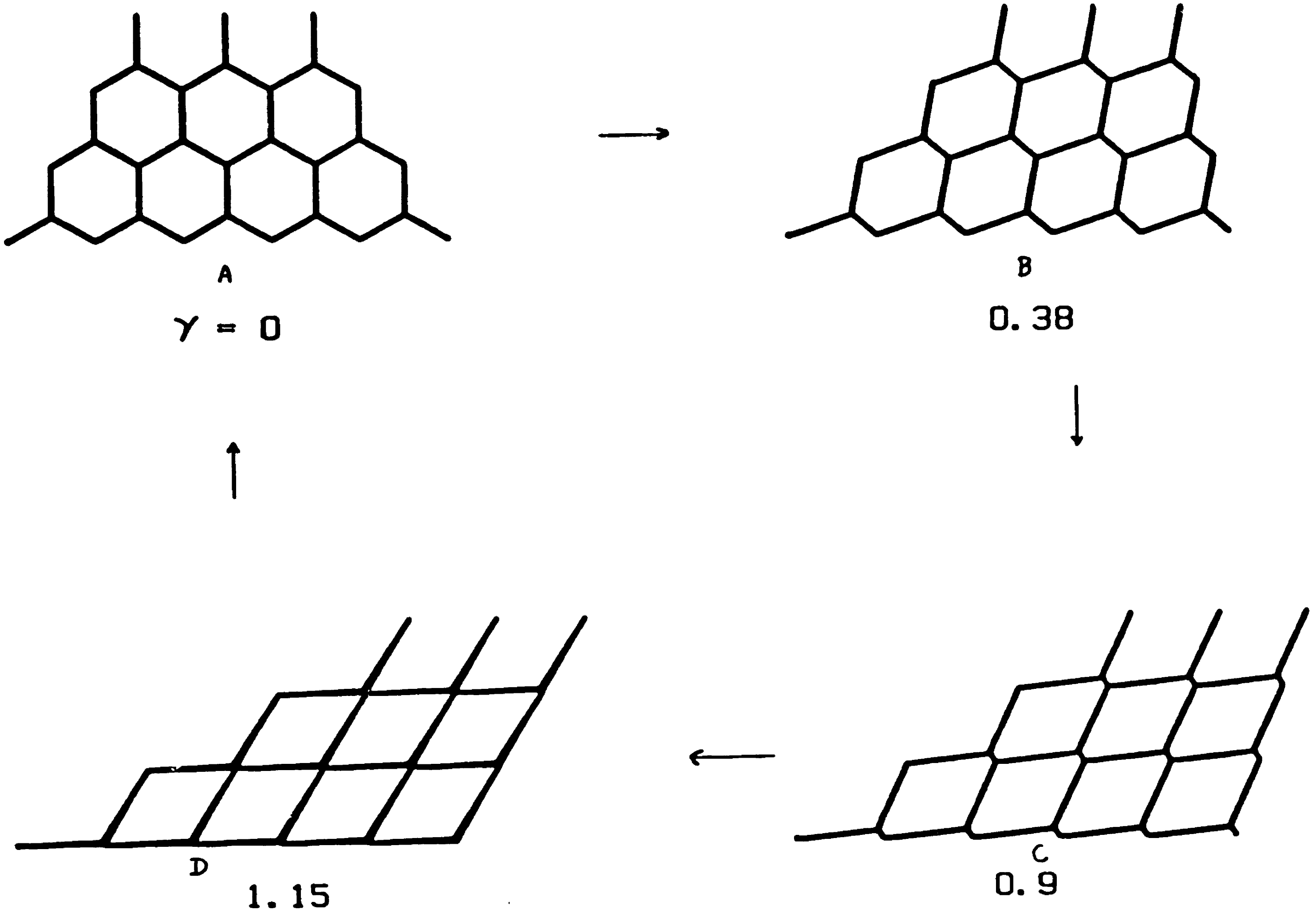

Figure III-11 Cell structures in a shearing deformation for initial orientation, $\theta=0^o$. Nca=.001 (bold lines) is compared with the equilibrium case (Nca=0). Nca is the ratio of viscous and surface forces. Note the complete overlap between the two.

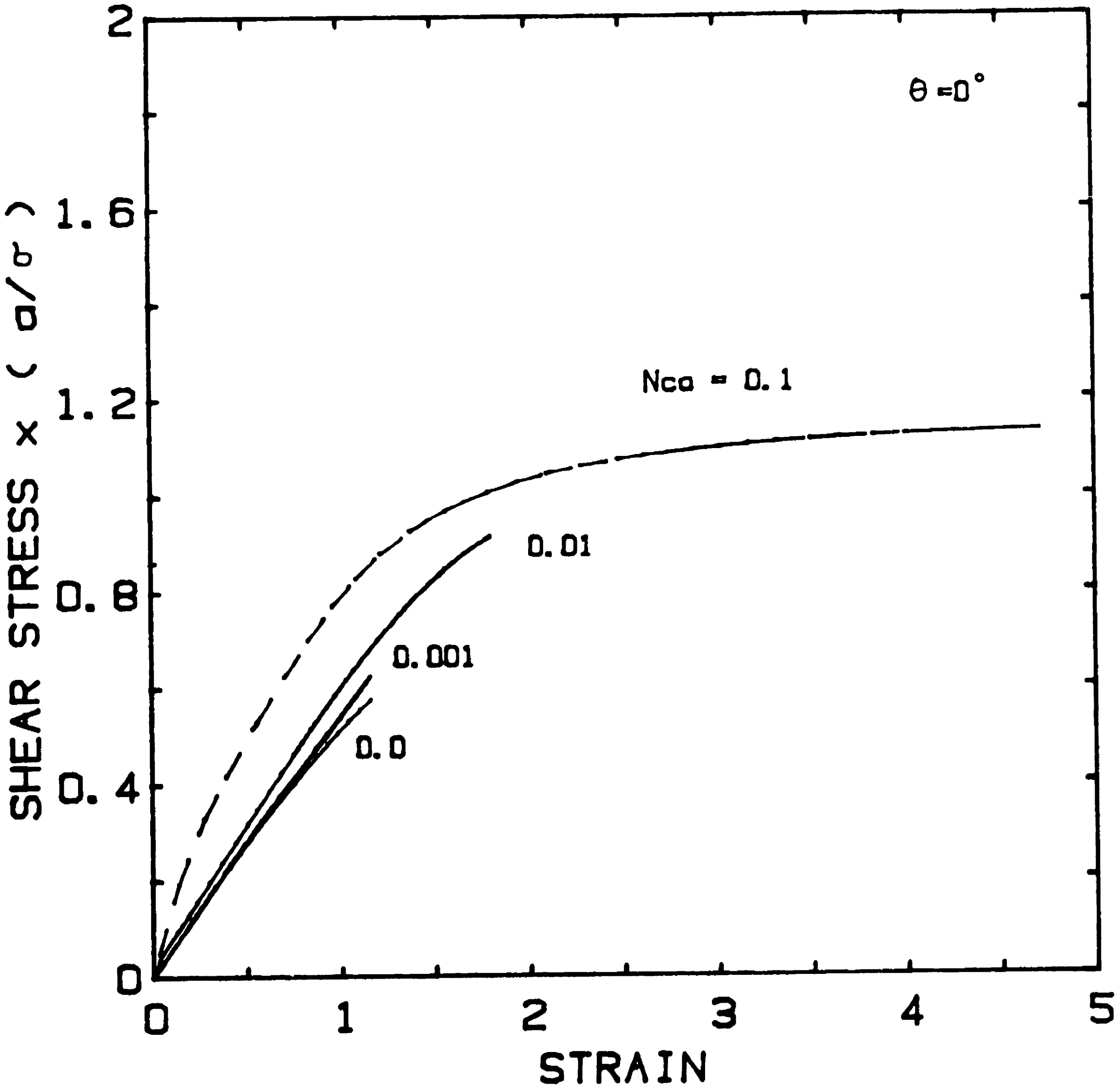

Figure III-12 Effect of viscous stresses in the stress-strain relation for initial orientaion, θ=0°. Nca is the ratio of viscous and surface forces. a=length of undeformed side of hexagon; σ=surface tension.

of the viscous forces in determining the cell structures. In Figure III-13, deformations for N_{ca}=0.01 and N_{ca}=0 are compared. We observe good overlap for strains up to ~0.5. At higher strains, the deviation is obvious (structure C). At this γ, the equilibrium foam has already reached the critical state. From Figures III-12, 13d we find the critical strain for the N_{ca}=.01 case to be two times larger. The cells are also more inclined in the direction of shear. The stress-strain curve also show deviations in this case but not as significant as that for N_{ca}=0.1 (Figure III-12). In the latter case, there is barely any overlap; the stresses rise much faster and then level off. γ_c is four times larger than the equilibrium case. The deformation pictures also reveal the differences (Figure III-14). Even at strains of ~0.14 (structure A) we start seeing deviations which increase with strain. At γ_c for the equilibrium case (structure C), unlike the two previous cases, the length of the shrinking film (for N_{ca}=.1) is still quite large. At γ=4.5 (D), which is close to γ_c for this case, the cells are elongated and inclined. Finally, in Figure III-15 are shown the plots for N_{ca}=1. Here viscous effects become evident even at such small strains as .07 (structure A). Two of the angles have already changed by more than one degree from 120° to 107 and 126°. With further increase in strain, the viscous forces stretches one of the films much more rapidly than the film which is shrinking. The resulting structures become very elongated and stretched out. Although deformations upto γ=3 are shown, the critical strain in this case is ~28. At such large strains the cells are very thin elongated structures and a typical cell goes well beyond a page in length in the x direction. Physically, one would expect the cells to rupture much

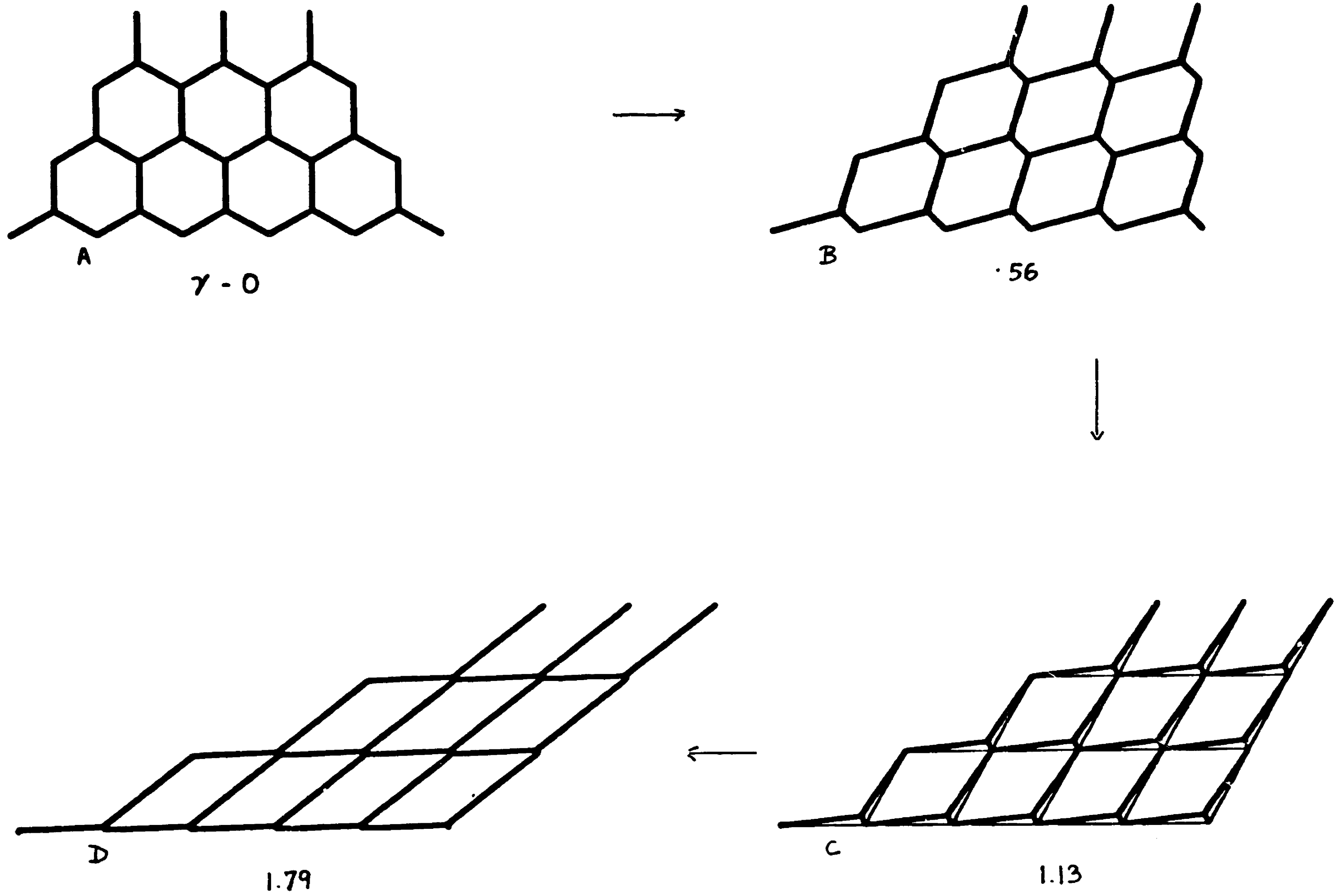

Figure III-13 Cell deformation for initial orientation $\theta=0^{o}$, Nca=.01 (bold) compared with the equilibrium model (Nca=0). Note the deviation.

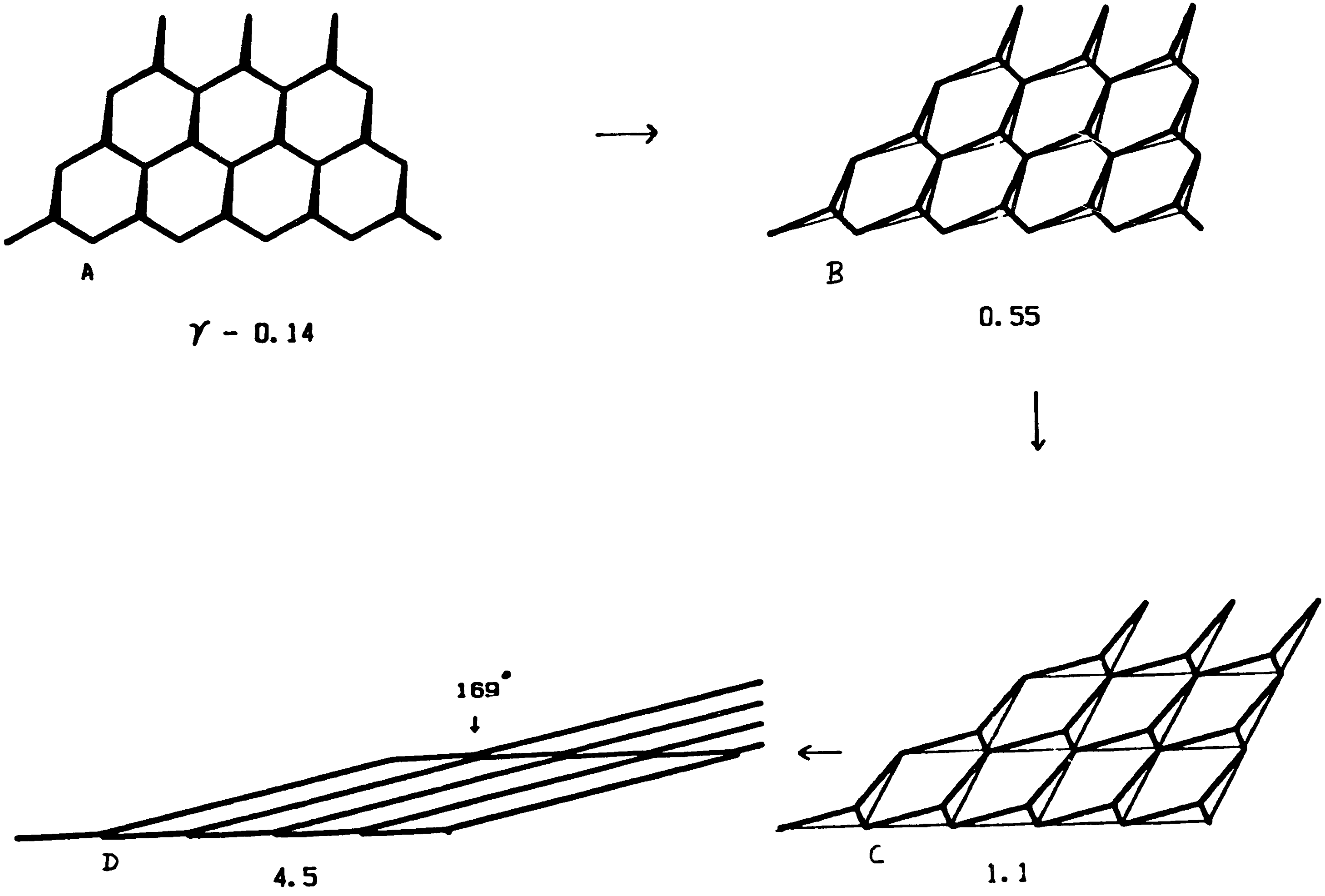

Figure III-14 Cell deformation for $\theta = 0^o$, Nca=0.1 (bold) compared with the equilibrium (Nca=0) case. Increased difference in cell structure is observed here. Nca=viscous/surface force.

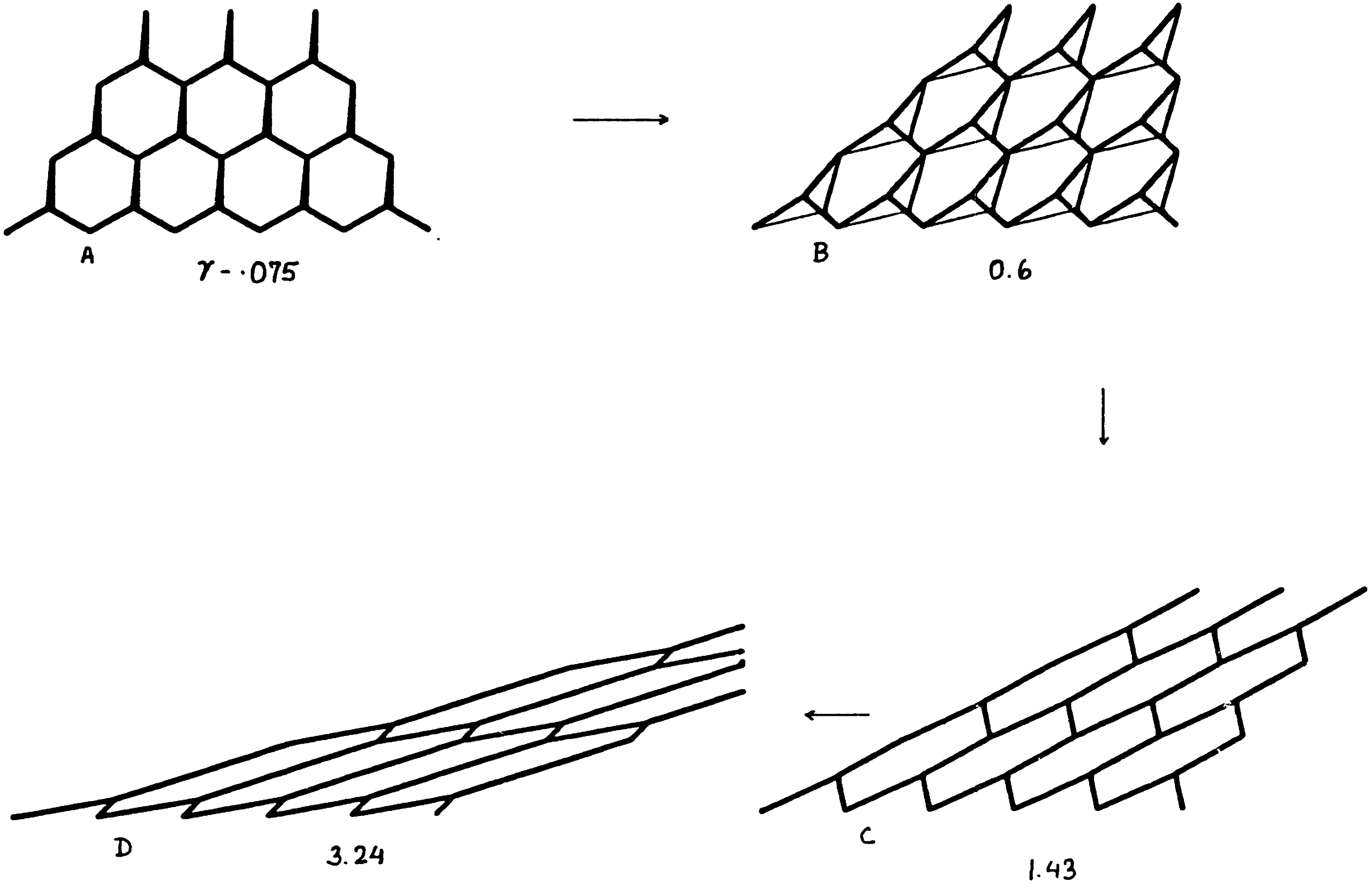

Figure III-15 Shear deformation in foam cells. Nca=1.0 (bold) and Nca=0 is compared here. Note that rapid elongation of cells reveal possible mode of cell rupture. Nca=viscous/surface force.

before this state is reached. Thus, at high $\dot{\gamma}$, this model predicts possible modes of cell rupture. In the stress-strain plot (Figure III-16), the stress reaches a maximum value almost instantaneously at the onset of deformation. The stress then goes through a couple of oscillations before approaching a constant value. The oscillations probably arise from the non monotonic changes in the angle betweeen the films. For example, angle BOC (ψ_1) decreases and then increases; angle AOC (ψ_3) increases, then decreases for strains up to 3 before finally increasing again. These changes are reflected in the humps. We also find side OA to increase up to γ~3 and then to decrease.

Figure III-17 has the cell deformation for $\theta=30^o$ and N_{ca} =.01. Analogous to the corresponding $\theta=0^o$ case, slight deviations from the equilibrium situation are observed here. For strains lower than 0.9 there is good overlap. However, beyond that we start observing differences. The critical strain, as can also be seen from Figure III-18, is larger than the $N_{ca}=0$ case. However, γ_c is not as affected as in $\theta=0^o$. From the stress-strain plot, we observe stress deviations around $\gamma=.9$. For $N_{ca}=0.1$, the behavior is very similar to the $\theta=0^o$ case with hardly any stress overlap. An interesting feature to note is the shoulder in the stress curve. This can be attributed to the same cause that caused the humps in the stress plot for $N_{ca}=1$ and $\theta=0^o$. Here, angle ψ_1 increases, then decreases, and then finally increases again with strain. ψ_2 shows the reverse behavior while film OB shows an initial decrease in length before starting to extend. However, their effect on stress is not as pronounced as the earlier case.

For an initial orientation of $\theta=45^o$, several observations can be

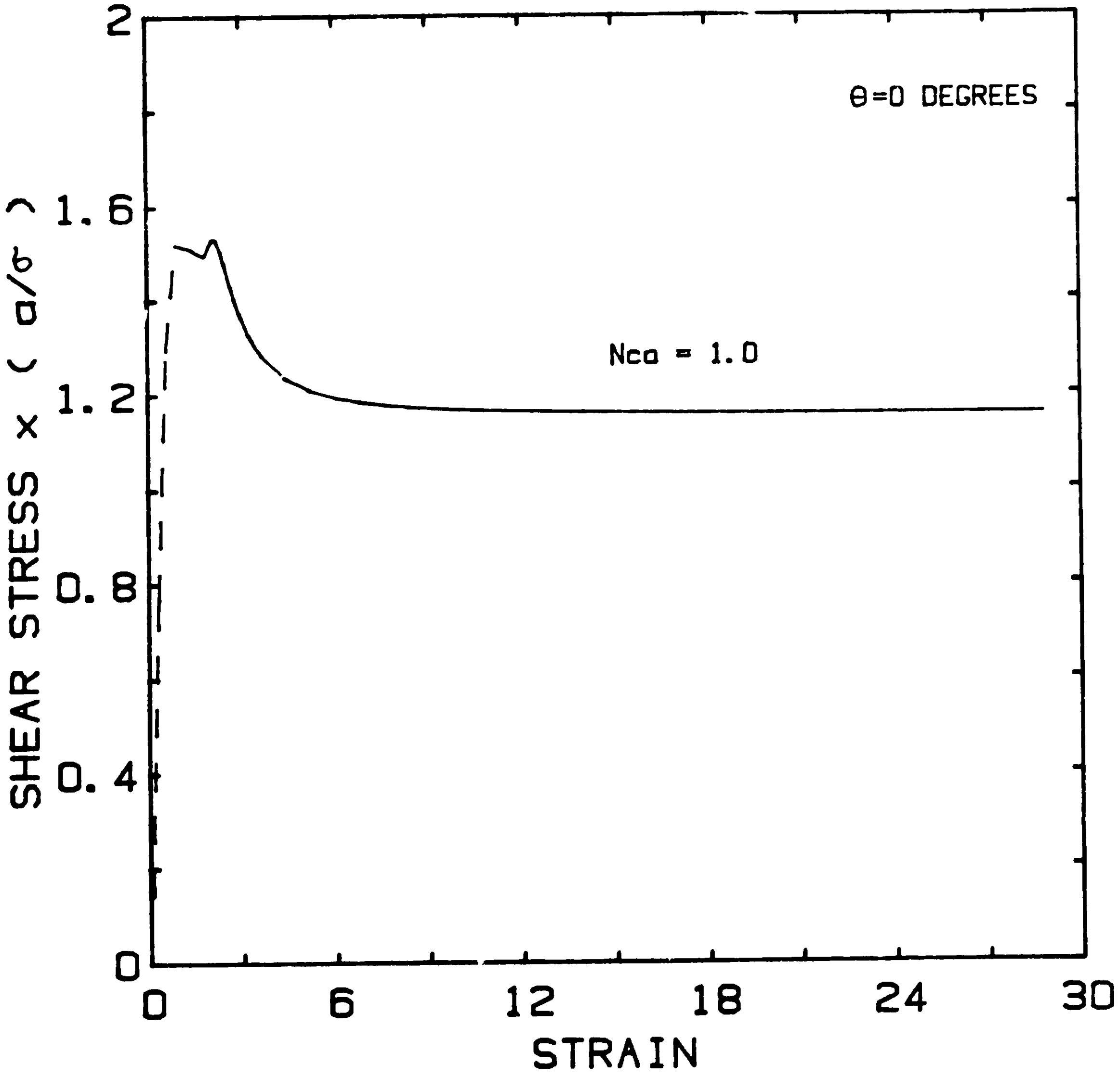

Figure III-16 Stress-strain relation for θ=0°, Nca=1.0. Critical strain, γ_c is much larger (28) here than the equilbrium case (1.15).

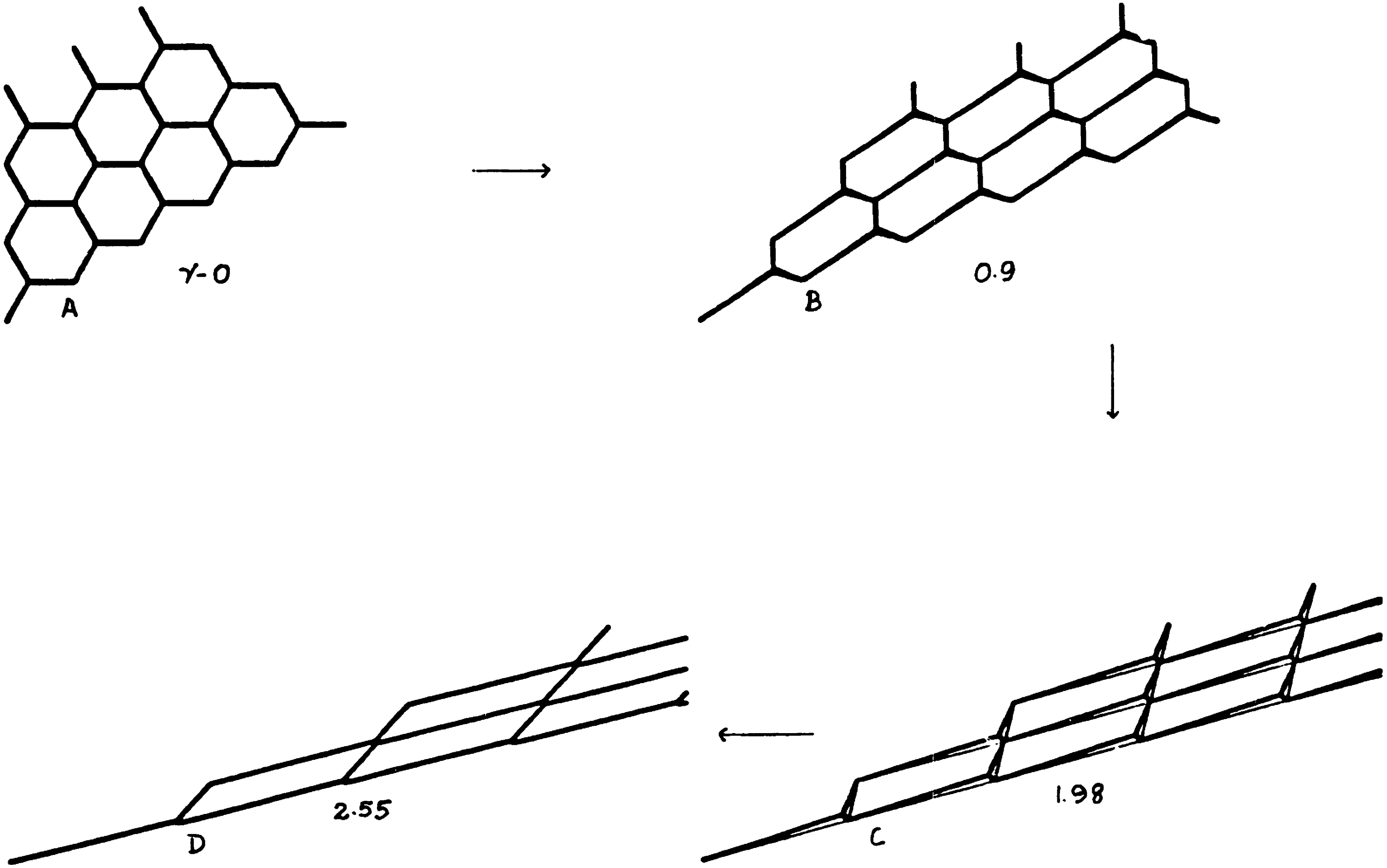

Figure III-17 Cell deformation for initial orientation θ=30°. Nca=.01 (bold) and Nca=0 is compared. Cells show fairly good overlap.

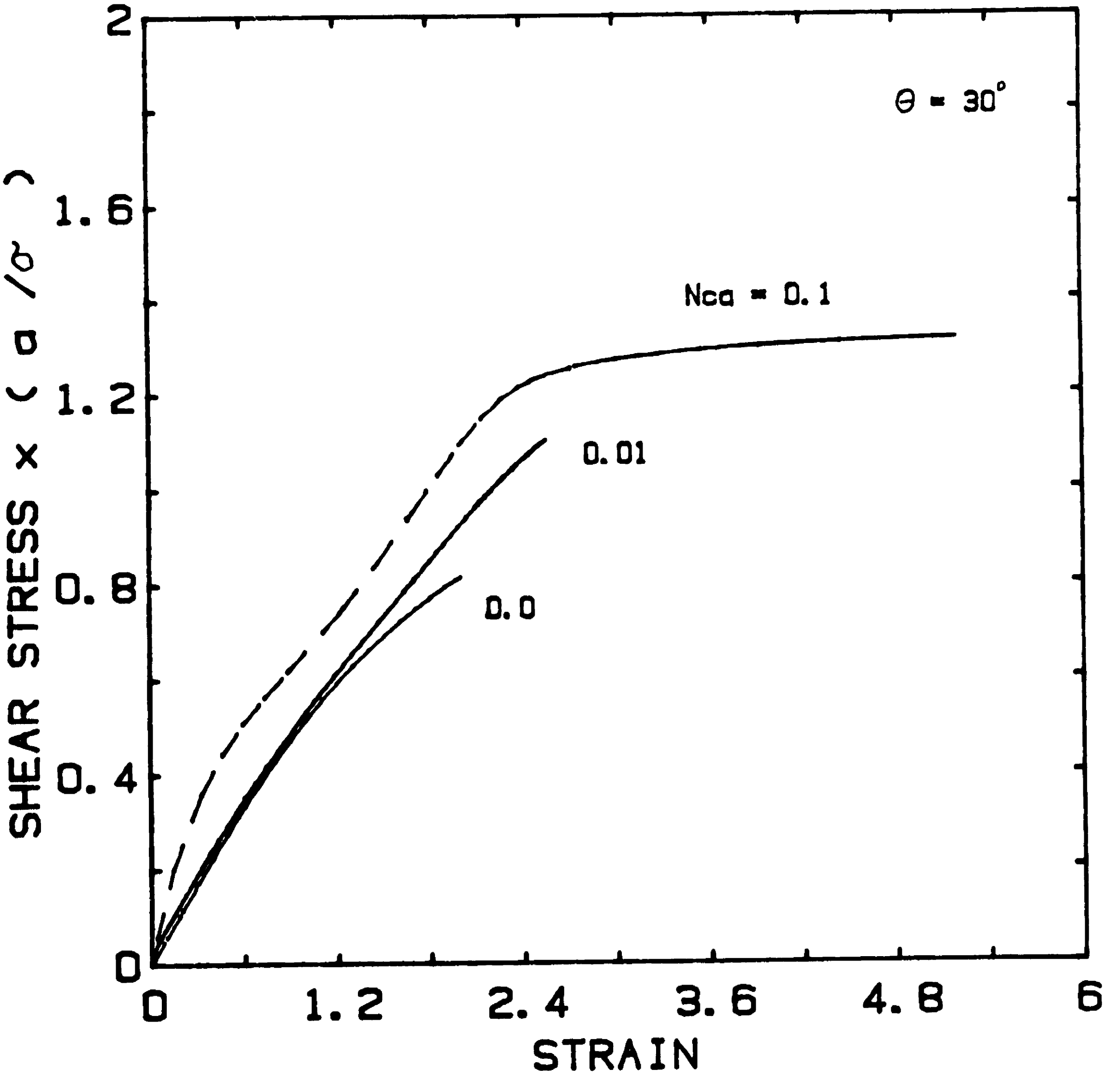

Figure III-18 Effect of viscosity on the shear stress-strain relation for θ=30°. σ=surface tension; a=undeformed side length of hexagon.

made. For N_{ca}=0.005, there is very good agreement with that for N_{ca}=0 both in the stress-strain plot (Figure III-19) and cell deformation (Figure III-20). The critical strain is a little larger (2.25 instead of 2) and the corresponding structure slightly different from the equilibrium case. For N_{ca}=.01 there is very good overlap in the stress plot (Figure III-19) up to the point where the equilibrium curve ends. Cell deformation (Figure III-21) also shows a similar behavior up to this point (structure B). Beyond this we observe a very interesting phenomenon. Earlier in the last Chapter, we found that at 45^{o} side OB goes to zero length at γ_c. Here, for strains up to 3 (structure C), we observe a decrease in the length of OB. But just before it can reach its 'zero' length, OB starts to grow again. So eventually it is film OC that goes to 'zero'. This flip-flop is observed in the structures C and D. Thus, here the shear rate influences the final shape of the cells. In the τ-γ curves for N_{ca}=.01 and .1 we observe maximums because of the reasons mentioned earlier. The critical strain for the latter is four times as large compared to the equilibrium situation.

For θ=50^{o}, we find the film OB and not OC to shrink to zero (Figure III-22) at γ_c for N_{ca}=.01. From the figure we observe good agrement for strain up to ~0.7. At γ=1.2, which is the critical point for the corresponding N_{ca}=0 case, we see small differences in the cell structures. For N_{ca}=0.1, however, things are quite different. The critical strain is eight times as large (Figure III-23) and the stress shows a pronounced maximum. The cell structures are strongly affected by the viscous forces (Figure III-24). We observe the flipping of sides (structures C & D). Further, the cells are highly elongated suggesting the possibility of

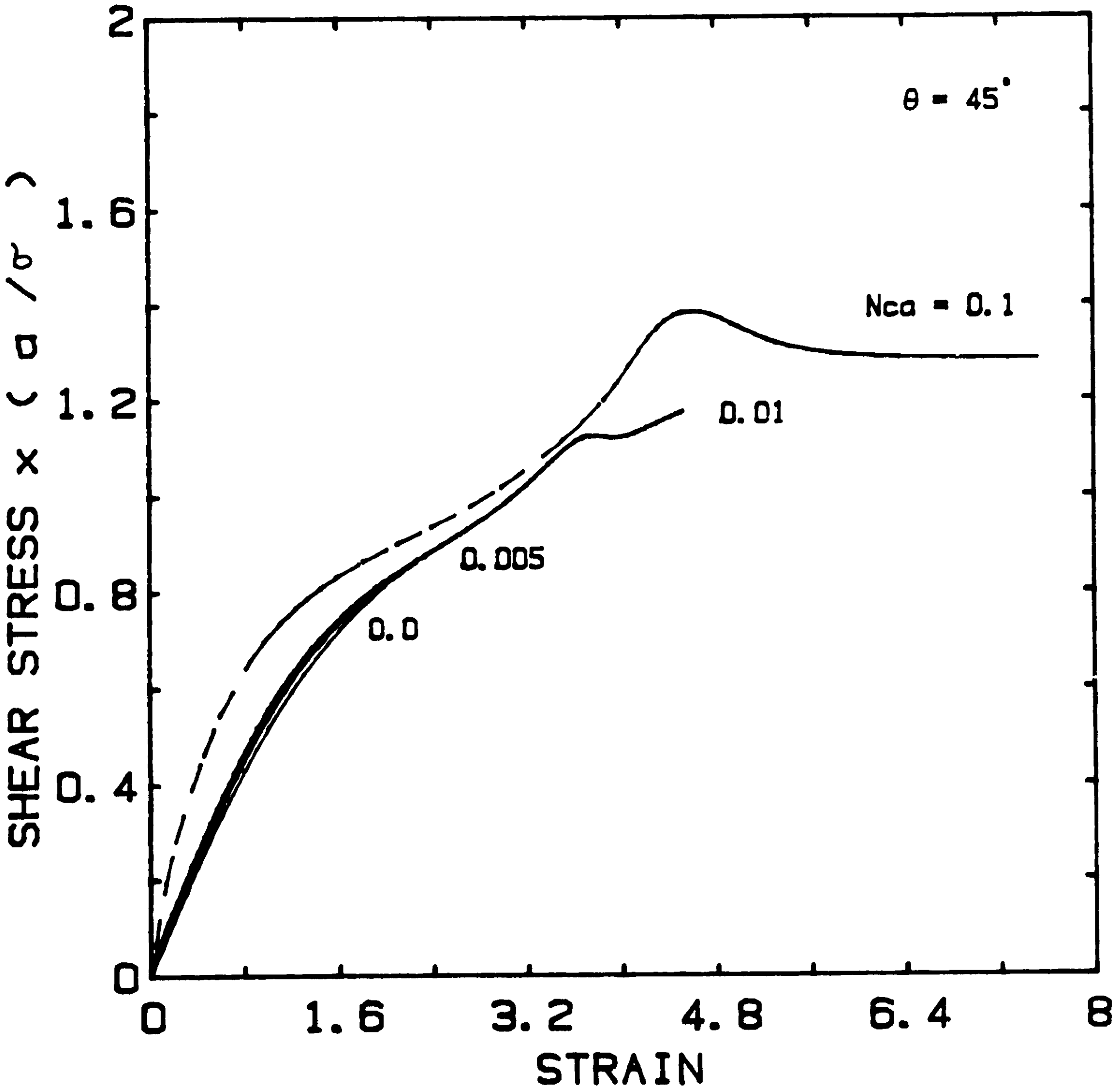

Figure III-19 Stress versus strain for different Capillary numbers, Nca. Initial orientation θ=45°. Curves for Nca=0 &.005 overlap.

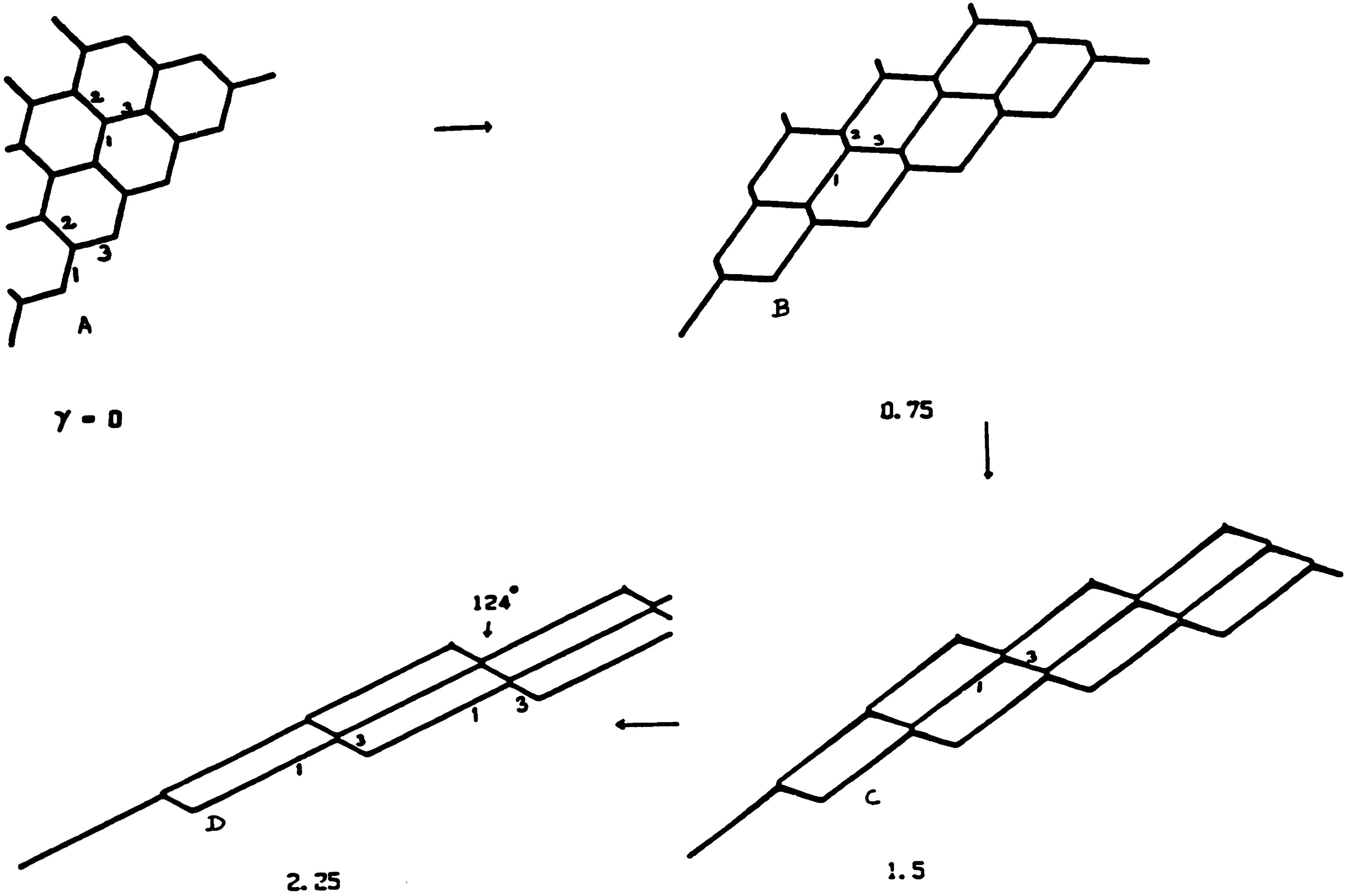

Figure III-20 Comparison of cell structures in a shearing deformation for Nca=0 (equilibrium) and Nca=.005 (in bold). Initial orientation, θ=45°. Nca=viscous/surface force. Very good overlap is observed.

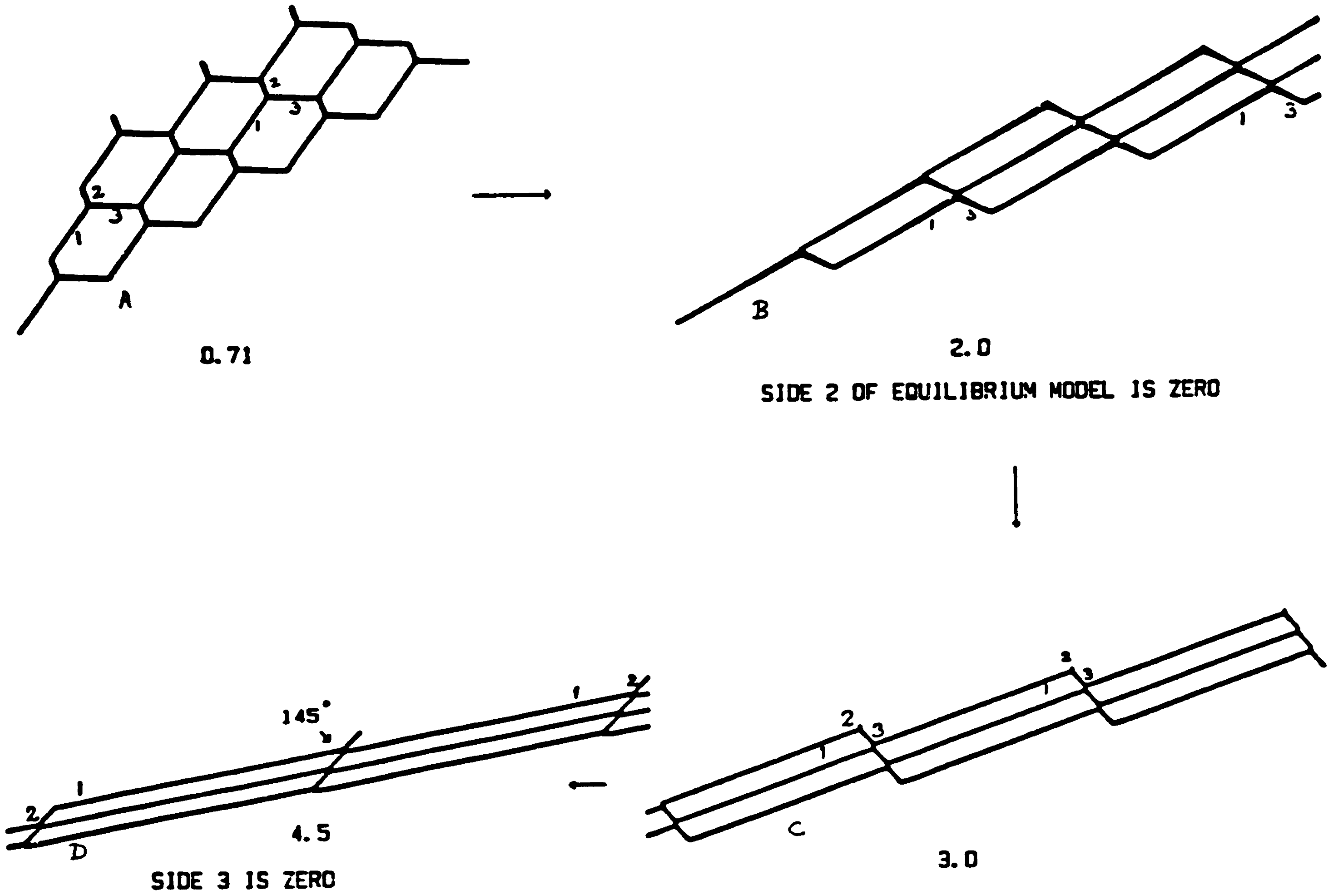

Figure III-21 Cell deformation for Nca=.01, θ=45°. Although initally side 2 reduces in length (C), side 3 eventually goes to zero (D).

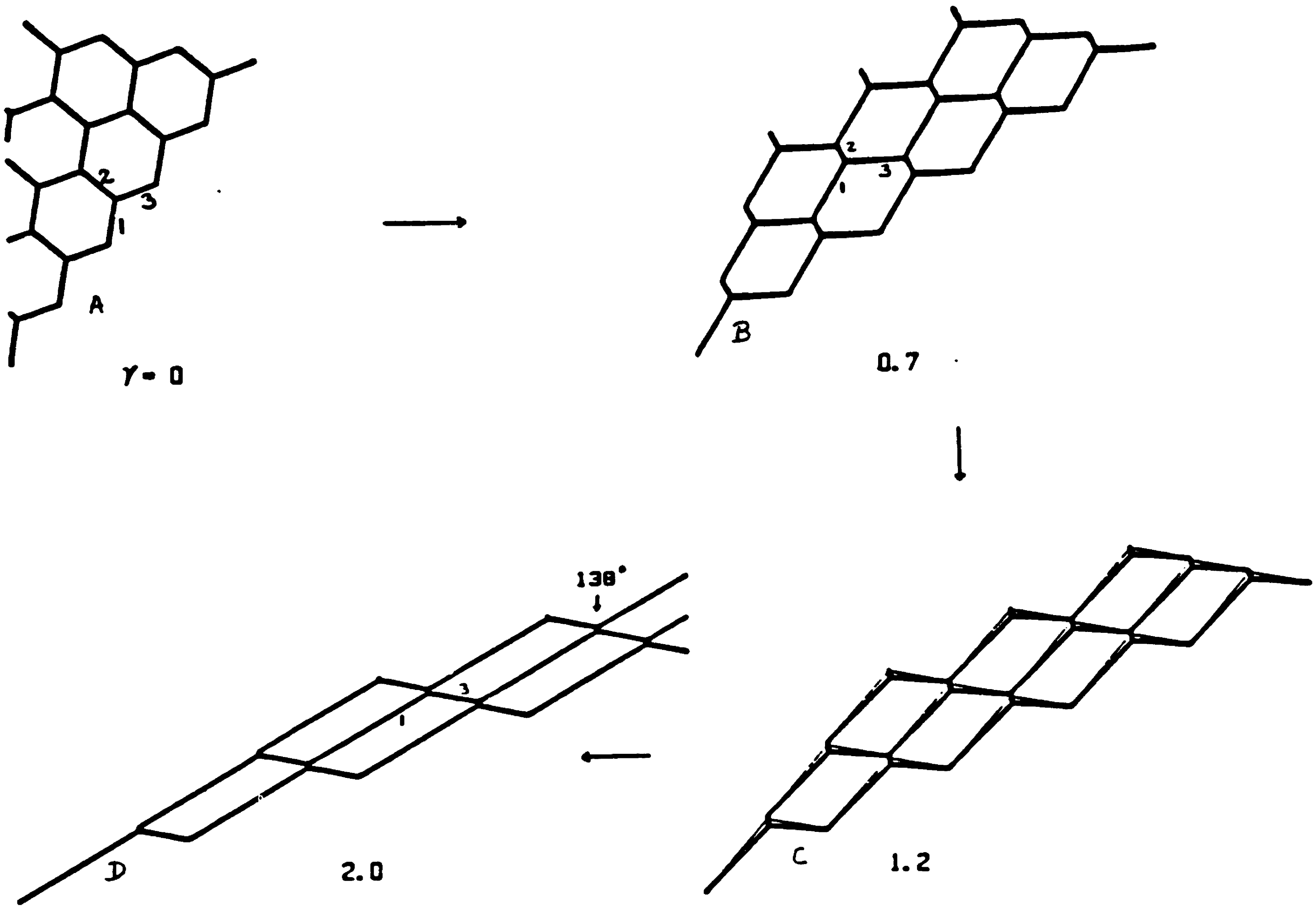

Figure III-22 Cell deformation for Nca=.01, θ=50°. Equilbrium model (thin line) is also compared up to C.

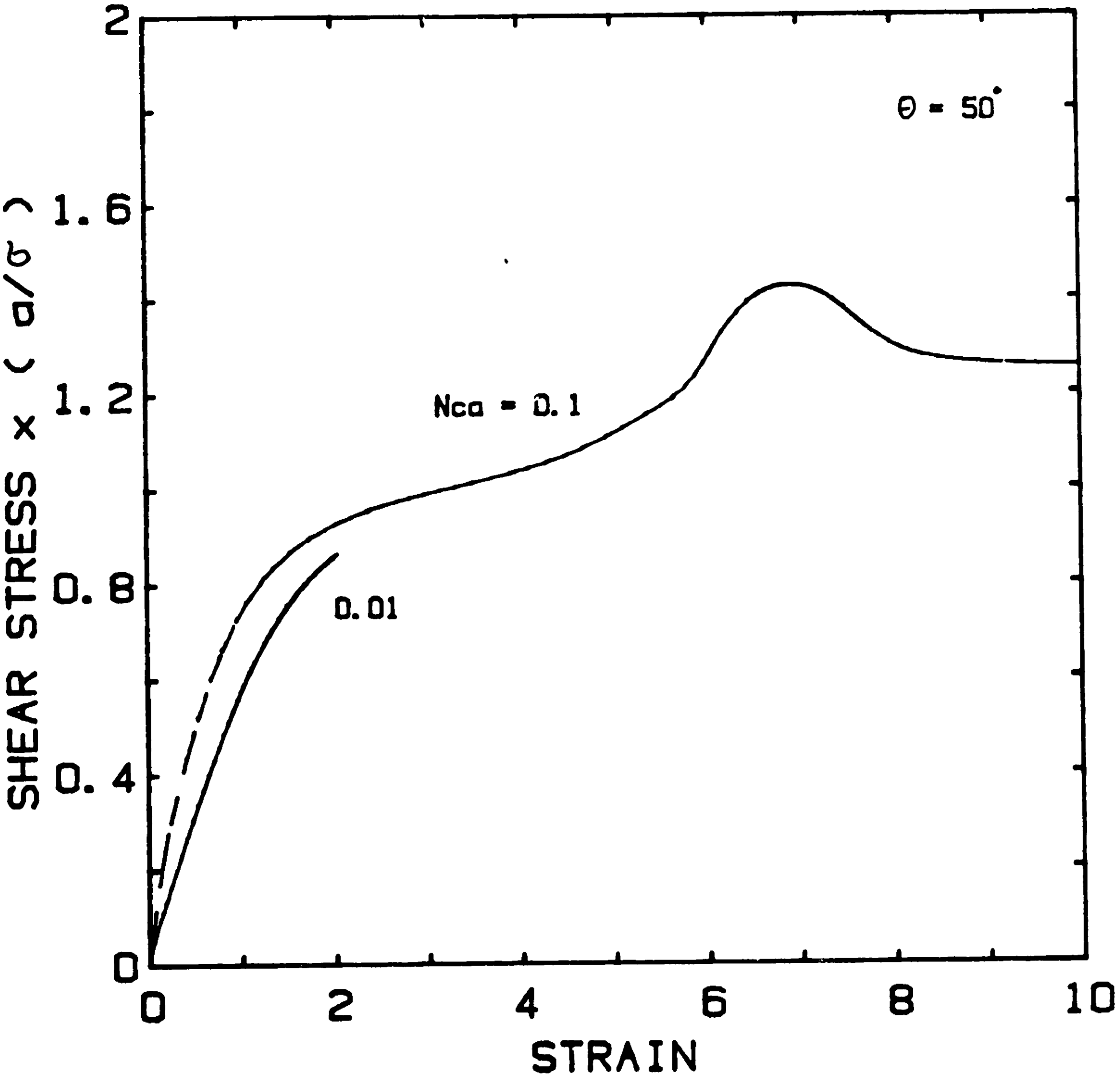

Figure III-23 Stress-strain relation for different Nca. Initial orientation, θ=50°. Nca is the ratio of viscous and surface forces.

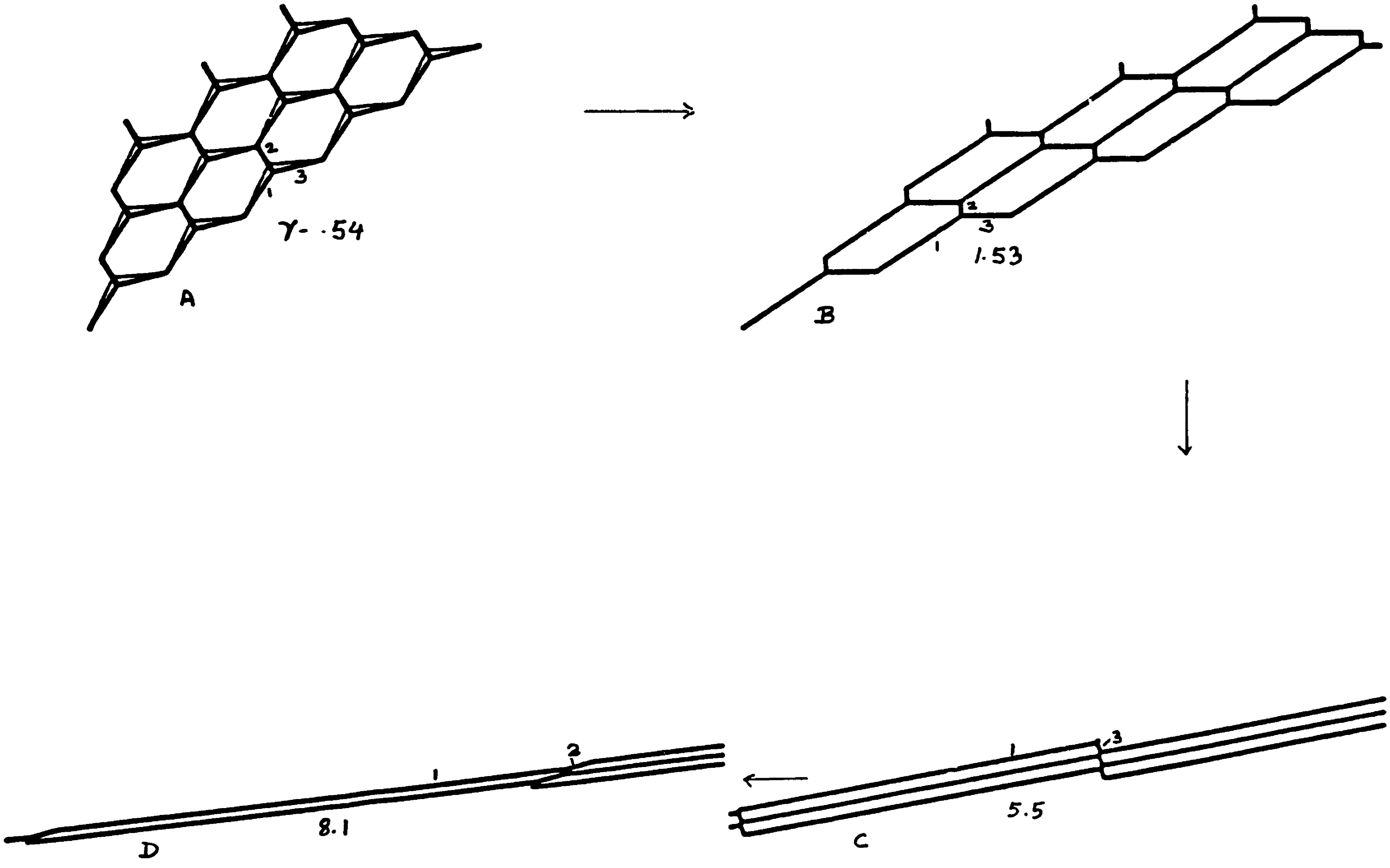

Figure III-24 Cell structures for θ=50°, Nca=0.1. Note elongation of cells. Also observe that side 3 finally goes to zero instead of 2 .

rupture to occur.

Based on all the information presented above it is clear that viscous force effects are strongly influenced by the initial orientation of the cells. For instance, even at the same capillary number (0.01), two different sides go to zero length for a five degree change ($45^o \rightarrow 50^o$) in orientation. Further the magnitude of the viscous stresses itself is not very large compared to the total stress.

In Figure III-25, we have plotted for $\theta = 0^o$ and Nca=0.1 the shear stress and its two components, the viscous force and the surface force, as a function of strain. These two components corresponds to the first and second term of Equation III-17 respectively. We observe the viscous stress to be much smaller than the stress due to surface forces, and asymptoting to a zero value at large strains. Recall from Equation III-16 that the viscous force is inversely proportional to l_i^2. At the onset of deformation, some side of the foam cell shrinks rather rapidly. Consequently, the viscous stress goes up quickly (Figure III-25). Beyond a certain point, however, this shrinking side shows no significant changes in length and the other sides stretches rapidly (Figure III-14) resulting in a monotonic decrease in viscous stress. It is evident from this and all cell deformation plots that the major effect of incorporating viscous forces in our model is the change in the orientation and shape of the cell structures. This change in structure and not the actual viscous contribution increases the total stress from the equilibrium model.

In our discussion so far we focussed on shear stress only. However, our method is general enough to give us the total stress tensor. Figure III-26 shows the normal stress difference, N_1, for $\theta = 0^o$ and three different

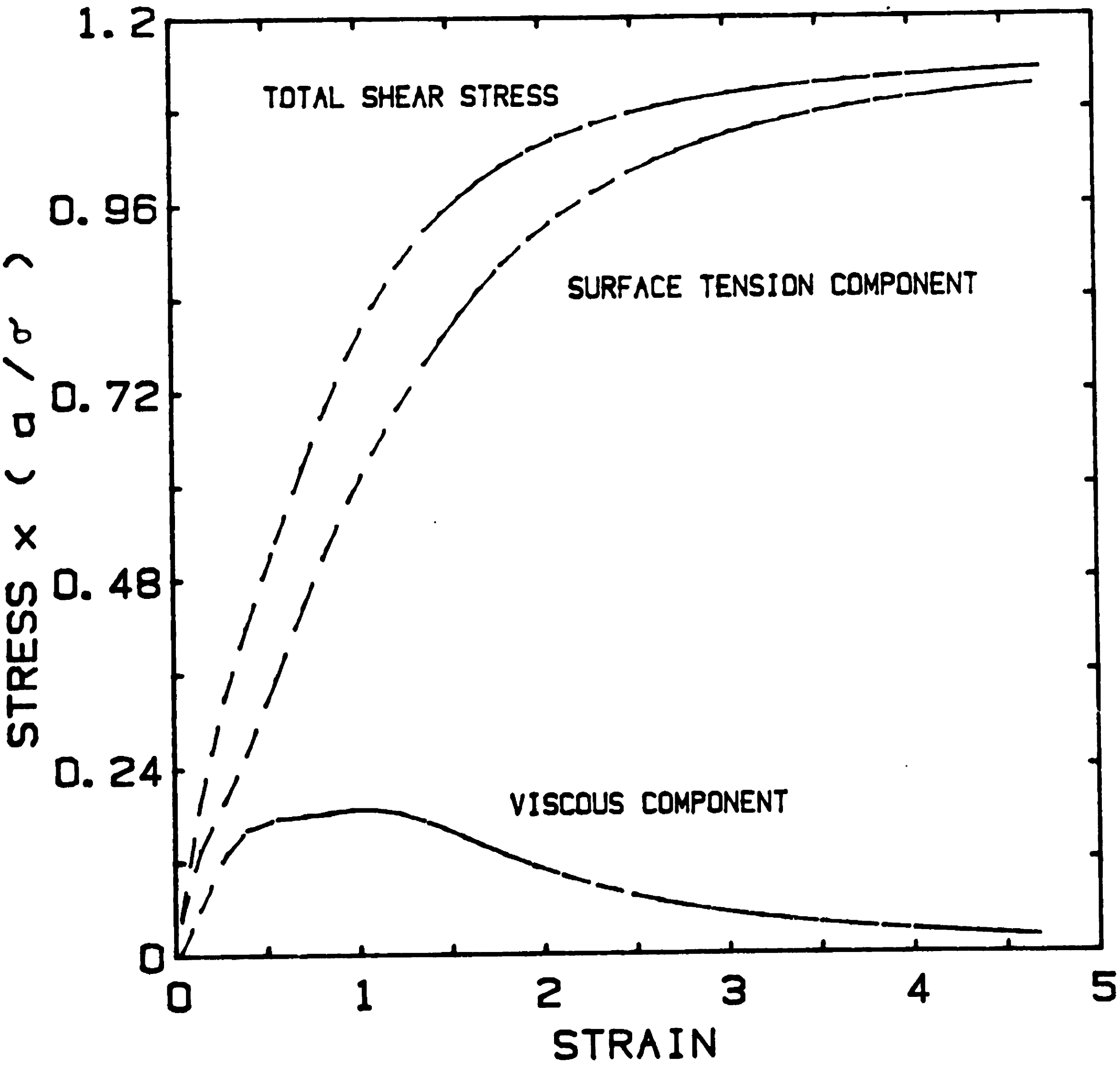

Figure III-25 Total shear stress and its viscous and surface tension components plotted as a function of strain. Initial orientation, θ=0°. Nca=0.1; σ=surface tension; a=side length of undeformed cell.

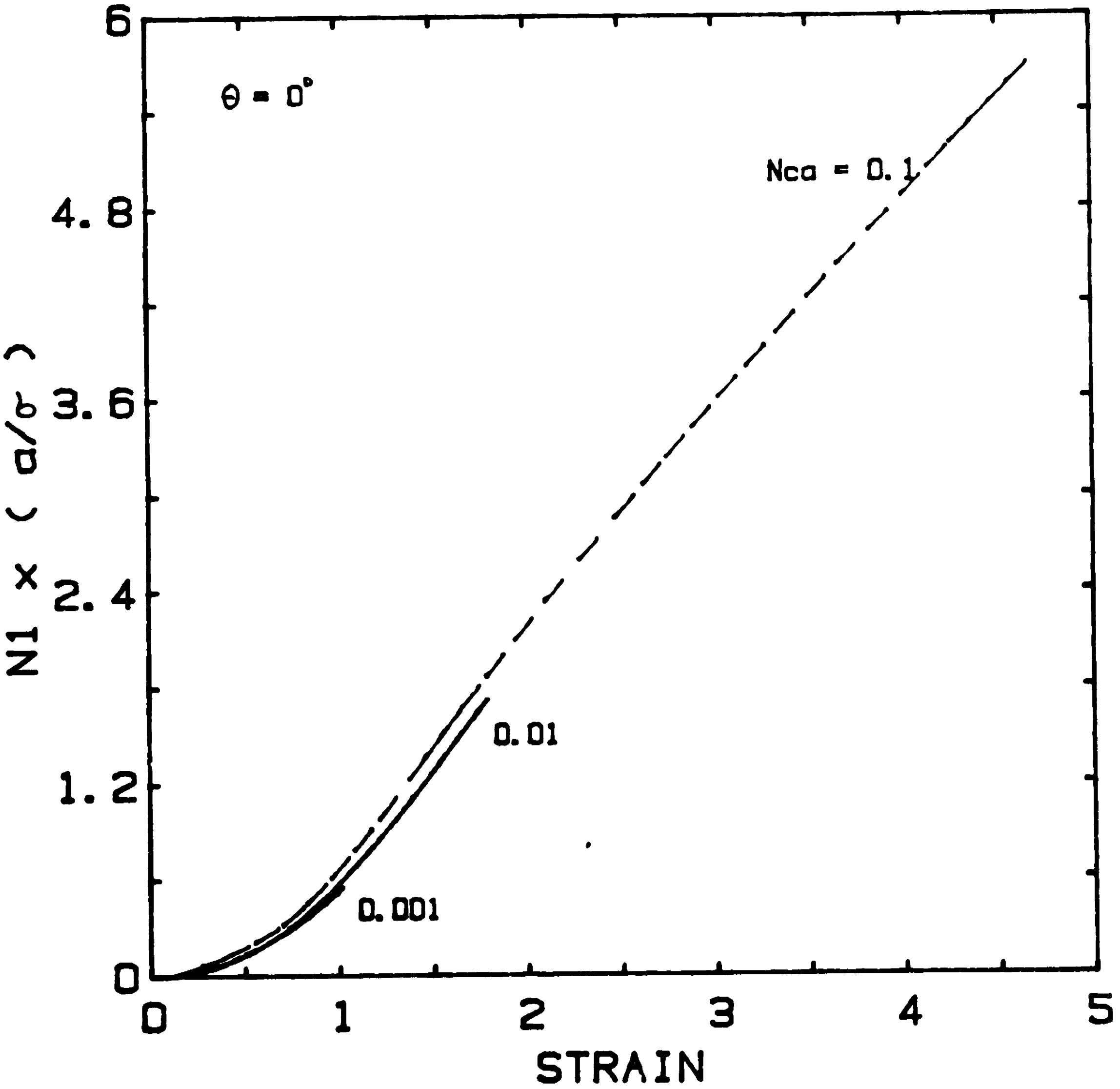

Figure III-26 Normal stress difference as a function of strain for different Capillary numbers, Nca. Initial orientation, θ=0°. σ=surface tension. a=length of side of undeformed hexagon.

capillary numbers. We observe good overlap among them for small strains. In Figure III-27 we plot N_1 for Nca=1.0. Unlike the shear stress, which showed overshoots and oscillations, we observe only a small kink in this stress strain curve. We also find N_1 to be almost linear and proportional to γ at large strains for both Nca=0.1 and 1. The corresponding shear stress curves (Figures III-12, 16) asymptote to constant values with increasing strain. From our equilibrium dry foam model of the previous chapter, we have:

$$\tau_{yx} = \frac{2\sigma}{a} \frac{\gamma}{\sqrt{(3\gamma^2 + 12)}} = \text{a constant (for large } \gamma)$$

$$\tau_{xx} - \tau_{yy} = \frac{2\sigma}{a} \left[\frac{\gamma^2}{\sqrt{(3\gamma^2 + 12)}} \right] = (\text{constant})\cdot\gamma \qquad (\text{for large } \gamma)$$

Thus, the simplified model also predicts such asymptotic behavior correctly.

Finally we address the question of the validity and usefulness of the equilbrium dry foam model developed earlier in the last chapter. As we have seen here, incorporation of liquid viscosity can result in significant changes in rheology. However, one should realize here that for typical values of cell size and interfacial tension even a very small capillary number like 0.001 corresponds to a macroscopic shear rate larger than 1000. It is indeed satisfying to see from the 0° (Figures III-11, 12) and 45° case (Figures III-19, 20) that even at such high shear rates the equilibrium condition is a very good assumption for foam deformation. Further, in most processes shear rates higher than this would

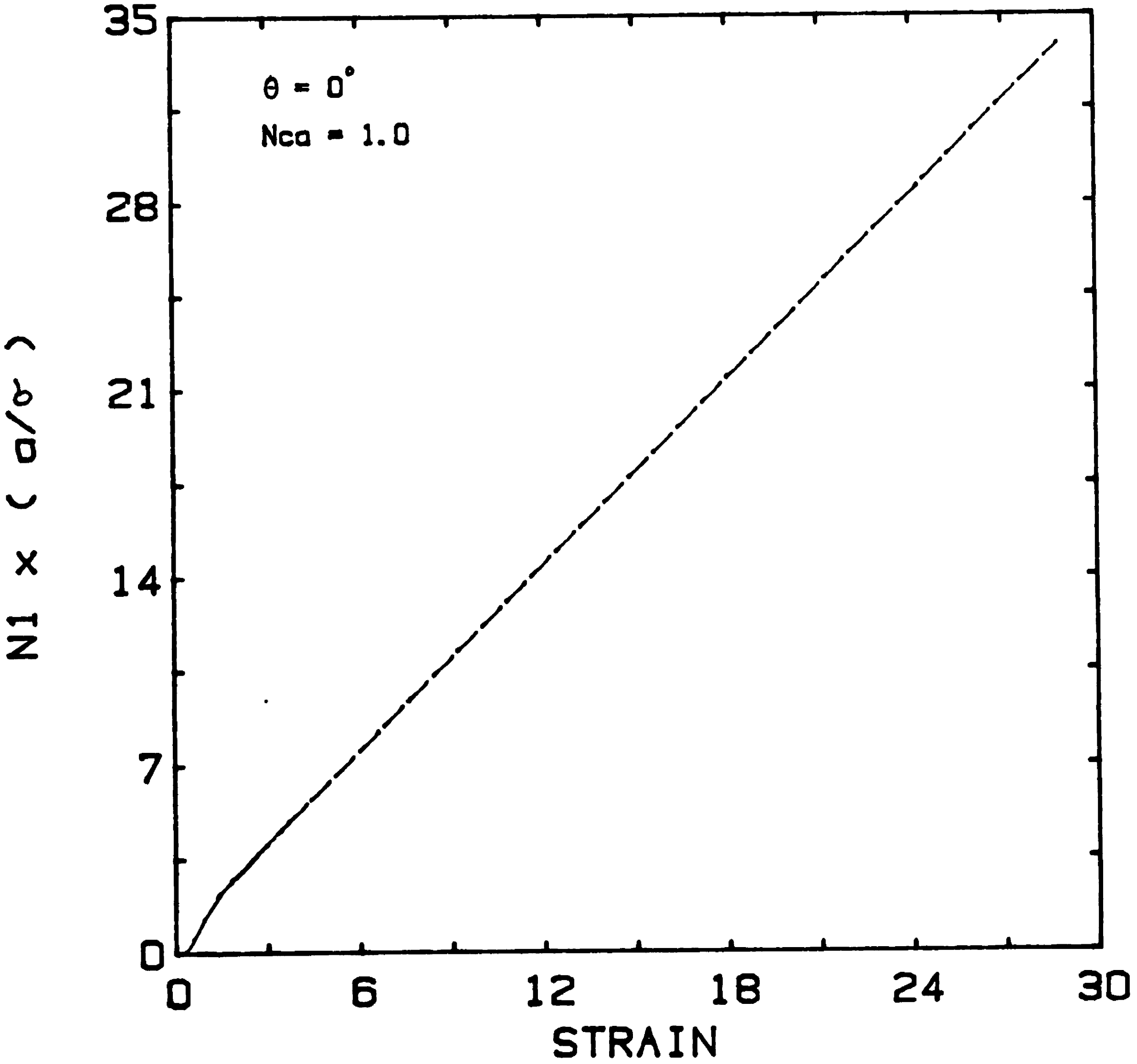

Figure III-27 Normal stress difference for $\theta = 0_0$, Nca=1. Observe kink in curve correponding to the overshoot in Figure III-16.

would be hard to reach without destroying the foam. Even if higher shear rates could be obtained, all practical foam flows are characterized by wall film formation. Most of the shearing would then be concentrated in this liquid film. All these go to show that the equilibrium model, although not as refined as this one, clearly is useful.

C. SUMMARY

Two separate effects, cell size and viscous forces in films, on the rheology of dry foam were studied here. In the former one, two subcases were considered. As an initial case, we derived the stress-strain relation for irregular foam cells i.e. foam cells with three different side lengths (Figure III-1b). Restricting ourselves to one specific initial orientation where one of the sides was vertical, we could draw the following conclusions:

a) The stresses were non zero even at $\gamma=0$ indicating that the initial configuration was not an equilibrium one. Thus one would expect such cells to reform immediately. This instability could also be seen from the fact that the liquid films intersect any shearing plane without any periodicity (Figure III-4) so that the resulting force across the plane is always finite.

b) In the case where only two of the sides were different ($c_3=1$), the system was stable at zero strain. This is apparent from the symmetry of the system with respect to the shearing plane. We also found the yield stress to be constant regardless of the cell side ratio. This suggests that the plug flow region in foam is unaffected by cell irregularities.

c) The critical strain ($c_3=1$ case) decreased with increasing cell side ratios, indicating that the strain required to reach the same stress level is smaller for elongated cells. Calculations however showed the horizontal displacements between cell centers of adjacent rows to be larger for larger c's.

In the second subcase, we considered repeat units of alternate layers of different sized cells, the cells differing only in the length of the vertical sides (Figure III-1a). We found the following in this case.

d) Similarities were observed between this and the irregular cell situation. The yield stress values were invariant with cell size ratio and γ_c showed the same trend as before. Further, the system was stable.

e) The mid points of the films (except the vertical ones) do not move affinely with the bulk. Rather, the points of affine motion divide the respective films in the ratio of the vertical films.

Finally, in this chapter we looked at the effect of viscous forces on cell deformation. In a shearing process, the liquid films undergo an extensional motion which sets up opposing viscous stresses in them (provided the shear rate is finite). The influence of these stresses, which are proportional to $\dot{\gamma}$, were studied in terms of a non dimensional modified capillary number, N_{ca}, defined as the ratio of viscous to surface tension forces. We found that:

f) For N_{ca} around 0.001 which corresponds to a $\dot{\gamma}$ of 10^3, the deformation essentially remained the same as in the equilbrium zero shear rate case. This means that the simple equilibrium model developed earlier is a useful one at these low shear rates.

g) For higher shear rates ($N_{ca} \geq .01$), cells started showing strong deviations from the 120^o film angle criterion. In some cases ($N_{ca} \geq 0.1$,

θ=0 & 50^o), the cells were very stretched out suggesting the possibility of rupture.

h) Further, the side reducing to zero length were affected by the shear rate. Thus for θ=45^o, side OC of the triangular subcell went to zero for N_{ca}=.01 wheras for lower and zero shear rate it is side OB which decreases to zero. This "flip-flopping" of sides was also observed for other initial orientations.

i) The actual magnitude of the viscous term in the stress equation was not large. The primary effect of the viscous stresses was to change the orientation and lengths of the films and thereby change the stress.

IV. EFFECT OF GAS VOLUME FRACTION

In this chapter, stress-strain relations for small shearing deformation up to the yield point are derived for foams having finite liquid content. The earlier dry foam model is generalized here to incorporate all gas volume fractions between the hexagonally close packed system (ϕ=0.9069) and unity (Figure IV-1). All possible initial cell orientation are taken into account. Two cases are studied here. In the first case, the liquid foam films are considered infinitesimally thin. In the second case, the finite thickness of the liquid films are taken into account; the thickness, δ, being determined by the van der Waals forces existing in such films. Details of each of these are discussed in the following sections.

In this chapter, the word "stability" is frequently used. We would like to caution the reader that this term does not refer to stability with respect to time for a given foam configuration. Rather, it refers to the stabilty of different foam cell shapes and structures, i.e certain foam configurations may reform instantaneously.

A. FOAMS WITH NEGLIGIBLE FILM THICKNESS

1. General Background

Several assumptions are made in order to derive the stress-strain relation. These are enumerated below.

1. As before, only two dimensional, monodisperse cells are considered. These cells, as shown in Figure IV-1, are made of straight line segments and rounded corners having same radii of curvature. Three of

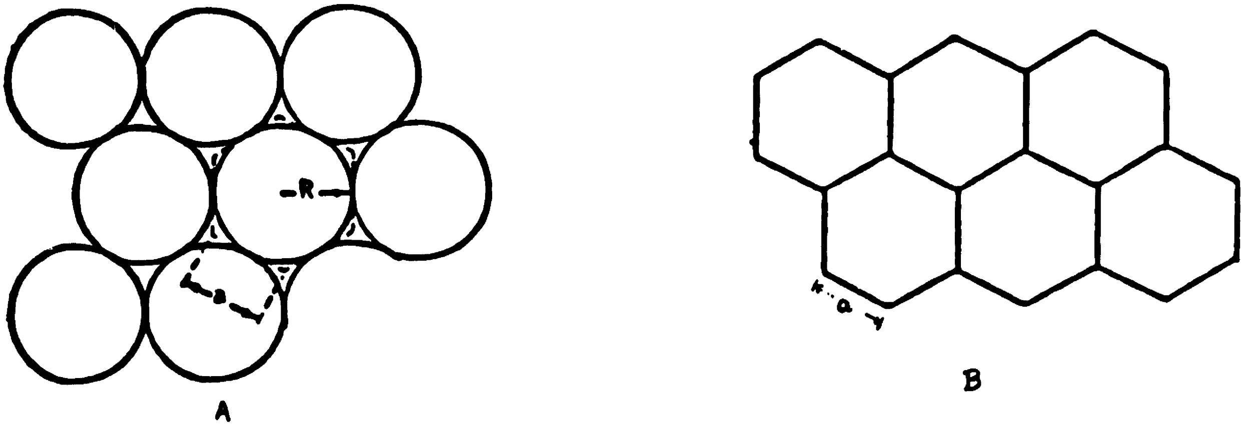

A
CLOSE-PACKED SPHERES

B
HEXAGONAL CELLS

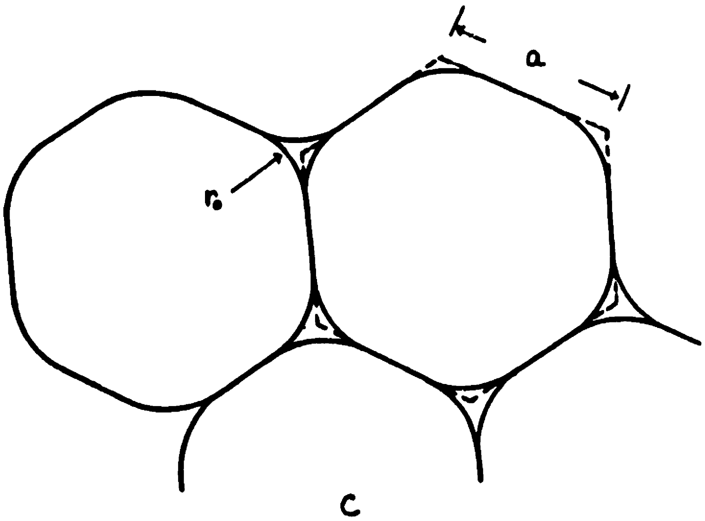

C

Figure IV-1 Two dimensional foam cell models. a) Hexagonally close packed sheres. b) Hexagonal cells for gas fraction approaching unity. c) Typical foam cells with straight line segments and rounded corners.

these curved edges meet to form a triangular cusp, the Plateau border. All the liquid resides in these Plateau borders and the linear films have negligible thickness.

2. In any deformation, the mid points of these cells move affinely with the bulk deformation. Further, total cell volume as well as the gas and liquid volumes are always conserved in any deformation.

3. The deformation is slow enough so that viscous forces in the films are not important and equilibrium interfacial forces determine the cell shape.

4. The only important force is the interfacial tension, σ, acting along the gas-liquid interface. Because of two such interfaces, the force along the linear films is 2σ whereas in the Plateau border region it is only σ acting along each curved surface.

5. In any deformation, the radius of curvature of the Plateau border can change. However, all cells must have the same radius. This follows from the fact that the pressure difference, which is inversely proportional to the radius of curvature, has to be the same across all three gas-liquid interfaces.

The stress-strain analysis is based on the same work-energy concept discussed in Section II-A. In this case, we have:

$$\begin{aligned} \tau_{yx} S &= \underline{F}_\sigma \cdot \frac{d\underline{L}_t}{dY} \\ &= 2\,\sigma \frac{dL}{dY} + \sigma \frac{dR}{dY} \end{aligned} \qquad \text{IV-1}$$

Here, $\underline{F}_\sigma$ denotes surface tension forces and $\underline{L}_t$ the total gas-liquid interface in a unit cell vectorially.

S = area of the unit cell

L = total length of the liquid films (straight line portion) in a unit cell

R = total length of curved interfaces in a unit cell

A very important point is that at the onset of deformation it is only the linear films that get stretched and compressed. The radii of the Plateau borders remain unchanged from the undeformed state up to the point when two Plateau borders meet i.e. one of the straight films shrinks to zero length (Figure IV-2). So for strains up to this point the second term in Equation IV-1 is zero and the rate of change of the liquid films wtih respect to γ is the same as in the dry foam case (Chapter II). This is because all asumptions, such as the 120 degree criterion, are still valid. Results of the dry foam therefore apply here.

However, for strains beyond this point the 120° criterion is no longer valid. The Plateau border radius now changes with γ, and both terms in Equation IV-1 are non-zero. The problem, therefore, reduces to finding the lengths of the two remaining liquid films and the radius of curvature as functions of strain. All equations derived in the next section pertain to this strain regime where the cusps have already met.

2. Governing Equations

Figure IV-3 shows a collection of deformed cells along with the unit cell DEF formed by joining the mid points of three adjacent cells. The area of this unit cell, which remains constant throughout the deformation process, is given by $3\sqrt{3}\ a^2/4$. "a" is the length of the side of the circumscribed hexagon to the undeformed foam cell (Figure IV-1). Also

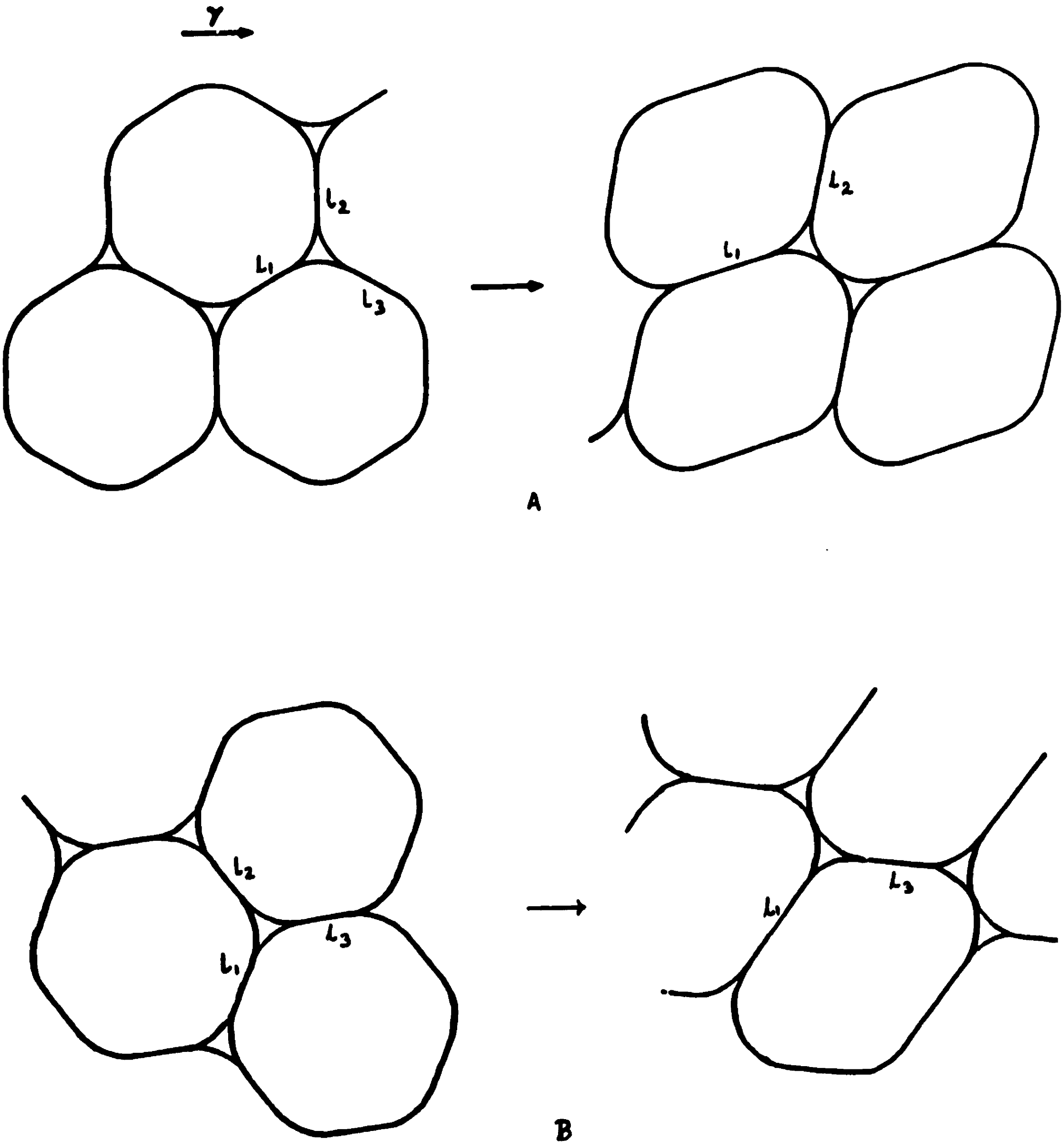

Figure IV-2 Cell deformation up to the point the Plateau borders meet. Gas fraction, $\phi=0.97$. a) Initial orientation, $\theta=0^{\circ}$. b) $\theta=40^{\circ}$. Note that two different sides go to zero for the two orientations.

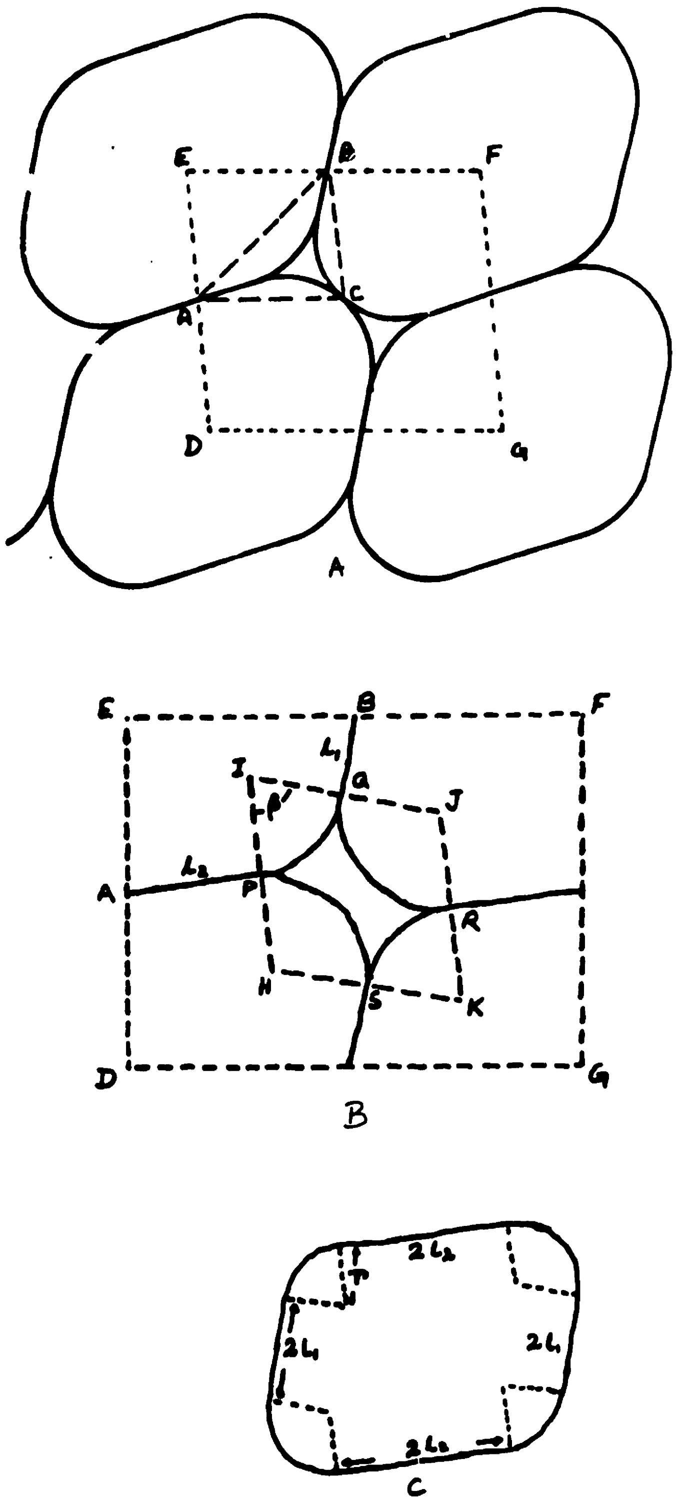

Figure IV-3 Foam cells with zero film thickness. a) Unit cell DEF along with subcell ABC. b) Two adjacent unit cells DEFG showing all microstructure. c) Isolated foam cell used to calculate gas volume fraction.

shown within the unit cell is the triangular sub-cell ABC, the vertices of which move affinely with the bulk deformation. Using the same approach as in Section II-A, the lengths of sides AB, AC and BC, denoted by b_1, b_2 and b_3 respectively, can be derived for any arbitrary orientation, θ. Thus,

$$b_1^2 = 3\, a^2 \,[1 + \gamma^2 \sin^2(\theta+60) + \gamma \sin (2\theta+120)\,] / 4$$

$$b_2^2 = 3\, a^2 \,[1 + \gamma^2 \sin^2 (\theta) + \gamma \sin (2\theta)\,] / 4 \qquad \text{IV-2}$$

$$b_3^2 = 3\, a^2 \,[1 + \gamma^2 \cos^2 (\theta+30) - \gamma \sin (2\theta+60)\,] / 4$$

In order to solve completely the problem, one still needs to know the film lengths l_1, l_2 and the radius of curvature r of the Plateau border. At this point, it is much easier to visualize the deformation process if one focuses on two adjacent unit cells instead of one. The parallelogram DEFG (Figures IV-3a, b) shows such a figure. Here all the liquid is confined in the cuspoid region PQRS. To find the amount of this liquid, let us construct a rhombus HIJK by drawing lines perpendicular to the radius of curvature at points P, Q, R and S respectively. The length of the sides of this rhombus is therefore 2r. If we denote the angle PIQ by β, then the area of this rhombus is $4\, r^2 \sin\beta$ and the total length of the curved interface in the two unit cells is $2\pi r$. Therefore, for a unit cell, R in Equation IV-1 is given by:

$$R = \pi r \qquad \text{IV-3}$$

Equations for the four unknowns, l_1, l_2, r and β are derived based on geometric and volume (area for 2-D) conservation constraints.

Geometric Constraints: Two relations are derived here using the cosine law for triangles. In triangle APC,

$$AP^2 + PC^2 - 2\,AP.PC \cos(90+\beta) = AC^2$$

Since AP = l_2, BQ = l_1, PC = r, AC = b_2 and BC = b_3, we get the following after rearrangement,

$$l_2 = -r \sin\beta + [\, b_2{}^2 - r^2 \cos^2\beta \,]^{1/2} \qquad \text{IV-4}$$

Similarly, from triangle QBC, we get

$$l_1 = -r \sin\beta + [\, b_3{}^2 - r^2 \cos^2\beta \,]^{1/2} \qquad \text{IV-5}$$

Volume Constraints: The area of the liquid contained in two adjacent cells is given by $4\, r^2 \sin\beta - \pi\, r^2$. Therefore, in a unit cell the liquid area A_L is given by:

$$A_L = 2\, r^2 \sin\beta - \pi\, r^2 / 2$$

If ϕ is the gas volume fraction in a unit cell, then by conservation of liquid volume we get

$$(1 - \phi)\, 3\sqrt{3}\, a^2 / 4 = 2\, r^2 \sin\beta - \pi\, r^2 / 2 \qquad \text{IV-6a}$$

This can be rewritten as

$$\sin \beta = \pi/4 + (1-\phi)\, 3\sqrt{3}\, a^2 / (8\, r^2) \qquad \text{IV-6b}$$

or, $$r^2 = (1-\phi)\, 3\sqrt{3}\, a^2 / (8 \sin \beta - 2\pi) \qquad \text{IV-6c}$$

Similarly, the gas volume (area) is also conserved in any deformation. From Figure IV-3c, the gas filled area is given by:

$$4\, l_1\, l_2 \sin \beta + 4\, l_2\, r + 4\, l_1\, r + \pi r^2$$

Now, this equals the area of the gas in the undeformed state i.e. $3\sqrt{3}\, a^2\phi/2$. Therefore, we have:

$$4\, l_1\, l_2 \sin \beta + 4\, r\, (l_1 + l_2) + \pi r^2 = 3\sqrt{3}\, \phi\, a^2/2 \qquad \text{IV-7}$$

Thus, solving the last four coupled equations one can get l_1, l_2, β and r as functions of γ. However, to calculate the stress one needs the derivatives of these terms with respect to γ, because

$$\tau_{yx} = 8\, \sigma\, [\, l_1' + l_2' + \pi/2\, r'] / [3\sqrt{3}\, a^2] \qquad \text{IV-8}$$

where the ' denote derivatives with respect to γ.

By using the above equations, one gets these derivatives in the forms:

$l_1' = f_1\, (r, \beta, b, r')$, $l_2' = f_2\, (r, \beta, b, r')$ and,

$r' = f_3\ (r,\beta,b)$

The explicit forms of the three functions along with all details are given in Appendix B. The stress can therfore be easily calculated from Equation IV-8 once γ, r and β are known.

There are two ways one can approach the numerical problem. The four coupled equations can be reduced to one by substituting Equations IV-4, 5, 6b into Equation IV-7. This gives r as a function of strain; and by choosing a range of strains, the corresponding r (and hence the stress) can be evaluated. In another method, which was the one we used, Equations IV-4, 5 are substituted into Equation IV-7. One then substitutes r here from Equation IV-6c to get a relation between β and γ. Although γ is the independent variable, this equation is solved for strain using a range of β values. From Figure IV-3 it is clear that when the Plateau borders meet, $\beta = 60^o$. Further, it cannot exceed 120^o. Thus, the non-linear equation was solved for different gas fractions using a bisector method for β values ranging from 60 to 120 degrees. The use of β as an input instead of γ makes it easier to observe multiplicity of solutions.

It should be pointed out that depending on the initial orientation, sometimes the liquid film l_1 may reduce to zero length instead of l_3 on applying a shear deformation (cf. Chapter II, Figure IV-2). In such cases, $L = l_2 + l_3$, where the respective l's are given by:

$$l_2 = -r \sin\beta + \surd\,[b_1^2 - r^2 \cos^2 \beta] \qquad \text{IV-9}$$

$$l_3 = -r \sin\beta + \surd\,[b_3^2 - r^2 \cos^2 \beta] \qquad \text{IV-10}$$

One can then obtain the stress-strain relation in this case by replacing

l_1, l_2 in Equations IV-7, 8 by l_2, and l_3.

3. Results and Discussion

The equations derived in the last section were solved for different gas volume fractions (ϕ) and initial orientations (θ). Figure IV-4 shows the effect of gas fraction on the stress strain behavior for cells having $\theta = 0^o$. Initially, the curves follow the stress-strain response of the dry foam case. This overlapping region represents the initial shrinking of one of the linear films. The point of deviation reflects the meeting of two Plateau borders. Thus, in the hexagonally close packed case, no overlap is observed as the cusps already touch one another at zero strain. One can also see from the plot that the maximum stress, which corresponds to the yield stress, decreases with decreasing gas fraction. The corresponding strains show similar trends. This observation can be explained from the fact that with decreasing ϕ the cells are less polyhedral and more rounded. Thus, a smaller force is required for the cells to go past one another.

Figure IV-4, which was obtained by solving the relevant equations as functions of increasing strain, contains only half the stress-strain response. A symmetric set of curves exists in the negative stress region with the center of symmetry at the point the stresses go back to zero again. Figure IV-5 shows the complete stress-strain plots of the hexagonal close packed system for the θ^o initial orientation while Figure IV-7 depicts the actual cell deformation. As the cells deform the stress increases until it reaches a maximum. This corresponds to the structure in Figure IV-7b. With further increase of strain, the stress gradually

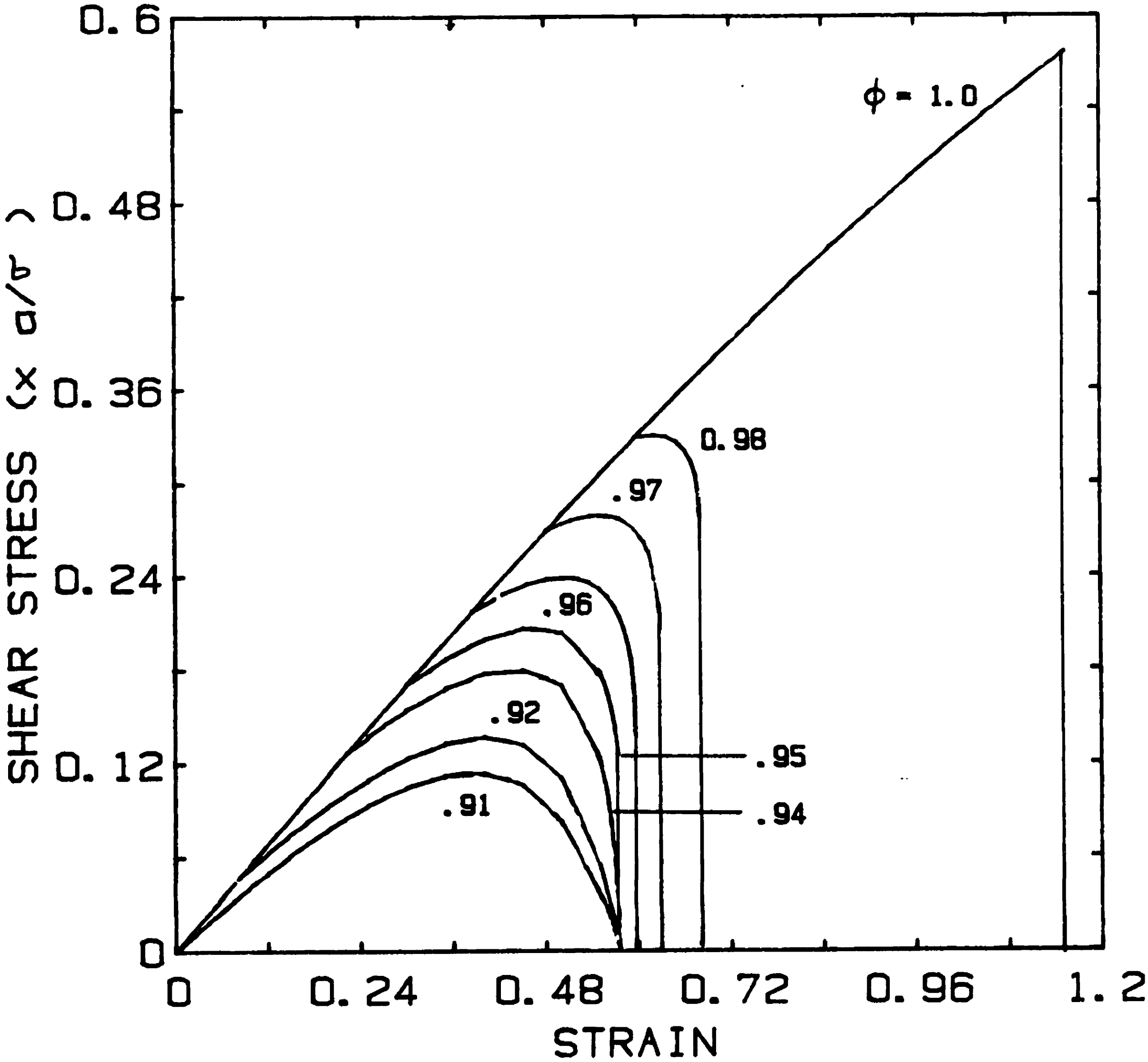

Figure IV-4 Shear stress as a function of strain for different gas fraction foams. Initial orientation $\theta = 0^{\circ}$.

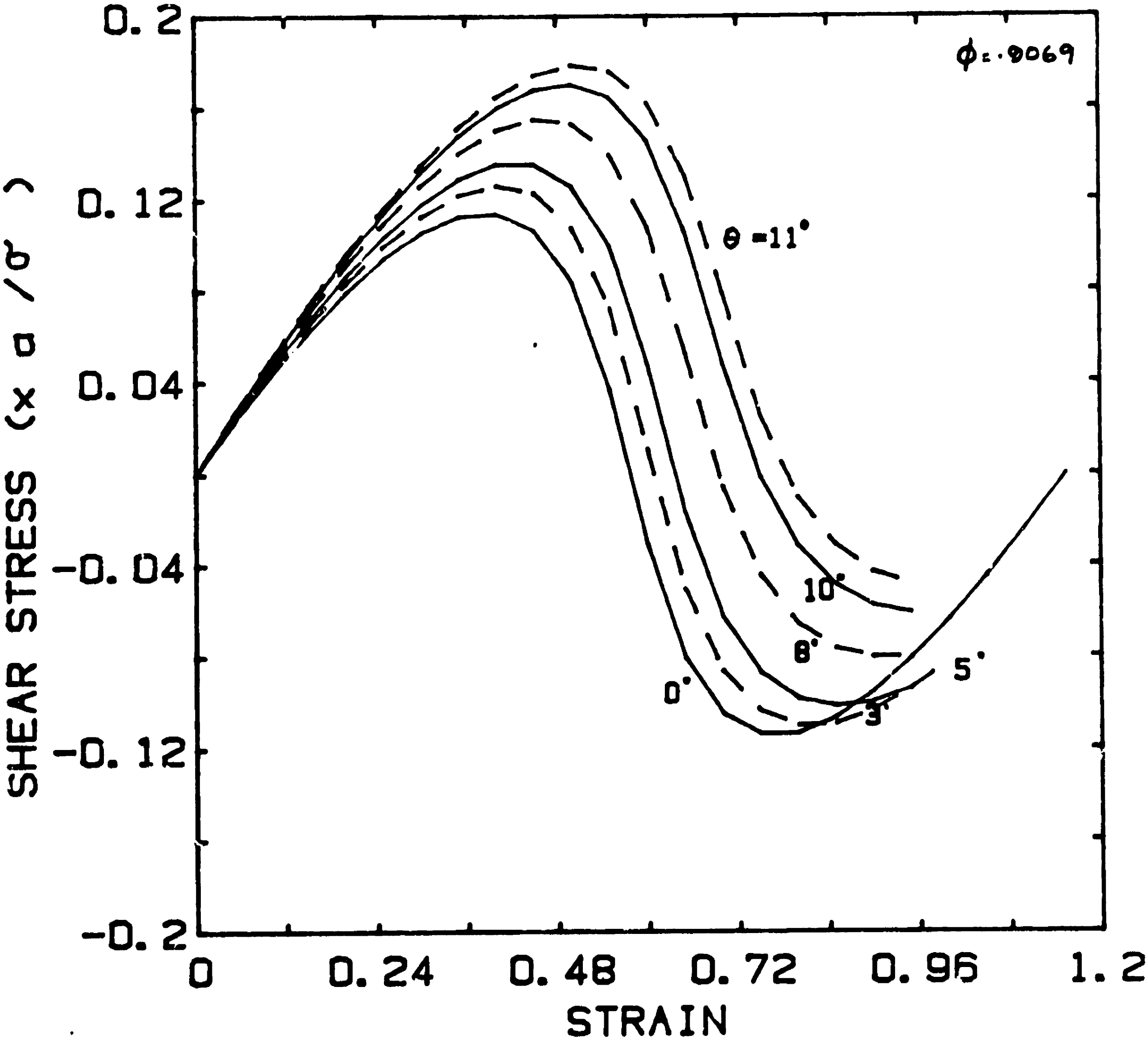

Figure IV-5 Shear stress versus strain for the hexagonally close packed system (φ=.9069). Initial orientation, θ, ranges from 0 to 11°.

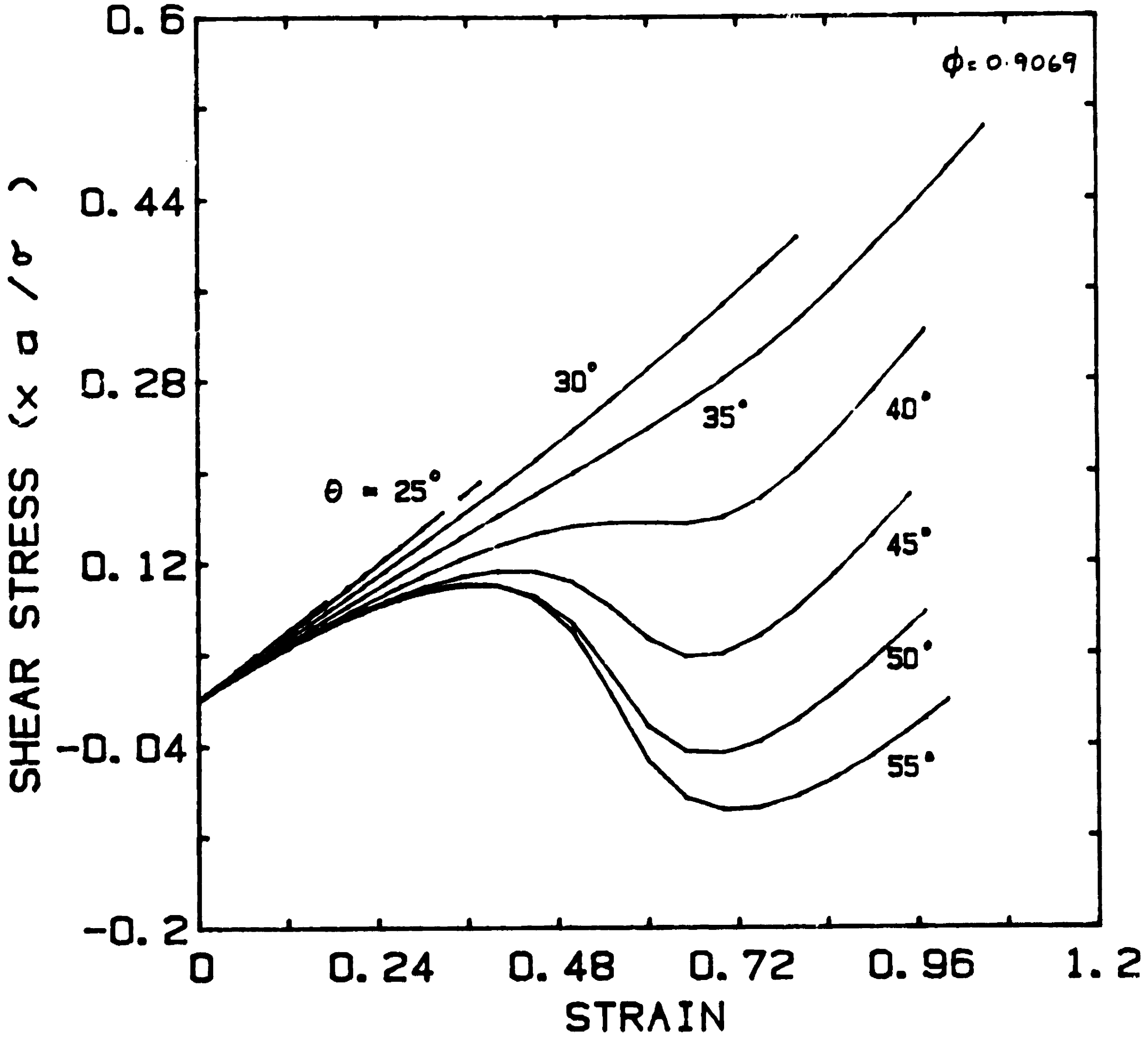

Figure IV-6 Effect of initial orientation on stress for a shearing displacement. ϕ corresponds to that of the hexagonally close packed system.

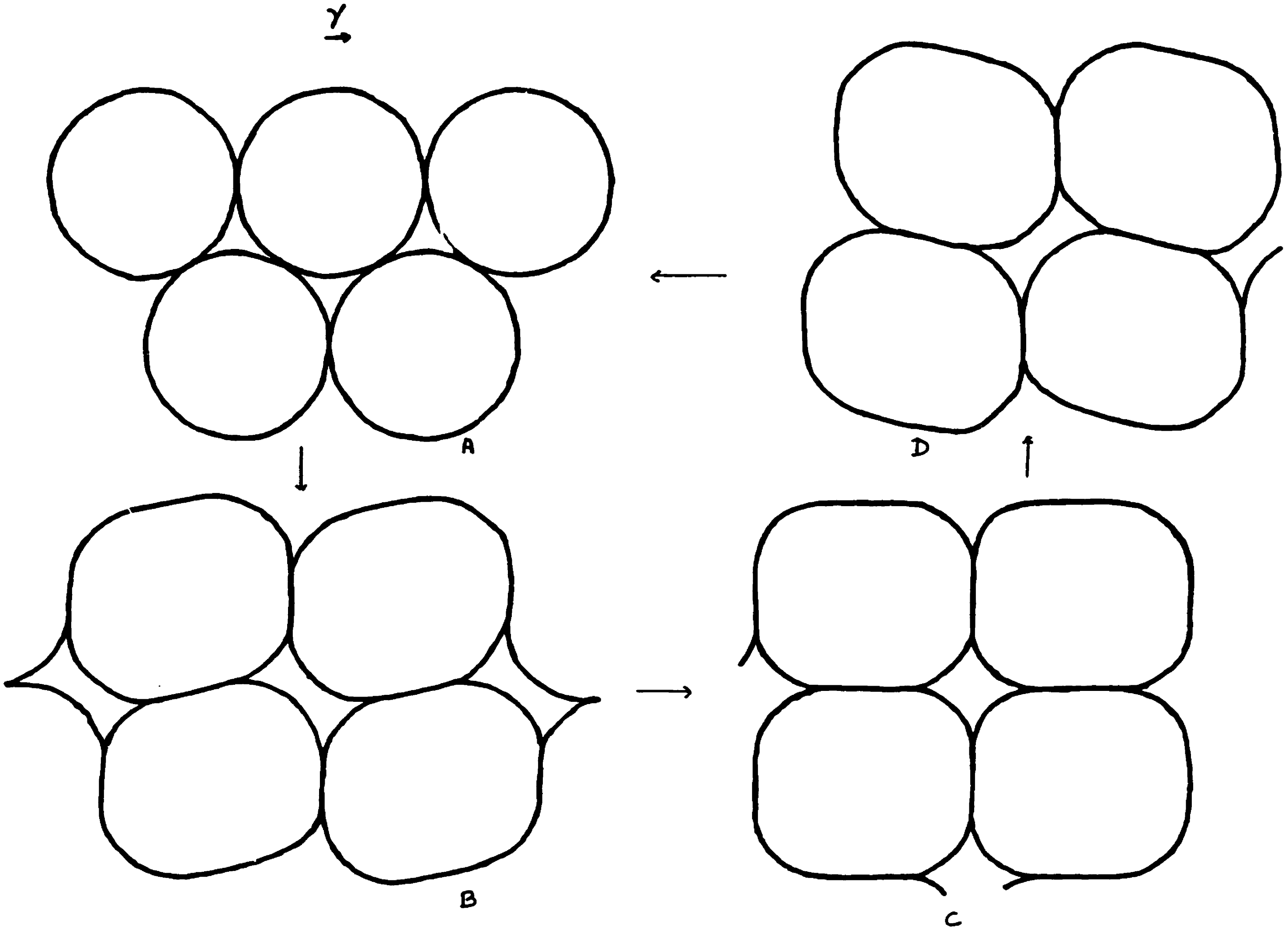

Figure IV-7 Cell deformation for the hexagonally close packed system. Increasing strain in counter clockwise direction. Initial orientation $\theta=0^{o}$.

decreases to zero. This is represented by Figure IV-7c. Beyond this strain, the stress switches sign reaching a minimum at D (Figure IV-7d). Finally at $\gamma=2/\sqrt{3}$ the cells return back to the original configuration and the stress to the starting value of zero. It should be clear from Figure IV-7 that at the strain the Plateau borders touch, $\beta=60^{\circ}$. With increasing strain, β increases and equals 90° at the point of symmetry of the stress strain curve (Figure IV-7c). Finally, when the cells reform back to the original state, β reaches a value of 120°.

The reason for the negative stress becomes quite apparent when one looks at the energy versus strain plot for $\phi=0.9069$ (Figure IV-8). Cell structures A, B, C, D of Figure IV-7 are marked correspondingly in Figure IV-8. The slope of this energy curve is directly proportional to the stress. Therefore at B, where the slope is maximum, the stress is maximum. C, the highest energy point on the other hand corresponds to zero stress. For strains above C the energy starts to go down and the corresponding stress becomes negative. One can also observe the existence of such negative stresses by merely looking at the cell deformation pictures. Let us focus on a shearing plane passing through the mid points of the cells in Figure IV-14. The shear stress in this case would be proportional to the x component of the intersecting films with this plane. Structures B and D clearly give positive and negative x components respectively for the intersecting liquid films.

Figure IV-5 along with Figure IV-6 also contain plots of the hexagonally close packed system for other initial orientations. As one can see, the stress-strain relation is strongly influenced by θ and the only symmetric curve is that for $\theta=0^{\circ}$. Undeformed cells for all initial orientations

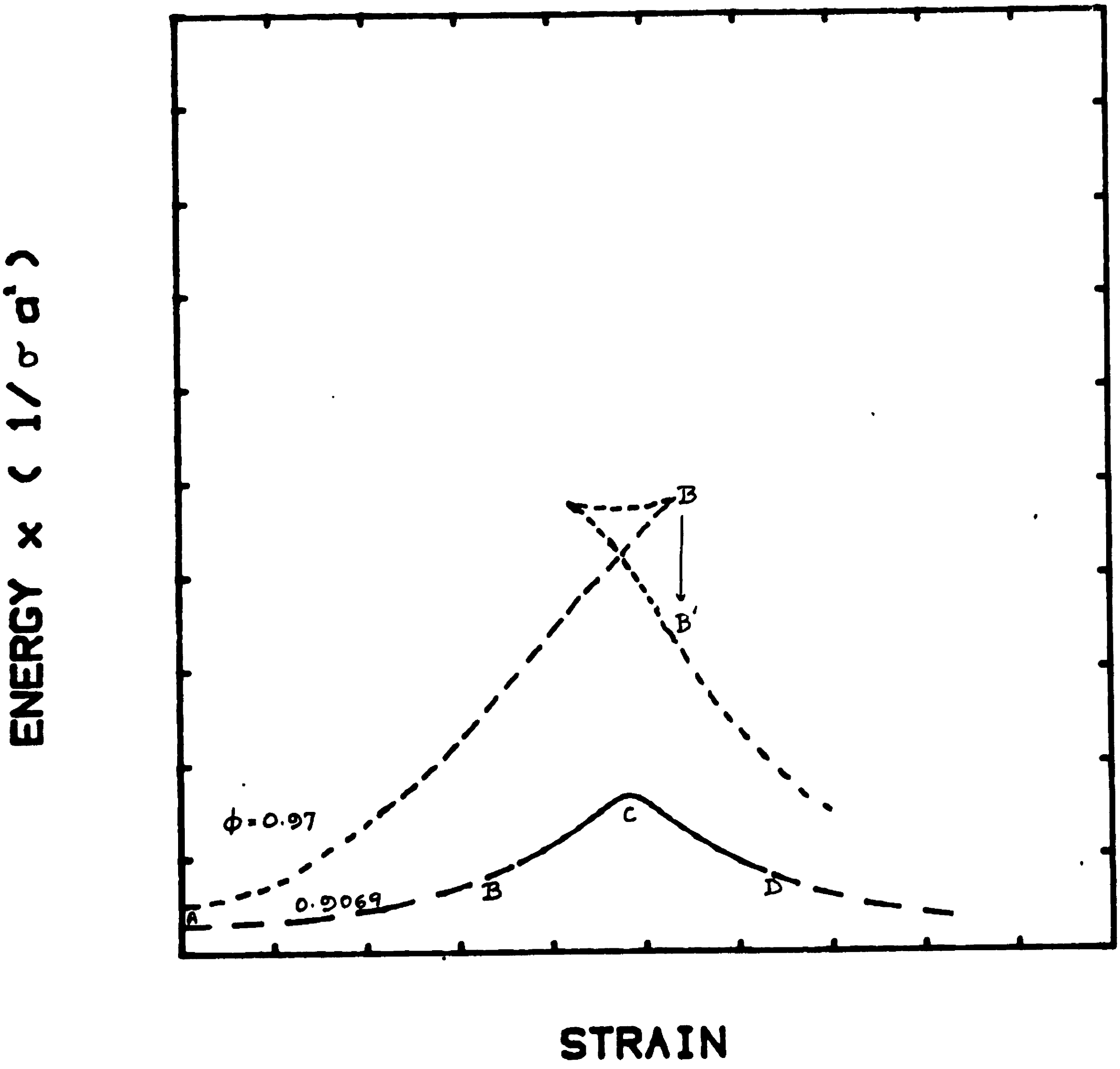

Figure IV-8 Qualitative behavior of energy vs. strain observed for different gas fraction foams. Initial orientation $\theta = 0^{\circ}$.

correspond to the stress free or "equilibrium" state. However, for initial orientations between 11 and 20 degrees, the cells become unstable for any applied strain. This is because the equations of the previous section have no solution for this regime, i.e. one cannot satisfy the affine deformation and volume conservation constraint simultaneously. Thus these orientations can be termed "inherently unstable", and the cells reform back to some stable state for any infinitesimal strain. We also find that $\theta=0^{\circ}$ is the only orientation where the cells reform back to the original configuration without passing through any unstable state. For any other orientations studied, the cells become unstable at a certain strain i.e. the equations no longer have solutions. There is no stress-strain relation beyond this and the cells reform back to some other state. In some cases this point is reached while the stress is positive ($\theta=21-45^{\circ}$). In other cases ($\theta=3-11,50-60^{\circ}$), the stability limit is reached after the stress has become negative. Figure IV-9 shows the actual cell deformation for one of the former case ($\theta=30^{\circ}$). Here, with increasing strain the two Plateau borders join to form a channel or cuspoid while two linear films are generated. At some strain, however, one of the films starts to shrink instead of elongating. The stability limit is reached when this reduces to zero length (Figure IV-9b) and the cells are made of two straight line portions connecting two circular sections. One other feature to note is that for θ greater than 20° the two Plateau borders which form channels are different than that for θ less than 11°. This phenomenon, which can be clearly observed from the cell deformation pictures (Figures IV-7, 9), is analogous to the change observed in the dry foam case for the side going to zero length at $\theta=45$ degrees.

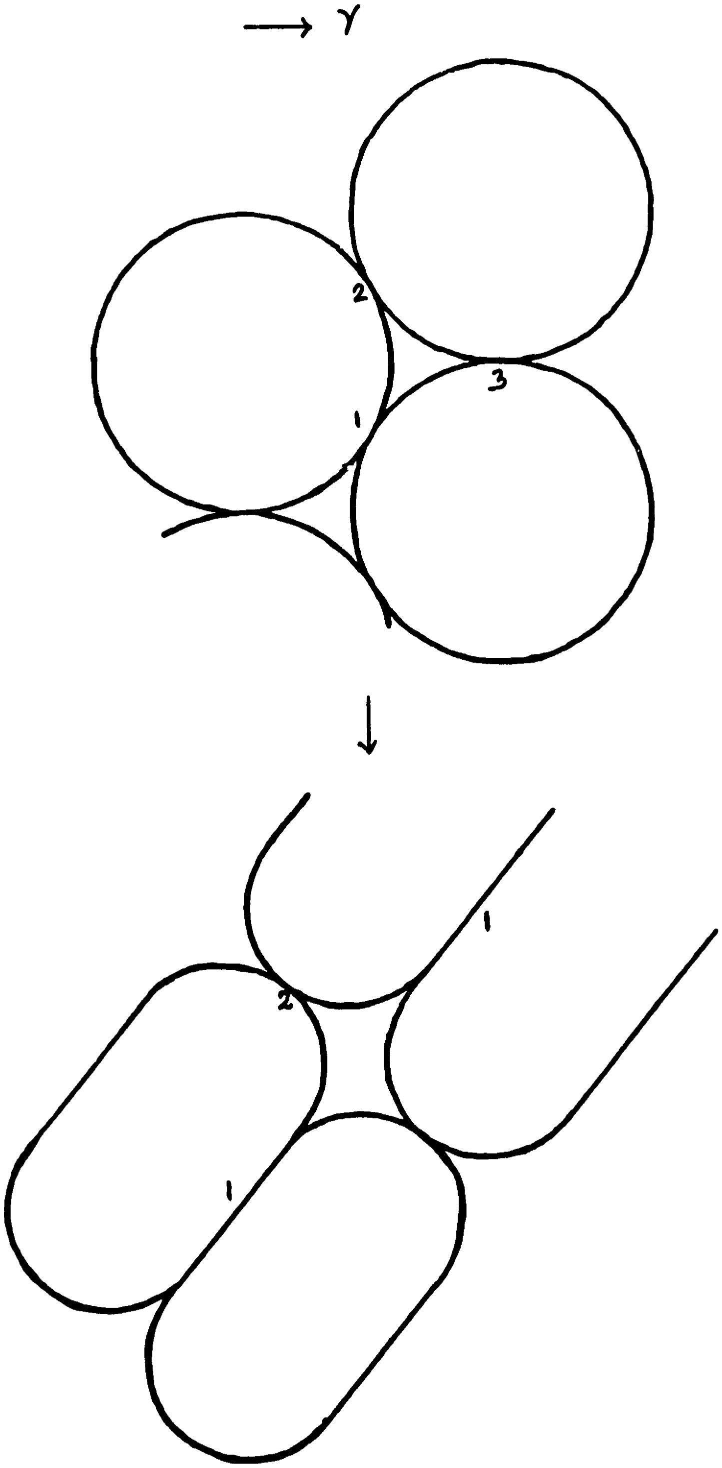

Figure IV-9 Cell deformation for the hexagonally close packed system. Initial orientation θ=30°.

In Figures IV-10 and 11 are stress-strain plots of different initial orientations for ϕ=0.92. Here, unlike the hexagonal packed system, there are no "inherent instabilities". This is because the cells here have a finite film length to begin with. Unless this becomes zero, no instabilities can occur. In this case θ=0°, 5°, and 55° are the only stable initial orientations in this figure. By stable initial orientation we mean that β=120° is reached without passing through any unstable state. At β=120°, the two Plateau borders which formed a channel are just touching again. For strains beyond this, a liquid film will be formed between them and the whole stress-strain mechanism will be similar to the dry foam case. For all other orientations we observe a loss of solution after a finite strain indicating reformation taking place at that strain. For initial orientations of 40° and 45° (Figure IV-11), the shear stress remain positive throughout but goes through a hump. This is observed for ϕ=.9069 also. All curves, such as these, which show a local minimum resemble a rotated and skewed 0° curve. The rotation probably adds to the distortion. The θ=50° curve represents a unique case as it becomes unstable at a positive stress after passing through a whole cycle of positive and negative stresses.

Plots for ϕ=0.97 are given in Figures IV-12 and 13. In this case, as the equations were solved as increasing functions of β, we observed multiple solutions and limit points i.e. the stress strain curve went back in strain after reaching a certain maximum value. Figure IV-14 shows the actual cell deformation for θ=0°. Focussing on this case, as one increases stress the strain increases until the maximum stress is reached. For any further increases in stress, the foam cells will

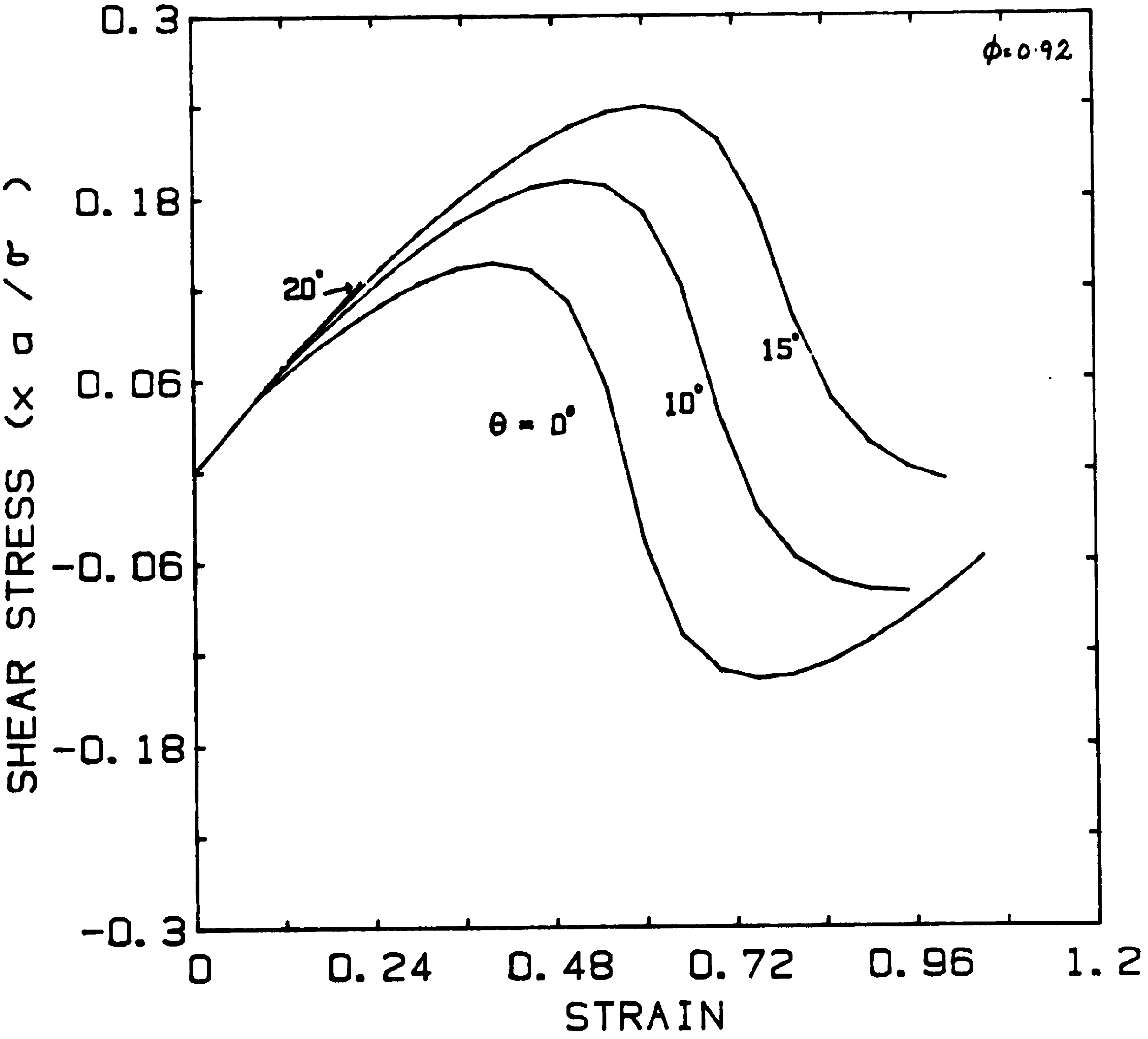

Figure IV-10 Stress versus strain in a shearing displacement. Initial orientation, θ, ranges from 0 to 15°. Gas fraction φ=0.92.

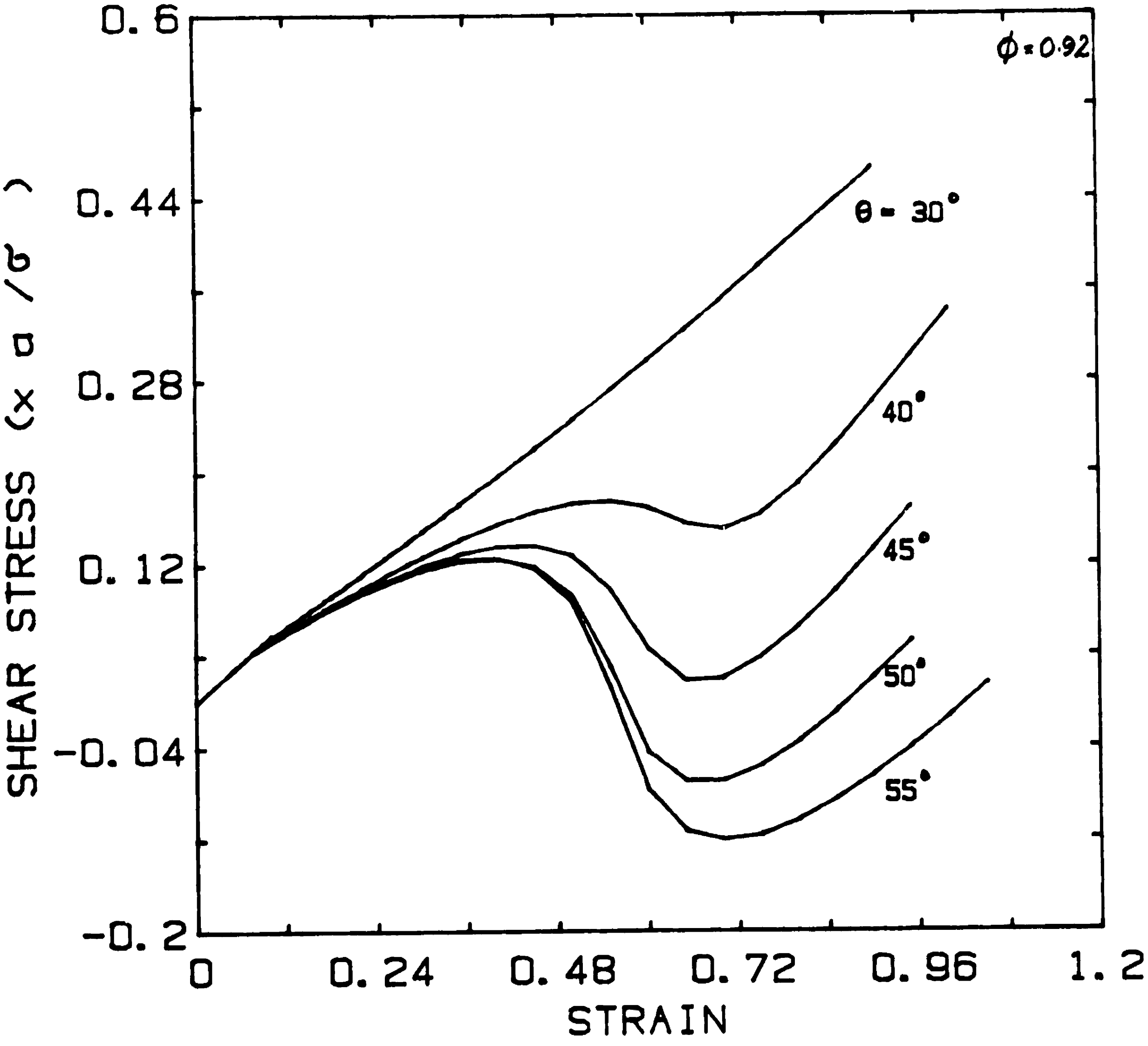

Figure IV-11 Shear stress as a function of strain for different initial orientations. ϕ=0.92.

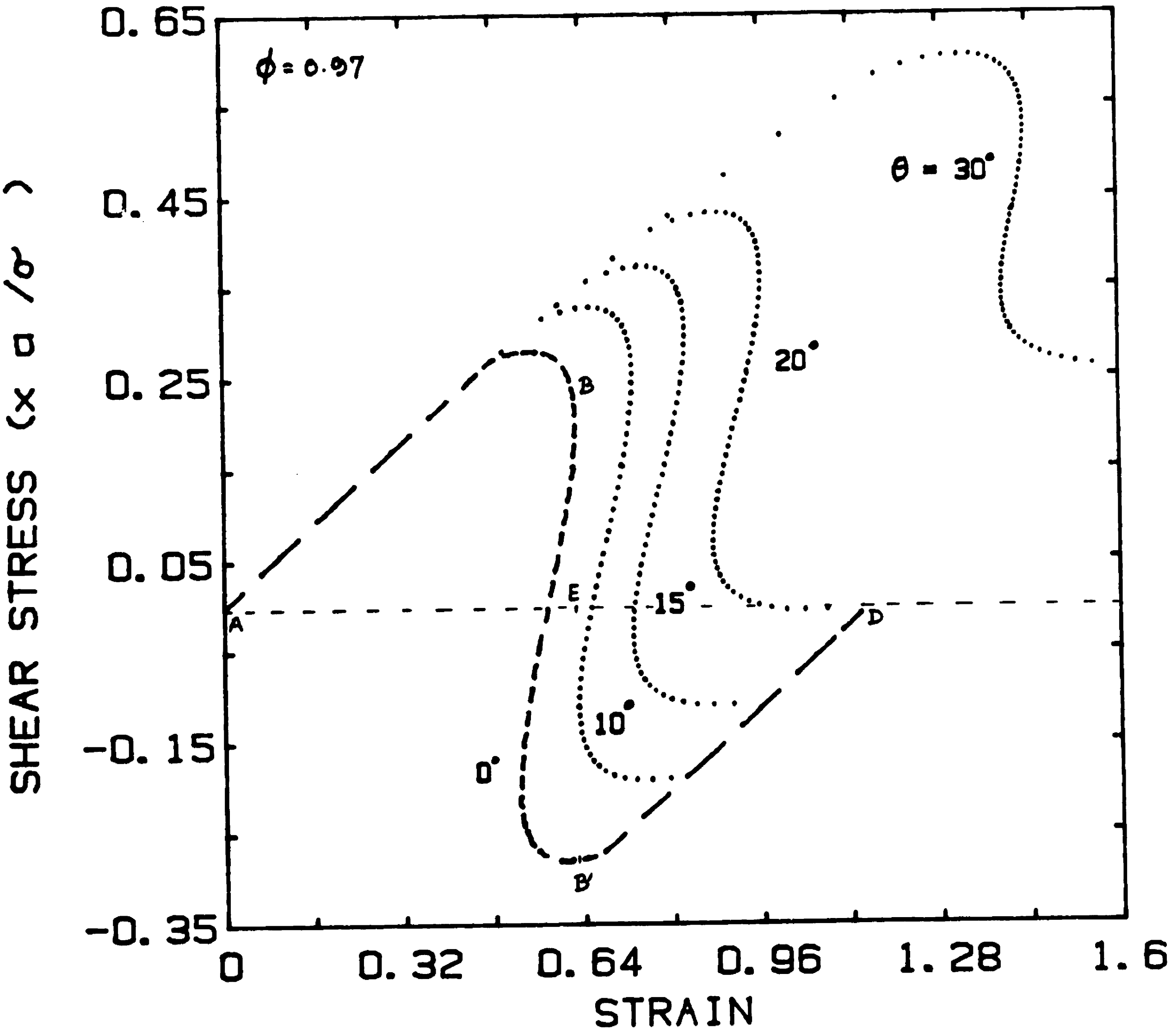

Figure IV-12 Stress versus strain in a shearing displacement. Gas fraction, φ, equals 0.97.

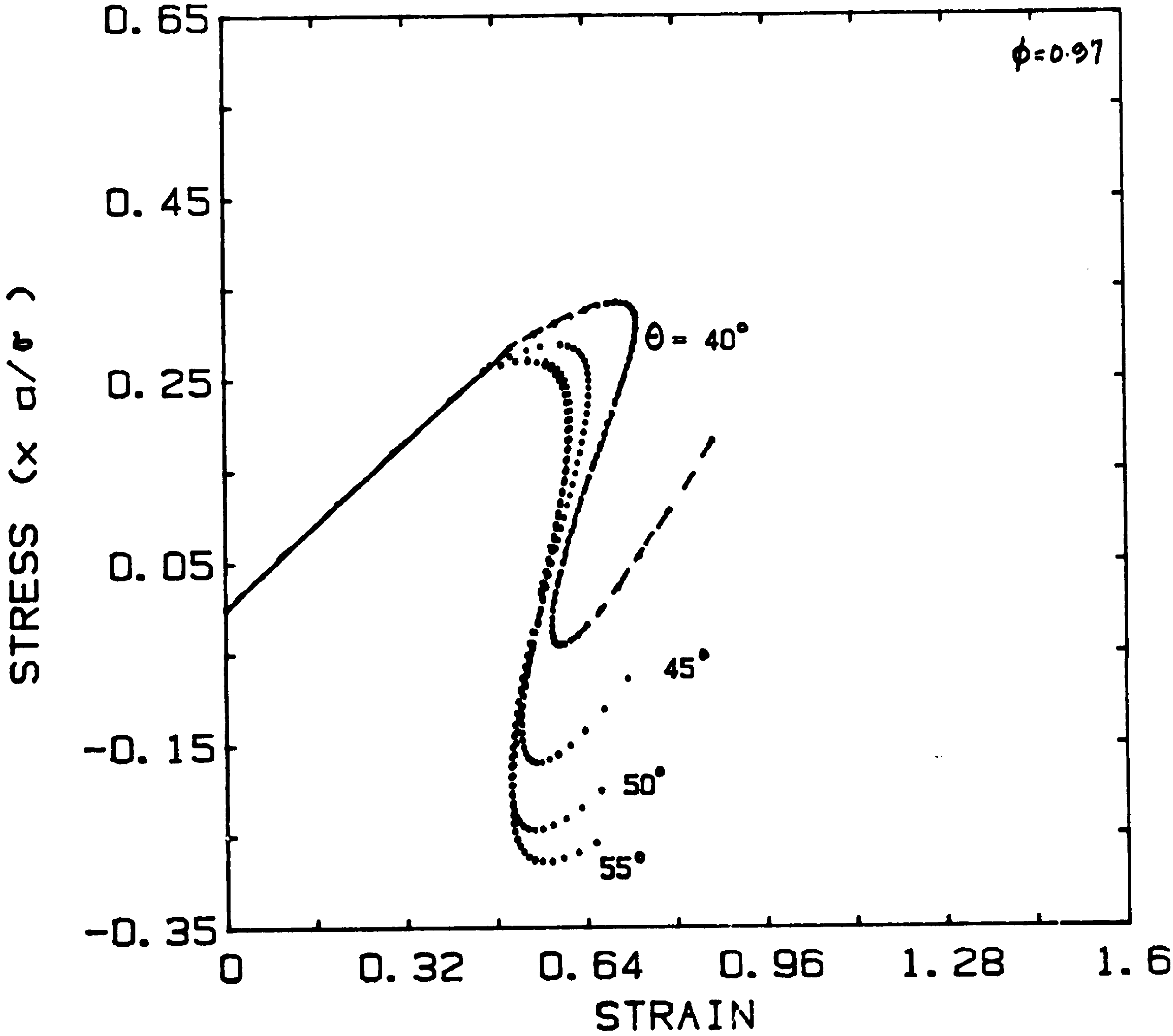

Figure IV-13 Shear stress vs. strain for initial orientations ranging from 40 to 50°. Gas fraction, φ, equals 0.97.

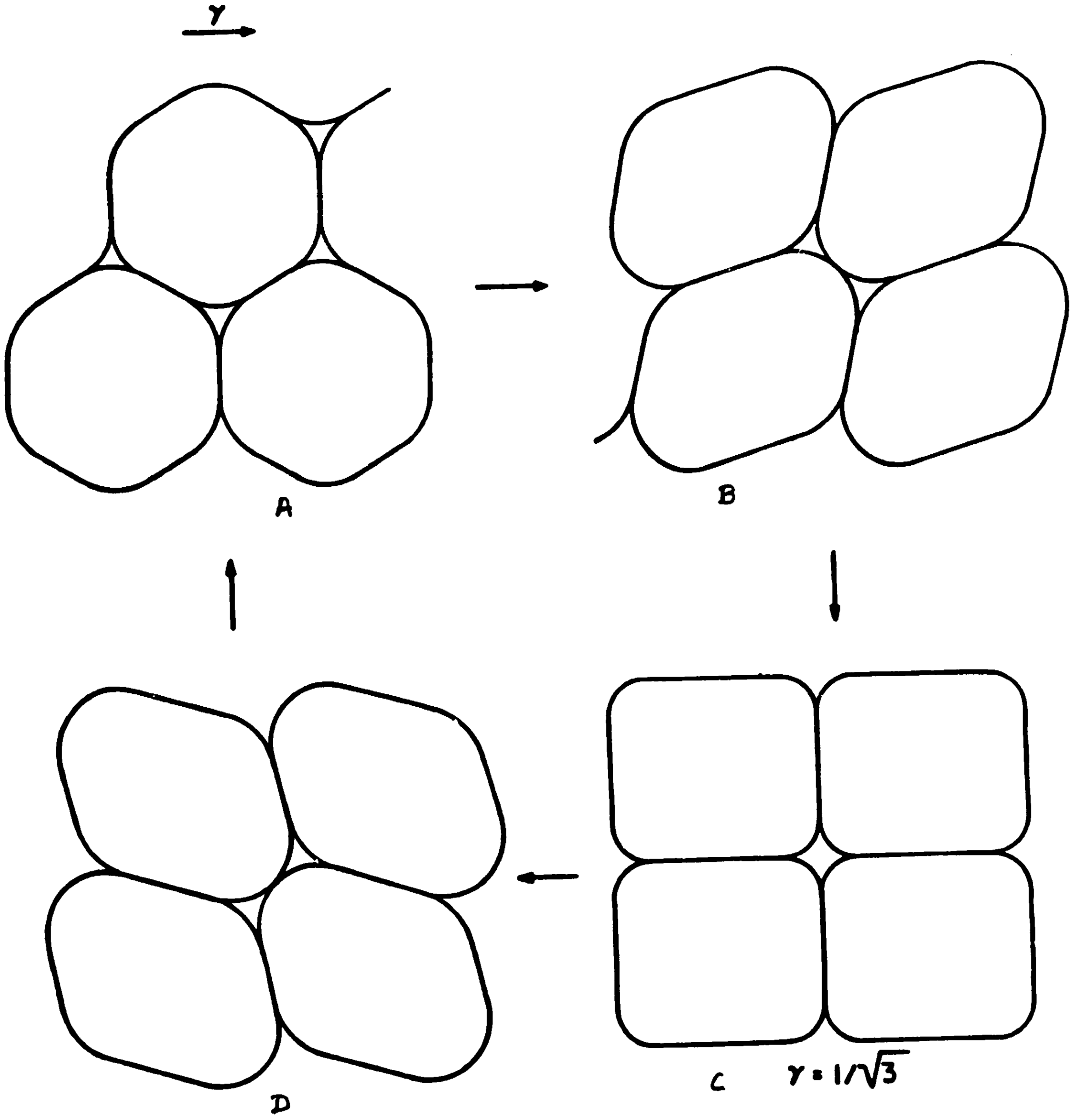

Figure IV-14 Cell structures in a shearing deformation. Increasing strain in clockwise direction. Initial orientation θ=0°. ϕ=0.97.

keep on repeating the reformation cycle. In other words, if one increases strain, point B corresponds to the strain at which the Plateau borders just meet (Figure IV-14b). With increasing strain, point B' is reached. For any strain above this, the shear stress becomes negative and the curve drops vertically down to point B''. So, the portion of the stress-strain curve to the left of this vertical line represents an aphysical region. In Figure IV-14c, the $\gamma=1/\sqrt{3}$ case corresponds to zero stress and is therefore an aphysical state. It is clear from the energy versus strain plot (Figure IV-8) that this zero stress, represented by C, cannot be an equilibrium state since it has a much higher energy. From the figure, we find this to be true for other gas fractions ($\phi=.9069$) too.

In Figure IV-15, which shows the cell structures for $\theta=30^{\circ}$, we find that the deformation looks very different from the 0° case. Here, the cell B corresponds to the maximum stress configuration. For any stress above this the cells reach the stability limit D (Figure IV-15) and reform. In the stress-strain plot of Figure IV-13, B' corresponds to the maximum strain beyond which stress discontinuity to B'' is observed. So C in both Figures IV-14 and IV-15 represent an aphysical configuration. It should be noted that β equals 90° for both these cases of C. Further, C represents the inflection point in the aphysical branch of the solution.

The reason for the stress discontinuity is apparent from the energy-strain plot for $\theta=0^{\circ}$ (Figure IV-8). Here, with increasing strain, region B, the maximum energy configuration is reached. Any infinitesimal increase in strain results in an energy drop to B'. This jump is reflected in the stress-strain plot. Further, the point B' lies on the descending slope of the energy curve. Hence, the stress at this point is negative.

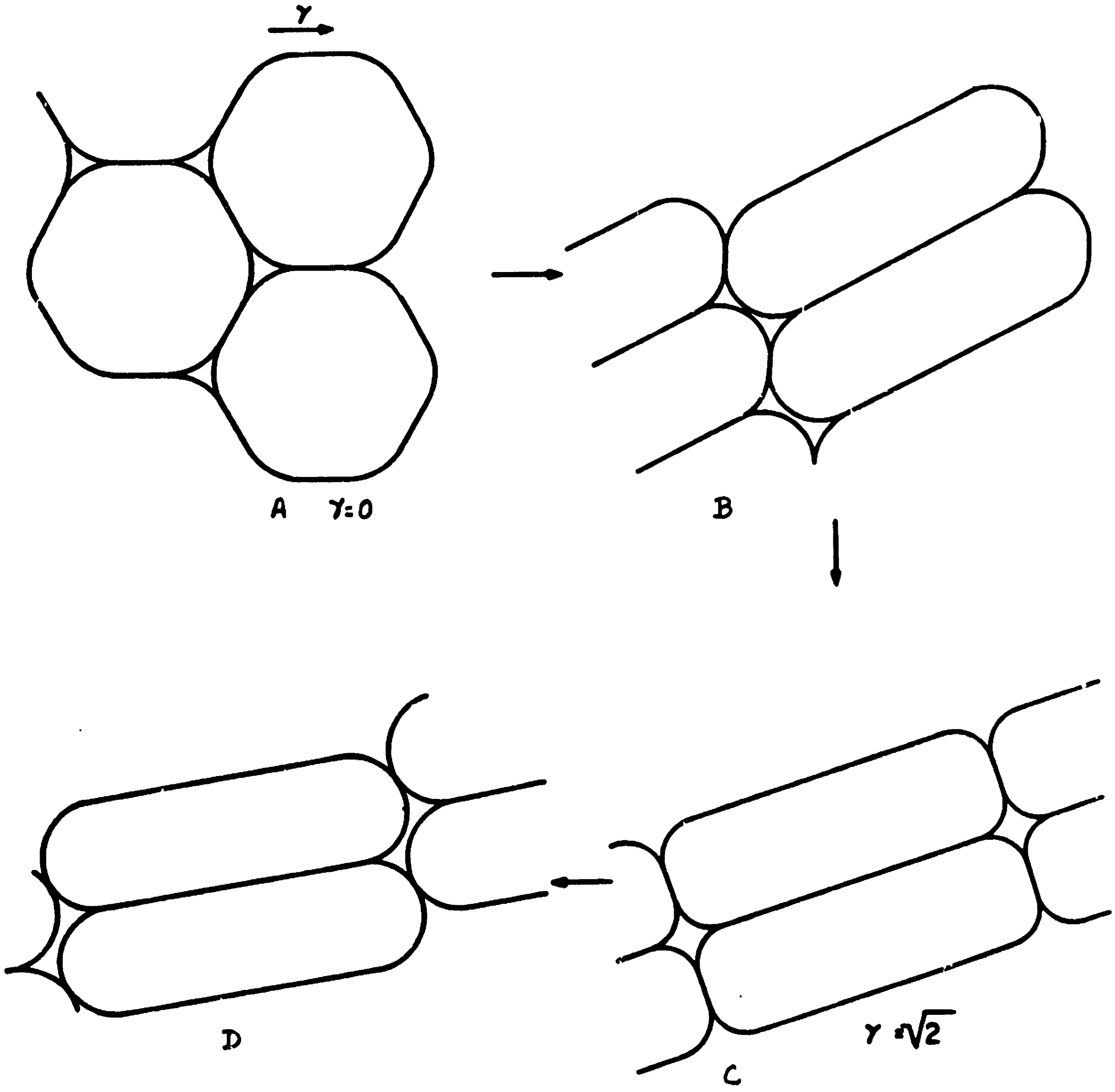

Figure IV-15 Effect of initial orientation on cell deformation. System reforms beyond structure D. ϕ=0.97; θ=30°.

In this process, an energy equivalent to the jump from B to B' is lost. One can see this energy loss from the stress plot (Figure IV-12) also. The energy input corresponds to the area of the envelope ABE whereas that recovered corresponds to the area of EB'D. Clearly these two areas are not equal and some energy is lost in the reformation cycle. However, in the hexagonal close packed case for $\theta=0^{\circ}$, there is no energy loss. This is evident from the equal areas in the positive and negative y-axis of the stress-strain curves and from the smoothness and symmetry of the energy curve. For other orientations, the stress curves show no symmetry and energy is lost in the cyclic deformation process.

For $\phi=0.97$, the 20° orientation is the only unstable orientation shown. In all other case $\beta=120^{\circ}$ is reached. An interesting situation occurs for $\theta=40^{\circ}$. Here, the stress goes through positive and negative values before becoming positve again when $\beta=120^{\circ}$ is reached. Figure IV-16 shows the actual cell deformation for this case. It is clear that on further deformation the cells would not go back to the original configuration.

Incorporation of liquid thus reveals that deformation in foam is a complex phenomenon with initial orientation playing a major influencing factor on stability.

B. FOAMS WITH FINITE FILM THICKNESS

As before, the stress-strain response of the foam can be divided into two deformation regions: Regime I, which starts with the onset of deformation and ends when two Plateau borders meet, and, Regime II, which starts at this strain, γ_1, and incorporates all higher strains. Because

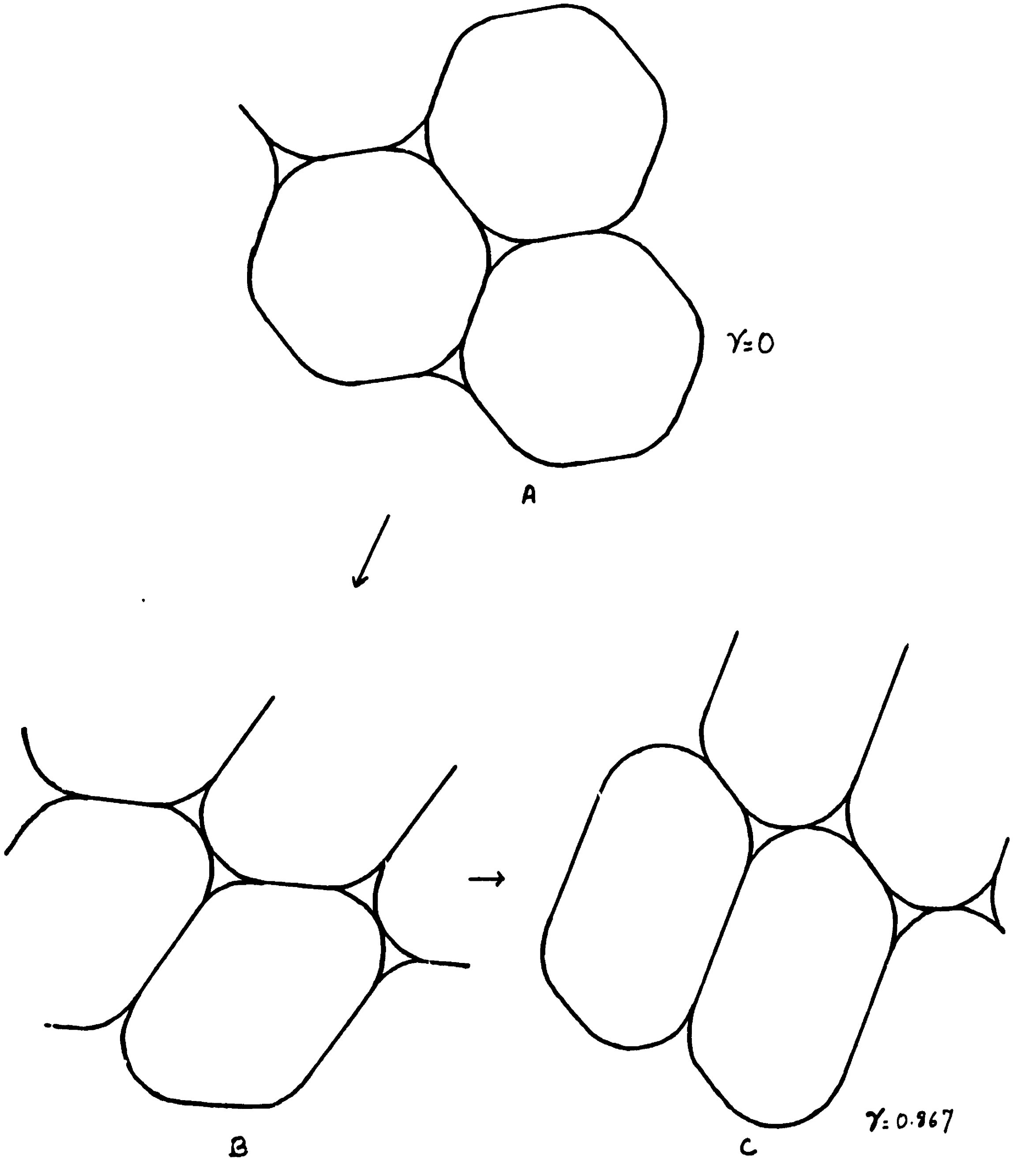

Figure IV-16 Cell defor mation for 0.97 gas fraction foam. Initial orientation θ=40°.

of the finite thickness of the liquid films, the dry foam model derivations are no longer valid for Regime I. This is because on applying a deformation, as the liquid films undergo an extensional motion, liquid flows into and out of them into the Plateau borders. Thus, the Plateau border radius changes with strain, and therefore the second term in Equation IV-1 is nonzero. Equations for each of the regimes are therefore derived separately here.

All assumptions listed in Section IV-A.1 are applicable here. The equations for cell deformation are derived based on geometrical constraints, gas and liquid area conservation, and the equal pressure difference constraint. This third requirement, arising from assuming equal pressures in all gas cells gives the additional relation needed between δ and r. It states that at equilibrium the pressure drops across all interfaces are the same, and for the curved interface, this pressure difference equals σ/r [Heimenz,1982]. Clearly, if this were the only relation to hold for the straight films, there would be no pressure drop across such films. There would be a net liquid suction toward the Plateau borders resulting in cell collapse in no time. However, other forces, known as disjoining forces, act in these films and prevent such localised thinning. Such forces arise from van der Waals forces, electrostatic repulsion, etc. and are related to the thickness of the straight films, δ. Liquid film theory states states that the pressure drop across linear films is given by A/δ^n [Wasan,1984; Teletzke,1984]. Here, A is the Hamaaker constant. The value of the exponent, n, depends on what the important forces are in the film i.e. electrostatic, van der Waals, etc. This in turn is determined by the thickness of the film. For foam films, where van der Waals forces predominate [Wasan,1984], n equals 3.

1. Regime I

Figure IV-17 shows the triangular unit cell DEF formed by joining the mid points of three adjacent foam cells. The dashed line represents the circumscribed hexagonal foam cell. Also shown in the figure is the subcell ABC which moves affinely with the bulk deformation, and the linear films l_1, l_2, l_3 along OB, OA and OC respectively. A triangle PQR is drawn by joining the three centers of the curved Plateau border interfaces. As the cells deform, the three angles at O remain 120°. Therefore, PQR is always an equilateral triangle having sides of length $2r+\delta$. But the lengths of the sides change with deformation as liquid flows in and out of the Plateau border in order to preserve overall liquid area.

Since the 120° criterion is assumed applicable in this regime, we know the lengths of OA, OB and OC as functions of γ from Chapter II (Equation II-20). Further, from Figure IV-17, we get:

$$\begin{aligned} l_1 &= OB - (r + \delta/2)/\sqrt{3} \\ l_2 &= OA - (r + \delta/2)/\sqrt{3} \qquad \text{IV-11} \\ l_3 &= OC - (r + \delta/2)/\sqrt{3} \end{aligned}$$

Thus,

$$l_1+l_2+l_3 = 3a\sqrt{(\gamma^2+4)/4} - (r+\delta/2)\sqrt{3}$$

The first term of the right hand side in the last relation was obtained using Equation II-20.

Now the total liquid in the films remains constant. Thus,

$$(l_1+l_2+l_3)\delta + \sqrt{3}\,(2r+\delta)^2/4 - \pi r^2/2 = (1-\phi)3\sqrt{3}\,a^2/4 \qquad \text{IV-12a, b}$$

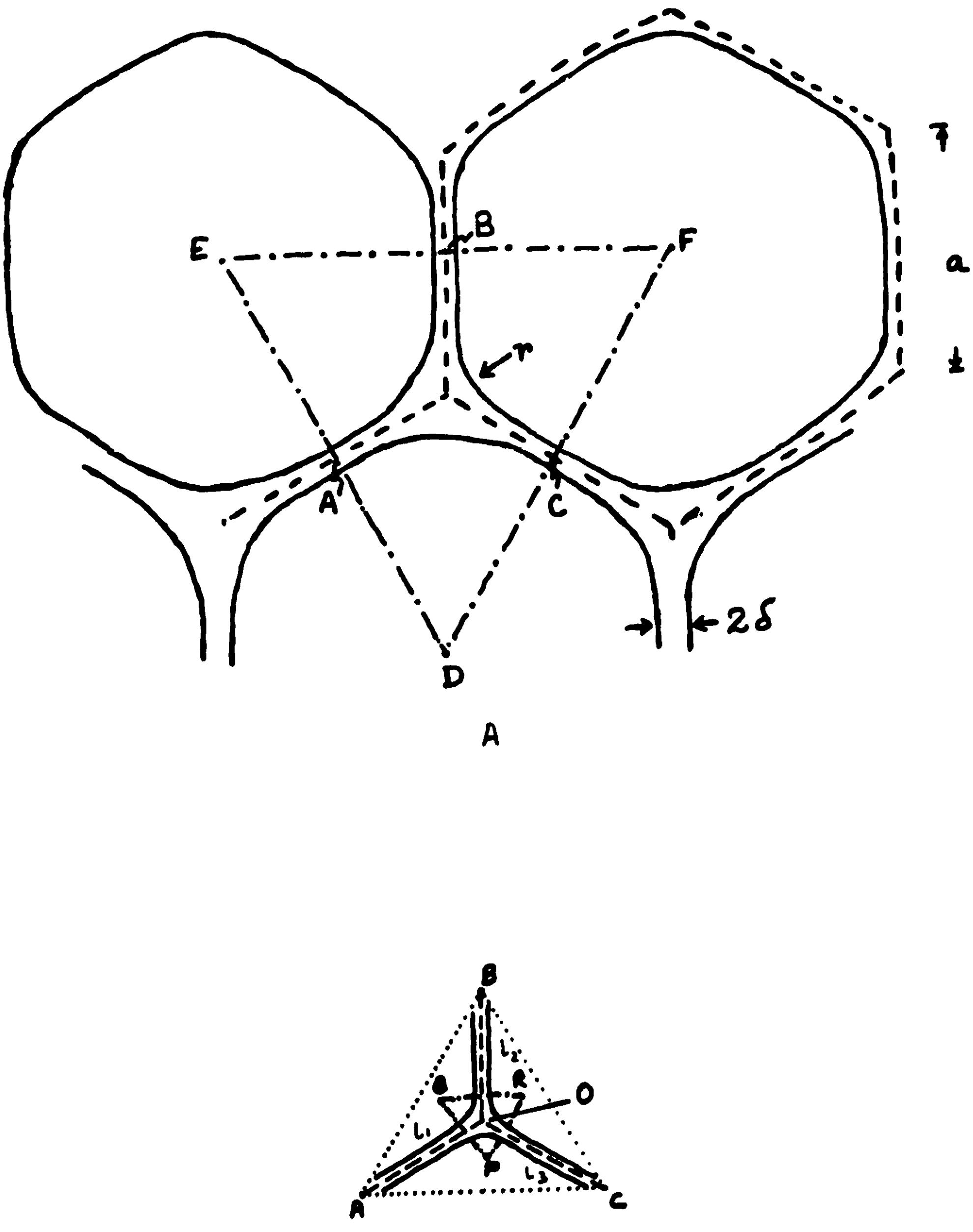

A

B

Figure IV-17 Foams with finite film thickness. a) Foam cells b) Unit cell used for deformations up to the point the Plateau borders meet (Regime I).

or,

$$3a\delta\ \sqrt{(\gamma^2+4)}\ /4 + \sqrt{3}\ (r^2-\delta^2/4) - \pi r^2/2 = (1-\phi)3\sqrt{3}\ a^2/4$$

Further, from the equal pressure drop requirement, we get

$$\Delta P = a/\delta^3 = \sigma/r$$

or IV-13

$$\delta = [Ar/\sigma]^{1/3}$$

This value of δ can be substituted into Equation IV-12 and the corresponding equation solved as a function of strain.

Now, stress in this case is given by Equation IV-8. By using the same approach as in Section IV-A.2, we get an explicit expression for stress given by:

$$\tau_{yx} = \frac{8\ \sigma}{3\sqrt{3}a^2}\{\ \frac{3}{4}\ a\ \frac{\gamma}{\sqrt{(\ \gamma^2+4)}} + \frac{dr}{d\gamma}[\ \frac{\pi}{2} - \sqrt{3} - \frac{\sqrt{3}}{6}\ (\ \frac{A}{\sigma\ r^2}\ )^{1/3}]\} \qquad \text{IV-14}$$

where $\frac{dr}{d\gamma}$ is given in Appendix B.

Thus once the radius of curvature, r, is obtained , one can get the corresponding stress. The non-linear equations, Equations 11-13, were solved by using the bisector method.

2. Regime II

The approach taken here is very similar to that of Section IV-A.2. Consequently, no geometric details are presented here. Figure IV-18 shows the two adjacent unit cells along with all the relevant foam structures. l_1, l_2 denote half the lengths of the actual linear films connecting two Plateau borders and therefore correspond to the lengths of the equivalent films (given by the dashed lines). The equations for the b's are same here as Equation IV-2. Based on Figure IV-18, the other relevant equations

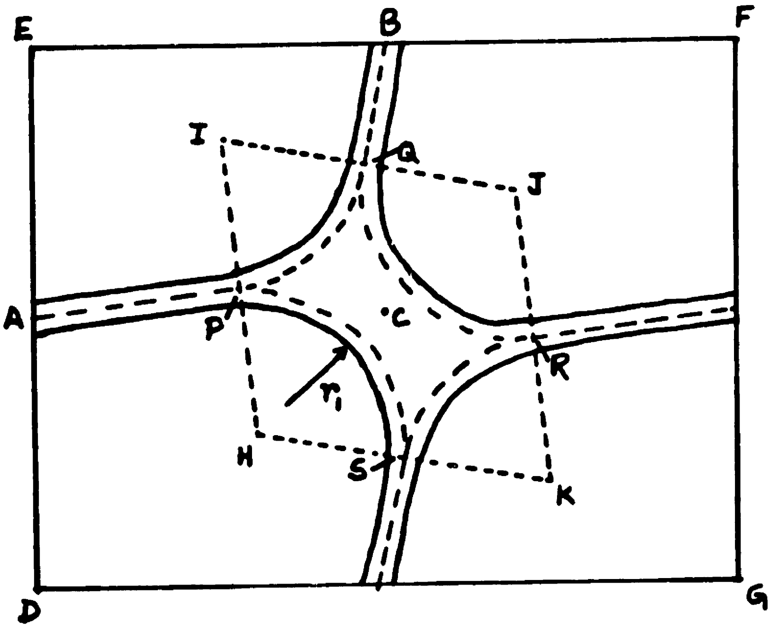

Figure IV-18 Adjacent unit cells used for calculating deformations in Regime II where Plateau borders have already met.

are given below.

Let $r_1 = r + \delta/2$ IV-15

Therefore,

$$l_1 = -r_1 \sin \beta + \sqrt{[\, b_3^2 - r_1^2 \cos^2 \beta \,]} \qquad \text{IV-16}$$

$$l_2 = -r_1 \sin \beta + \sqrt{[\, b_2^2 - r_1^2 \cos^2 \beta \,]} \qquad \text{IV-17}$$

The area of the rhombus HIJK is: $(2r+\delta)^2 \sin\beta$

The area of the circle in the rhombic region is: πr^2

Liquid area conservation within DEFG gives:

$$2\delta(l_1+l_2) + (2r+\delta)^2 \sin \beta - \pi r^2 = (1-\phi)\, 3\sqrt{3}\, a^2/2 \qquad \text{IV-18}$$

Gas area conservation gives:

$$4r(l_1+l_2) + \pi r^2 + 4\, l_1\, l_2 \sin \beta = \phi\, 3\sqrt{3}\, a^2/2 \qquad \text{IV-19}$$

The equal pressure drop relation gives:

$$\delta = (\, Ar/\sigma \,)^{1/3} \qquad \text{IV-13}$$

All these equations can be combined into one and solved in the same way as in the zero film thickness case. Then the stresses can be obtained from Equation IV-8. The derivatives in this case are similar to the previous case although much more complicated.

For certain initial orientations, the film l_1 may go to zero length instead of l_3 (Figure IV-17). In such cases, b_2 should be replaced by b_1 in all equations.

3. Results and Discussion

An important aspect of the model developed here is its realistic nature. Real foams have finite film thickness which vary with deformation. Liquid is not confined within the Plateau border regions. In our model, too, allowance is made for liquid movement in and out of the Plateau borders. The radius of the Plateau border region and the film thickness are determined by the pressure drop relation and vary with the gas volume fraction and state of strain. However, since this is an equilibrium model all films have the same thickness δ at all times.

Shear stress-strain results of the two strain regimes for different ϕ's and θ's have been combined and compared with the zero film thickness case in Figures IV-19, 20. In order to solve the equations, a Hamaaker constant of 10^{-12} and an interfacial tension of 22 dynes/cm were used. The latter number is the actual surface tension of the liquid used in our experiments (see Chapter V). The Hamaaker constant value is typical for thin films. However, using values three orders of magnitude higher or lower than this showed no effect on the results. From the figures we observe that although the equations in this case are different, the stress-strain results are the same as the δ=0 case. The same instabilities were observed in the hexagonal close packed case for θ between 11° and 20°. In this case, however, the cells have a very small film at zero strain. The solutions therefore become unstable beyond these infinitesimally small strains.

The excellent agreement between the two results can be explained from the following reasons. With the Hamaaker constant used, the film thickness calculated is significantly smaller than the cell size and

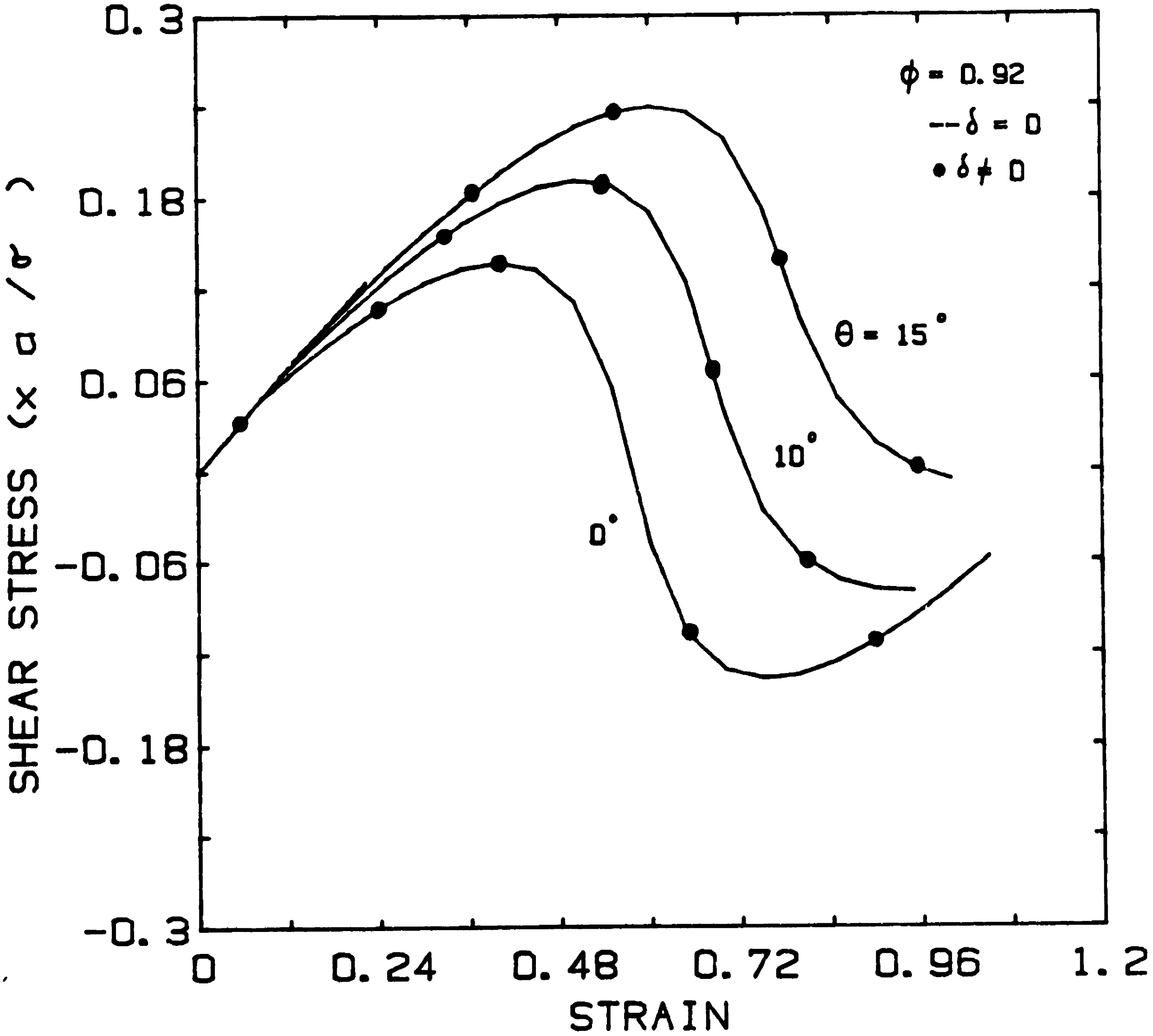

Figure IV-19 Shear stress vs. strain for foams with and without finite film thickness. φ=gas fraction; θ=initial orientation.

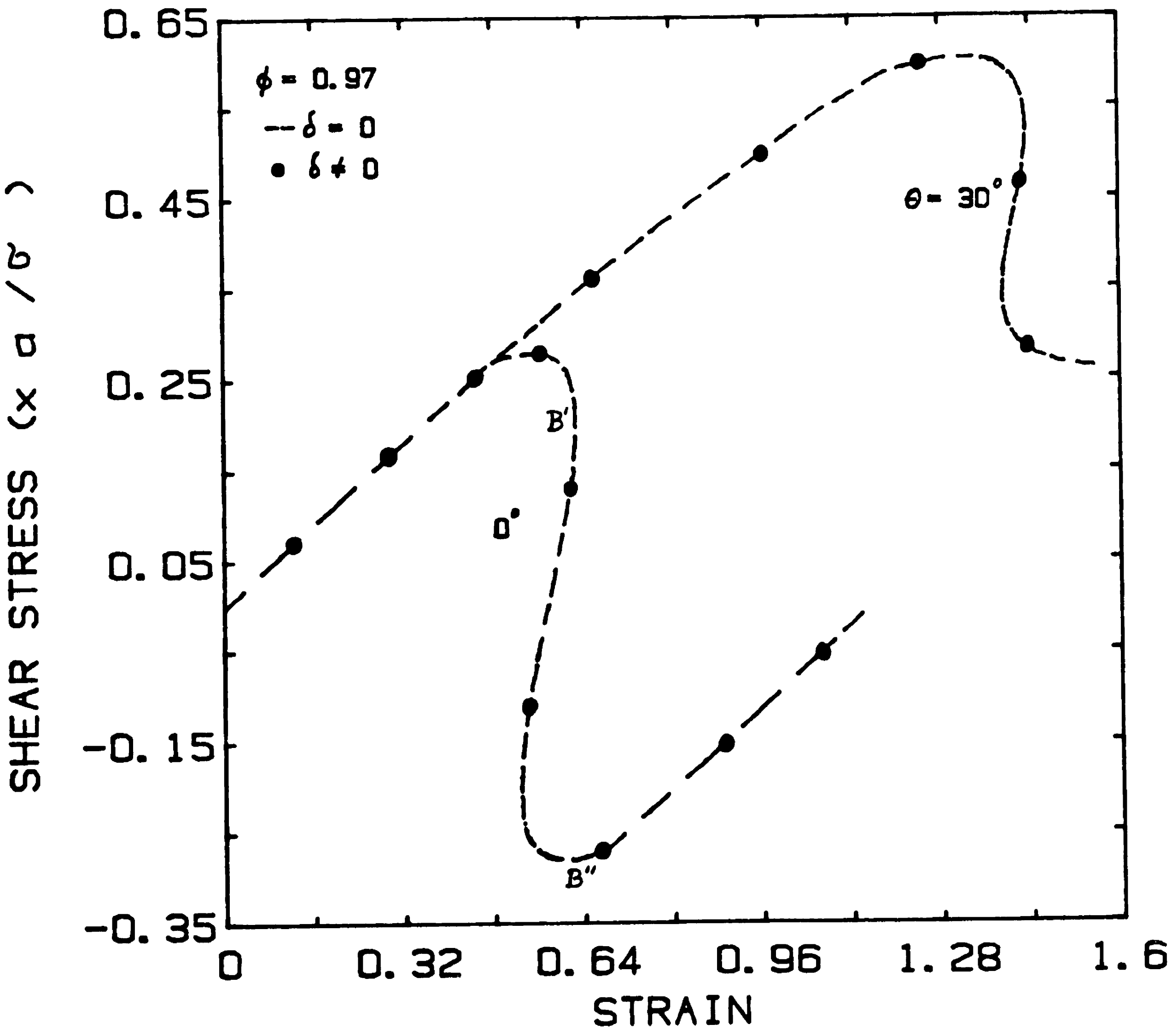

Figure IV-20 Shear stress as a function of strain for foams with and without finite film thickness. φ=gas fraction; θ=initial orientation.

the radius of curvature. Consequently, the values of r obtained are almost exactly the same as in the δ=0 case. As the cells deform, liquid flows in and out of the Plateau borders; r and δ changes. However, the change in δ is too small to affect the change in r and the film lengths in any significant way from the zero thickness case. One can also observe this from an order of magnitude analysis. From Equation IV-15, we get:

$$r_1/r = 1 + 0.5\ (\delta/r)$$

Using the equal pressure drop relation (Equation IV-13) to relate δ and r, and using values of 10^{-12} and 25 dynes/cm for the Hamaaker constant and surface tension respectively, we get:

$$r_1/r = 1 + \sim 10^{-5}\ r^{-2/3}$$

where r is in cms.

Clearly, the error involved in using r instead of r_1 is negligible. Since the stress is related to the total interfacial length, we obtain the same results as before. This close correspondence of the results show that the negligible film thickness assumption, which has been used in all our calculations so far, is a justifiable one.

Throughout this chapter, we have looked at shear deformations only. However, one can use this approach to describe other kinds of deformation such as extension. All assumptions, such as the affine motion of the cell center and the pressure drop requirement, are general enough to be carried over to this case.

One last point regarding critical strain needs to be mentioned here. In the dry foam case, the critical strain corresponded to the value of the strain when one of the cell sides reduced to zero length. The corresponding stress was the yield stress. For foams with $\phi<1$, there is no such obvious way to define γ_c. We could define the strain corresponding to the maximum stress, or the strain at which the system goes unstable as the critcal strain. For cases where the system is always stable (e.g. $\phi=.92$, $\theta=0^o$) or the two are synonymous ($\phi=.92$, $\theta=30^o$, 40^o), γ_c is unambiguous. For other cases (e.g. $\phi=.97$, $\theta=30^o$), one could use either definiton since the stress-strain relation is unaffected by it.

C. CONCLUSIONS

In this chapter, the effect of gas volume fraction on small shearing deformation of foams were studied. All possible initial cell orientations and cells with finite film thickness were taken into consideration in this study. Based on our calculations, we found:

a. Incorporation of finite liquid into our model affected the stress-strain relationship. Thus, for $\theta=0^o$, the yield stress or the maximum stress decreased with decreasing gas fraction.

b. Unlike the dry foam case (cf. Chapter II), initial cell orientation influenced the stress-strain relationship significantly. For some orientations and gas fraction, limit points and instabilties were observed indicating possibilites of preferential cell orientation. Thus, for $\phi=.97$, we observed limit points, while for $\phi=.9069$ and θ between 11^o and 20^o, the system became unstable opon applying any strains.

c. Negative stresses were observed in the stress-strain cycle in many cases. This is because the energy of the system passed through a maximum as the cells were being deformed.

d. Introducing finite film thickness, δ, into our model did not change any of the results.

V. EXPERIMENTS IN SHEAR FLOW

Experiments have been designed and conducted to characterize systematically the shear flow properties of foam. Both steady and time dependent experiments were done. The influence of gas volume fraction, ϕ, on different material functions was also examined.

This study, which was done in three phases, consisted of: i) developing a method to produce stable foam physically, ii) devising a suitable experimental technique to characterize the foam rheologically, and finally, iii) measuring the different material functions of interest. A detailed description of each of these are presented below.

A. FOAM GENERATION

Experimental study of foam is complicated by cell collapse and film drainage. In order to isolate rheological information from these, we needed a system which could generate stable, reproducible foam. Foam produced in the laboratory met these requirements, and were used in all our experiments. The gas volume fraction of this foam could also be controlled and its effect on rheology studied.

1. Foam Formulation

A polymer-surfactant based aqueous solution was used as the foaming liquid. The exact formulation, which is given in Table V-1, was an outgrowth of the recipe used by Rand [1982] to make foam. The major differences between the two is in the relative amounts of the different components and in the polymer used. With this modification, we were able to produce foam having large gas fractions (ϕ>.90) as well as small cell size (~100

TABLE V-1

FOAM FORMULATION AND PREPARATION

A. CONCENTRATE FORMULATION

	% wt.
n-dodecanol	4
n-butyl alchohol	10
surfactant (Witconate AOK, Witco Chemicals)	7.5
5 wt.% PEO (300K M.W., Scientific Prods.) solution in water	40
water	38.5

Add 20 wt.% of concentrate in water to make final product.

B. PREPARATION OF FOAM SOLUTION

1. Prepare PEO solution. Use rollers or other mixers to dissolve polymer. Mix it for a day.
2. Dissolve n-dodecanol in butyl alchohol. Time required for this to dissolve is 15 minutes. Add PEO solution to this.
3. In a different container, pour the powdered surfactant into water slowly. Mix until it dissolves (~15 minutes).
4. Add solution 2 to 3 to get concentrate.
5. Dilute solution as required.

microns in diameter). Rand could not achieve both of these simultaneously with his formulation.

In the formulation shown in Table V-1, the polymer n-dodecanol combination served as a stabilizer. Polyethylene oxide was chosen as the polymer because it was water soluble and, more importantly, the resulting solution was Newtonian. Thus any non Newtonian behavior observed in foam could be directly attributed to its structure. The butyl alchohol was used as a solvent. Foam produced using this formulation was stable for about an hour.

2. Apparatus

Figure V-1 shows a schematic diagram of the foam generator used in our laboratory. This kind of foam generator, which is a modified version of one first built at Sandia Laboratories [Rand, 1982], works on the principle that mixing a stream of gas and liquid solution in some porous structure such as a steel wool mesh, produces foam. As seen from the figure, the surfactant solution is kept in a stainless steel tank capable of withstanding pressures upto 125 psi. Figure V-2 gives a detailed diagram of the tank along with the different dimensions. As can be observed, the lid of the tank, which is screwed on to it, has four openings. To these are attached: i) a Nitrogen source tank to pressurize the surfactant solution when needed, ii) a pressure gauge (0-100 psi) to monitor tank pressure, iii) a Nupro relief valve, and iv) an on-off valve to depressurize the system after use.

The bottom of the tank is attached to a tube which connects to the stainless steel mixer. This mixer, which is 4.6 inches long and 0.18 inches in inner diameter, is packed with 1.6 gm of coarse stainless steel

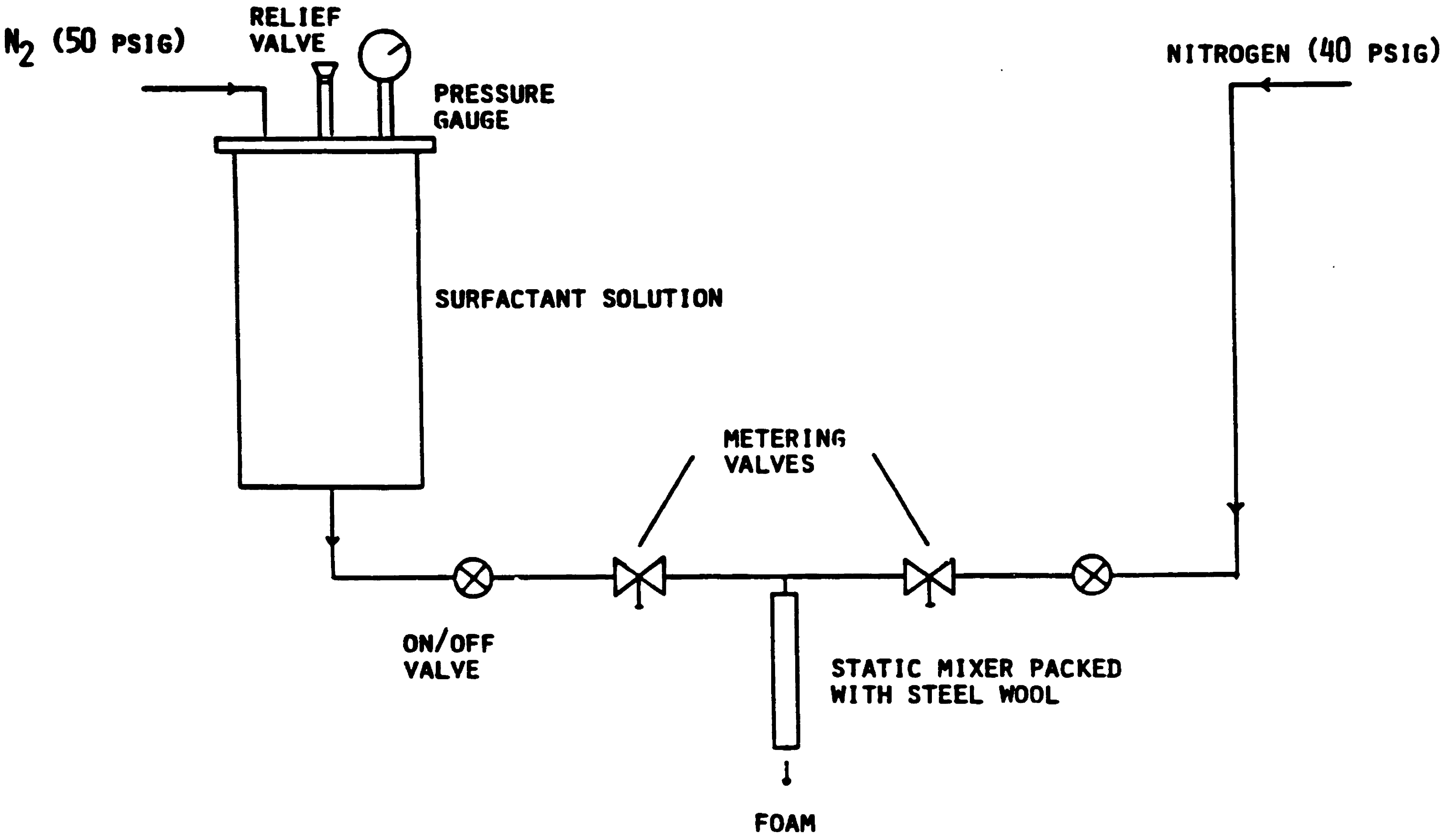

Figure V-1 An Aqueous Foam Generator.

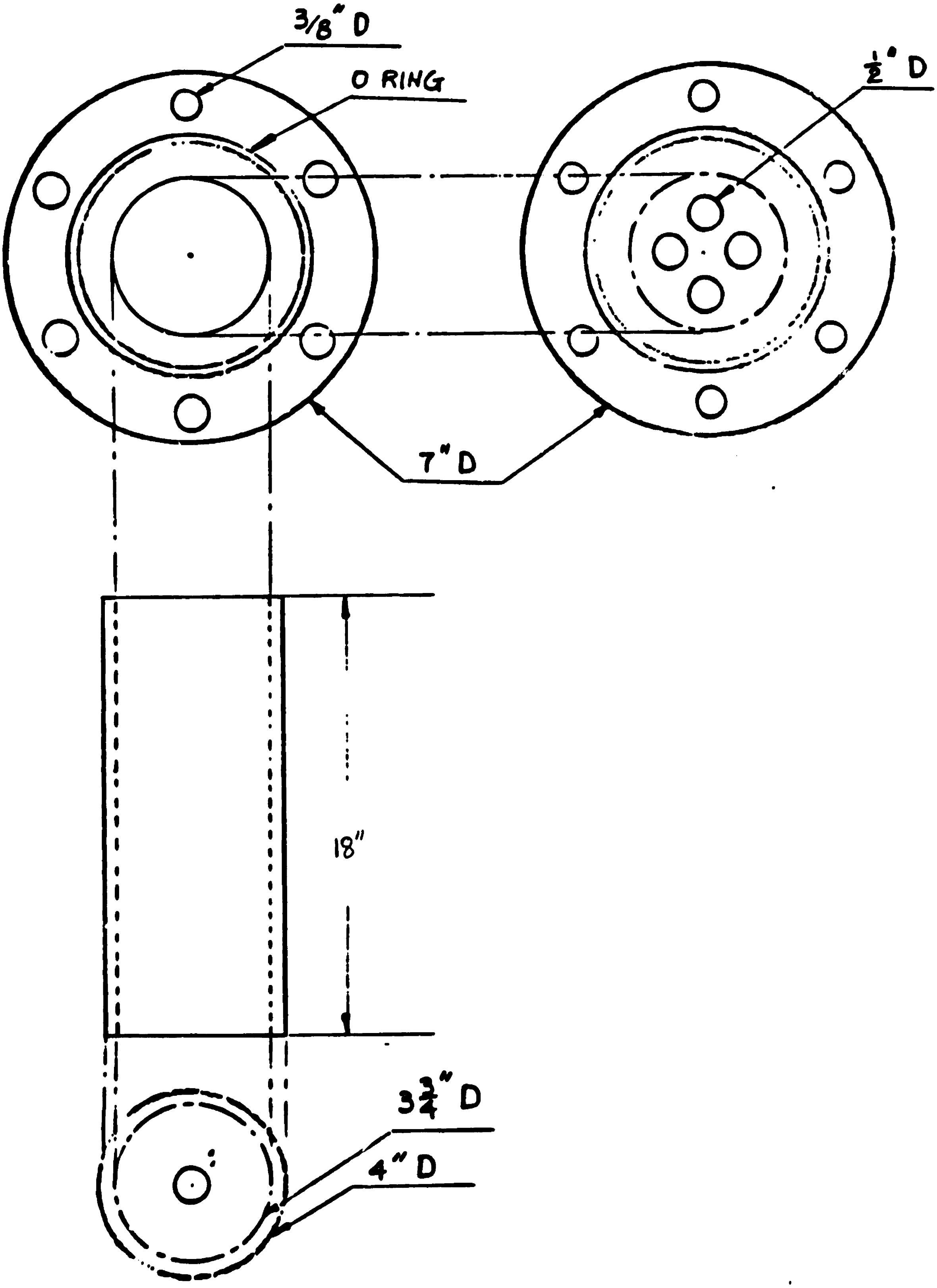

Figure V-2 Sectional view of the surfactant solution tank.

wool up to 3.8 inches of its length. All tubings in the system are made of polyethylene (0.25 inches O.D) and all fittings are Swagelok fittings.

In order to produce foam all valves in the system are shut and the tank filled with the surfactant solution. Having closed the tank, the two Nitrogen pressure sources are turned on. Successively, the two on-off valves leading to the metering valves are opened. When the two metering valves are opened, the nitrogen pressing down on the liquid solution causes it to flow down the tube to the mixer. At the same time the gas flows through the other tube towards the steel wool packing. The liquid and the gas mix here to create foam. With this generator, foams having gas fraction as high as 0.98 could be produced. The gas volume fraction is controlled by changing the liquid and gas flow rates. When foam production is no longer required, the above procedure is repeated in reverse order. The liquid tank is then depressurized using the valve on the lid, the liquid emptied and the whole system flushed with distilled water.

3. Surface tension, Gas fraction and Bubble size measurements

In order to characterize fully the generated foam and to be able to compare the model predictions, the liquid surface tension, the average bubble diameter and the gas volume fraction have to be known. The first of these was measured using a tensiometer. Details on the operation of this instrument can be found in the Dunoi Tensiometer Handout. The gas volume fraction of foam was found by filling a tube of known weight and volume with foam and measuring the difference in weight with a sensitive balance. This tube, which had the same inner diameter as the mixer in the generator, was filled by attaching it to the end of the mixer. Tubes of different lengths were used and agreement between them was excellent.

Reproducibility was also checked by taking data at different time intervals.

The average bubble diameter was determined by taking microscopic photographs of a sample of foam squashed between two glass slides separated from each other by a lens paper. By counting the number of bubbles from the photograph and calculating the volume of the sample between the slides, an average bubble diameter could be obtained. In order for the method to give the correct number of bubbles, the foam sample had to be one layer thick. The thickness of the paper had to be less than the bubble diameter to ensure this.

B. EXPERIMENTAL TECHNIQUE

1. Equipment Description

For all our rheological measurements the Rheometrics Mechanical Spectrometer was used. The rationale for such a choice will be discussed later. This instrument gives a sample a known deformation at a specified rate and temperature. The measured outputs give the resulting stresses in the sample. Figure V-3 shows a schematic overview of the instrument.

Deformations are produced through rotary motion, as shown in Figure V-4. A dc torque motor drives the upper spindle. Speed is controlled by a feedback loop from a precision tachometer over a wide range, 0.001 to 100 radians/sec.

The lower spindle is an air bearing. It can rotate freely or be locked with the thumb screw at the bottom end of the spindle. The lower spindle serves to transmit stresses from the sample to the transducer which supports it. Small deflections of the transducer are converted to electrical signals by semiconductor strain gauges. These are amplified

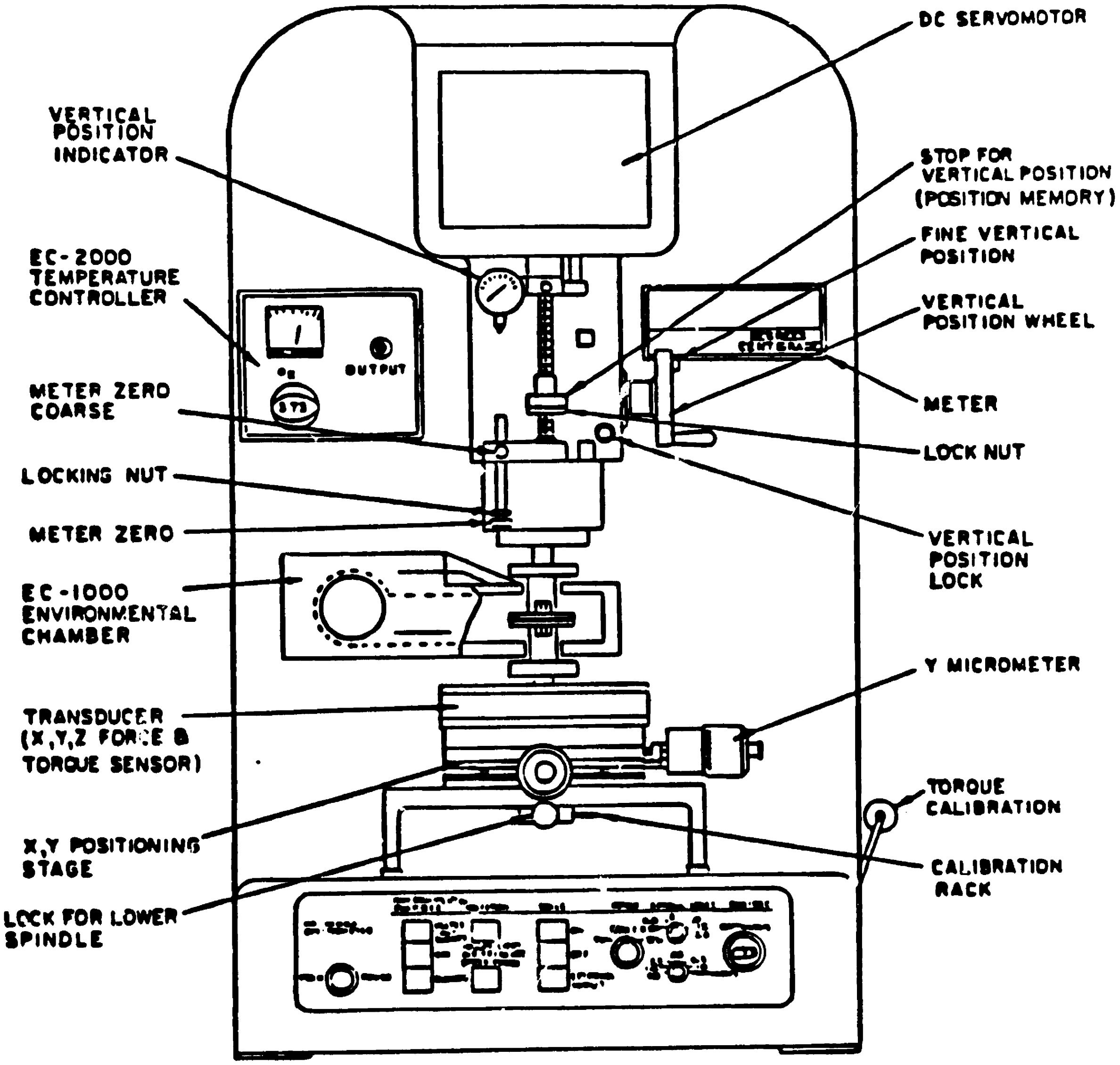

Figure V-3 Front view of the Rheometrics Mechanical Spectrometer.

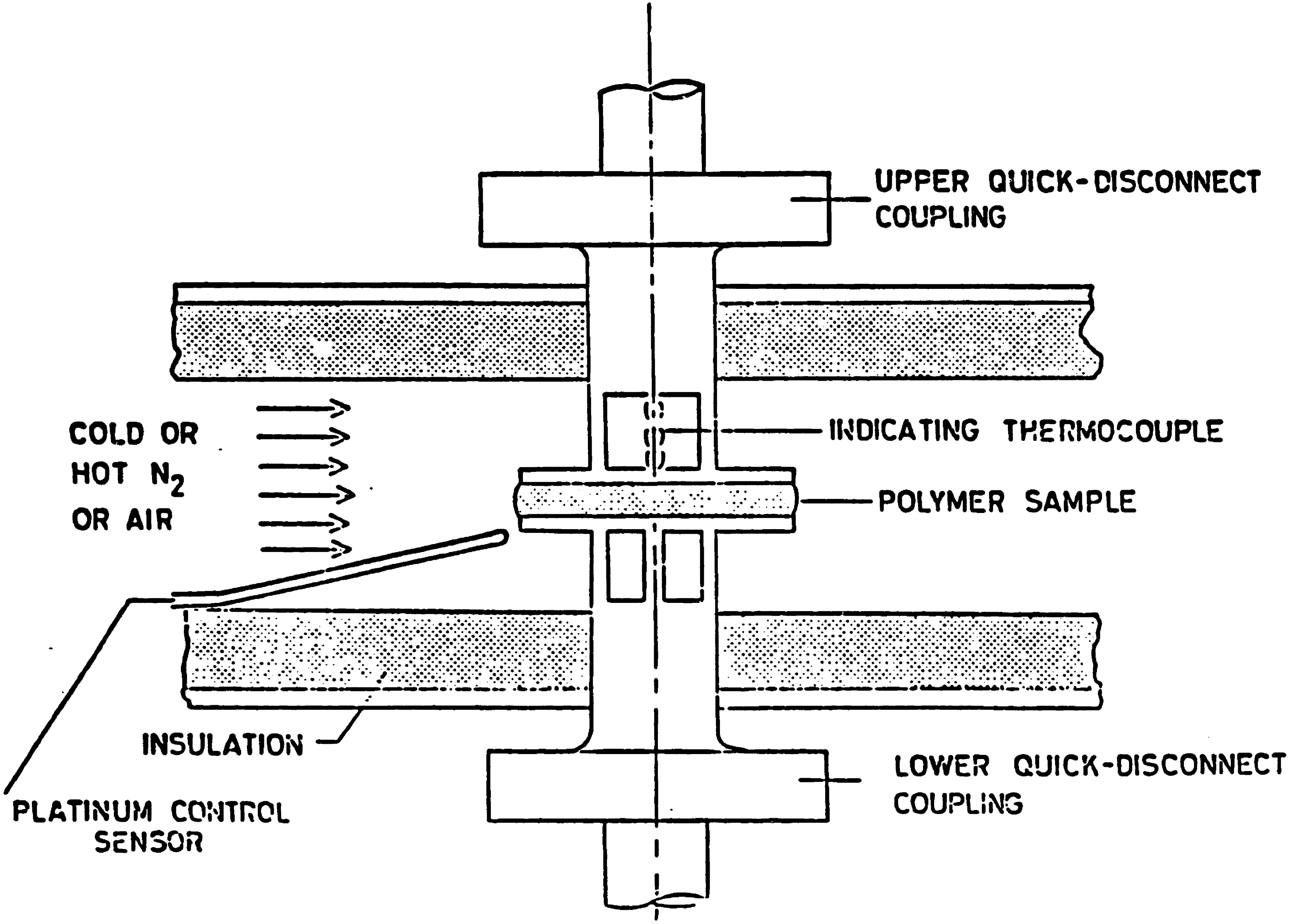

Figure V-4 Cross section of test area in the Mechanical Spectrometer.

and may be read on a strip chart recorder or fed directly to a computer.

Samples are held between test fixtures mounted on each of the spindles. The upper fixture and spindle can be raised and lowered with the positioning wheel, which has a coarse and fine motion. Vertical position is read by a dial indicator which moves with the spindle. Figure V-4 shows a disk-shaped sample confined between two flat plate fixtures. These are readily installed or removed by the quick-disconnect couplings.

The sample temperature is controlled by forced convection with the environmental chamber. As shown in Figure V-4, a platinum resistance probe in the gas stream controls the temperature. A thermocouple in the upper test fixture combined with slip rings allows the sample temperature to be monitored directly. With an external supply of liquid nitrogen, the chamber is capable of temperature control from -150 ^{o}C to 350 ^{o}C. All our experiments were, however, done at room temperature without the use of the controller. Experiments repeated on different days and times revealed that the slight variation in room temperature did not affect rheological measurements.

There are a number of fixtures available for use with the Mechanical Spectrometer, including cone and plate, parallel plates, eccentric rotating discs (ERD) and concentric cylinders. For all foam experiments, we used the parallel plate flow mode of the mechanical spectrometer in which the foam is put between two concentric parallel discs (Figure V-5). The lower disc is kept locked, and the upper one rotated at a specified angular velocity ω. By changing the gap and frequency of rotation, the shear rate can be varied. The outputs measured are the torque and the normal force required to keep the distance between the plates fixed.

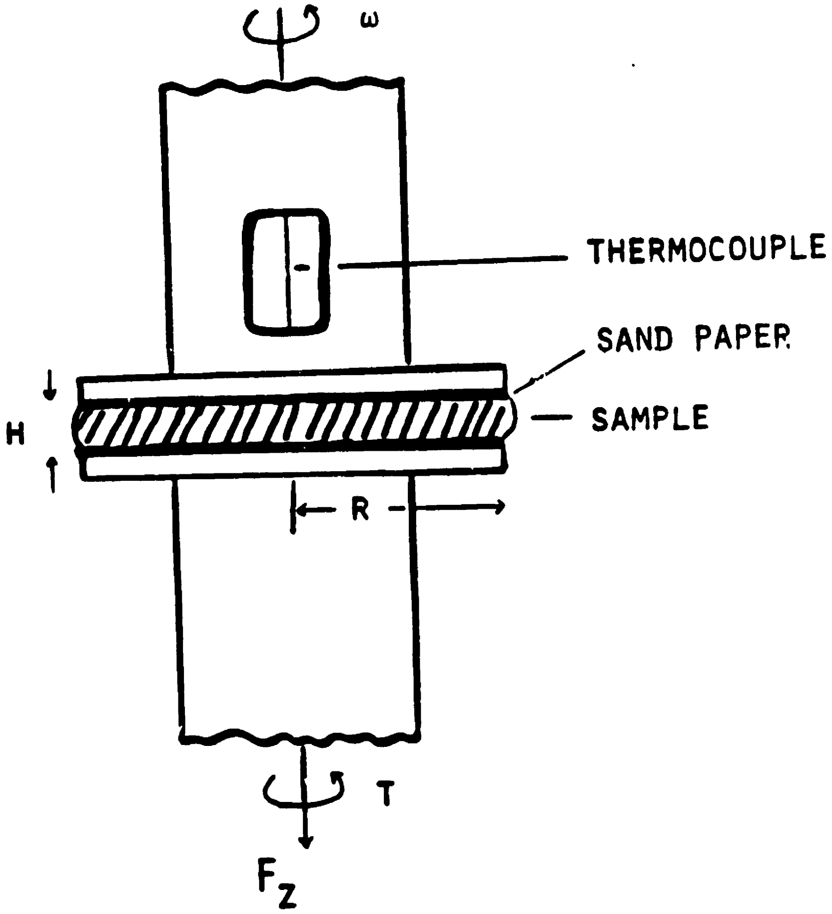

Figure V-5 Parallel Plate mode in a Mechanical Spectrometer. Note that sandpaper has been pasted on both plate surfaces.

In practice, however, the output of the normal force is small and is plagued with noise.

2. Procedure

In any kind of foam flow, considerable wall slippage is observed. This is because a thin liquid film forms at the walls thereby interfering with getting accurate rheological information about foam. By pasting sandpaper (3M 120) on the circular discs so that the liquid could reside in the troughs of the sand paper, the effect of the liquid film on rheological measurements was eliminated. The grit size of the sand paper did not affect the results as long as the particles were commensurate with the bubble size.

To do the experiments, the foam sample was loaded carefully in the gap between the plates and any excess sample protruding beyond the rim was removed. However, before doing any systematic experiments, the dynamic stability of the foam was checked by running a sample at a particular shear rate and observing how long the foam could sustain a constant torque reading. A declining torque value indicated the breakdown of the foam structure. In all cases, the foam was stable for about ten minutes and most of our experimental runs were completed within a couple of minutes. Further, to eliminate effects of foam drainage, fresh foam was used to get each data point.

3. Advantages of Experimental Technique

The reasons for choosing the current experimental procedure are discussed below.

a) The use of sand paper eliminates the liquid slip layer in foams. Readings obtained thus pertain to pure foam. In other methods, such as the capillary viscometer [David, 1968, 1969; Fan, 1981] or Couette device, this is not possible. Raw data has to be reduced by making some assumptions on the liquid film layer in order to get information on the rheology of foam only. This introduces some uncertainties into the measurements.

b) Experiments can be run at very low shear rates using the Mechanical Spectrometer. In this regime, there is little cell breakdown and experimental conditions are closer to the assumptions in the model. Further, the sand paper along with the low shear rates enable us to do stress relaxation experiments and measure yield stress directly. In other techniques this is not possible. Moreover, in capillary viscometry, the shear rates are high leading to large presure drops and higher probability of bubble collapse and compressibility effects.

c) The small gap in Couette flow and the tube diameter in capillary tubes are often of the same order as the foam cells. This affects rheological information. With the parallel plates, this is not a problem since the gap can usually be made larger than the cell size.

d) Film drainage can be ignored with the Mechanical Spectrometer by putting in fresh sample for each data point. Data taking requires only a couple of minutes, which is considerably shorter than the collapse time of the foam.

e) The entire sample is at atmospheric pressure. Compressibility effects are therefore negligible.

C. EXPERIMENTS AND MATERIAL FUNCTIONS OF INTEREST

Most useful models and experiments are expressed in terms of a few material functions. These functions can be found from relatively simple experiments and applied to other situations. We focussed our attention on some material functions describing different shearing flows (steady and dynamic) because these are the most important flows in engineering and processing applications. Further, they are also most amenable to quantitative experiments.

In the laboratory, however, the directly measured quantities are not the the desired material functions but rather the torques and forces exerted on different pieces of equipment, rotation rates, certain physical dimensions of the equipment and so forth. These measurable parameters can then be directly related to the material functions. In the ensuing sections, these relationships along with a brief description of the experiments are given. Further details on these have been discussed by Bird, Armstrong and Hassager [1977], Dinh [1981] and Weinberg [1981].

1. Steady Shear Flow

Three material functions completely describe a simple shearing flow. These are,

the viscosity, $\eta = \tau_{yx} / \dot{\gamma}$

the first normal stress coefficient, $\Psi_1 = (\tau_{xx} - \tau_{yy})/\dot{\gamma}^2$

the second normal stress coefficient, $\Psi_2 = (\tau_{yy} - \tau_{zz})/\dot{\gamma}^2$

In order to simulate such flow in the Mechanical Spectrometer, the bottom plate is kept fixed and the top rotated at a constant frequency, ω. The measured outputs are the normal force F (gms) and the torque T (gm-cm) exerted on the lower plate. However in the parallel plate mode, the shear rate $\dot{\gamma}$ is not constant throughout but a linear function of the plate radius and is given by $\dot{\gamma} = \omega r/H$. Hence, the viscometric function are derived with repect to the rim shear rate $\dot{\gamma}_R$. They are given by:

$$\eta(\dot{\gamma}_R) = \frac{(T/2\pi R^3)}{\dot{\gamma}_R}\{3 + \frac{d\ln(T/2\pi R^3)}{d\ln\dot{\gamma}_R}\}$$

$$\Psi_1 - \Psi_2 = \frac{(F/\pi R^2)}{\dot{\gamma}^2}\{2 + \frac{d\ln(F/\pi R^2)}{d\ln\dot{\gamma}}\}$$

$\dot{\gamma}_R = \omega R/H$ is the rim shear rate,

R and H are the disc radius and separation respectively,

ω is the angular velocity of the top plate, and

F and T are the normal force and torque readings in gm and gm-cm

2. Stress Relaxation after Steady Shear

This experiment, which is illustrated in Figure V-6, was done to check the presence of a yield stress in foam. Boger [1983] was one of the first to use a similar technique for yield stress measurement purposes. Here the foam is put between the two discs as before, the upper plate is rotated at some low frequency until steady state is reached and then shut off. For a material having no yield stress, the torque reading would fall off to zero, but for a material with finite yield point, the torque would relax back to some residual value associated with the yield stress. This procedure should be repeated for different frequencies and the yield stress should be independent of shear rate. The stress

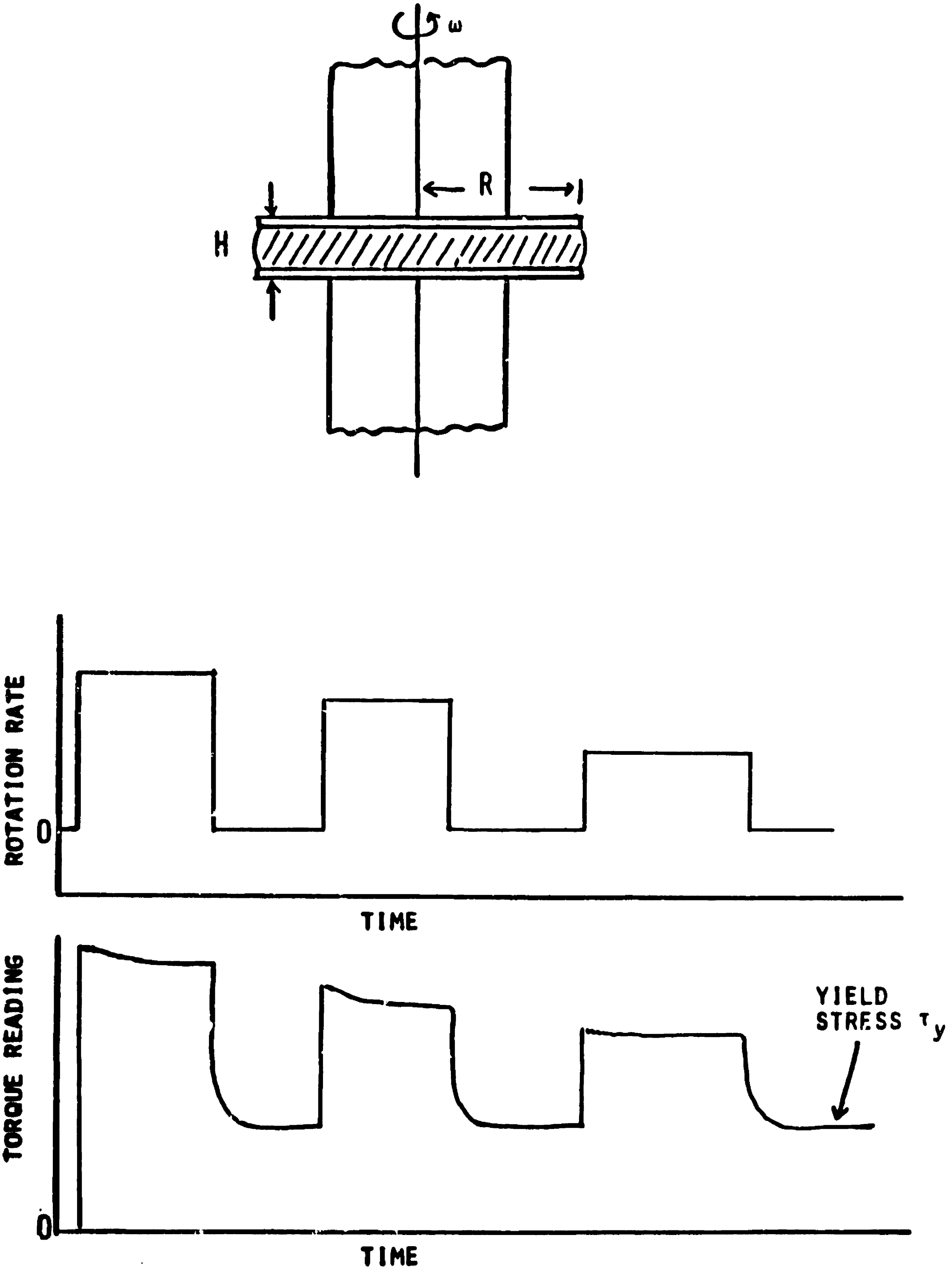

Figure V-6 Stress Relaxation technique used to measure yield stress in foam directly. The residual stress after a steady shear flow corresponds to the yield stress.

is calculated using the same equation as before.

So far, only steady flow experiments have been described. However, these experiments do not provide adequate insights into a material's response, especially for short time scales. One then has to resort to dynamic methods. Two such experiments, small amplitude oscillatory flow and start up of shear flow, were done on foam to measure some of its viscoelastic properties as well as observe its response to different time scales.

3. Small Amplitude Oscillatory Shear Flow

In this experiment, a sinusoidal strain is applied to the material by oscillating the top plate at a specified frequency, ω. Thus $\gamma = \gamma_0 \sin \omega t$, where, γ_0 is the maximum strain amplitude of the top plate and is given by,

$$\gamma_0 = R \times (\text{maximum angular displacement in radians})/H$$

The corresponding stress in the material is also oscillatory in nature and is given by [Bird, Armstrong and Hassager, 1977]:

$$\tau_{yx} = G'(\omega)\, \gamma_0 \sin \omega t + G''(\omega)\, \gamma_0 \cos \omega t + \ldots$$

Please note that Bird, et al. uses a different sign convention and therefore their equation have negative signs on the right hand side for the above equation.

For small enough strains, the higher order terms are negligible i.e. the material has a linear-viscoelastic behavior. One can then directly measure the elastic modulus (G') and loss modulus (G'') from such experiments. Note that for a perfectly elastic solid the above equation reduces to,

$$\tau_{yx} = G_o \gamma_o \sin \omega t$$

and for a viscous Newtonian liquid to,

$$\tau_{yx} = \mu \gamma_o \omega \cos \omega t$$

where, G_o and μ are the modulus and viscosity respectively.

To run this experiment on the Mechanical Spectrometer, a microcomputer (IBM-PC) was used for input/output purposes. The input was the sinusoidal strain and the measured outputs were the stress amplitude τ_o and the phase angle ψ between the stress and strain. The moduli were then calculated from the following equations [Weinberg, 1981].

$$G' = \frac{\tau_o}{\gamma_o} \cos \psi \qquad G'' = \frac{\tau_o}{\gamma_o} \sin \psi$$

However, for these relations to be valid, the material has to be in the linear viscoelastic region. The first step in this experiment was therefore to run a strain sweep keeping frequency constant. As long as the moduli were invariant with strain, the material was linear [Bird, Armstrong and Hassager, 1977; Ferry, 1982]. A particular strain within this range was then selected to run a frequency sweep and observe the time scale responses of foam.

4. Stress Growth

In a stress growth experiment, a constant shear rate is imposed on a material initially at rest. The object here is to observe how the shear stress changes with time as it approaches the steady state value. The importance of this experiment lies in the fact that materials often show strong transient behavior whose nature depends on the rate of deformation. These short time scale responses, such as viscosity overshoot, go unnoticed in steady flow experiments.

As in the steady shear flow case, this deformation can be characterized by three corresponding material functions. Our interest, however, was in the transient viscosity $\eta^{+}(\dot{\gamma}_R,\gamma)$ which can be calculated from the torque versus time output [Dinh, 1981]. Again the microcomputer was used to impose the deformation as well as to record the outputs. Here also the material function was determined at the rim shear rate.

The following is a derivation of the equation relating the transient viscosity to measurable parameters.

The torque, T, measured in the Mechanical Spectrometer is the total shearing force times moment arm on the circular surface of the lower plate. Thus,

$$T = 2\pi \int_0^R \eta^{+}(\gamma)\, \dot{\gamma}\, r^2 \, dr$$

$$= \frac{2\pi R^3}{\dot{\gamma}^3} \int_0^{\dot{\gamma}} \eta^{+}(\gamma)\, \dot{\gamma}^3 \, d\dot{\gamma}$$

$$= \frac{2\pi R}{t\gamma_R^3} \int_0^{R} \eta^{+}(\gamma)\, \gamma^3 \, d\gamma$$

To get the last relation , we used the fact that $\gamma=\dot{\gamma}t$. This relation when differentiated with respect to γ_R and simplified gives:

$$\eta^{+} (\gamma) = \frac{T}{2\pi R^{3}\dot{\gamma}_{R}} \{ 3 + \frac{d \ln(Tt/2\pi R^{3})}{d \ln \gamma_{R}} \}$$

In a given experiment $\dot{\gamma}_R$ is set and the transient viscosity obtained as a function of strain or time.

VI. EXPERIMENTAL RESULTS AND DISCUSSION

Results of the experiments described in the last chapter are presented here. Almost all experiments were done for three different gas volume fractions of foam: 0.92, 0.95 and 0.97. Fresh foam was used to get each data point except in the stress growth experiments where it was used to get each single run. The surface tension of the surfactant solution and the average cell radius were found to be the same in all cases: 23 ± 1 dynes/cm and 65 ± 3 microns respectively. Two different transducers were used interchangeably for the bottom plate of the viscometer depending on the magnitude of the force/torque readings. For the regular transducer (10^4 gm-cm maximum range), plates of 72 mm diameter were used whereas for the sensitive transducer(10 gm-cm maximum scale), plates of 50 mm diameter were used. The gap between the plates was kept constant at 2.4 mm for all runs; however, test runs made with different gap widths showed the material functions to be independent of it.

A. RESULTS

1. Viscosity

The viscosity of foam was measured from the steady shear flow experiment. Figure VI-1 shows a plot of viscosity as a function of shear rate for three different gas volume fractions. As can be seen, foam behaves like a shear thinning material with its viscosity being a strong function of shear rate even at very low shear rate values. This is in contrast to the Newtonian behavior of the parent liquid (Figure VI-2). The viscosity of the PEO based solution, which was measured using a Haake

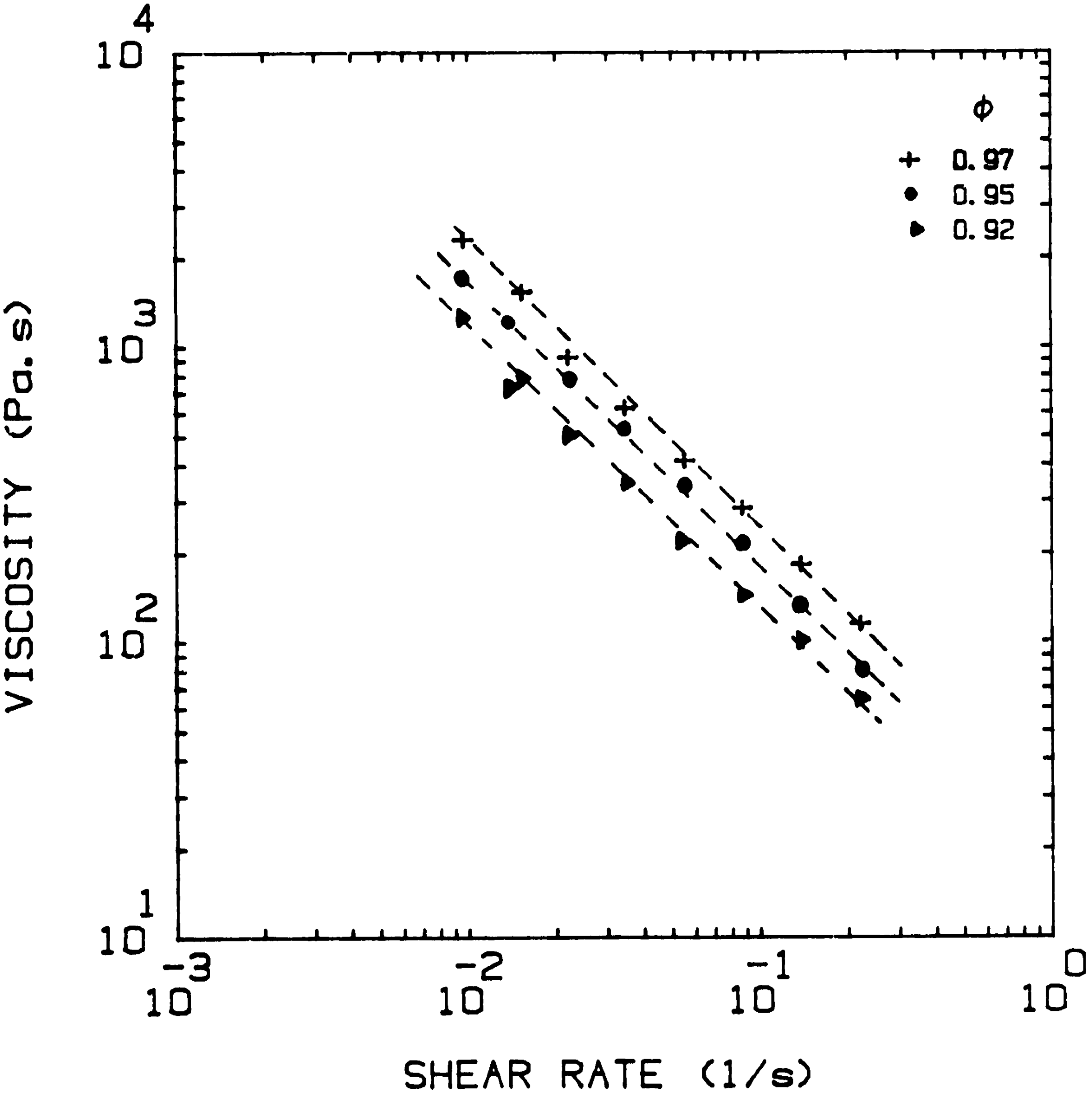

Figure VI-1 Foam viscosity versus shear rate for three different gas fractions.

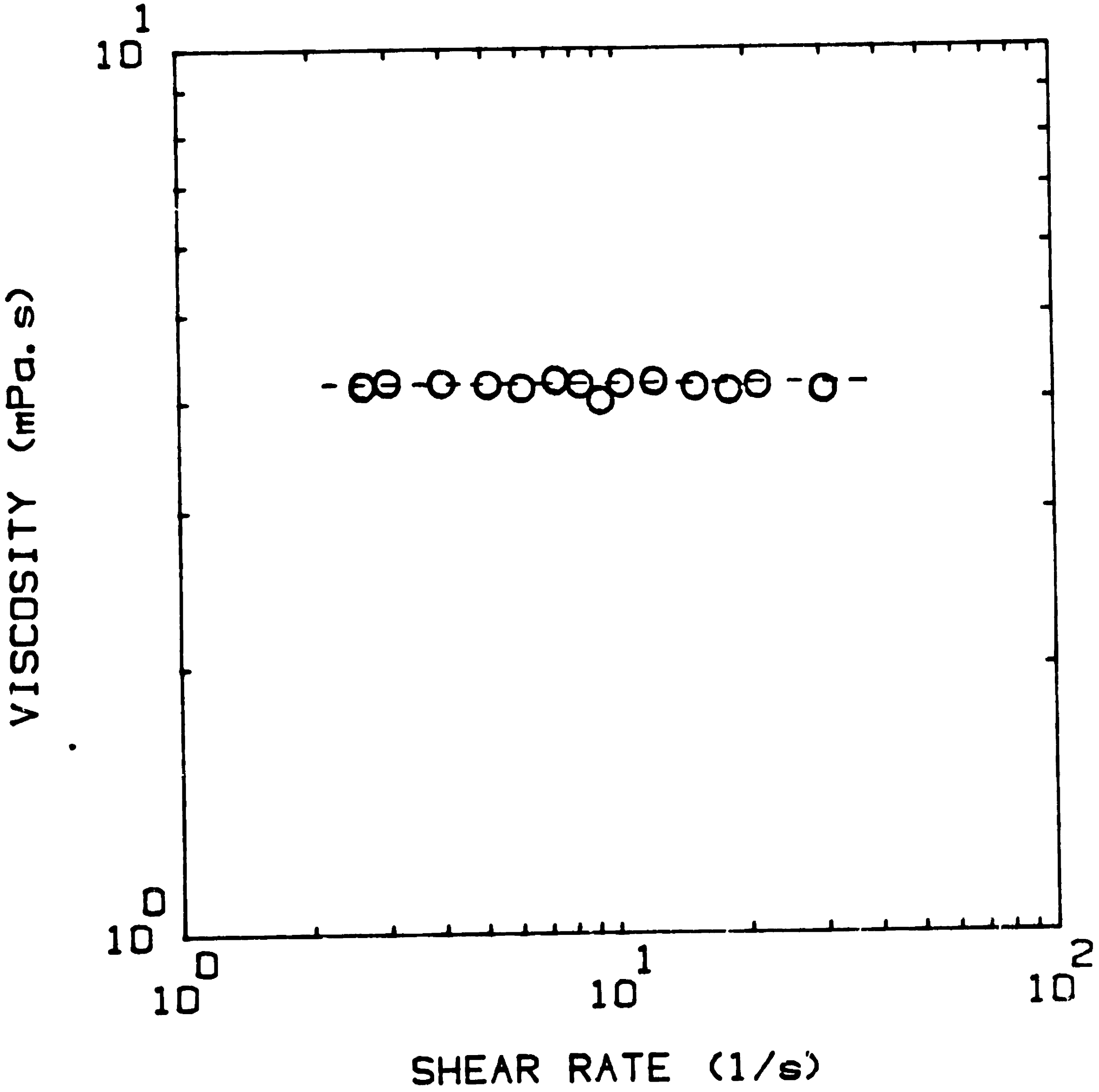

Figure VI-2 Viscosity of surfactant solution as a function of shear rate. Formulation of solution is given in Table V-1.

Couette viscometer, was found to be about 5 mPa.s. Thus the foam viscosity is significantly higher than that of the surfactant solution.

The plot also reveals two other things. First, the viscosity is influenced by the gas volume fraction, a higher gas fraction resulting in an upward shift of the viscosity-shear rate curve. Secondly, all curves are linear and have slopes very close to -1. This suggests that foam has a yield stress and all our experiments were done around this region. Hence, in this shear rate regime, the yield stress dominates the viscosity of foam.

2. Yield Stress

Indirect confirmation of the presence of yield stress comes from Figure VI-3 where we have replotted the previous data in terms of viscosity versus shear stress. We observe here that the viscosity of foam is approaching an infinite value at a certain stress. This corresponds to the yield stress.

We also find the yield stress (τ_y) to be higher for a larger gas volume fraction. This is because with increasing gas fraction the foam cells become more polyhedral in structure. Consequently, larger stresses are required for the cells to hop past (yield point) one another. The same trend is reflected in the viscosity data (Figure VI-1) because viscosity is dominated by the yield stress.

Direct measurements of the yield stress were obtained using the stress relaxation technique described in Section V-B. Figure VI-4 shows the yield stress as a function of shear rate for two different gas fractions. As should be the case τ_y is independent of $\dot{\gamma}$. Further, the values of

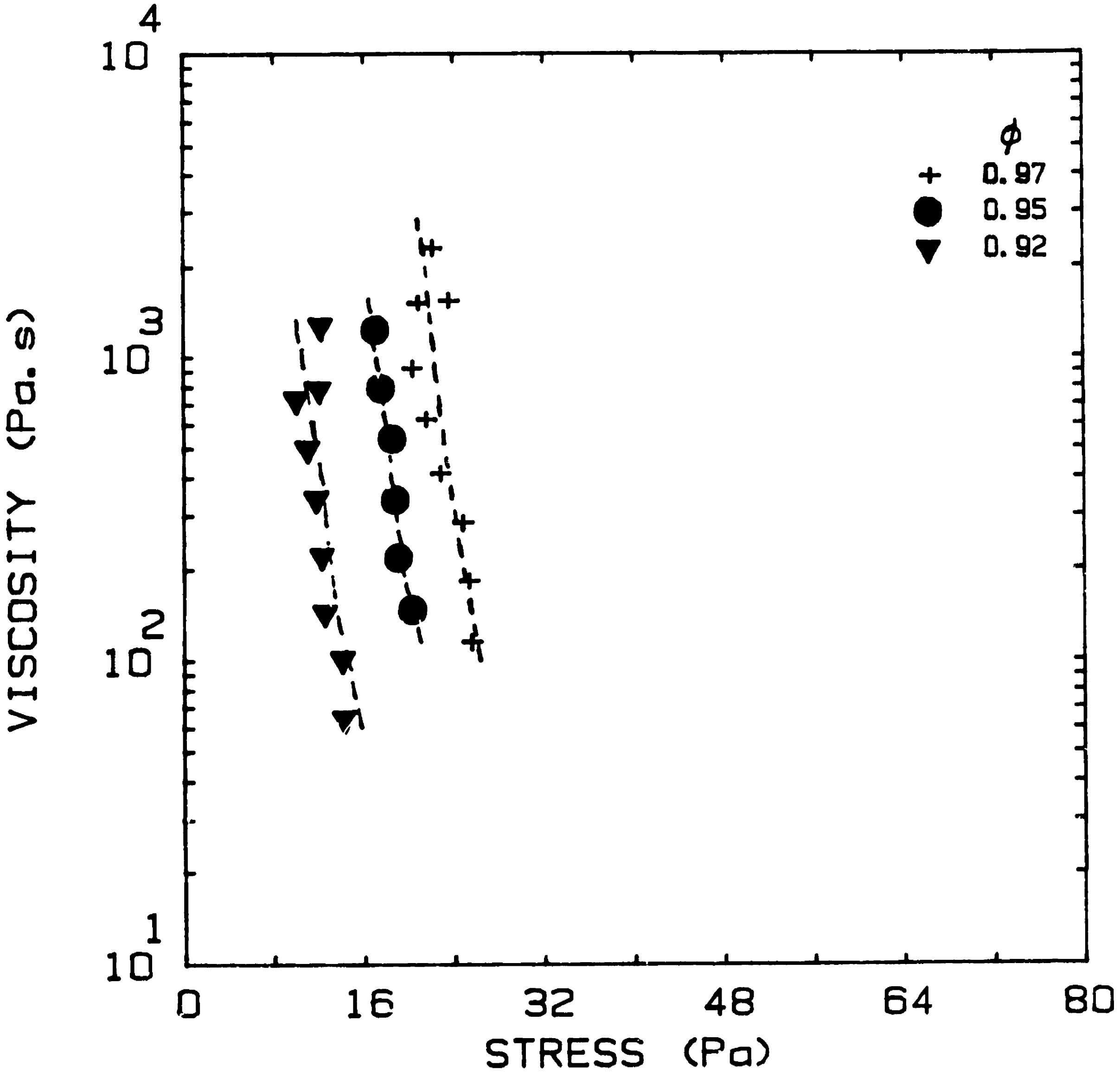

Figure VI-3 Viscosity versus shear stress plots reveal presence of yield stress in foam.

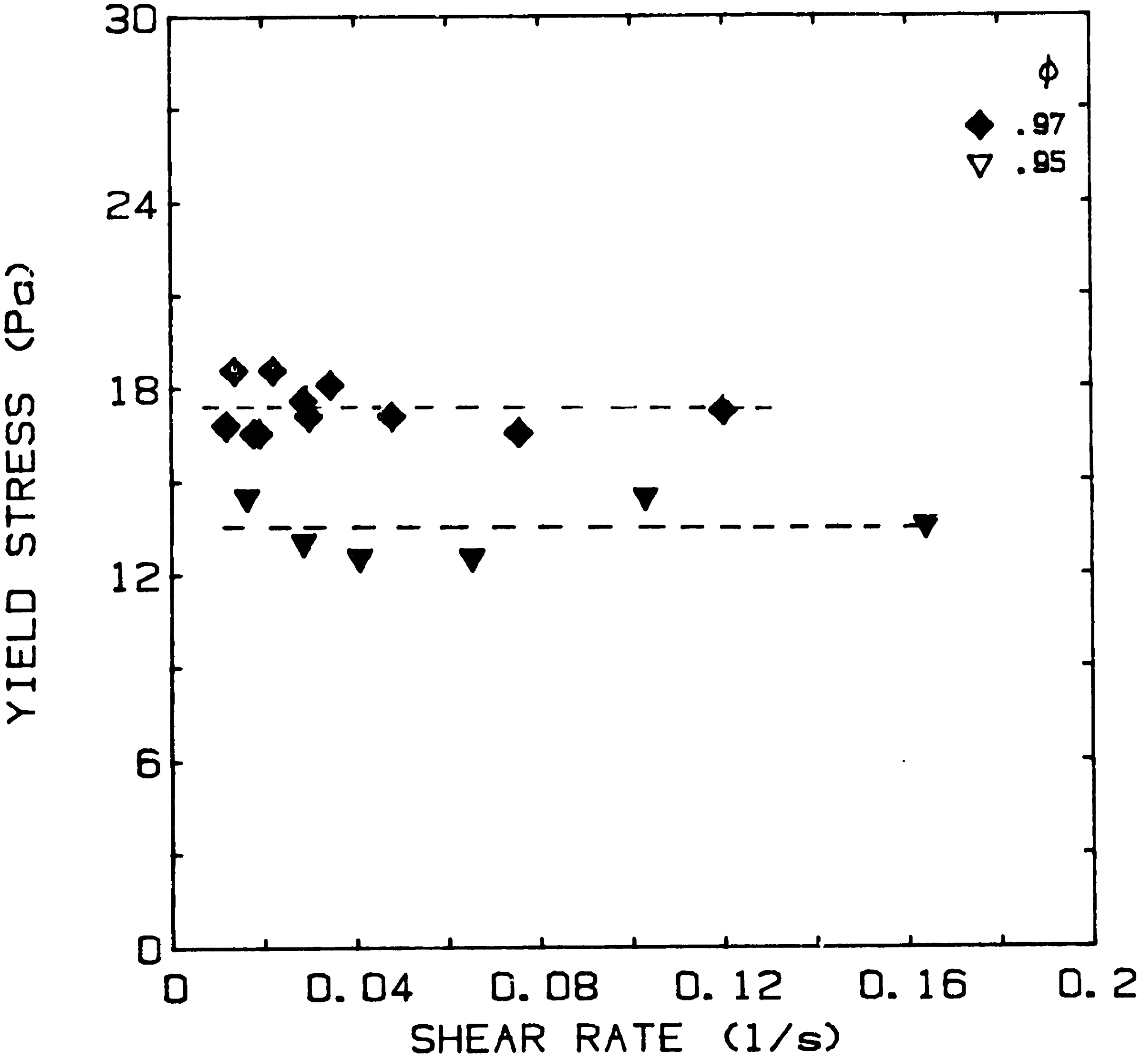

Figure VI-4 Measurement of yield stress using Stress Relaxation technique. The stresess are independent of shear rate as it should be.

the yield stress (13.5, 17.5) for the two gas fractions agree reasonably well with the corresponding ones obtained by extrapolating the viscosity-shear stress data (13, 18). It may be mentioned here that this method fails at high shear rates because of irreversible breakdown of foam structure. We, therefore, started our experimental runs at the lowest possible shear rate of the machine and worked our way upwards. As can be seen from the plot, the structure was stable for a fairly large shear rate range.

3. Elastic and Loss Modulus

The elastic (G') and loss (G'') moduli of foam were found from the small amplitude oscillatory shear experiments. Initially, a strain sweep was made keeping frequency, ω, constant at 2.5 rad/s. This is shown in Figure VI-5. We found the moduli to be fairly constant for strains up to 15% indicating that the material was linearly viscoelastic in this region. Next, the effect of frequency was studied keeping strain constant at 9.6%. Figure VI-6 shows plots of G' and G'' as a function of frequency for three different gas volume fractions. One can observe that the moduli are flat and fairly invariant with frequency which is typical of highly elastic materials. Further, the storage modulus in all cases was larger than the loss modulus by a factor of 5. Confirmation of the strong elastic nature of foams was found by plotting strain and the corresponding stress in the material as a function of time. Figure VI-7 shows such a plot where the strain has been normalized with respect to the maximum torque value. The thing to note from this plot is that the torque (stress) and position (strain) are almost in phase with each other. Thus, based

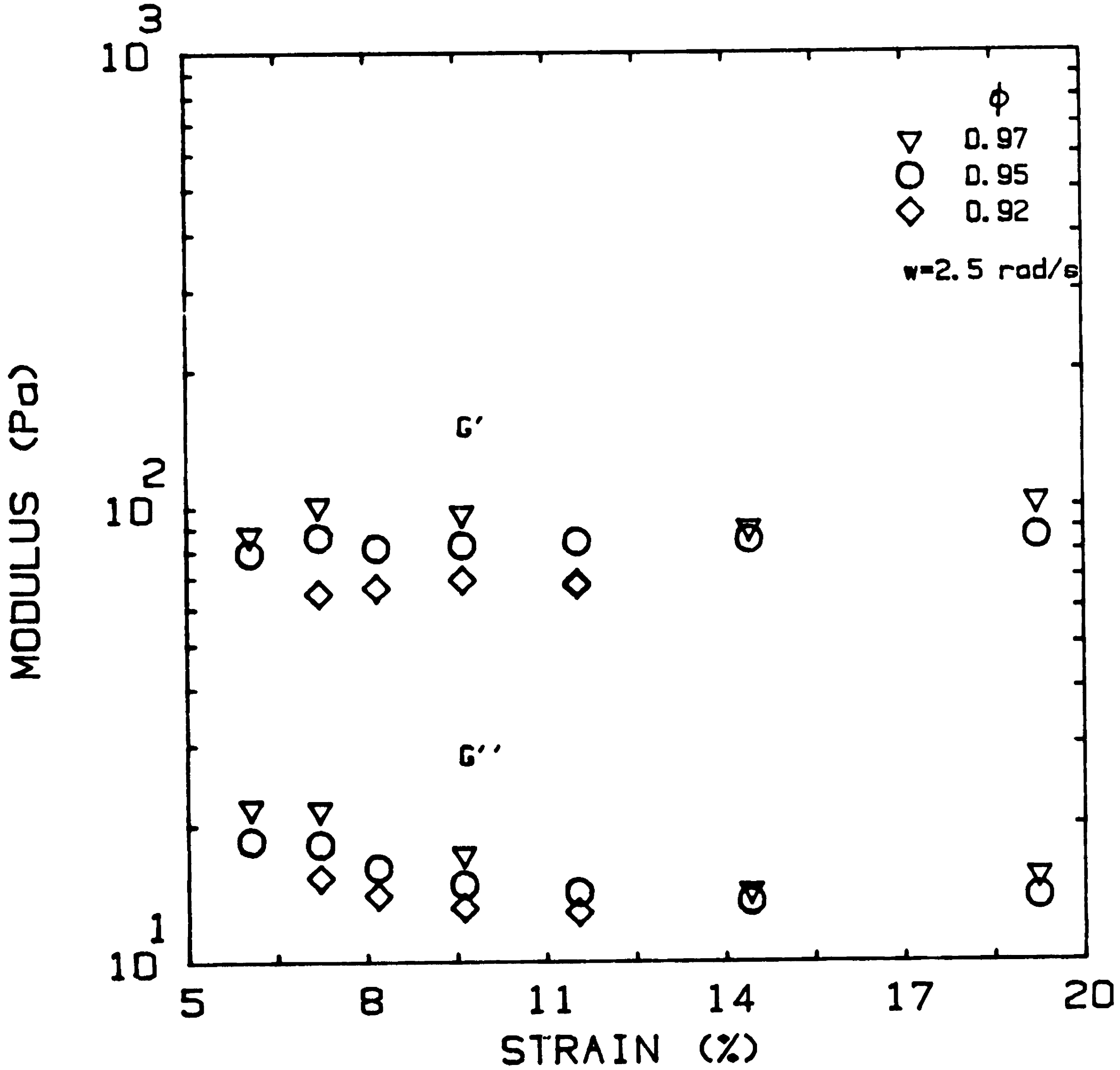

Figure VI-5 Elastic (G') and Loss (G'') Modulii of foam as a function of strain. The material is linearly viscoelastic for strains up to 18.

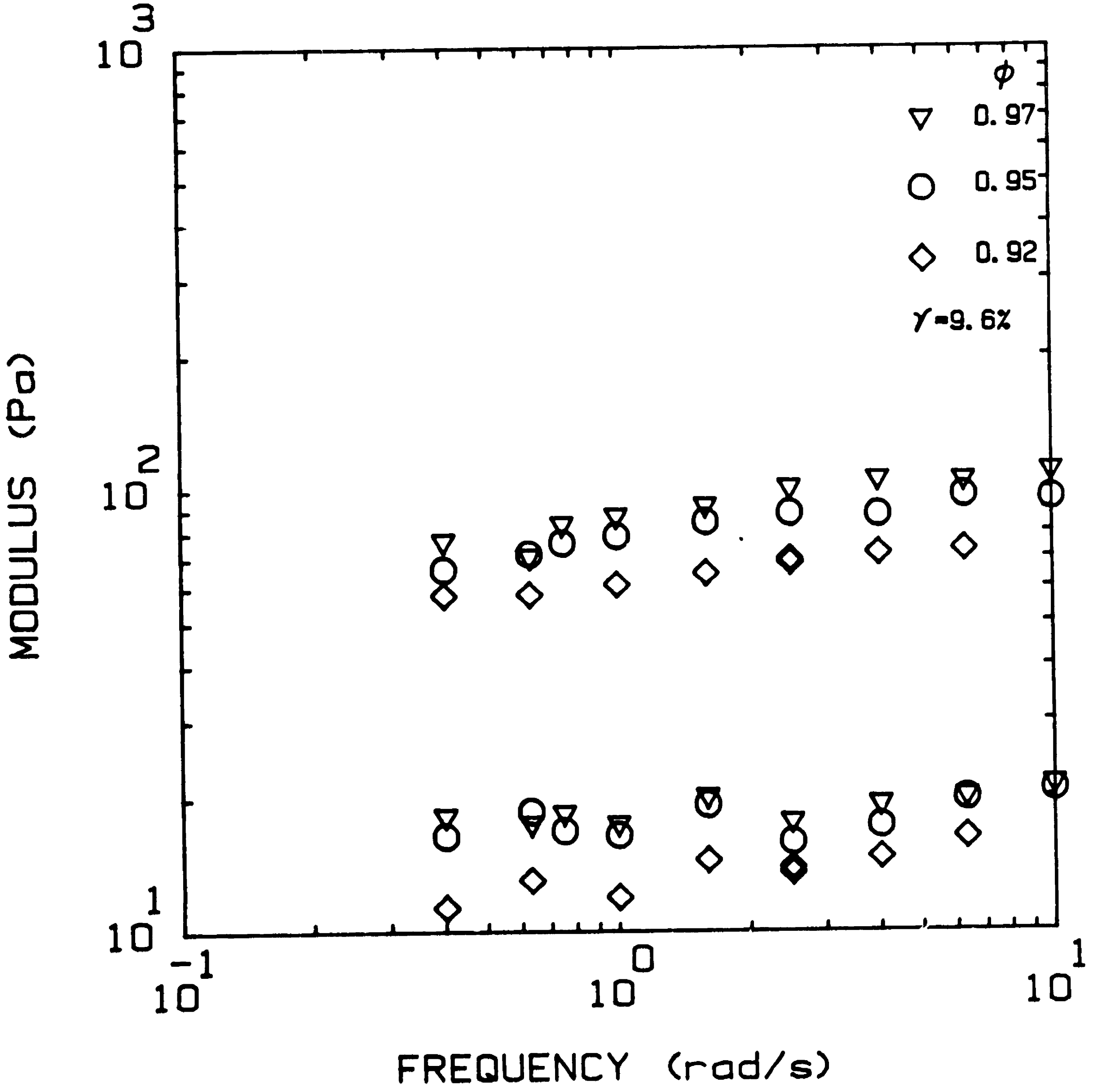

Figure VI-6 Elastic (G') and Loss (G'') Moduli of foam as a function of frequency for different gas factions.

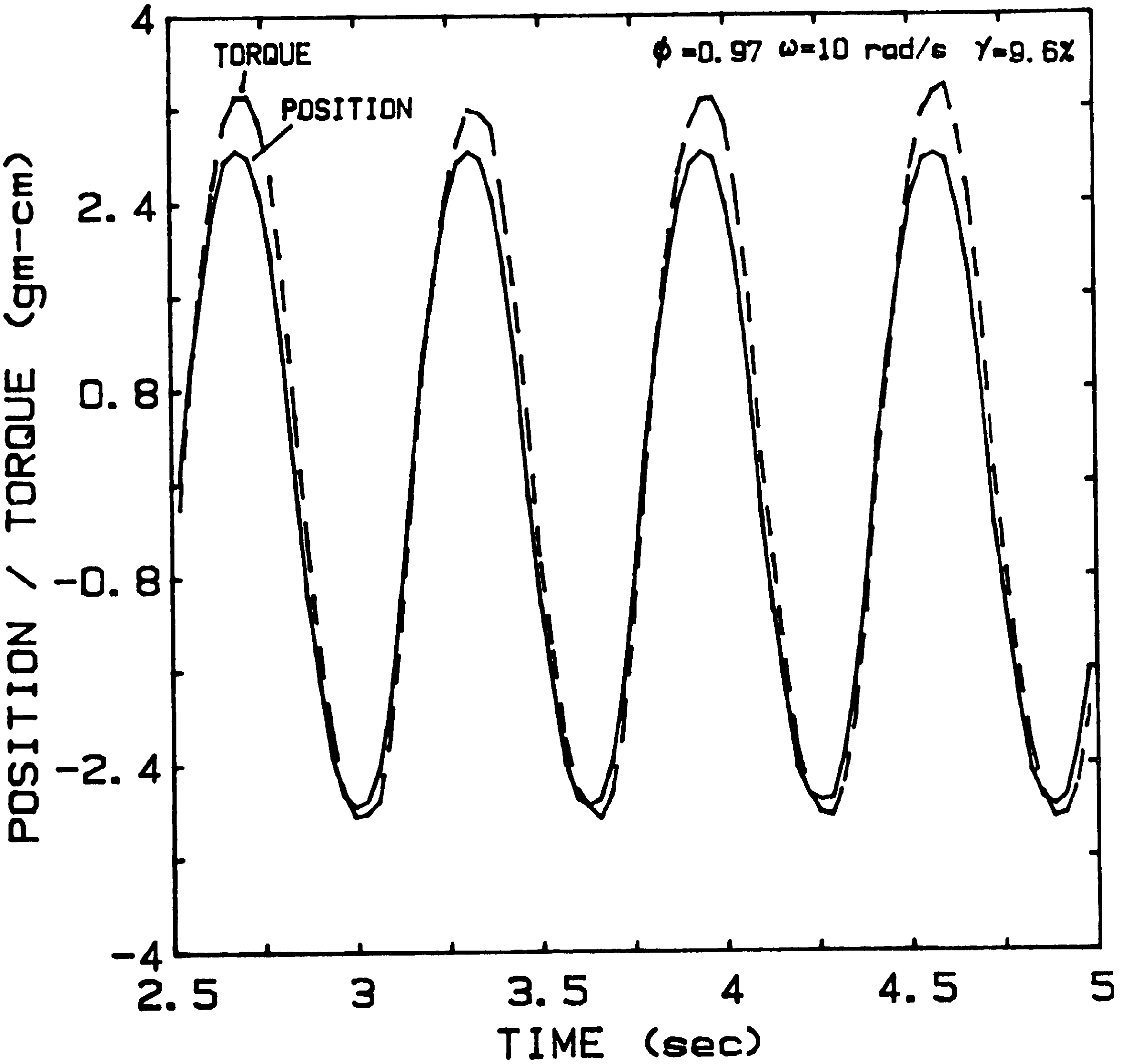

Figure VI-7 Position input and Torque output in an oscillatory shear flow experiment. Note that the two are almost in phase with each other.

on viscoelastic theory (Equation V-4), the response of foam to small oscillatory deformation is essentially elastic. The same trend is observed for different strain and gas fraction values as depicted in Figures VI-8 through VI-10.

4. Transient Viscosity

In Figures VI-11 through VI-13 are plots of transient viscosity, η^+, versus strain for three different gas fractions. Each run was made at a constant shear rate. The effect of shear rate on η^+ was studied by keeping gas volume fraction constant and running the experiments at three different shear rates. Each of the figures shows this. We find that the steady state viscosities approached are dependent on the shear rate, a lower shear rate giving a higher steady state value. This is expected because of the shear thinning behavior of foam.

The plots also reveal that the stress or viscosity overshoots are fairly small in foam. Figures VI-14 through VI-16 show normalized plots of transient viscosities over the corresponding steady state viscosities as functions of strain. Note that these curves also correspond to the normalised shear stress. We find that for a specific gas fraction, data for different shear rates collapses into a single curve. Further, in all cases the overshoot is no greater than 15% of the steady state value. In Figure VI-17, we compare the normalized stress curve for two different gas fractions. .92 and .97, for the same shear rate. Although the curves are very similar in shape, the maximum stress and the corresponding strain are slightly larger for the higher gas fraction (0.97) case.

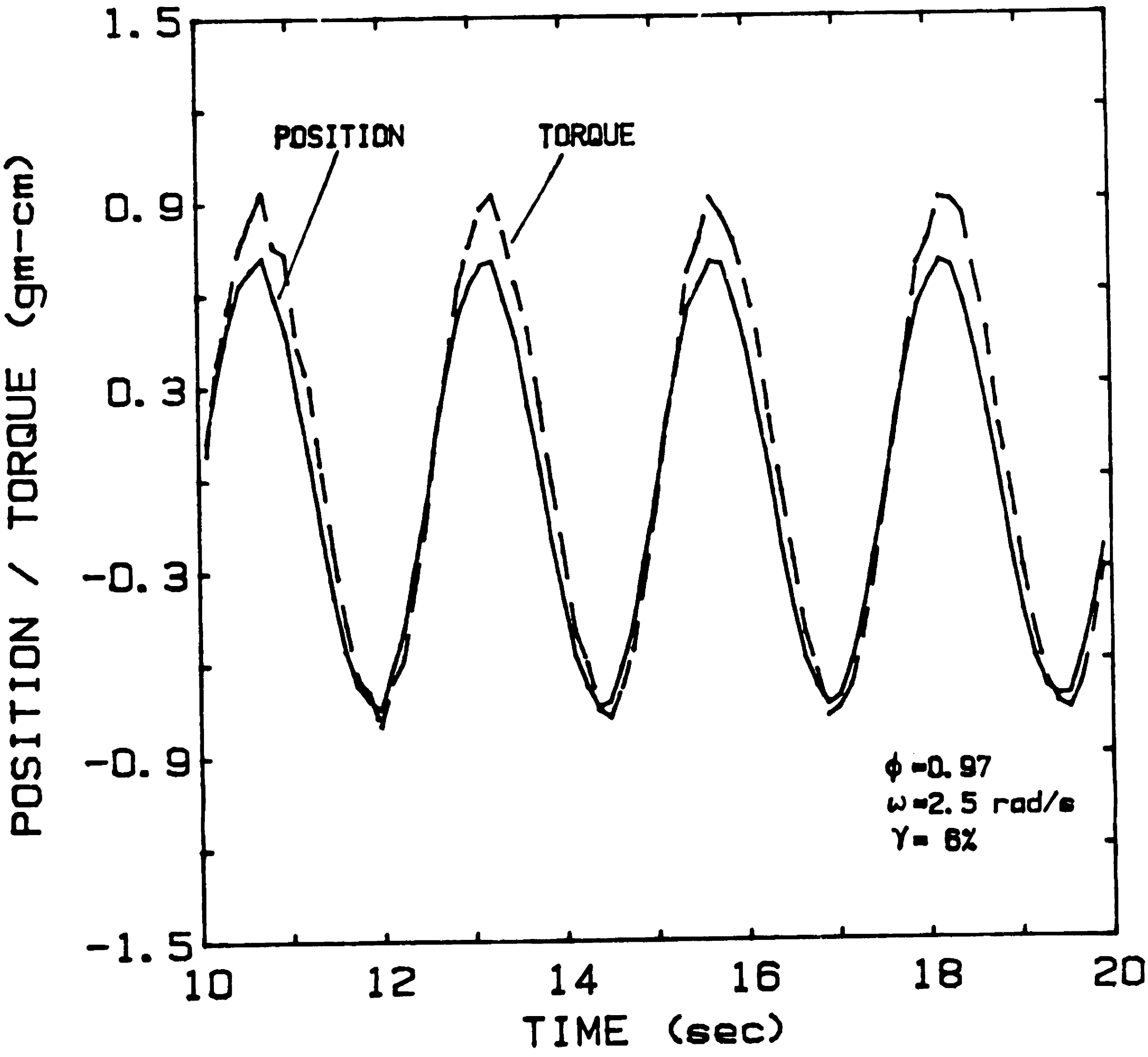

Figure VI-8 Normalized position (strain) and torque output in a dynamic experiment. γ=strain. ω is the frequency of oscillation.

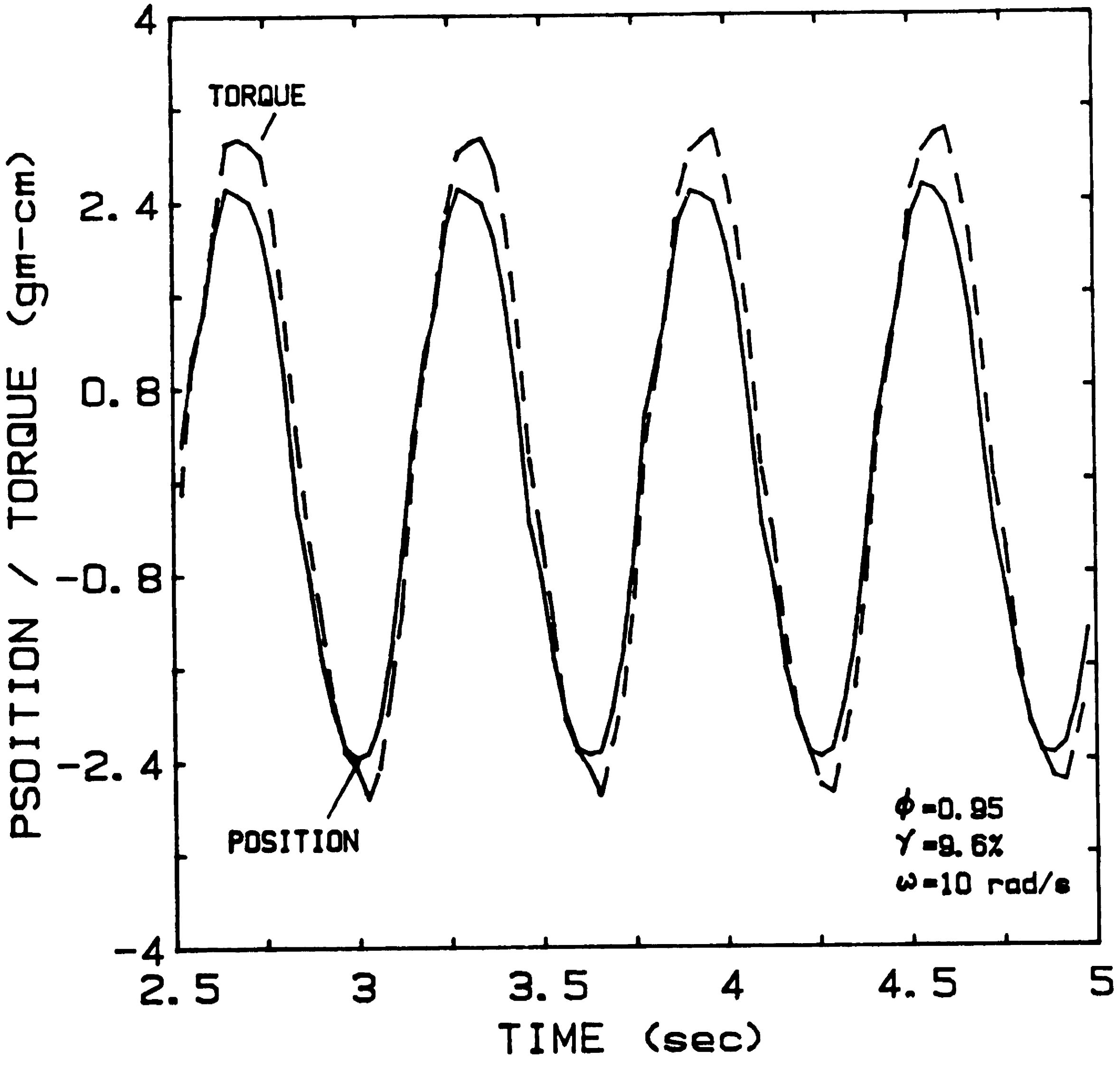

Figure VI-9 Position and torque as a function of time for 0.95 gas fraction foam. ω, γ are the frequency and maximum strain of oscillation.

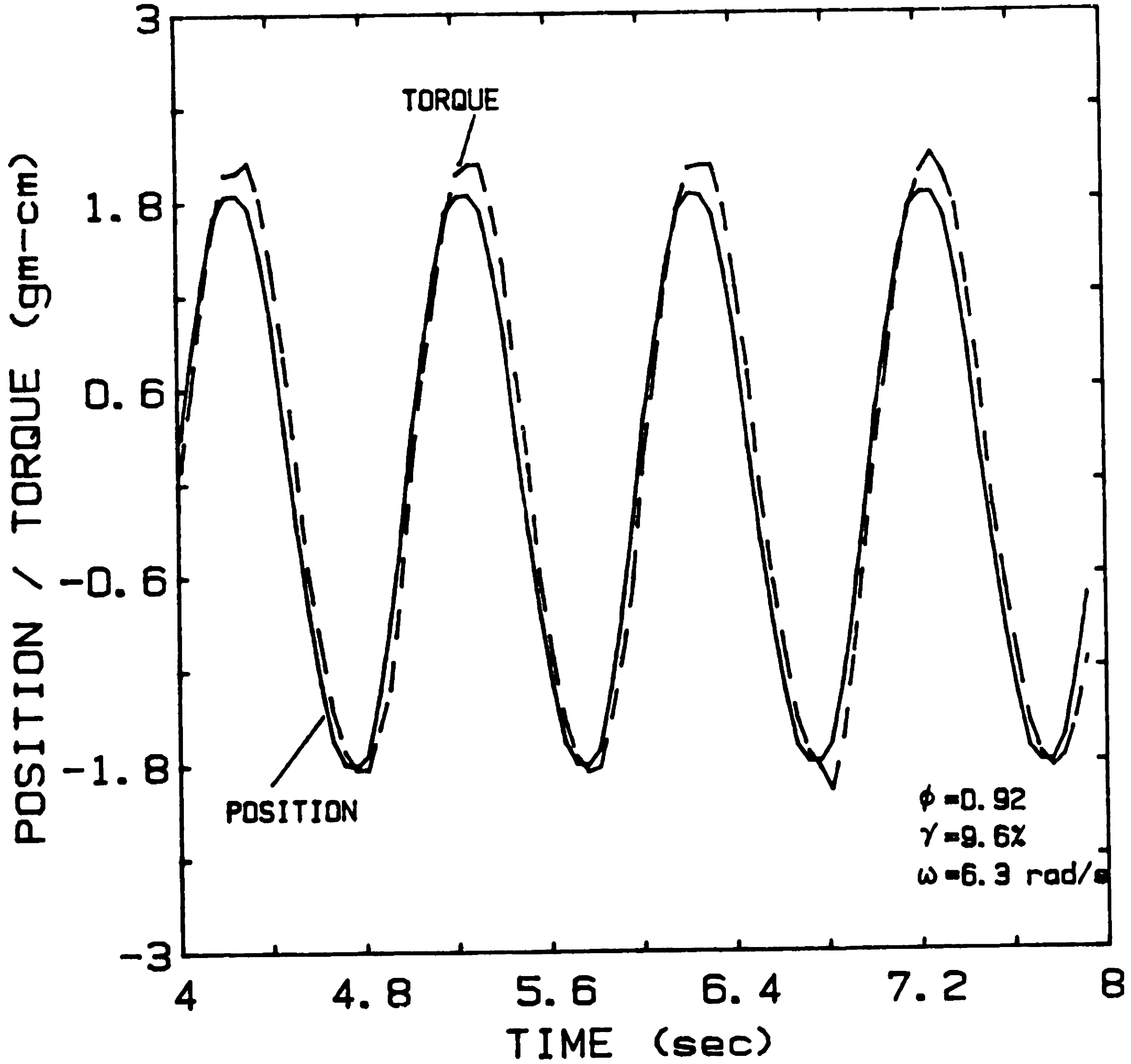

Figure VI-10 Torque and position as a function of time for 0.92 gas fraction foam. ω=frequency of oscillation. γ=strain.

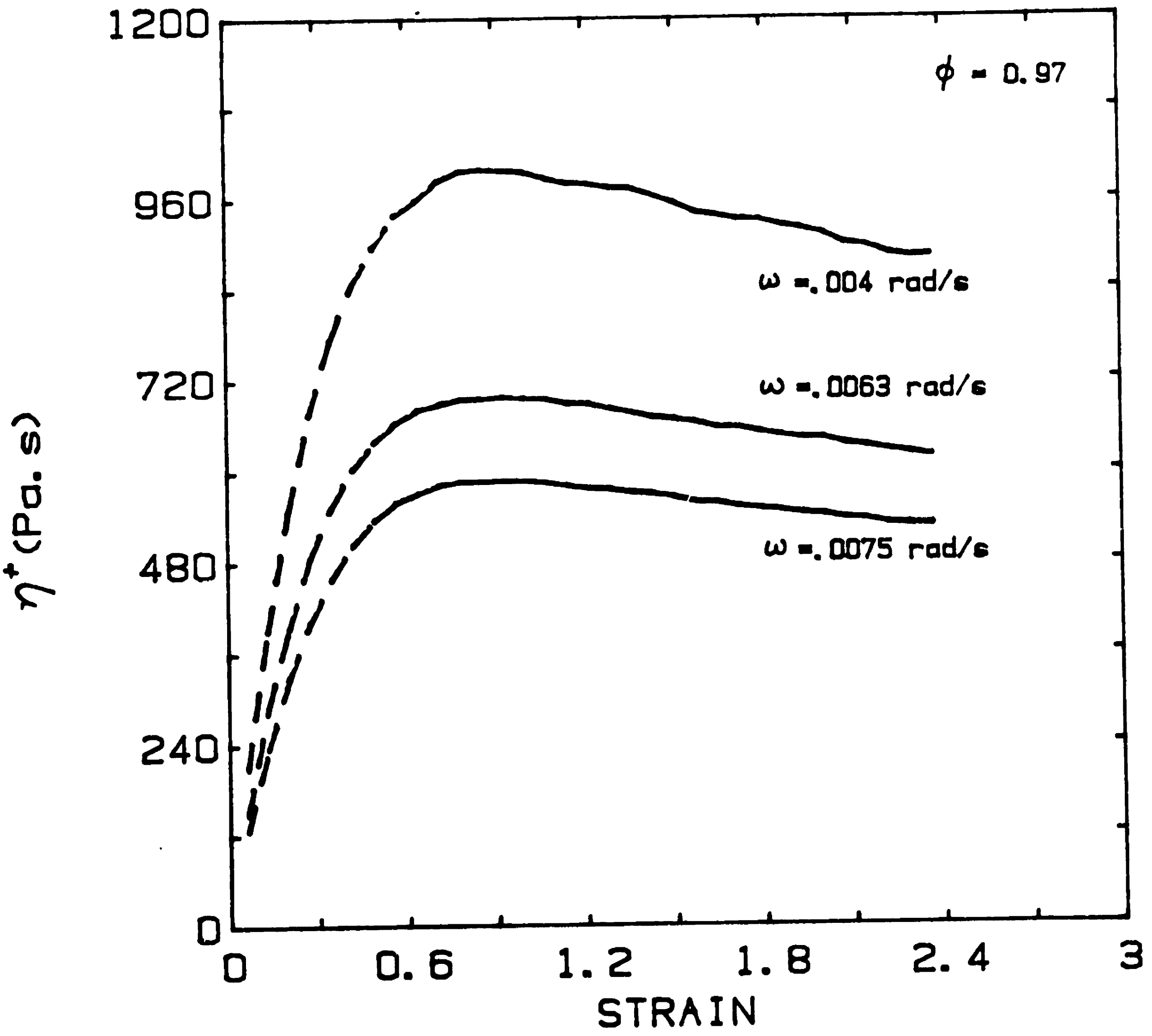

Figure VI-11 Transient viscosity as a function of strain. ω is the rotation rate of the upper plate. ϕ=gas fraction.

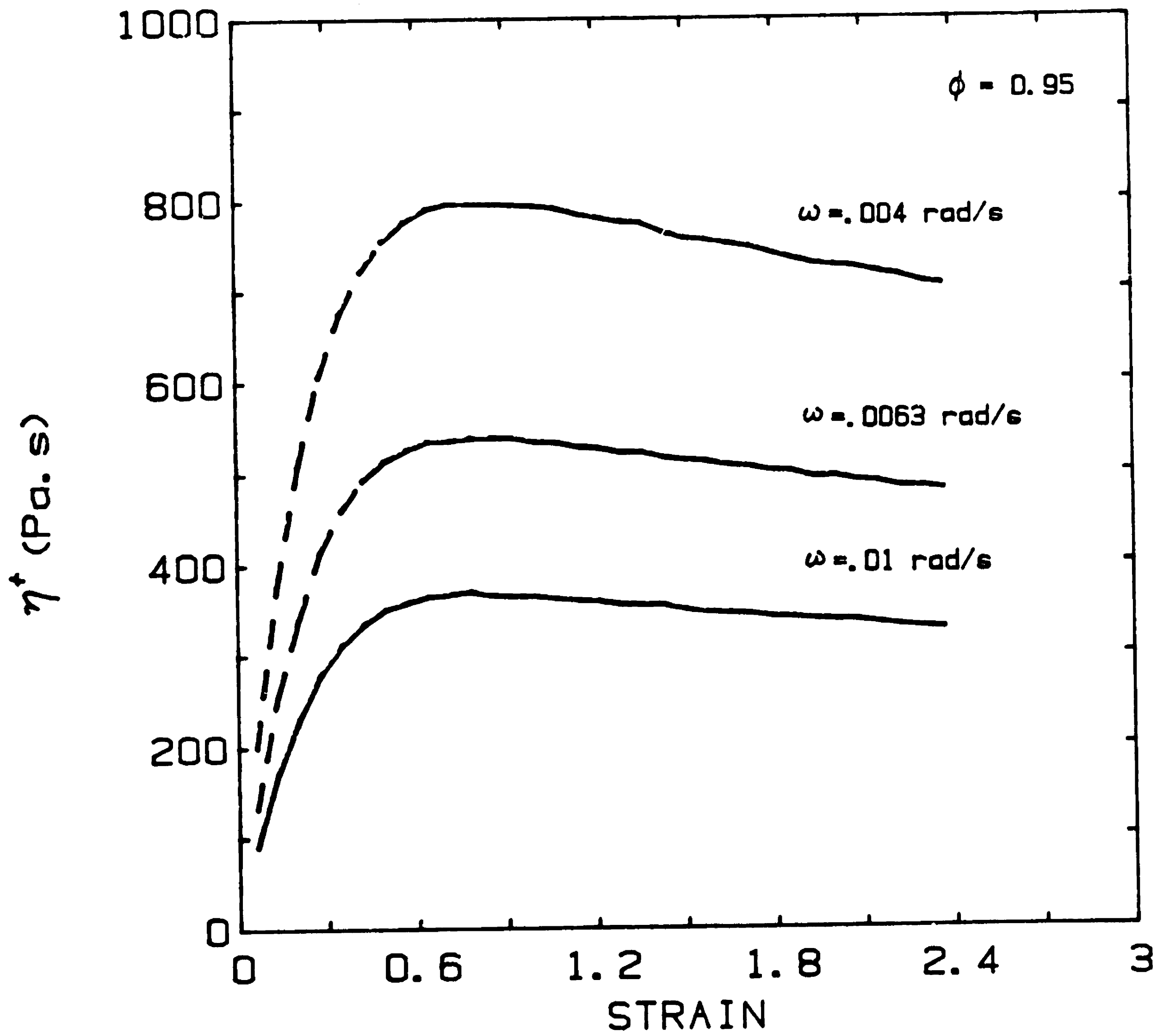

Figure VI-12 Transient viscosity as a function of strain for 0.95 gas fraction foam. ω is proportional to shear rate.

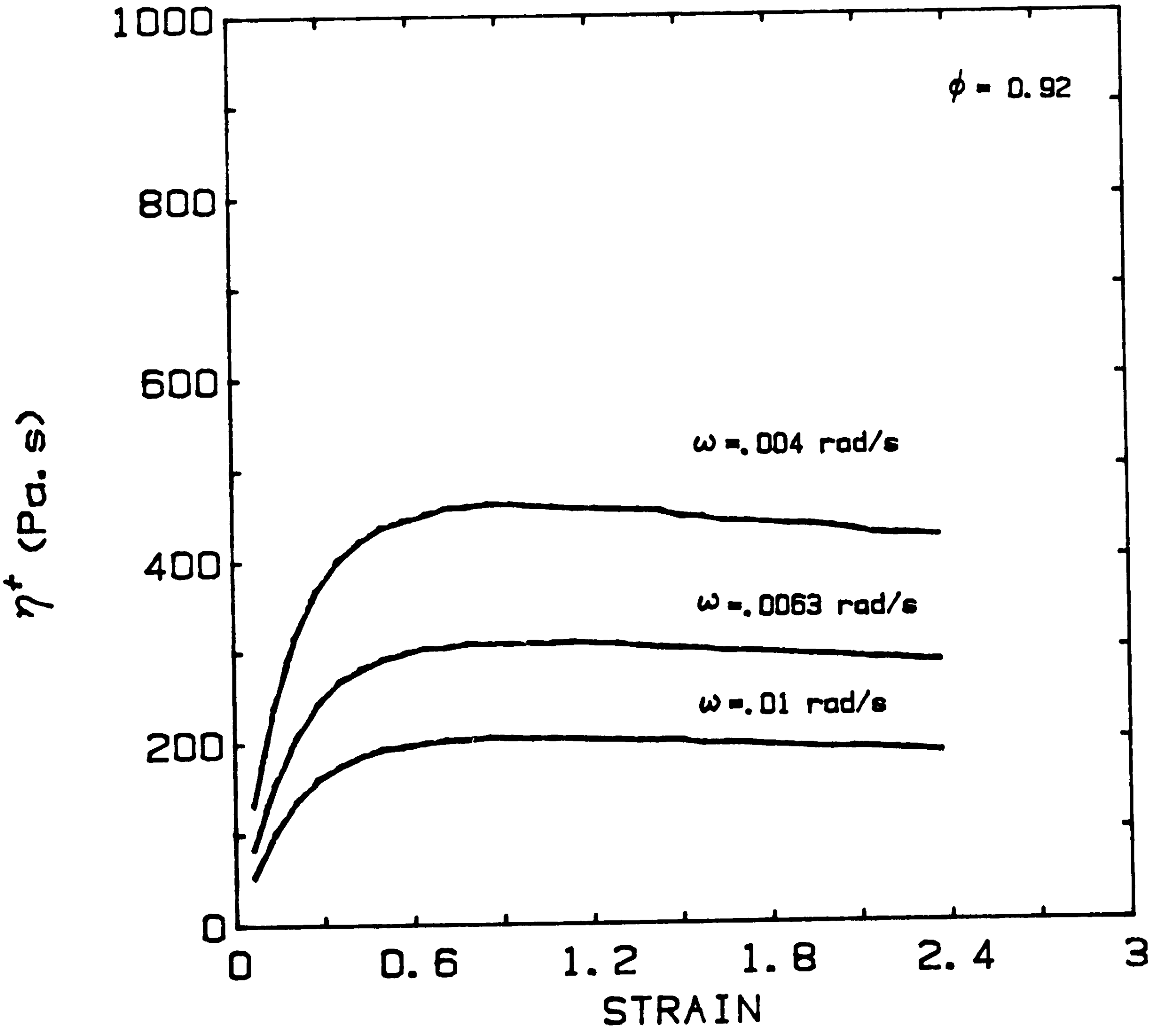

Figure VI-13 Transient viscosity of foam for different shear rates, ω. ϕ=gas fraction.

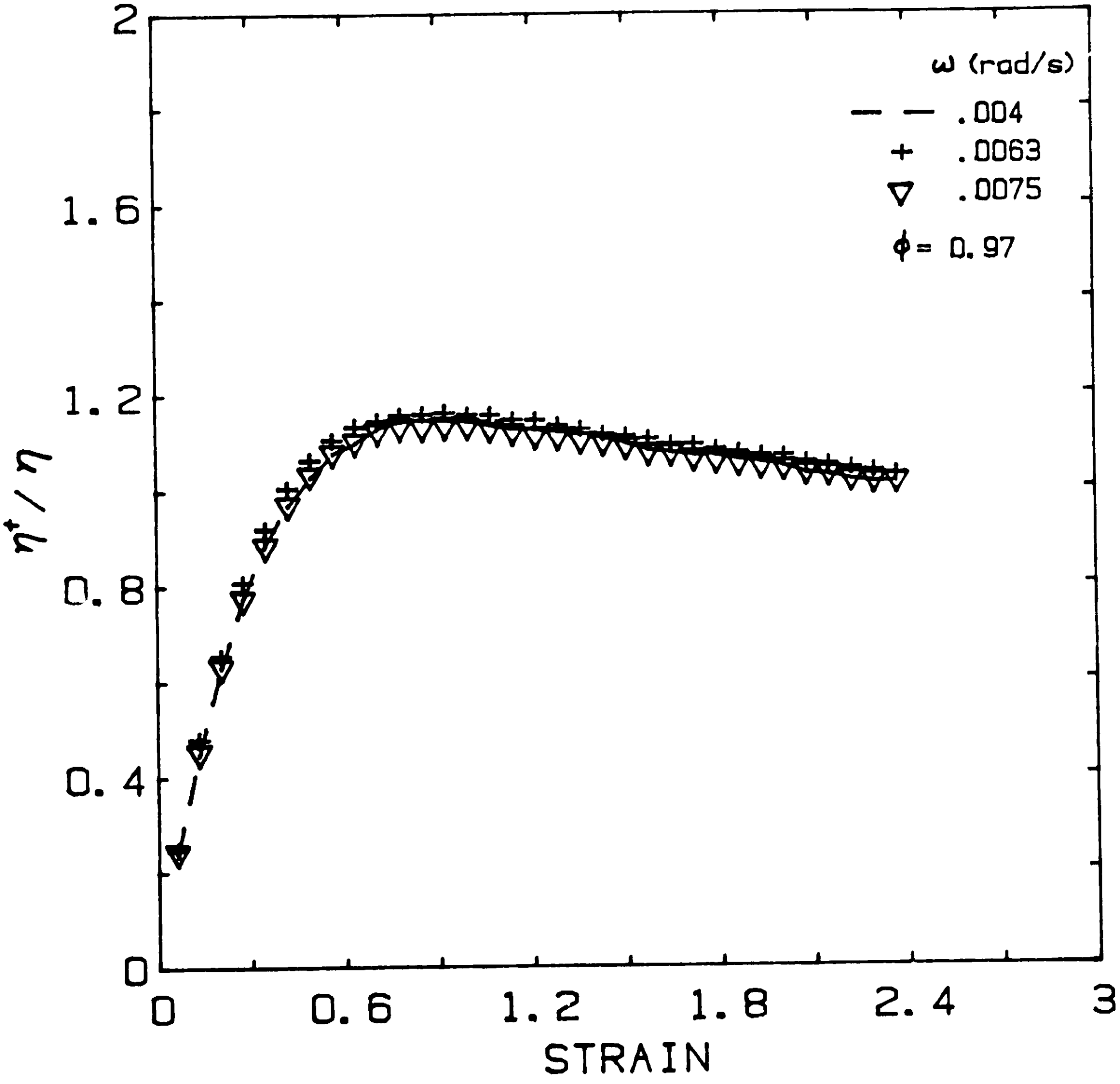

Figure VI-14 Normalized transient viscosity for three different shear rates. ω is proportional to shear rate. η is the steady state viscosity.

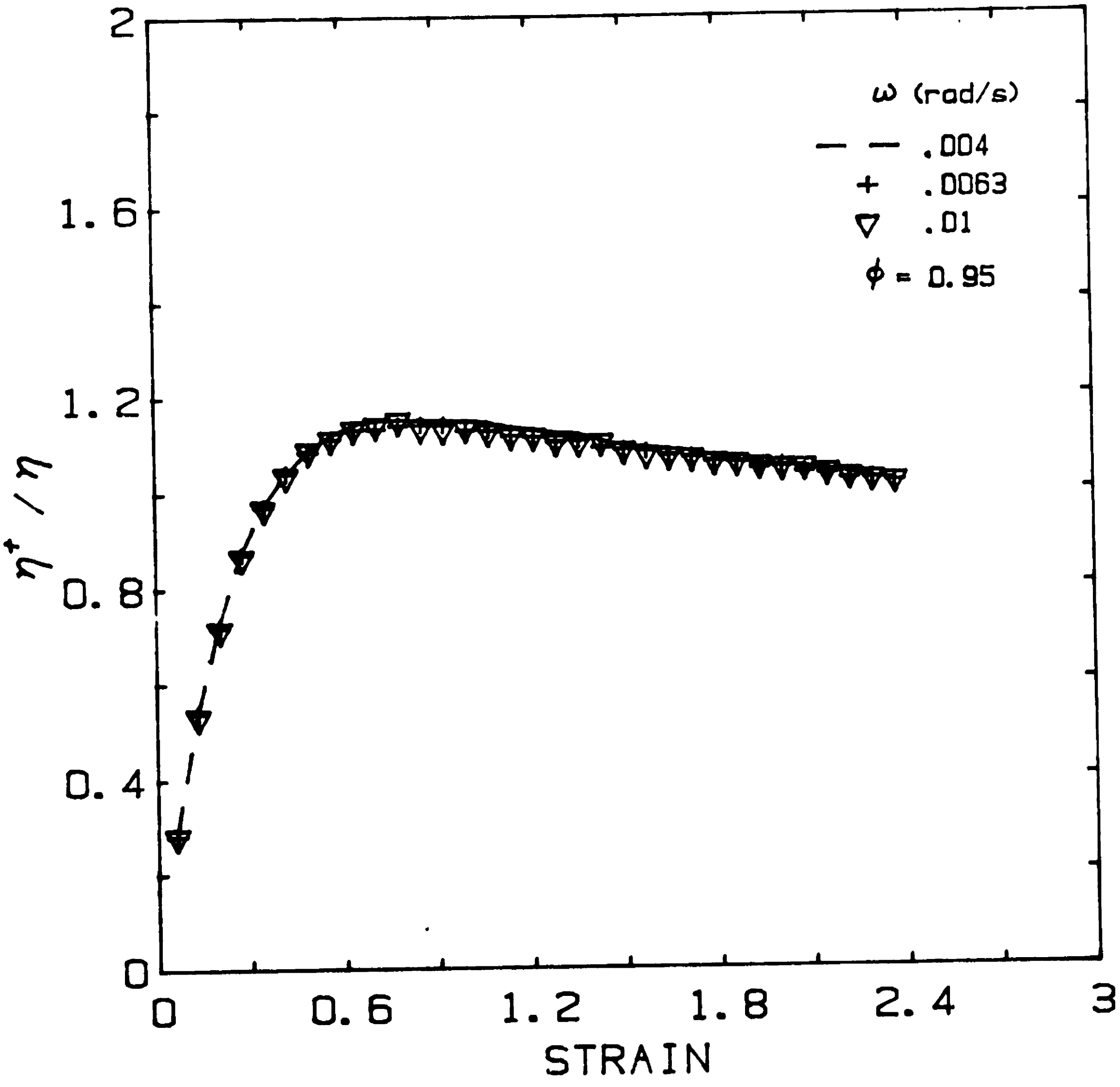

Figure VI-15 Normalized transient viscosity for 0.95 gas fraction foam. η is the steady state viscosity. ω is proportional to shear rate.

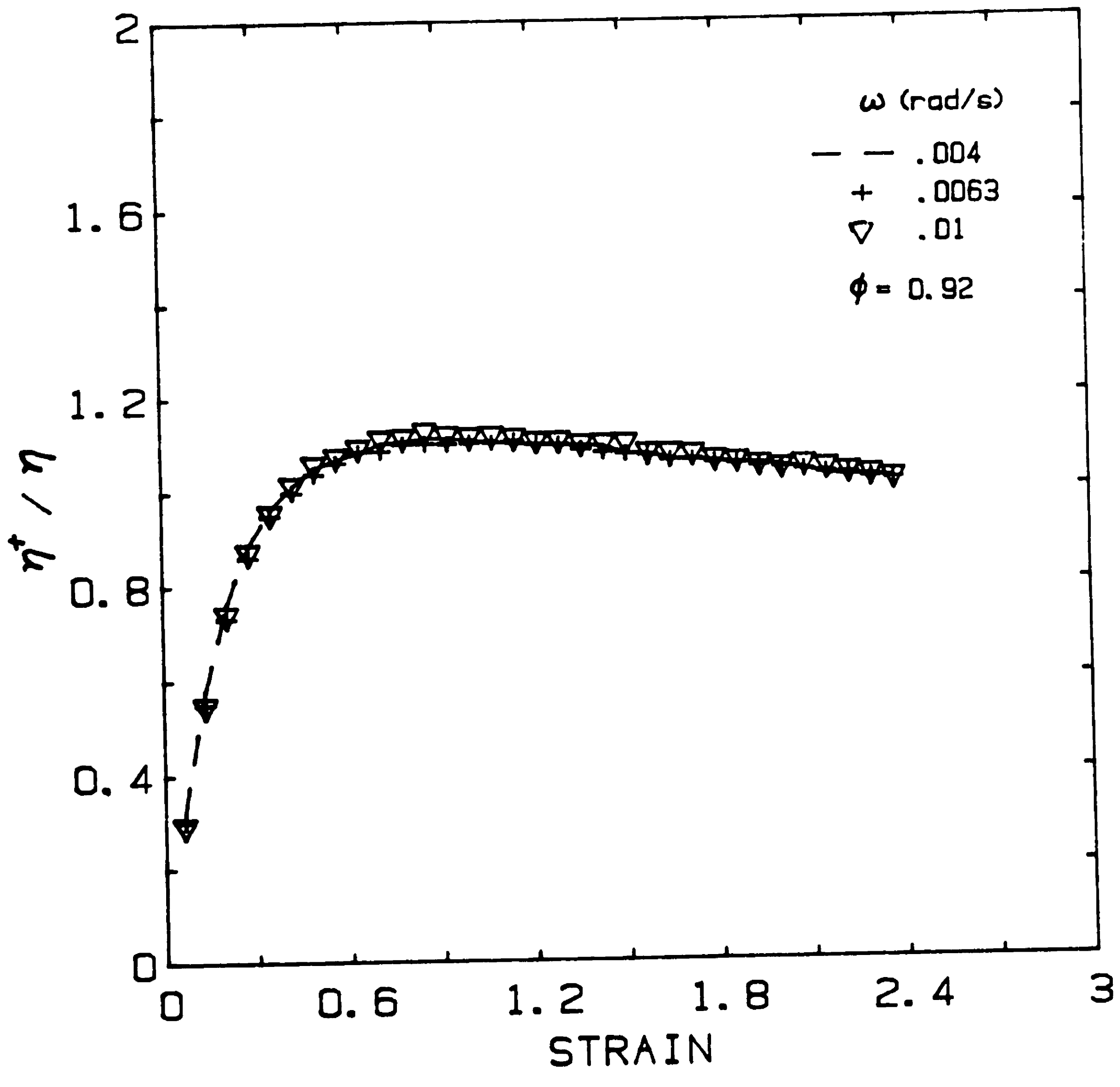

Figure VI-16 Normalized transient viscosity vs. strain for 0.92 gas fraction foam.

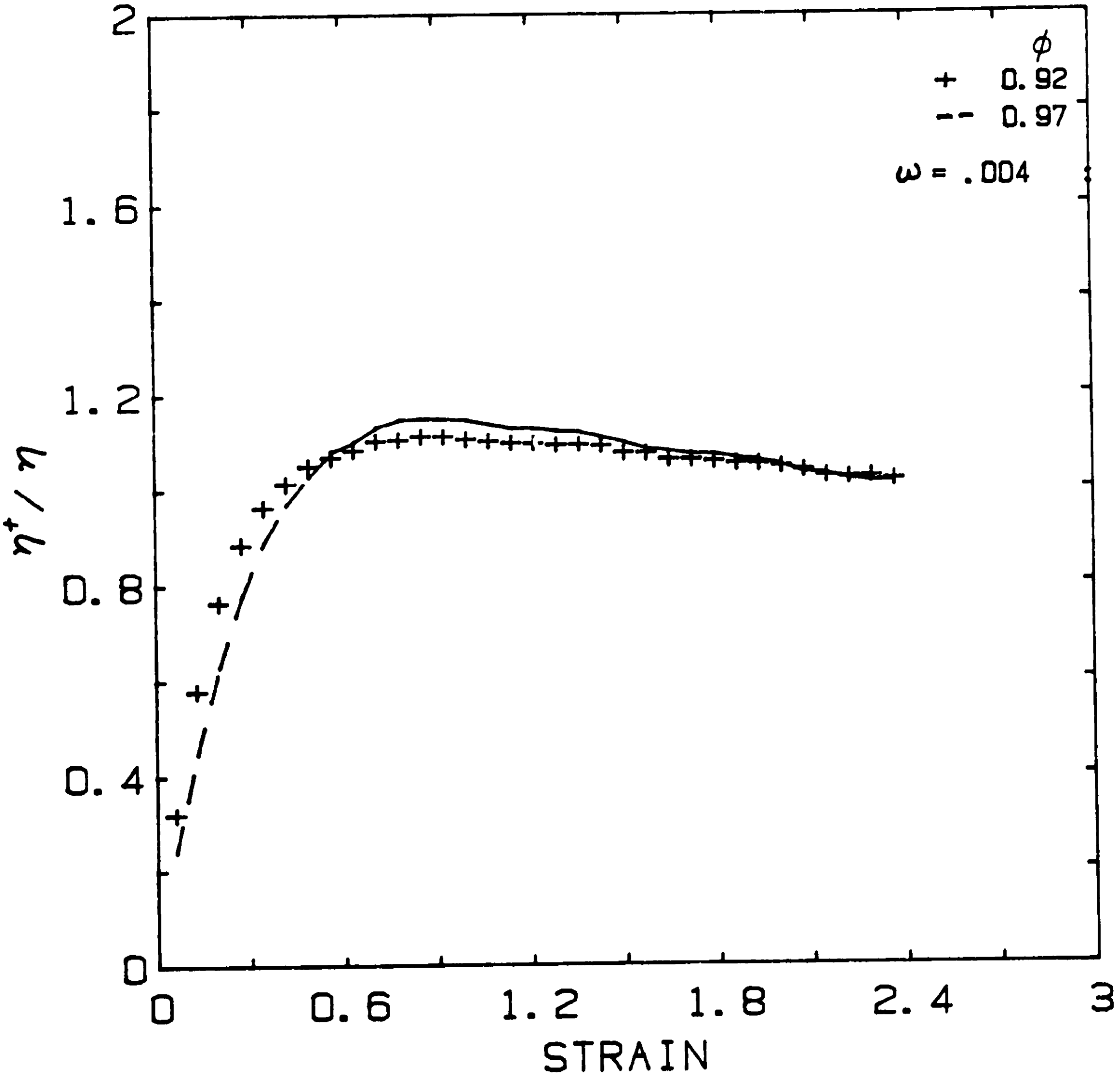

Figure VI-17 Normalized transient viscosities of two different gas fraction foams. ω is proportional to shear rate. Note that overshoot and corresponding strain are slightly larger for the higher gas fraction.

B. DISCUSSION

In this section some of the experimental problems encountered in working with foams are discussed. Physical insights into the experimental results are also provided. Finally, the predictive and interpretive ability of the theoretical model is compared with the measured quantities.

1. Steady Shear Experiments

In Figure VI-1, the viscosity of foam has been plotted. As can be observed, the viscosity goes down with increasing shear rate with a slope approximating -1. This shear thinning effect should not be confused with the power law behavior typical in polymeric materials. Foam has a yield stress and all our data had been taken around the yield point. Thus, the shear stress have been fairly constant for each of the runs. This yield stress effect is reflected in the powerlaw behavior of foam with a power law index very close to zero.

As has been mentioned before, η goes up with increasing gas fraction. This is so because the yield stress increases with larger gas fraction. This becomes clear when one looks at two dimensional foam structures shown in Chapters II-IV. With increasing gas volume fraction, the cells become more stuctured and polyhedral and it takes a larger force for the cells to go past one another. At high shear rates too, one should expect ϕ to influence viscosity. In this regime the viscous dissipation in the foam films become important. This dissipation depends on the thickness of the liquid films and Plateau border which in turn are clearly related to ϕ.

In Figure VI-18, the dry foam model prediction has been compared

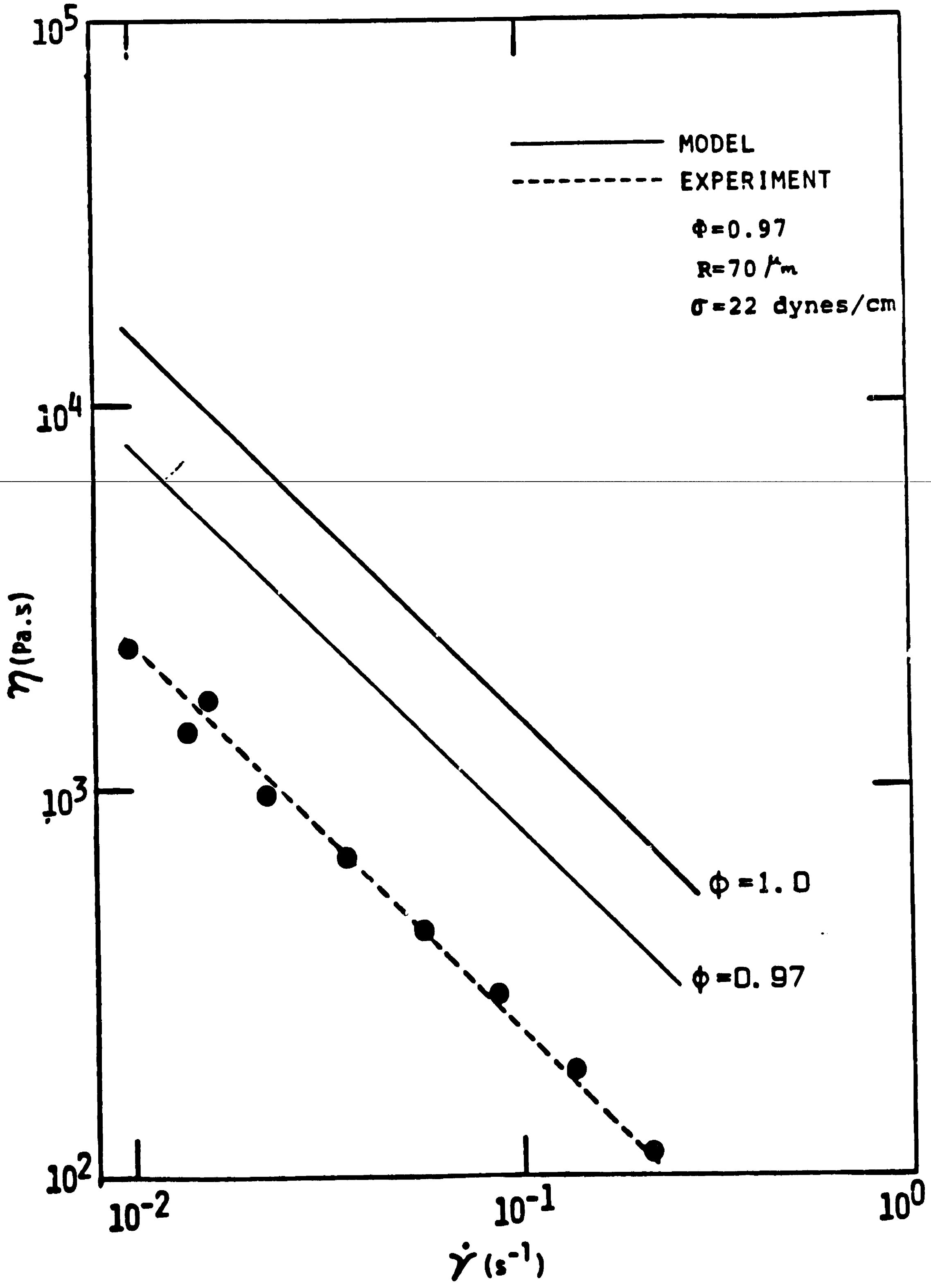

Figure VI-18 Viscosity as a function of shear rate. Model prediction for $\phi=1$ and $\phi=0.97$ are compared with data for 0.97 gas fraction foam. R=average bubble radius; σ=interfacial tension.

with the .97 gas volume fraction foam data. We find the model to give the correct trend but overpredicting the data by a factor of six. Also shown in the plot is the prediction of the more refined model with finite liquid content (3% in this case). As expected the discrepancy is reduced to a factor of 3. Considering the fact that the models are two dimensional, neglect cell growth, film drainage and have some limitations in terms of explaining cell reformation, we consider the agreement very good. As a mean to interpret data they are even better. Although our calculations show that a "bidisperse" system does not affect the yield stress and consequently the viscosity at low shear rates, we feel that randomness along with polydispersity could also account for some of the differences between model and experiment.

In calculating the model prediction the measured surface tension, average cell diameter and liquid viscosity were used. However, only the yield stress part of the Equation II-44 was used to calculate the viscosity. This is because the film dissipation term, $C_1(\phi)\mu_L$, is negligible in this shear rate regime. The viscous force effects, calculated in Chapter III, are also negligible and therefore the equlibrium model based on the 120 degree criterion could be used.

It would be interesting to compare the model prediction with experiments at high shear rates. Unfortunately, the foam structure breaks down in this region. This, along with film drainage, is a major problem in experimenting with foam. One possible way to do such experiments would be to use a liquid-liquid emulsion and a modified Couette device or the parallel plate device. By using liquid emulsions one would reduce cell breakage and the driving force for drainage considerably. Problems associated with the parallel plate device at high shear rates, such as the sample coming out of the gap, could also be avoided by using a couette geometry. One could also reduce the gap between the parallel plates and increase shear rate without increasing inertial effects.

Although we have done steady shear experiments, we did not report any normal stress data. This does not imply the absence of normal stress in foams but rather our inability to measure them. The problem in trying to measure the normal stresses in foam lies in the very long relaxation time of the material. When the foam is put between the parallel plates and the plates brought closer together, one inevitably has to squeeze the sample to properly fill the gap between the plates. This puts a normal force on the transducer. Because of the yield stress of the material, it does not relax back. Any measurements thus made are meaningless. This problem, which has also been encountered by Yoshimura and Prud'homme [1984], is more severe with the sand paper backed plates. Some efforts made to get qualitative readings without using sand paper so that the wall film helped in removing some of the residual stress, also did not prove successful.

It should be mentioned here that this residual stress did not affect our viscosity measurements. We verified this by running experiments at different residual stresses and observing the obtaining the same viscosity measurements.

2. Dynamic Experiments

In Figures VI-14 through 16, the normalized transient viscosity of foam has been plotted. As mentioned before, the three curves representing three different shear rates collapses into a single one when normalized. This indicates that the stress-strain reponse of foam is independent of shear rate. Thus, in a physical process such as injection or compression molding, the compression or injection rate would not be an important processing parameter provided the foam retained its structure. The invariance of η^+ with $\dot{\gamma}$ is typical of elastic materials and agrees very well with our model. The dry foam model assumes the foam to be primarily elastic when strained and give a non-linear stress-strain expression (Equation II-24). In the experimental plot, at very small strains the material is linearly elastic but with increasing strains non-linear effects become important. Similar behavior is predicted by the model (Figure II-6). Thus, in terms of interpreting non-linear response of foam, the model is good. However, the model fails to account for the observed stress overshoot.

Usually, in a polymer solution, stress overshoots occur because of molecular reaarangements [Ferry, 1982] with the maximum corresponding to the breakdown of the initial structure. Such overshoots, which are very large compared to the 15% observed in foam, increase with increasing shear rate. In foams, for a given gas fraction, the normalised curves of the transient viscosity (which is the same for stress) are independent of shear rate with the maximum occuring at the same strain for different shear rates. This leads us to believe that the maximum stress represents the yield stress and the corresponding strain, γ_c, the critical strain at which the initial foam structure reforms. This maximum stress is also independent of shear rate which it should be if it is the yield stress. Further corroboration of this idea also comes from Boger [1983] who observed small stress overshoots in materials with yield stress. More importantly, however, γ_c from the experiments are respectively ~.8, .85 and .92 for ϕ=.92, .95 and .97. From the model in Chapter IV, we find that depending on initial orientation, γ_c ranges from from .36 to 1 for ϕ=.92 and from .57 to 1.3 for ϕ=.97. These are clearly in the correct range. The stress growth experiments also show the maximum stress to be larger for a larger gas fraction. This is observed for the yield stress in our model and also in the steady shear experiments.

Since the stress overshoots are only about 15% higher than the steady stress value, the equilibrium foam cell structure in a steady flow at any instant is not much different from the inital structure. Thus for our experimental runs, foam structure was preserved in the steady shear deformation. One important point to note here is that the yield stress values obtained from the stress growth experiments are roughly 15% higher than the ones measured using stress relaxation and extrapolation of viscosity versus shear stress data. This is because in the steady experiments we are measuring τ_y from equilbrium foam structures that are in motion. In the stress growth experiment, we are measuring τ_y at the onset of steady flow when the inital structure is about to breakdown. Clearly, the inital and the equilibrium structures are slightly different which leads to this slight discrepancy.

One other information can be obtained from the $\eta^+ - \gamma$ curves. For strains below γ_c, where the predominant mode of deformation is the extensional motion of the liquid films, we can get the shear modulus, $G(\gamma)$, of foam from its definiton $G(\gamma) = \tau_{yx}/\gamma$. Figure VI-19 shows the experimental shear modulus along with the dry foam model prediction (Equation II-24).

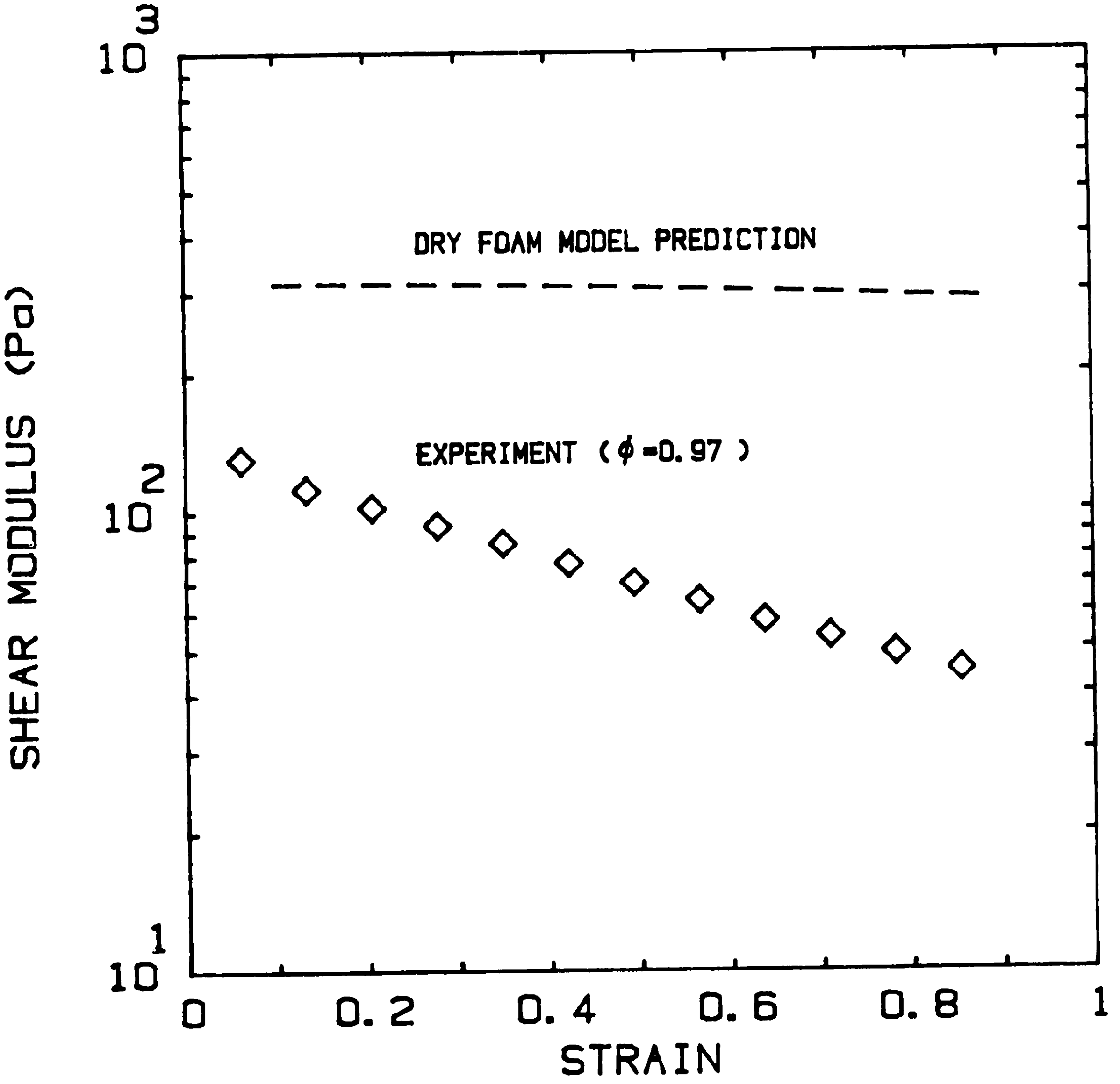

Figure VI-19 Shear modulus as a function of strain. Model predictions and experiments are compared.

Although both curves show the same trend, the experimental one decreases faster with strain.

In the oscillatory experiments, the flat nature of G' and G'' (Figures VI-5, 6) for both strain and frequency sweeps go very well with expectation. As can be seen from the η^+ versus γ plots, the stress-strain relation is well within the linear regime. For such small sinusoidal deformation it is the linear liquid films of the foam cells that is being stretched and compressed. Since these films are also very thin, the response of the material would be predominantly elastic. We may point out here that for such small strains and frequencies, viscous stresses in the films are negligible and the foam structure is essentially at equilibrium (cf. Chapter III). For such equilibrium deformations, although the film thickness in reality may changes with strain, the extensional motion of the films are insensitive to it. This is evident from Chapter III where we find the results for the finite film and zero film thickness models to be the same and the deformation essentially elastic. However, if we had strains going past the point where the cusps of two Plateau borders meet (Figure IV-2), the response would clearly be nonlinear. Viscous effects would be more important and the stress-strain phase shift would be larger. This non linearity is reflected in a non-sinusoidal torque output as observed by Prud'homme and Yoshimura [1984].

In the oscillatory shear flow experiments, we observe the moduli to decrease slightly with decreasing ϕ (Figure VI-6). However, the ratio of G'/G'' is constant for the gas fractions measured, suggesting that the relative predominance of elastic over viscous effects do not change with ϕ. This happens because the experimental phase shifts between the torque output and strain, which is directly related to G'/G'' (cf. Equation V-6), are same for all ϕ's (Figures VI-7, 8 and 9). Only the maximum torque amplitude, which is related to the absolute value of the moduli, change with ϕ. Based on the modelling work, one would expect this. With a lower ϕ, the film thickness would be slightly more; so, the absolute values of the moduli would go down a little. The response mode, still being the compression and stretch of the liquid films, would essentially be elastic.

C. SUMMARY

Steady and dynamic shear flow experiments done on foam revealed the following information.

In steady shear flows, foam behaves like a Bingham plastic material. In our low shear rate experimental regime, it showed a shear thinning viscosity inversely proportional to the shear rate, indicating yield stress to be the predominant component of the viscosity. The value of the viscosity, which was over four orders of magnitude higher than the liquid solution viscosity, was an increasing function of the gas volume fraction. Comparison with model prediction showed the model to give the correct trend but overpredict the viscosity by a factor of three.

Indirect measurement of the yield stress of foam, τ_y, by extrapolating the viscosity versus shear stress data showed τ_y to increase with larger gas fraction. Direct measurement of τ_y using stress relaxation confirmed this.

Oscillatory dynamic experiments showed foam to behave like an elastic solid for small deformation (consistent with theory). This was concluded from the facts that the moduli of foam were insensitive to frequency of oscillation, G' was much greater than G'', and finally the phase shift between torque output and strain input was very small.

Stress growth experiments revealed the stres-strain behavior of foam to be independent of shear rate confirming the elastic nature of the material, and also indicating shear rate to be an unimportant processing parameter. Small stress overshoots with the maximum corresponding to the yield stress and critical strain, and independent of γ and shear rate, typical of material with a yield stress, was observed for each gas fraction of foam.

VII. LARGE DEFORMATIONS AND PERIODICITY IN FOAMS

The goal of this chapter is to extend the dry foam model of Chapters II and III to large deformations beyond the critical point. We focus on shearing deformations only and study the periodicity of the stress-strain relation and influence of initial orientations for large shear strains. Deformations of hexagonal foam cells of any arbitrary initial cell orientation with only surface forces present (equilibrium) as well as with surface and viscous forces present are considered.

A. FORMULATION OF PROBLEM

The physics of foam deformation have already been discussed in Chapters II and III and all assumptions from these chapters carry over here. Results up to the critical point are therefore the same as in the earlier chapters. In this section we focus on formulating the problem beyond the critical point or first "disproportionation". The stress tensor is given from Equation II-14 as:

$$\underline{\underline{\tau}} = \sum \frac{F_i}{S} \frac{\underline{g}_i \underline{g}_i}{g_i} \qquad \text{VII-1}$$

where F_i is the magnitude of the force along the liquid film g_i. For the equilibrium case, $F_i = 2\sigma$ whereas when both surface and viscous forces are present F_i is given by (cf. Equations III-15, 16):

$$F_i = 2\sigma \left(1 + \frac{N_{ca}}{g_i^2} \frac{dg_i}{d\gamma}\right) \qquad \text{VII-2}$$

Here, N_{ca} is the Capillary number defined by Equation III-15.

As before, we need to know the micromechanics to evaluate the stress tensor. Let us choose the same unit cell and triangular subcell ABC as in Chapter II. Thus A, B, and C represent points of affine motion. We embed vectors $\underline{b}^o{}_1$, $\underline{b}^o{}_2$ along AB and AC respectively and assume these to be known for any initial orientation from Chapter II. Thus, for any deformation the vectors $\underline{b}_1$, $\underline{b}_2$ along AB and AC are given by:

$$\underline{\underline{\beta}} = \underline{\underline{E}} \cdot \underline{\underline{\beta}}^o$$

where,

$\underline{\underline{E}}$ is the deformation gradient tensor defined in Equation II-3. $\underline{\underline{\beta}}$, $\underline{\underline{\beta}}^o$ are defined as:

$\underline{\underline{\beta}} = (\underline{b}_1, \underline{b}_2)^\dagger$ $\qquad$ $\underline{\underline{\beta}}^o = (\underline{b}^o{}_1, \underline{b}^o{}_2)^\dagger$

For a shearing deformation at a strain γ, this reduces to:

$$\underline{b}_1 = (b^o{}_{1x} + \gamma\, b^o{}_{1y})\underline{\delta_x} + b^o{}_{1y}\, \underline{\delta_y} \qquad \text{VII-2}$$

$$\underline{b}_2 = (b^o{}_{2x} + \gamma\, b^o{}_{2y})\underline{\delta_x} + b^o{}_{2y}\, \underline{\delta_y}$$

Here, the subscripts x and y denote the respective components of the vectors.

At the point of disproportionation when one of the films reduces to zero length, we reinitiate the problem based on the following rules. If film OC or g_3 goes to zero, then the new β^o is given in terms of β for this point by:

$$\underline{\underline{\beta}}^o = (\underline{b}_1 - \underline{b}_2, \underline{b}_2)^\dagger \qquad \text{VII-3}$$

If film OB or g_2 reduce to zero then,

$$\underline{\underline{\beta}}^o = (\underline{b}_1, \underline{b}_2 - \underline{b}_1)^\dagger \qquad \text{VII-4}$$

If film OA or g_1 goes to zero length, then β^o is given by:

$$\underline{\underline{\beta}}^o = (\underline{b}_2, -\underline{b}_1)^\dagger \qquad \text{VII-5}$$

The above formalism becomes clear if one looks at a cell at the point of disproportionation. Figure VII-1 shows the cell structure for initial orientation $\theta=0^{o}$ and $N_{ca}=0$. Here, side OC has reduced to zero length. Since angle QPR is 60^{o} and represents an unstable configuration, we would expect the film to grow in direction 1 as shown so as to attain the 120 stable configuration. Growth of the film in direction 2 is not expected because this would lead to the original foam structure. A much better explanation for the film growth comes a force balance argument. Since point P in Figure VII-1 experience forces along PQ and PR, this would cause a film to emanate in direction 1. Thus, we can reinitiate the problem by choosing PQR as the new subcell and embedding vectors $\underline{b}_1$, $\underline{b}_2$ along PQ and PR. Similar arguments hold for the two other films going to zero.

A very important point to note here is the initial direction of the growing film. For the equilibrium case, the forces along PQ and PR are same (2σ) and hence the film will initially bisect the angle QPR. When viscous forces are present, however, the forces along PQ and PR are different and the direction of the growing film is given by the direction of the resultant force.

In order to get the cell shape, we use the 120^{o} criterion and Equations II-5 and 6 for the equilibrium case. This gives the coordinates of point O, the Plateau border, in terms of the vectors $\underline{b}_1$ and $\underline{b}_2$ as:

$$x = 2 \, [\, (\underline{b}_1+\underline{b}_2)\cdot\underline{\delta}_x/\sqrt{3} + (\underline{b}_1-\underline{b}_2)\cdot\underline{\delta}_y \,] \, C1 \,/\, [\, D1 \sqrt{3} \,]$$

$$y = 2 \, [\, (\underline{b}_2-\underline{b}_1)\cdot\underline{\delta}_x + (\underline{b}_1+\underline{b}_2)\cdot\underline{\delta}_y/\sqrt{3} \,] \, C1 \,/\, [\, D1 \sqrt{3} \,]$$

where,

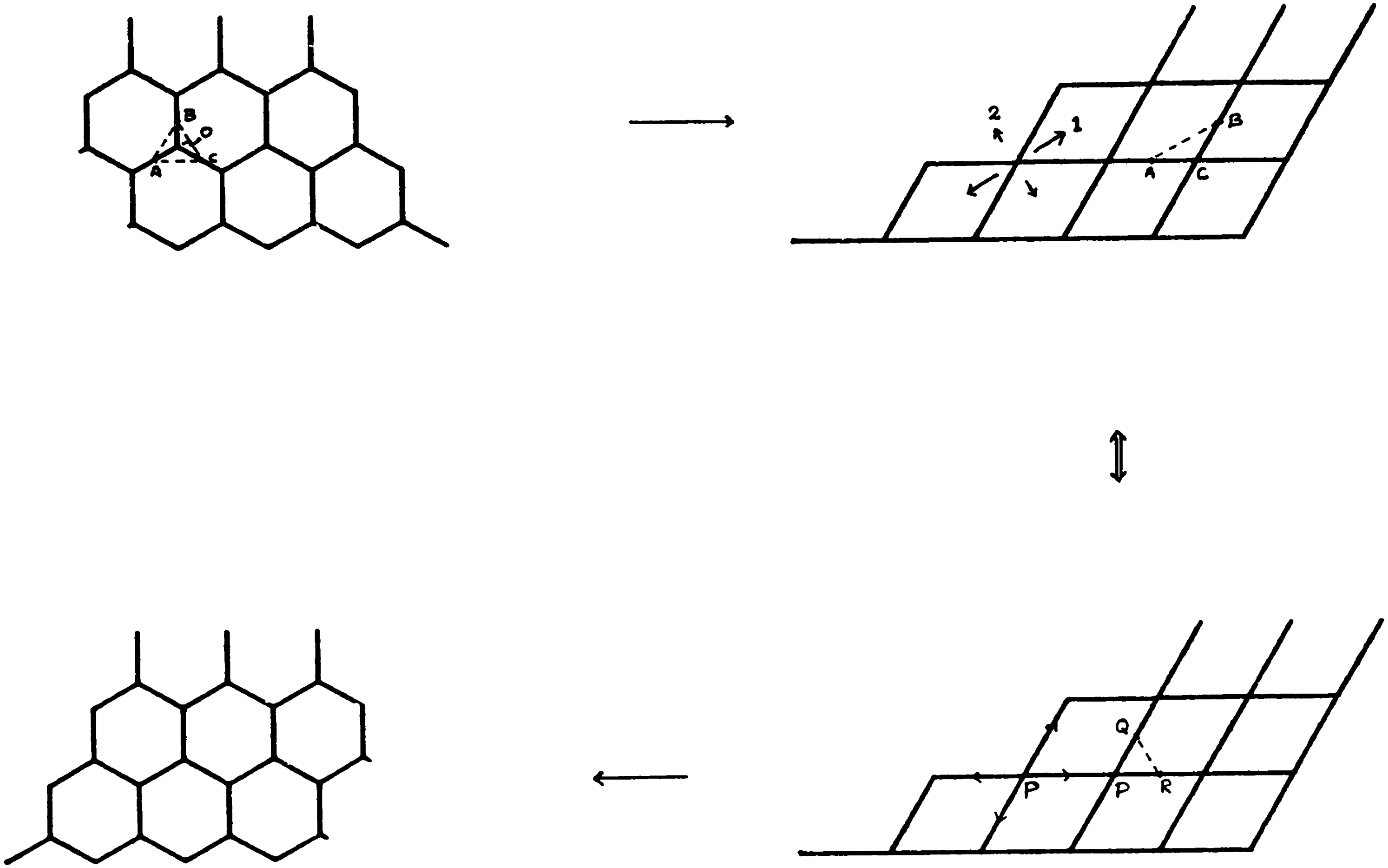

Figure VII-1 Cell structures showing periodicity in large shearing deformations. Initial orientation θ=0°; Capillary number $N_{ca}=0$.

$$C1 = \underline{b}_1 \cdot \underline{b}_2 + (\underline{b}_2 x \underline{b}_1) \cdot \underline{\delta}_Z / \sqrt{3}$$

$$D1 = [(\underline{b}_1 + \underline{b}_2) \cdot \underline{\delta}_X / \sqrt{3} + (\underline{b}_1 - \underline{b}_2) \cdot \underline{\delta}_y]^2 + [(\underline{b}_2 - \underline{b}_1) \cdot \underline{\delta}_X + (\underline{b}_1 + \underline{b}_2) \cdot \underline{\delta}_y / \sqrt{3}]^2$$

Thus at the point of disproportionation, once we reinitialize the tensor β, we get a different foam cell structure at that same strain using the above equations. Thus the new film grows instantaneously and this new configuration corresponds to a lower energy state.

When viscous forces are present, we solve for the microstucture using Equations III-18 and 19 and reinitialize the equations after each disproportionation. Here, however, at the point of disproportionation we specify the initial direction of film growth and the cells do not reform instantaneously as viscous forces do not allow an instantaneous extension of the new film.

B. RESULTS AND DISCUSSION

Kraynik [1984] has been the first to look at large deformations in high gas fraction foams. Based on the methods in Chapter II, he developed a formalism to study large deformations. Our model, in turn, builds up on his work. The major difference between the two studies lies in the method of reinitializing the problem after each disproportionation. In his work, Kraynik chose the bisector of the angle between the two films, i.e. angle QPR of Figure VII-1 as the initial direction of the growing film. Clearly, this is not correct when viscous forces are present as the direction is determined from the direction of the resultant of the forces along the two films PQ and PR.

In Figure VII-2 are shown the shear stress (τ_{yx}) and first normal stress difference (N_1) of foam for $\theta=0^o$ and $N_{ca}=0$. Clearly, the system is periodic after one disproportionation with the stresses returning to their original values. This is easily seen from the cell structures (Figure VII-1) where at the point of disproportionation ΔPQR, the new subcell, is equivalent ot the original subcell ΔABC, and the system reforms to the original configuration.

In Figure VII-3 are plotted the stress-strain relation for initial orientation $\theta=30^o$ and $N_{ca}=0$. The plots reveal the system to be periodic after three disproportionation. The first disproportionation occurs at C and the system jumps to D; the second one occurs at F and the final one at I. At this point the stresses jump back to its initial values. Observe from the plot that the shear stress jumps to a nonzero value after the first disproportionation (D) and becomes negative after the second disproportionation at G. Such values are indicative of irregular cell strucutres as revealed by our calculations in Chapter III. In Figure VII-4, we show the actual cell deformation for this orientation with the labels corresponding to those of the stress plot. At C, side 3 has reduced to zero length and the structure reforms with a film growing in the direction shown by the arrows. The new subcell along with the new film is shown in D. Structure F represents the next disproportionation where side 2 or OB has gone to zero length. G shows the reformed foam structure and subcell. As this is deformed side OB shrinks in length to zero at I; the cells then reform back to the original 30^o orientation at J. The cycle is repeated for larger strains. Note that D, G represent irregular cell structures and the subcells have been drawn based on our

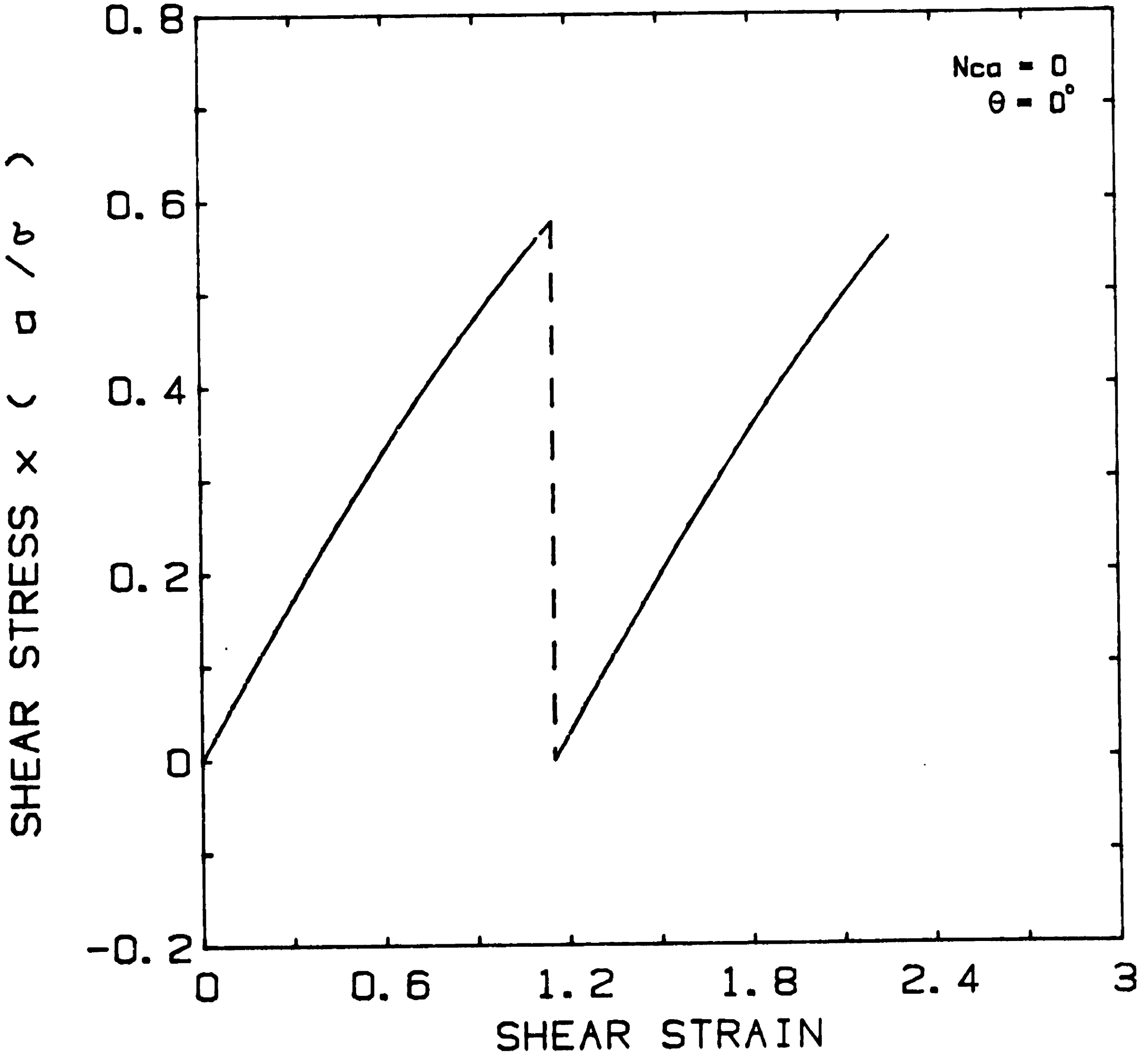

Figure VII-2 Stress-strain relations in large shearing deformations under equilibrium conditions. Here, initial orientation θ=0°. σ=surface tension; a=side length of hexagon. a) Shear stress b) First normal stress difference.

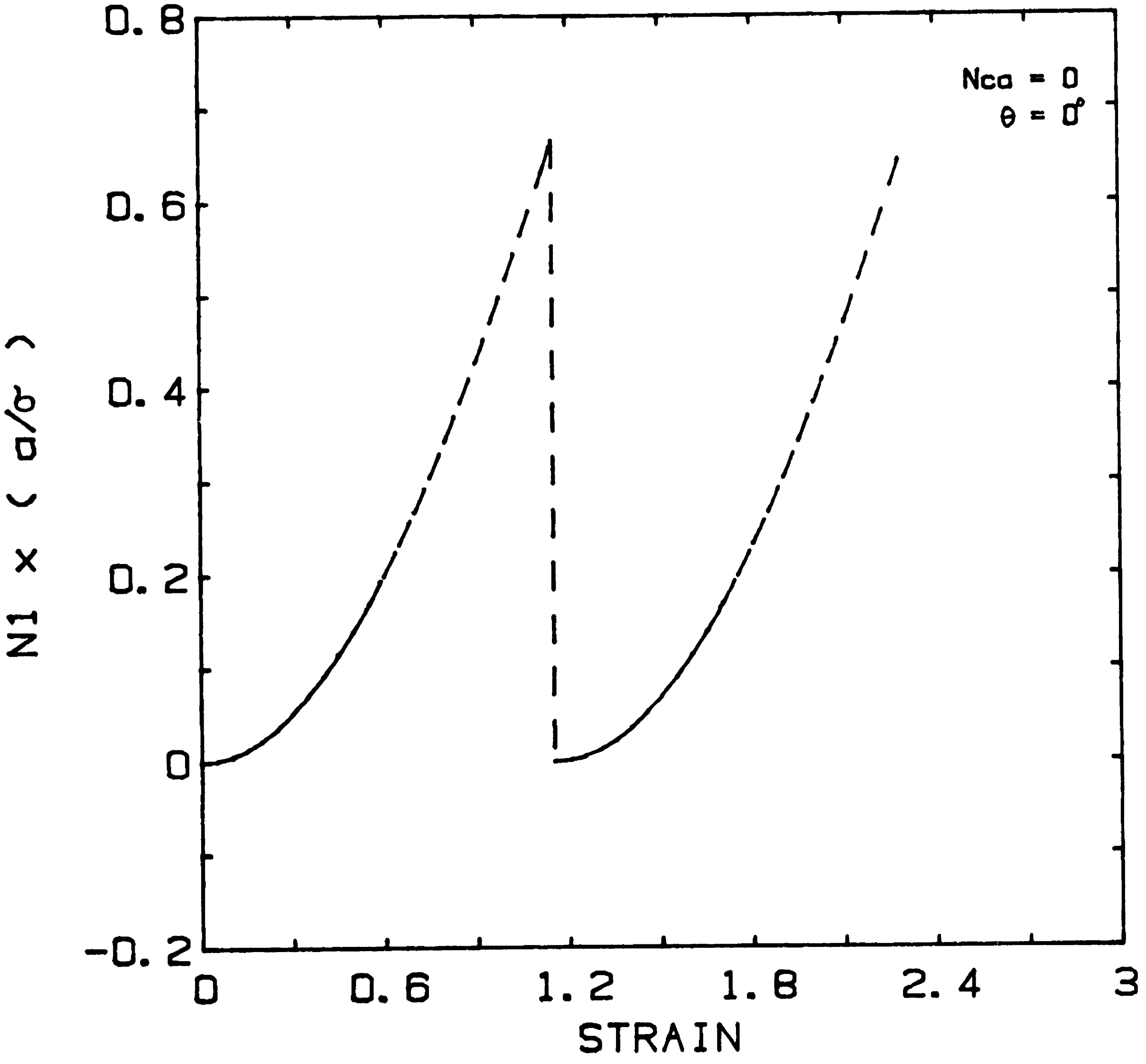

Figure VII-2 (continued)

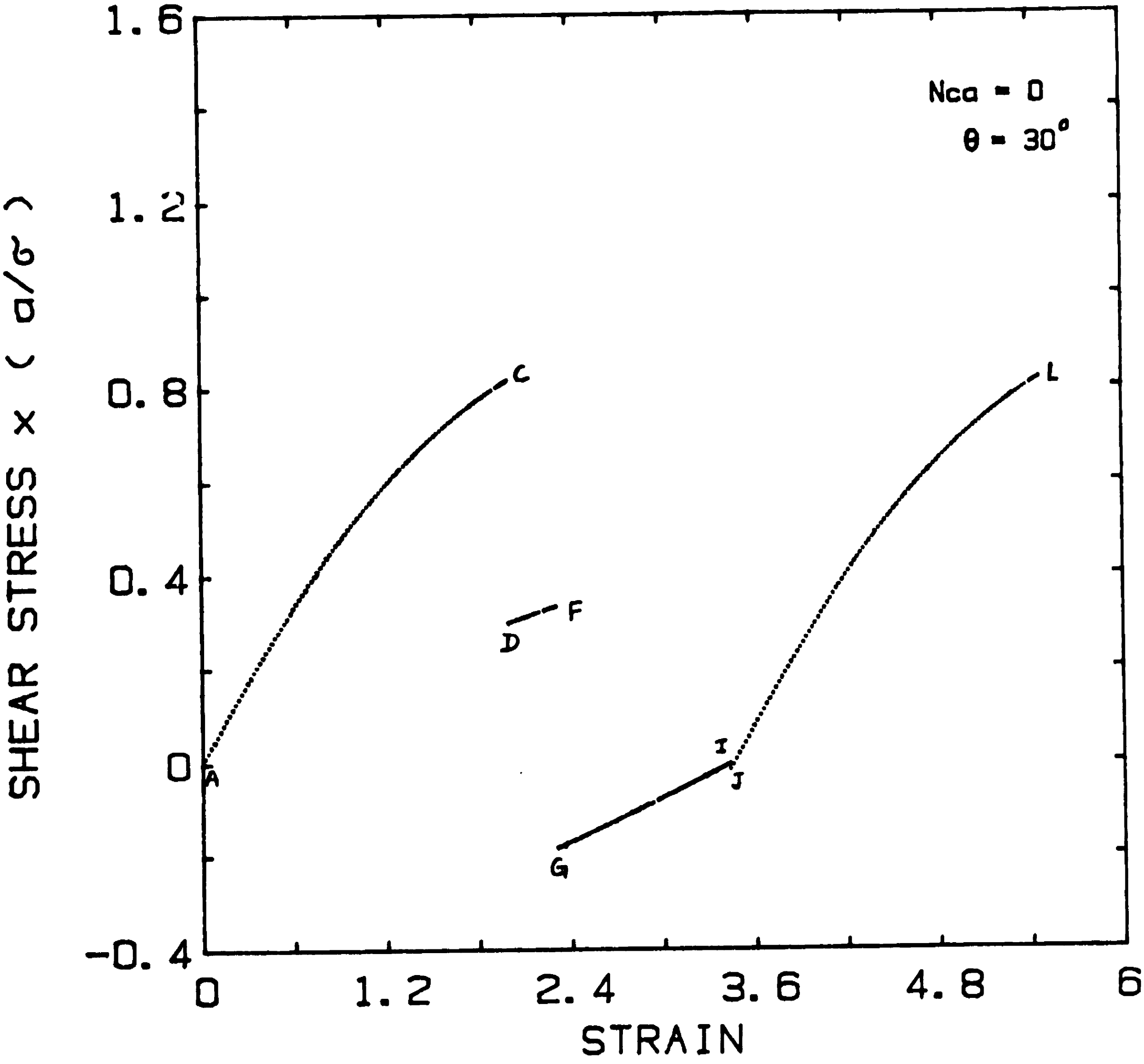

Figure VII-3 Stress-strain relations in large shearing deformations. Here, initial orientation θ=30° and Capillary number N_{ca}=0. σ=surface tension; a=side length of hexagon. a) Shear stress b) First normal stress difference.

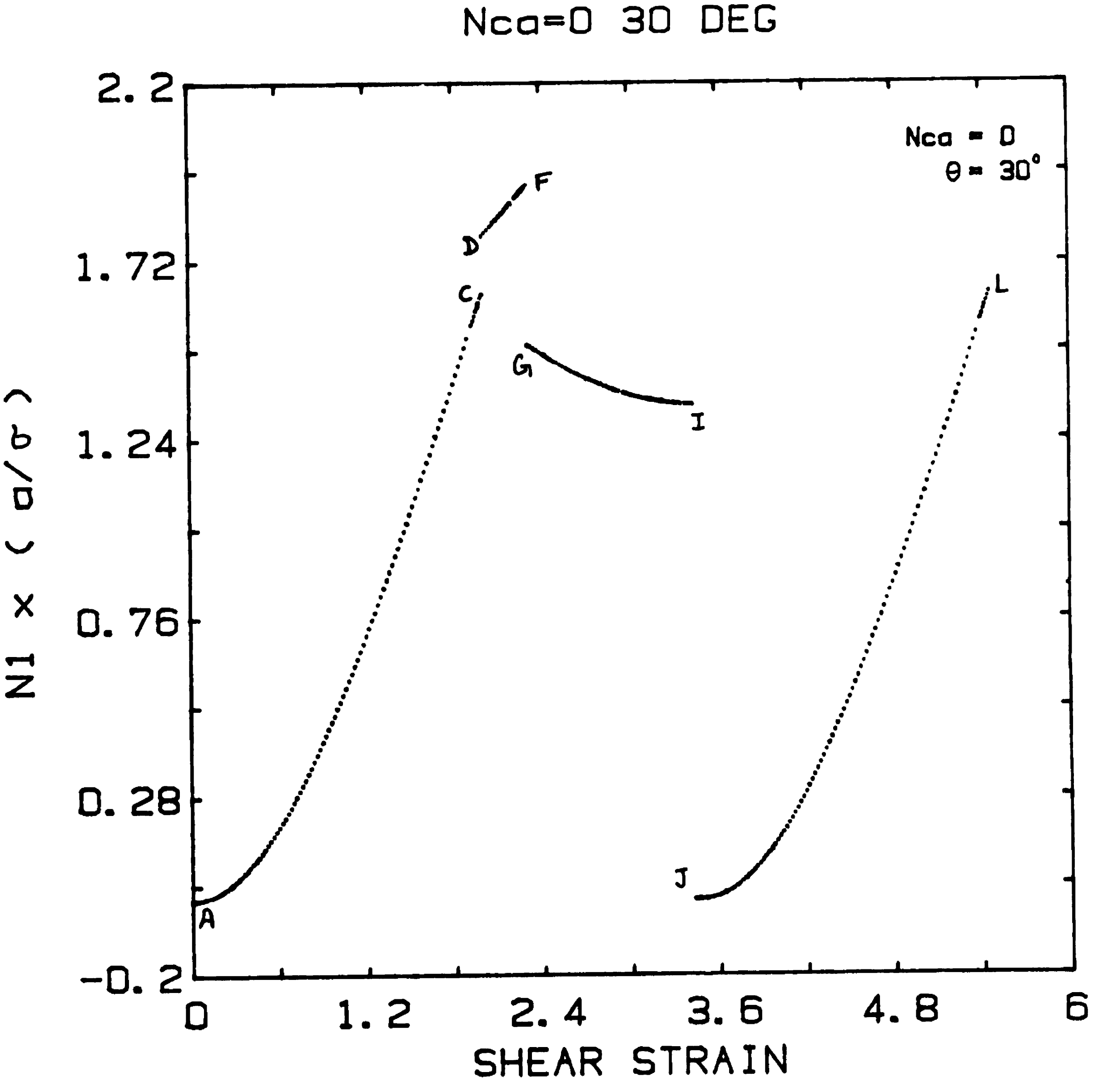

Figure VII-3 (continued)

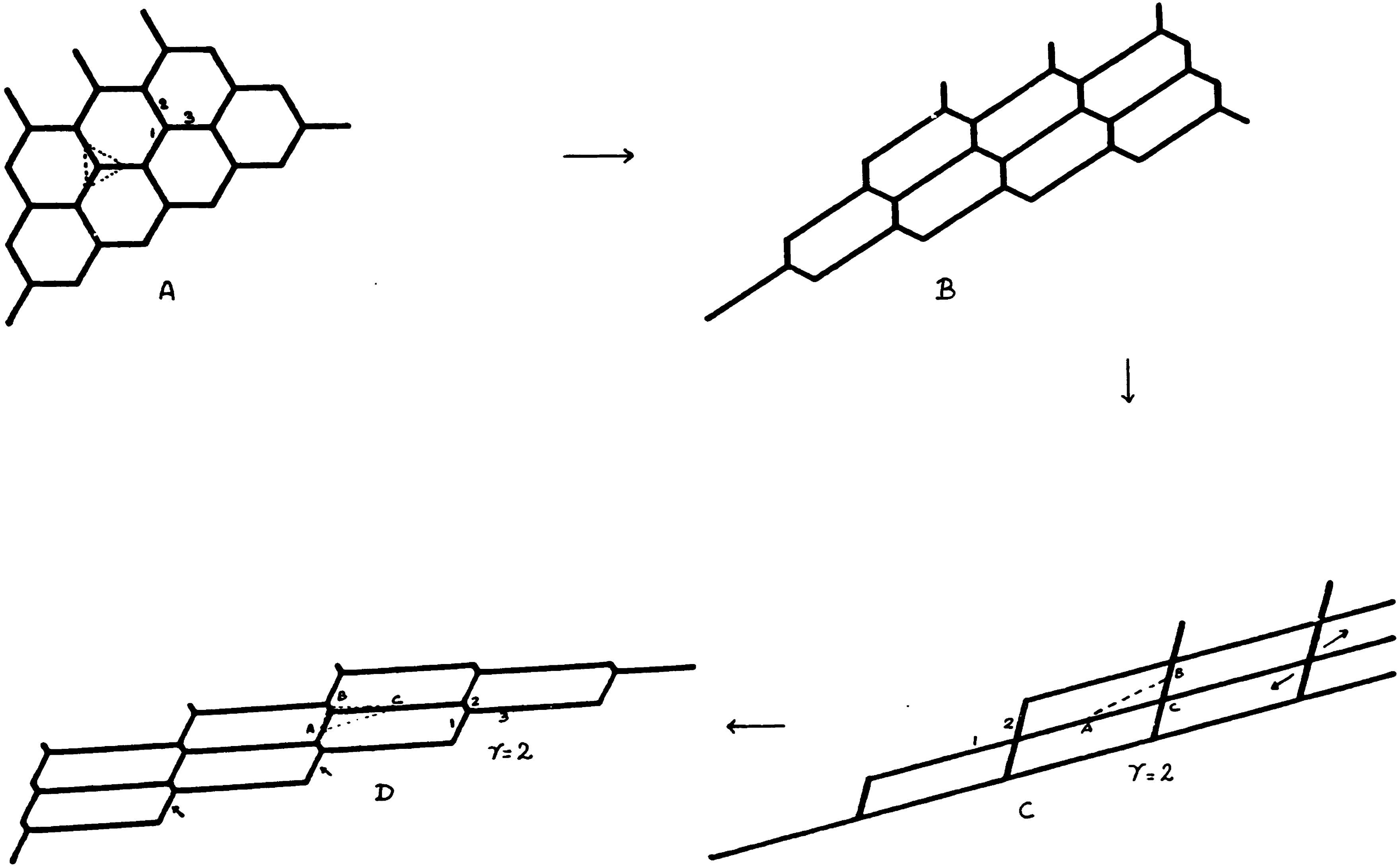

Figure VII-4 Cell deformation for large shearing strains. Initial orientation $\theta=30^{\circ}$ and Capillary number $N_{ca}=0$. Structures A through L showing cell shapes in order of increasing strain. Note the periodicity.

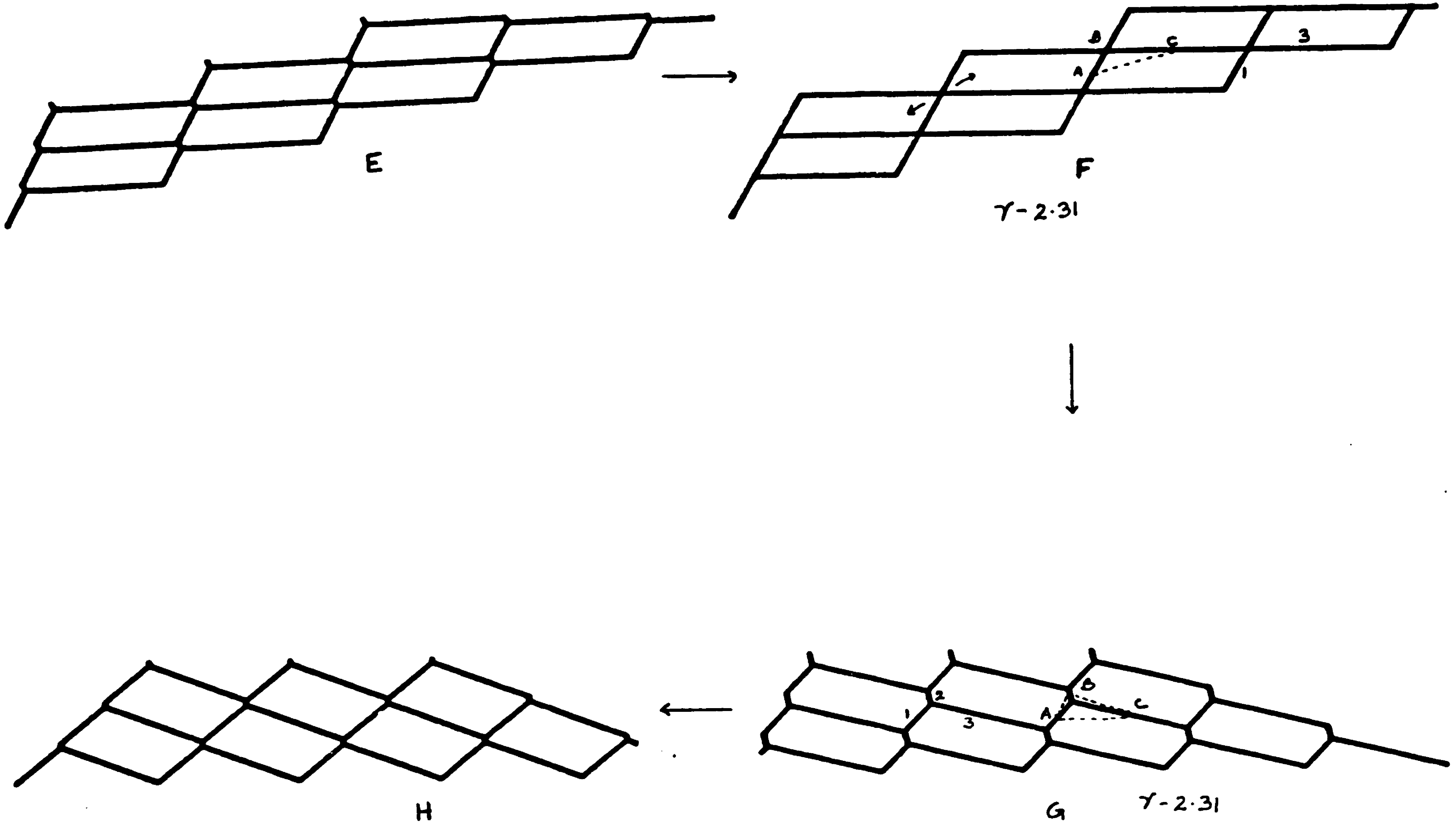

Figure VII-4 (continued)

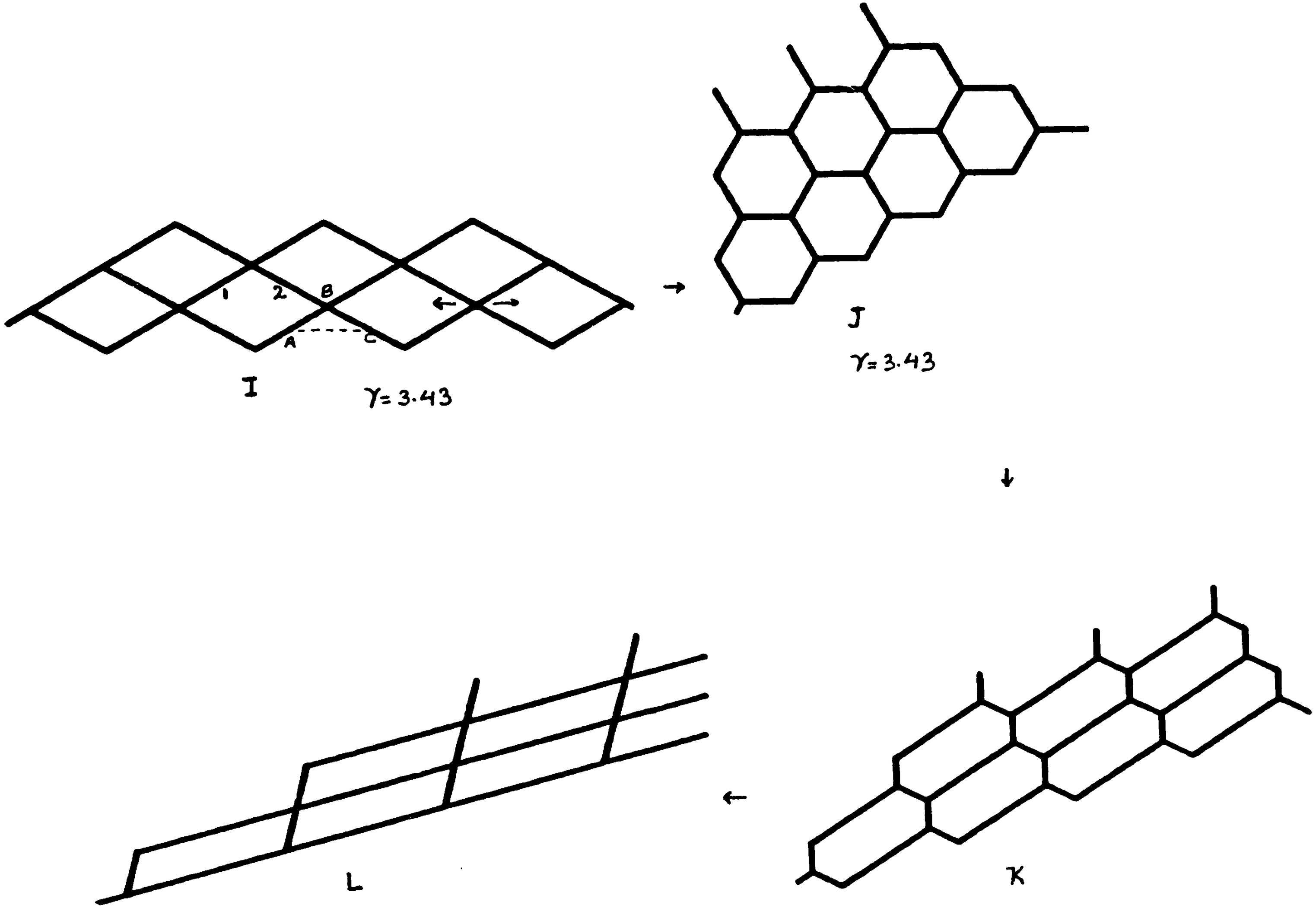

Figure VII-4 (continued)

formalism.

In Figure VII-5 are shown the shear and normal stress plots for initial orientation $\theta=15^o$ and $N_{ca}=0$. We observe no periodicity even after four disproportionations. This leads us to believe that the 15^o orientation is not a periodic one and although the structures reform they never return to their original configuration.

From our study of equilibrium systems we found initial orientation to affect periodicty in foams. We felt that aperiodicity would become more pronounced with viscous forces present because we introduce more asymetry at the point of disproportionation by specifying the direction of the growing film. In order to study the effect of viscosity we looked at the stress-strain relation for $\theta=0$ and $N_{ca}=0.006$ and .01. Figures VII-6 and 7 show the stress-strain plots for these two Capillary numbers. For both cases we observe periodicity after one disproportionation. However, the stress values never come back to the original one and the original stucture is never attained. As we noted earlier, this is not the case for the equilibrium deformation. These plots along with that for $N_{ca}=0$ also reveal that the amplitude of oscillation goes down with increasing N_{ca} indicating the structures at D to move further from the equilibrium structure at A. At larger N_{ca}, such as 1.0 and .1, we noted in Chapter III that the structures start to elongate rapidly indicating possibilities of cell rupture.

In Figure VII-8 is shown the cell deformation as increasing functions of strain for $N_{ca}=.01$ and $\theta=0^o$. Structure B represents the first disproportionation point of the stress plot. Here the forces along the films causes the new film to grow in the direction shown. C in Figure VII-8

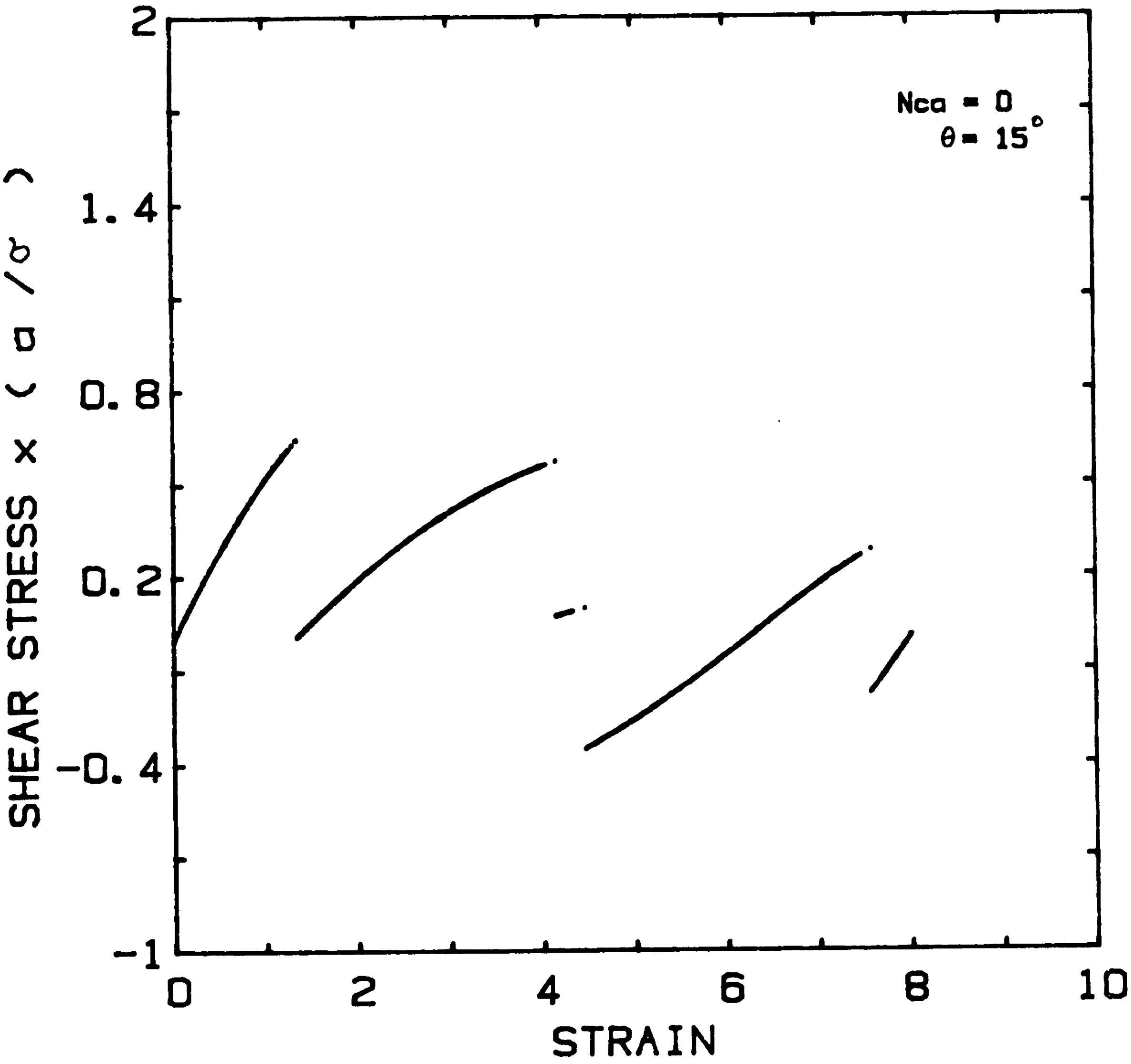

Figure VII-5 Stress-strain relations for initial orientation θ=15° under equilibrium conditions. a) Shear stress b) First normal stress difference. Note that the system is not periodic.

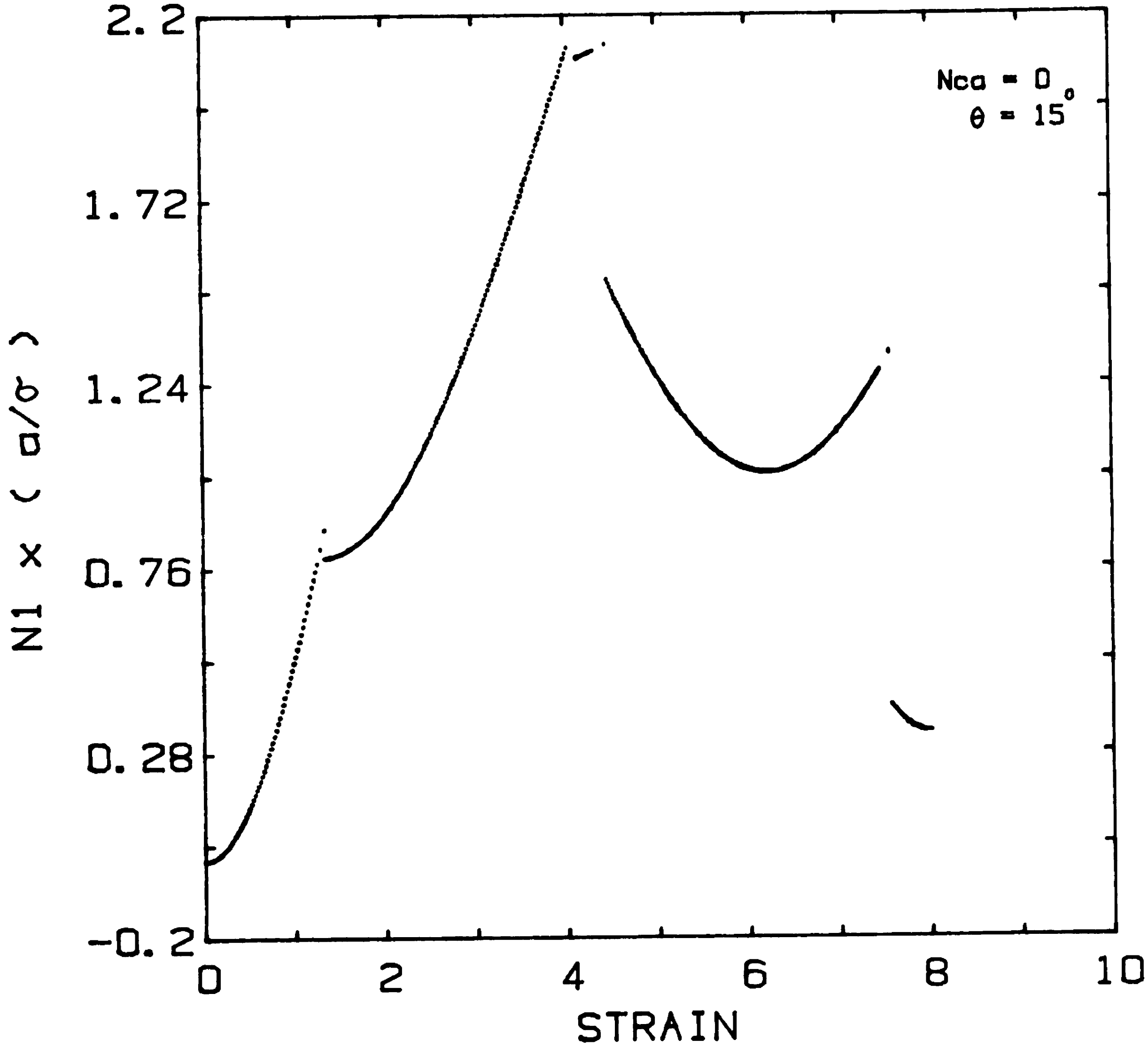

Figure VII-5 (continued)

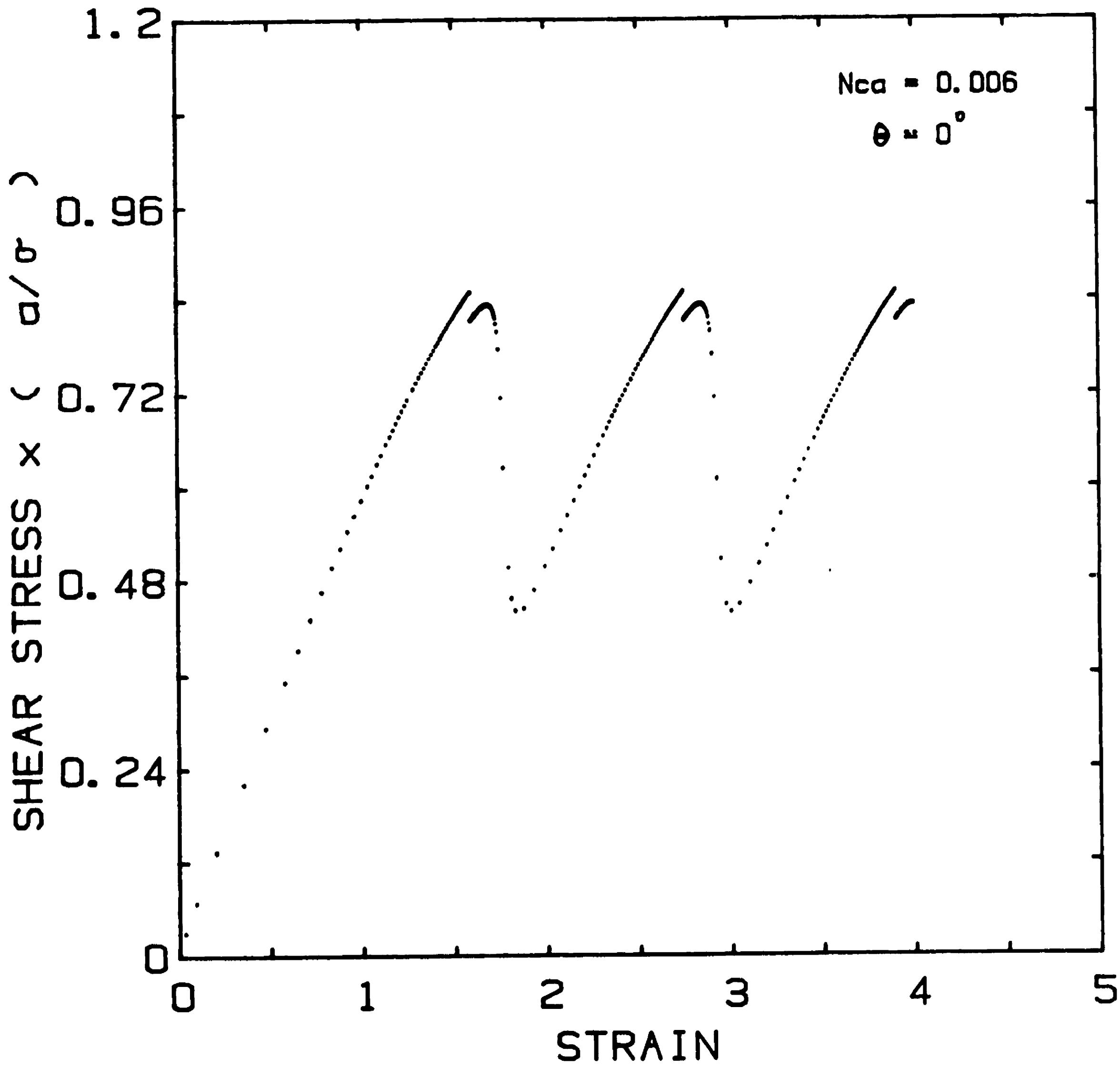

Figure VII-6 Stresses as functions of strain for initial orientation θ=0° and Capillary number N_{ca}=.006. a) Shear stress b) First normal stress difference. σ and a are the surface tension and cell side length respectively.

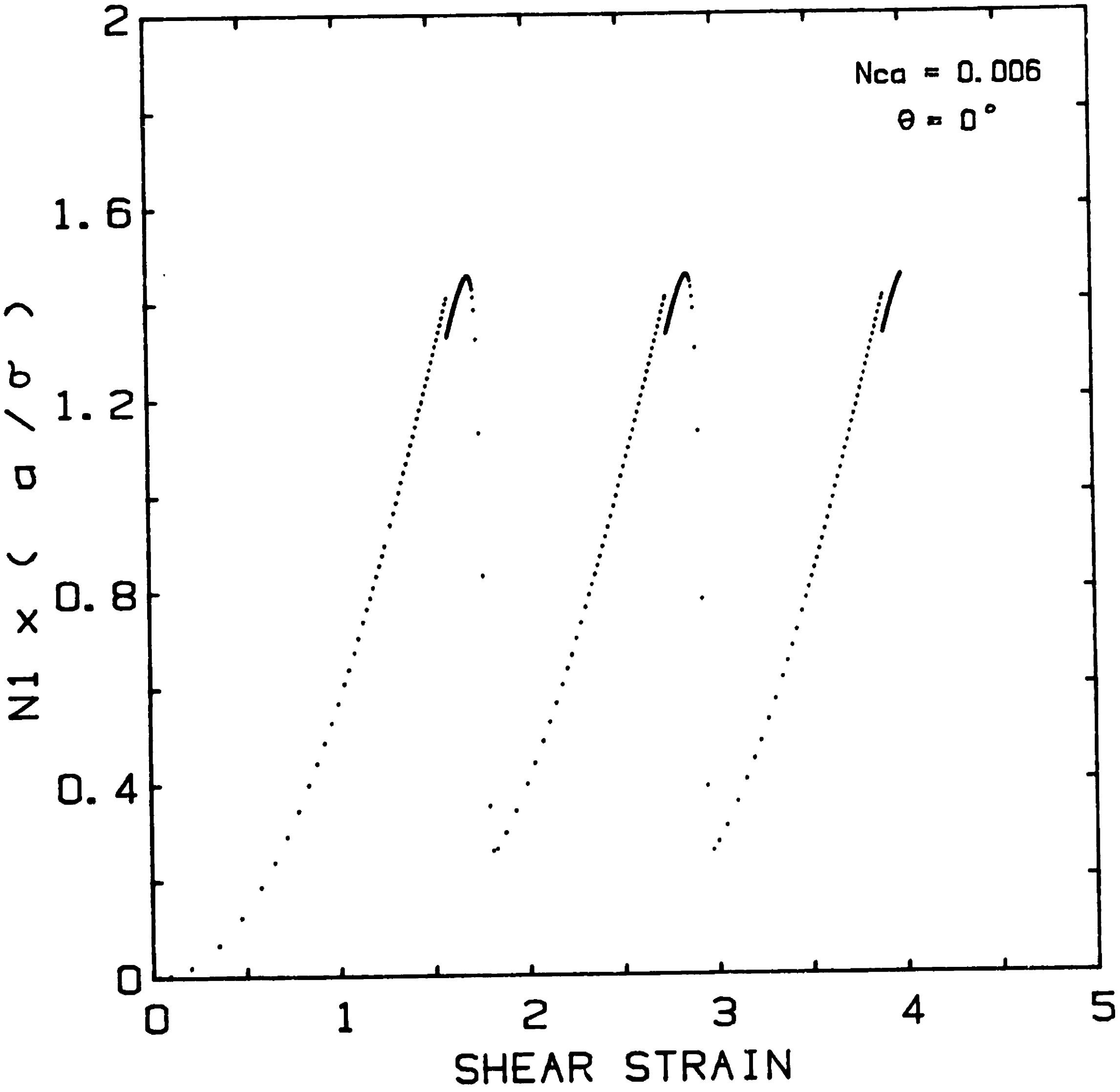

Figure VII-6 (continued)

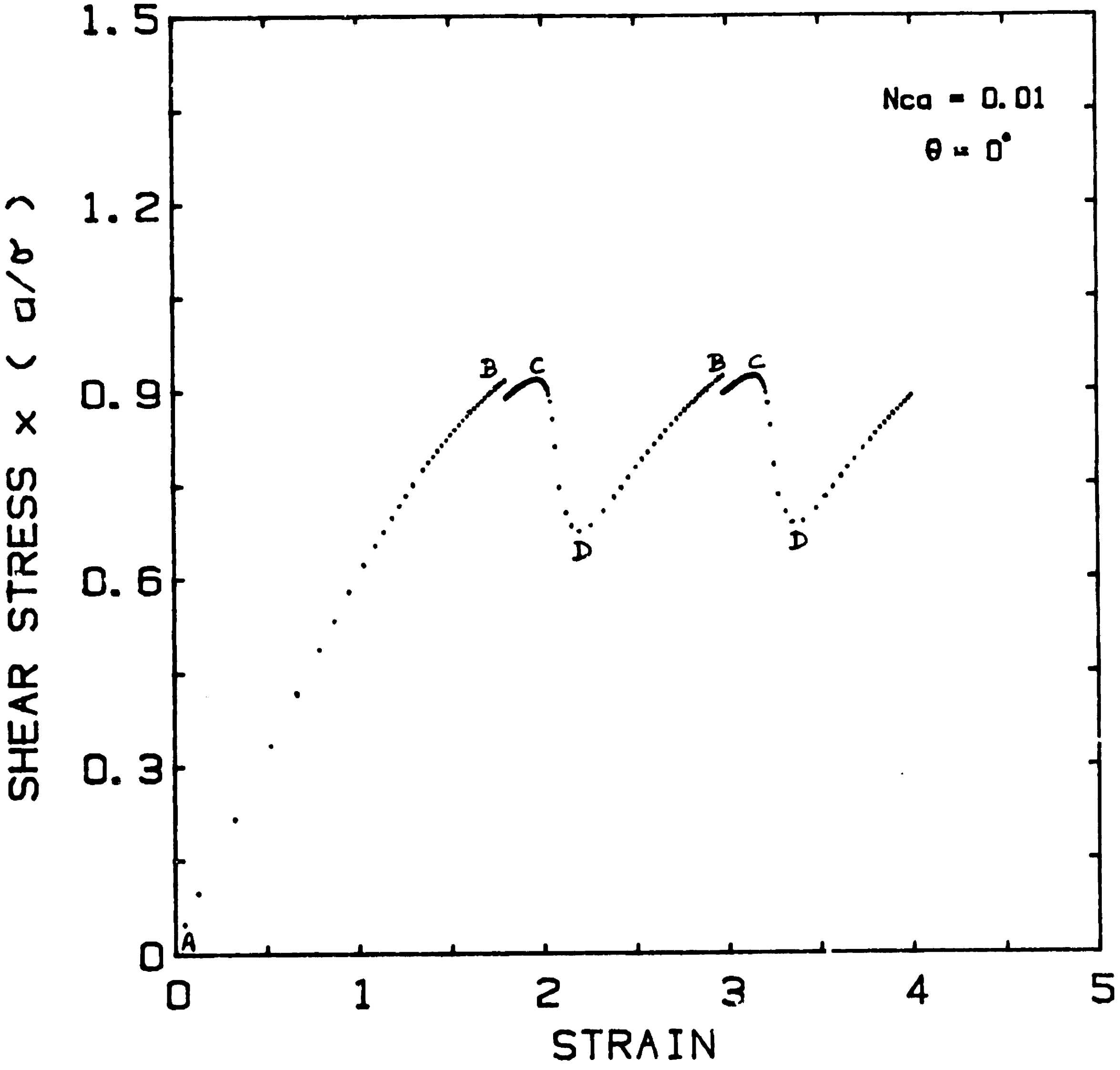

F.gure VII-7 Stresses as functions of strain for initial orientation $\theta=0^{\circ}$ and Capillary number $N_{ca}=.01$. a) Shear stress b) First normal stress difference. σ is the surface tension and a the cell side length.

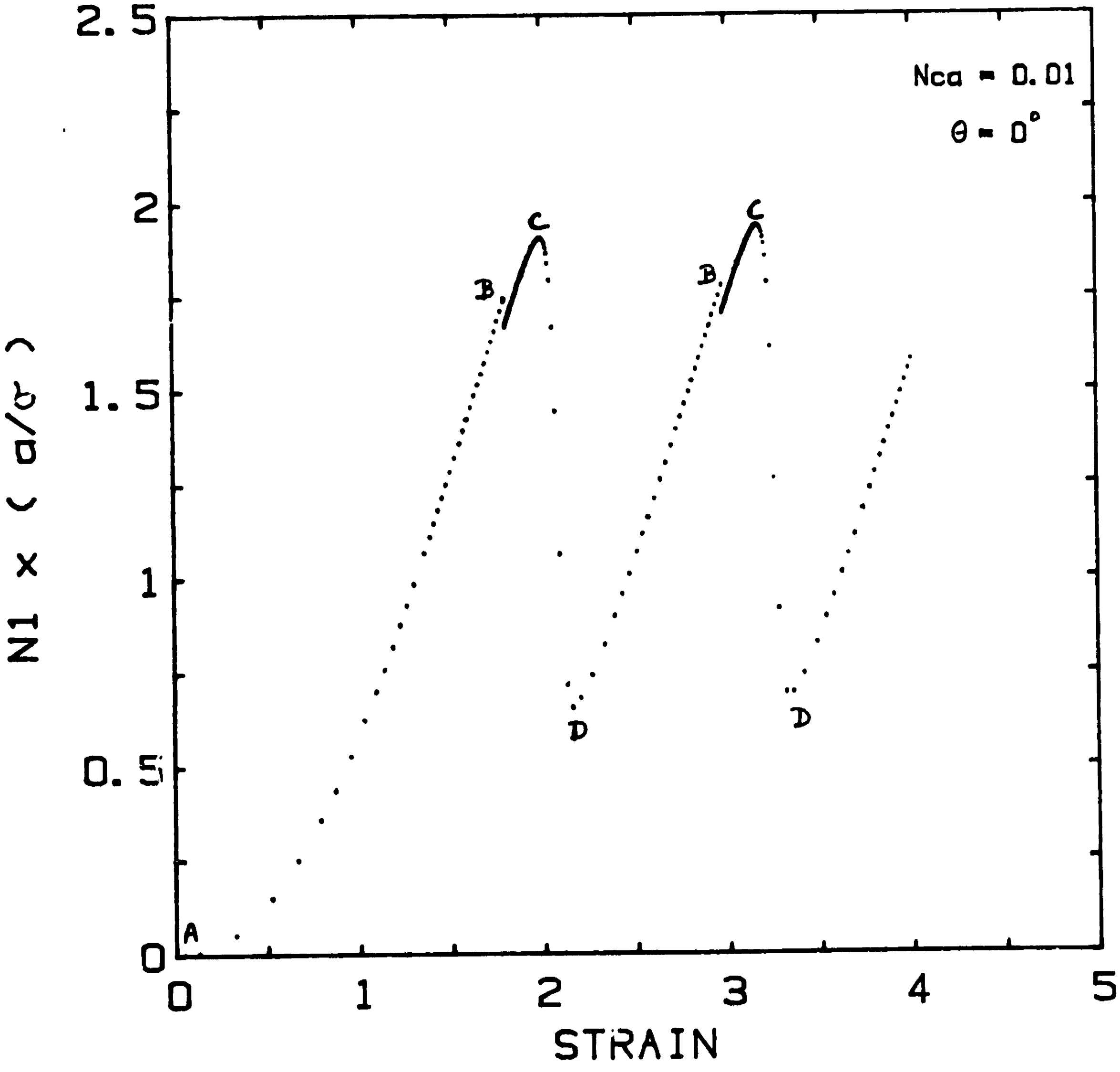

Figure VII-7 (continued)

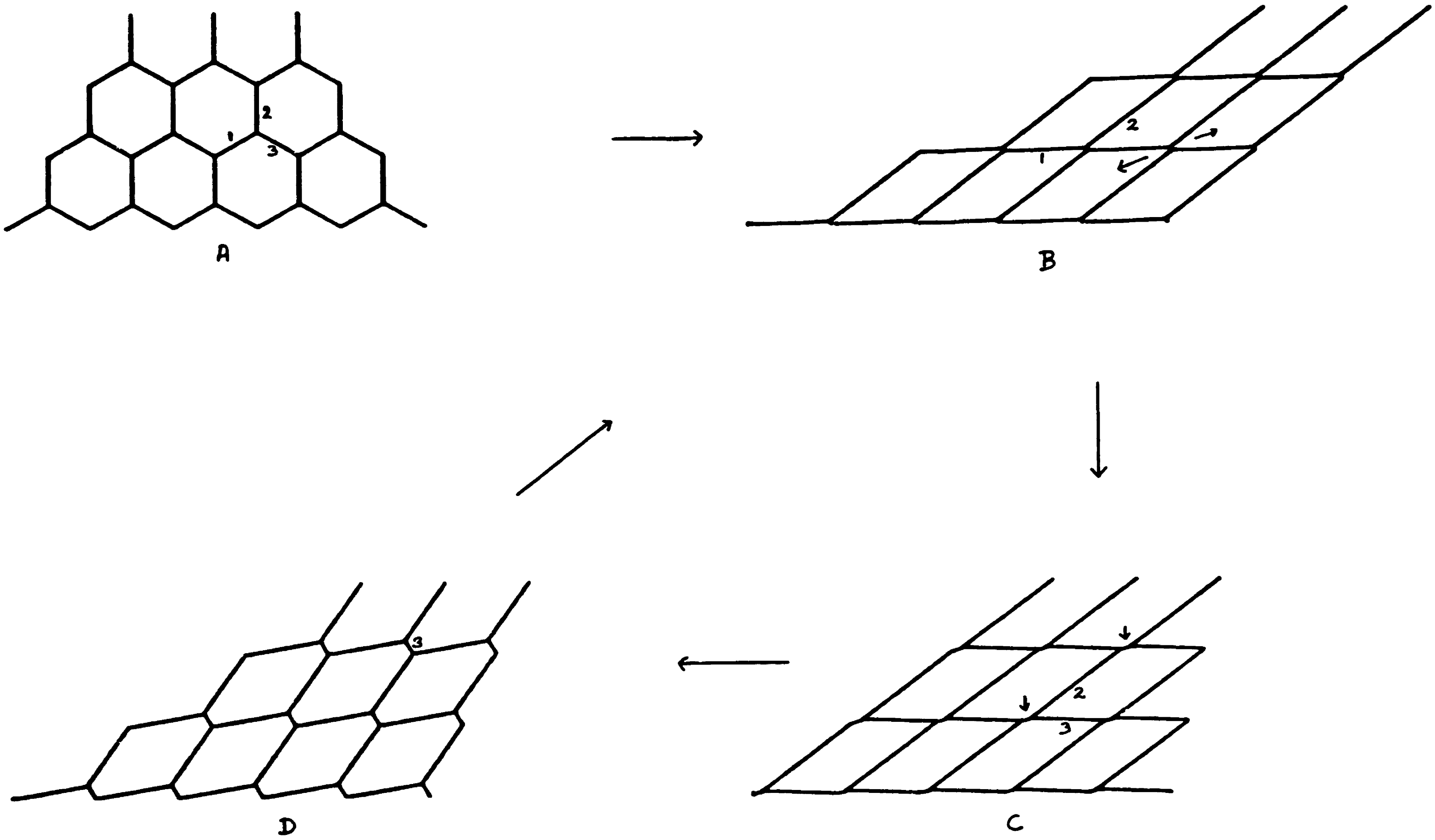

Figure VII-8 Cell deformations for large shear strains under nonequilibrium conditions. Initial orientation $\theta=0^{\circ}$; Capillary number $N_{ca}=.01$. Increasing strain in clockwise direction.

corresponds to the stress at C. The small newly formed film can be observed distinctly here. Further, the films 2 and 3 in C correspond to the films 2 and 1 in the previous structure B. As the cells deform, film 3 decreases in length and structure D corresponds to the local minimum in the shear stress plot. Further deformation causes the cells to reach structure B. Beyond this strain the cells follow the BCD cycle and the initial configuration (A) is never attained.

In Figure VII-9 are plotted the shear and normal stresses for $\theta=30^{o}$ and $N_{ca}=0.001$. From the figures we observe the system to be "almost" periodic. The shear stress seems to be periodic with increasing amplitude; the normal stress, however, does not show such increasing amplitude. We feel that the sytem is not periodic because of the asymetric conditions at the point of disproportionation in terms of the direction of the growing film. This is in contrast to Kraynik's [1984] observation of periodicity with his symmetric film growth condition for $\theta=30^{o}$ and similar Capillary numbers. Further, our results for $\theta=0^{o}$ also differ from Kraynik's result for the same Capillay number because of our conditions.

It is apparent from this study that for certain initial orientations there are no steady state material functions for foam. For instance, for $\theta=15^{o}$ and $N_{ca}=0$, we would be unable to define a steady state viscosity as the system always reforms to a new configuration after each disproportionation. In the cases presented here for $\theta=0^{o}$, however, we can define a time averaged viscosity since the system is periodic. The question that needs to be answered at this point is how can we explain the experimentally observed steady state viscosity of foam. This observed phenomenon can be attributed to the random, three-dimensional, polydisperse cell

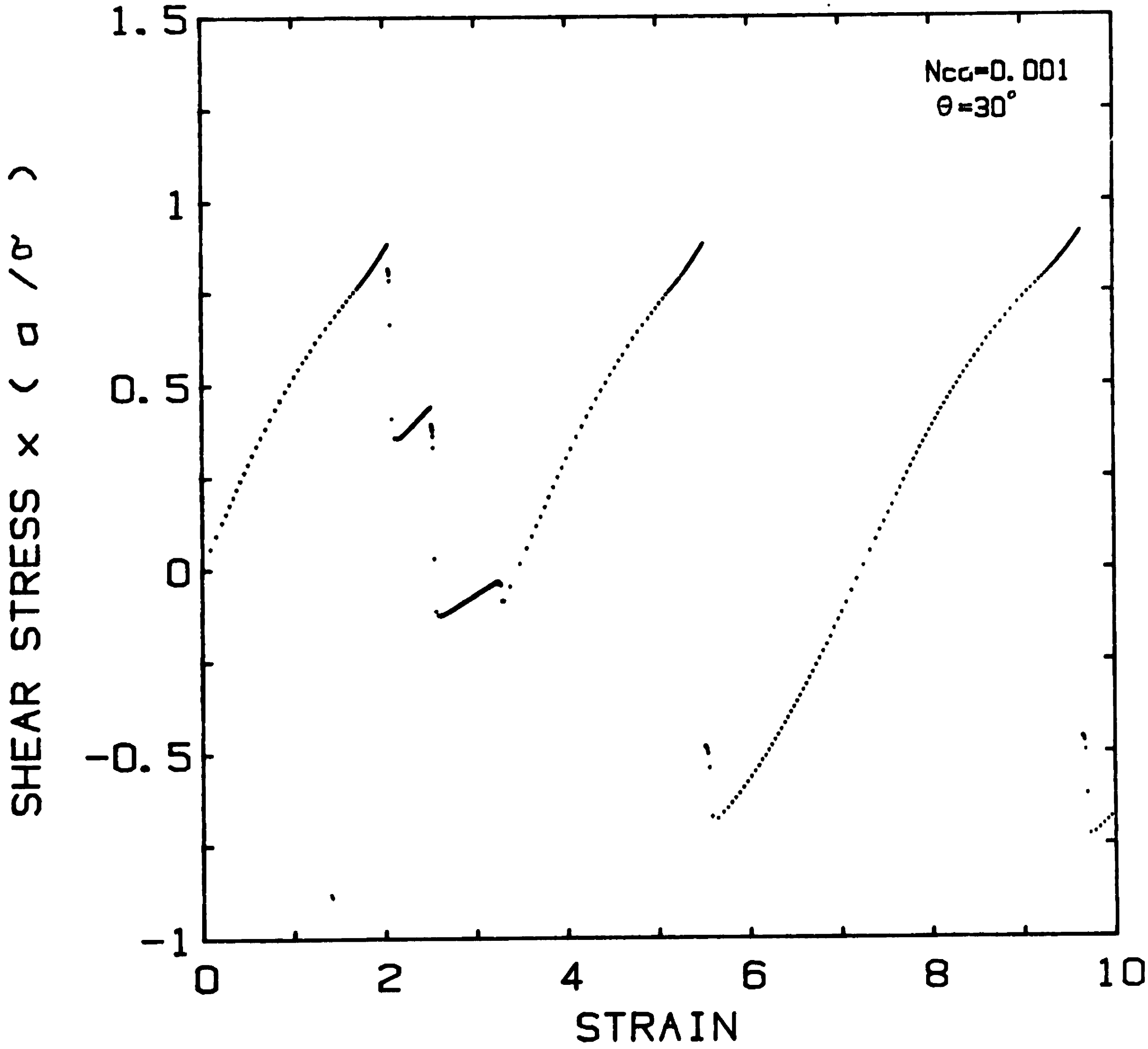

Figure VII-9 Stress-strain relations for initial orientation $\theta=30^{\circ}$. Capillary number $N_{ca}=.001$. a) Shear stress b) First normal stress difference. Note that the system is not periodic.

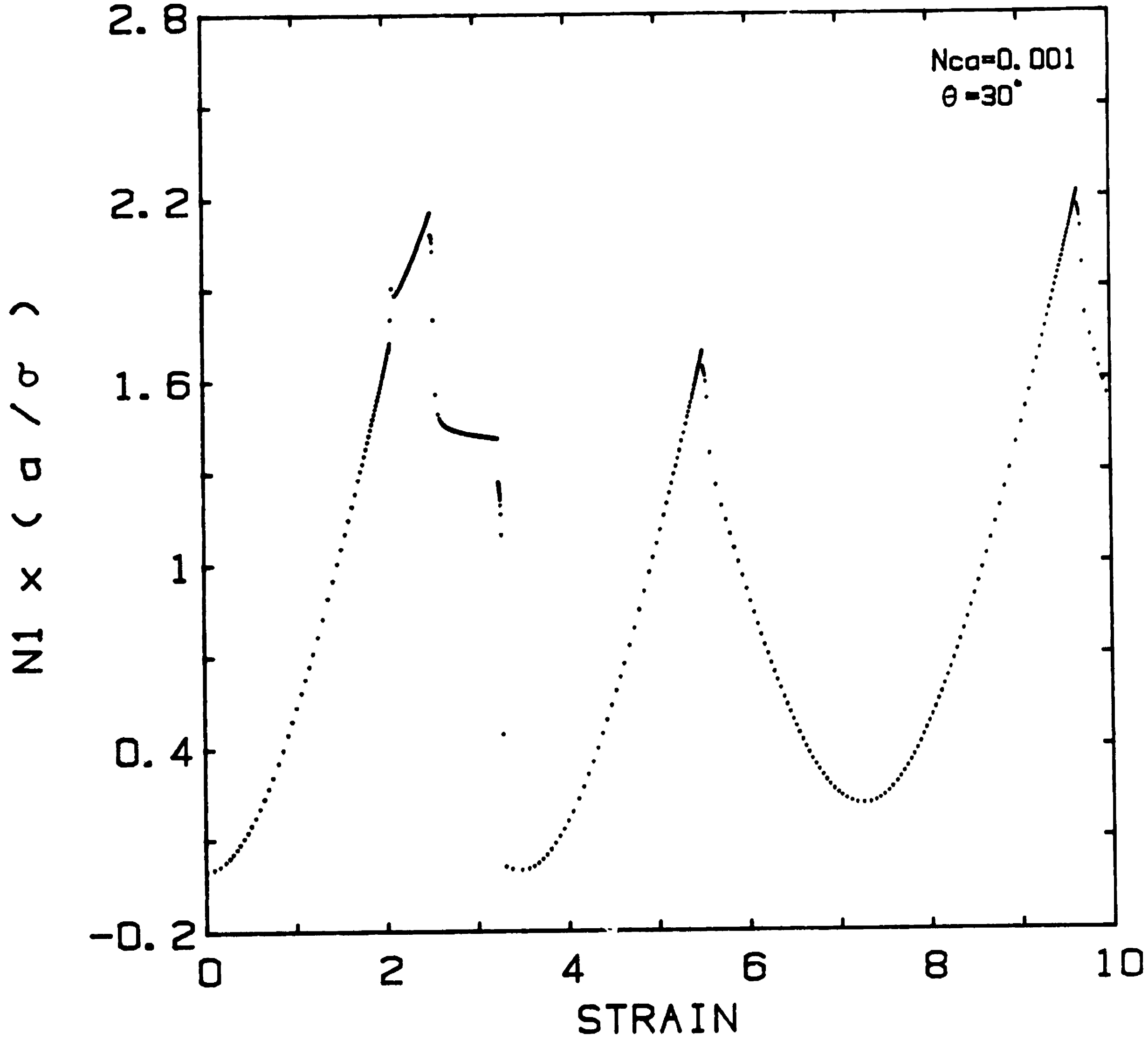

Figure VII-9 (continued)

structure of real foams which our model fails to take into account. Incorporation of all these factors into the model may reveal steady state material functions.

Based on our study for large deformations, one last word needs to be said about the steady shear viscosity expression derived in Chapter II for the equilbrium dry foam model. In our calculations there for the viscous dissipation in the foam films, we time averaged the dissipation over the first disproportionation. This infers the first disproportionation to be the period for the foam system. This is clearly not true in the 30° case and one should time average the viscosity expression over one cycle rather than the first disproportionation. Thus, the expression derived in Chapter II is correct as long as it refers to one disproportionation and not the entire period. The errror involved, however, is very small since the the yield stress does not change from that at the fist disproportionation. One should recall that for $\theta=0^{\circ}$, the period equals one disproportionation.

C. SUMMARY

In this chapter, large shearing deformations of foam was looked into. A force balance approach was used to determine the direction of the growing film after each cell disproportionation. We found that initial orientation and viscous forces strongly affected the periodicity of the system. For $\theta=0^{\circ}$ the system was periodic for equilibrium conditions and when viscous forces were present. In the equilibrium case the system always returned to its original configuration. For a finite yet small Capillary number, the system was periodic but did not return to its original configuration. For larger N_{ca}, the cells were very elongated indicating possibilities of cell rupture.

For $\theta=15^{\circ}$ and $N_{ca}=0$, the system showed no periodicity. For $\theta=30^{\circ}$ under equilibrium conditions the system was periodic and returned to its original configuration in the reformation cycle. Incorporation of viscosity however led to a loss of this periodicity.

VIII. SUMMARY AND RECOMMENDATIONS

The study of the rheology of foam is complicated by the inherently unstable nature of foam. In this study, such effects were eliminated by using stable foam capable of retaining its structure for a long period of time. The emphasis of this work had been to understand the physics of microstructural deformation and relate it to observable macroscopic material properties from a theoretical and experimental viewpoint. A formulation for describing arbitrary deformation in foams in terms of basis vectors along film edges was developed. This enabled, for the first time, to calculate the total stress tensor for high gas fraction, 2-D foam cell model for any arbitrary initial cell orientation and arbitrary homogeneous deformation. Experimental technique was developed which eliminated all previous problems associated with wall slippage in foam flow and allowed us to do experiments without resorting to any empiricisms for the wall region. The major findings in this regard is put into perspective in this chapter along with some relevant applications of this study and possible areas of future research.

A. THEORY

Two dimensional foam cell models were used to determine the stress strain relation and understand the underlying physics of foam deformation. Central to all our calculations was the assumption that the foam system was spatially periodic so that the centroid of the cells moved affinely with the bulk deformation.

1. Results in the limit ϕ approaches unity

In this limit the foam cells were hexagonal and the stress tensor for any deformation was related to the microstructure by the following relation.

$$\underline{\underline{\tau}} = \sum \frac{F_i}{S} \frac{\underline{g}_i\,\underline{g}_i}{g_i}$$

Here $\underline{g}_i$ represents the film i vectorially, F_i the magnitude of the force along it and g_i the length of the film. S is the area of a unit cell and the summation is over the three liquid films in the unit cell.

For small shearing deformations under equilibrium conditons, i.e. shear rate is zero and surface forces dominate so as to make the angles between films 120°, the above expression reduces to:

$$\tau_{yx} = \frac{2\sigma}{a} \frac{\gamma}{\sqrt{(3\gamma^2 + 12)}}$$

$$\tau_{xx} - \tau_{yy} = \frac{2\sigma}{a} \left[\frac{\gamma^2}{\sqrt{(3\gamma^2 + 12)}} \right]$$

Similar expressions were obtained for elongational deformation. These equations show that the stress in foam is independent of the initial cell orientation, proportional to the surface tension and inversely proportional to the cell side length. At the "micro" level, such a deformation leads to extensional motions of the films with one film shrinking in length with increasing strain. At a critical strain, γ_c, this film reduces to zero length and the corresponding stress represents the yield stress.

For stresses below τ_y, the material essentially behaves like an elastic solid and retracts back to its original configuration upon removal of the applied stress. τ_y, which has the same proportionality in terms of σ and a, did not change for a bimodal cell size distribution suggesting that the fluid mechanics of foam may be well described by a monodisperse cell model.

For deformations at finite shear rate, viscous forces opposing the extensional motion of the films are produced and the cell structure is determined from a balance of viscous and surface forces at each Plateau border. The influence of these viscous forces was studied in terms of a non-dimensional Capillary number, N_{ca}, giving the ratio of viscous to surface forces and defined as:

$$N_{ca} = \mu_L \, C(\phi) \, \dot{\gamma} a/2\sigma$$

For N_{ca} around .001 which corresponds to a shear rate of approximately 10^3 for typical values of surface tension, cell size and liquid viscosity, the deformation essentially remained the same as in the equilibrium case. This meant that the simple equlibrium model is valid for such shear rates. For $\dot{\gamma} > 10^3$, however, the cell structure and stresses started showing deviations from the equilibrium 120° case. The stress became a function of initial orientation and the critical strain and τ_y increased. At larger shear rates, the cells became very elongated suggesting possible modes of cell rupture.

The actual magnitude of the viscous stress in the films was however small. Its primary effect was to change the orientation and lengths of the films and thereby change the total stress.

In a real process, shear rates as high as 10^3 are hard to reach without destroying the foam. Even it were possible, most of the shearing would be concentrated in the thin wall films and the actual $\dot{\gamma}$ within the foam would be a lot lower enabling one to predict such deformations by the equilibrium model.

Calculations for large strains revealed the foam deformation to be periodic depending on initial orientation and Capillary number. Under equilibrium condition, initial orientations of 0° and 30° showed periodicity although for the latter three disproportionations were required before the system returned to its original configuration. For $\theta=15^{\circ}$, no periodicity was observed. With the inclusion of liquid viscosity the 30° orientation showed no periodicity; the 0° orientation was still periodic about some intermediate configuration. In all cases however, the yield stress corresponded to the stress at the first disproportionation and magnitude of the viscous disspation was negligible to affect the viscosity, thereby rendering the small deformation models applicable in most cases.

For steady shearing flows, foam behaves like a Bingham plastic with its viscosity being given by:

$$\eta = \tau_y/\dot{\gamma} + C_1 \mu_L$$

Here, μ_L is the liquid viscosity and C_1 has a value of ~.05 assuming $\phi=.99$. Thus the foam viscosity is the sum of two components: the first contribution comes from its yield stress and is proportional to σ/a; the second contribution comes the viscous dissipation in the liquid films because of their extensional motion. The shape of the viscosity versus shear rate curve will depend on the relative magnitudes of the two terms. At low shear rates, the viscosity will vary as $1/\dot{\gamma}$; at high shear rates, the second term will dominate and the viscosity will become independent of $\dot{\gamma}$. However, in most cases as in ours, $\tau_y >> C_1\mu_L$ and makes the second term negligible.

2. Results for finite liquid content

Incorporation of finite liquid into the model results in cell structure having straight line edges and rounded corners. Cases of zero and finite film thickness (δ) were considered. In both cases, the radius of curvature changed with deformation but all cells had the same radii in order to preserve equal pressures in cells [Heimenz, 1982]. For films having finite thickness, allowance was made for in and outflow of liquid from the Plateau border so as to maintain a δ determined from the equal pressure drop constraint given by [Wasan, 1984; Teletzke, 1984]:

$$A/\delta^3 = \sigma/r$$

We found that incorporation of finite liquid into our model affected the shear stress-strain relation. The yield stress or the maximum stress increased with gas fraction. This observation can be explained from the fact that with decreasing ϕ, the cells are less polyhedral and more rounded, thereby requiring a smaller force to go past one another. Initial cell orientation influenced the stress-strain relationship significantly. For some orientations instabilities were observed beyond a certain strain, i.e. for strains larger than this the volume conservation and affine motion criteria could not be satisfied and the cells reformed. This indicated possibilites of preferential cell orientations. Thus for ϕ=.9069 and θ between 11 and 21°, cells were unstable for any applied strain.

Introducing finite film thickness, δ, into the model did not change any of the results. This is because the change in δ was too small to affect the radius of curvature, r, and the film lengths any significant way from the zero thickness case. Since the stress is related to the total interfacial length, we therefore obtain the same results as for $\delta=0$. This close correspondence of the results shows that the negligible film thickness assumption, which has been used in all our calculations so far, is a justifiable one.

B. EXPERIMENTAL RESULTS

Both steady and dynamic experiments were conducted on foam using the parallel plate mode of the Rheometrics Mechanical Spectrometer. Sand paper was pasted onto the plates to eliminate wall slippage. In steady shear flows, foam behaved like a Bingham plastic. In the low shear rate experimental regime, it showed a shear thinning viscosity inversely proportional to the shear rate, indicating the yield stress to be the predominant component of the viscosity. The value of the viscosity, which was over four orders of magnitude higher than the constant liquid solution viscosity (5 mPa.s), was an increasing function of the gas volume fraction. Comparison with model predictions showed the model to give the correct trend but overpredict the viscosity by a factor of three. The discrepancy can be attributed to the monodispersity and two dimensionality of the model.

Indirect measurement of the yield stress of foam τ_y, obtained by extrapolating the viscosity versus shear stress data showed τ_y to increase with larger gas fraction. Direct measurement of τ_y using stress relaxation confirmed this. Values of τ_y obtained from the two techniques agreed reasonably well.

Oscillatory dynamic experiments showed foam to behave like an elastic solid for small deformations (consistent with theory). This was concluded from the facts that the moduli of foam were flat and insensitive to frequency of oscillation, G' was much greater than G'', and finally the phase shift between torque output and strain input was very small. All these are typical of highly elastic materials.

Stress growth experiments revealed the stres-strain behavior of foam to be independent of shear rate confirming the elastic nature of the material, and also indicating shear rate to be an unimportant processing parameter. Small stress overshoots with the maximum corresponding to the yield stress and critical strain and independent of γ and shear rate, typical of material with a yield stress, were observed for each gas fraction of foam.

C. APPLICATION TO PROCESSING PROBLEMS

Clearly, the findings of this study have direct and indirect uses for industry. Two applications are mentioned here. Both model and experiments predict the foam yield stress to increase with gas fraction. Further we found τ_y to be inversely proportional to cell size. Thus in any molding processes where uniform product is required, large gas fraction foam with small cell size is desirable. This is because the yield stress for such systems will be high and the foam will flow as a plug without cell deformation inside the mold. In terms of particle transport, the findings here can be used to obtain the bound on what gas fraction and cell size foams can support such particulates. A force balance around the particle determines the shear stress required to support it. From this stress, which should be larger than the yield stress of foam, one can determine the cell size and gas fraction of the foam.

D. RECOMMENDATIONS FOR FUTURE WORK

Although there is good qualitative agreement between theory and experiments, quantitative discrepancies exist. Further work needs to be done in the modelling area in terms of introducing three-dimensional foam cells and randomness in the foam structure. Some of the differences between model and experiments could be accounted for by introducing a third dimension to the model foam cells. One could concieve the foam cells as pentagonal dodecahedra with the centroids moving affinely with the bulk. In such a case the tetrahedral structure formed by joining four adjacent cell centers represents the unit cell and the vertices of this tetrahedron move affinely with the bulk. One can then use energy minimisation approach to determine the area of the liquid films and the cell microstructure. The macroscopic stresses can then be related to the microstructure by using either the force projection approach or the work argument.

Real foams also show a random structure. Such randomness can be computer generated with the resulting stucture being called a Voronoi network. Weaire and Kermode [1983, 1984] are one of the first to have used such techniques to generate a random two dimensional soap froth structures. One can use such structures along with the proper physics and dynamics learnt from this work to look at deformation of random cells. Because of the randomness in the stucture, one cannot use the affine motion assumption for each cell center. One would therefore have to define the domain of spatial periodicity and solve this as a boundary value problem along with some restictive conditons for each node. We feel that the results obtained for such systems would reduce the observed discrepancy between our monodisperse (or bidisperse) model and experiments.

Another area in which this research can be extended to is reactive systems. All real foam processes involve reactions. It is therefore important to understand the time dependent behavior of such systems. One can extend our results to such systems by introducing time dependence into all our derived material functions.

REFERENCES

Adamson, A.W., *Physical Chemistry of Surfaces*, 3rd ed., Wiley Interscience, New York, 1976.

Akers, R.J., ed., *Foams*, AP, New York, 1976.

Barber, A.D., Hartland, S., *Trans. Instn. Chem. Engrs.*, *53*, p.106, 1975.

Beris, A.N., *private communications*, Massachusetts Institute of Technology, 1984.

Beyer, A.H., Millhone, R.S., Foote, R.W., *Soc. Pet. Eng. J.*, No. 3986, 1972.

Bickerman, J.J., *Foams*, Springer-Verlag, New York, 1973.

Bird, R.B., Armstrong, R.C., Hassager, O., *Dynamics of Polymeric Liquids*, Vol.1, John Wiley & Sons, New York, 1977.

Bird, R.B., Hassager, O., Armstrong, R.C., Curtiss, C.F., *Dynamics of Polymeric Liquids*, Vol.2, John Wiley & Sons, New York, 1977.

Boger, D.V., Dzuy, N.Q., *J. Rheol.*, *27* (4), p.321, 1983.

David, A., Ph.D dissertation, Stanford University, 1968.

David, A., Marsden Jr., S.S., *Soc. Pet. Eng. J.*, No. 2544, 1969.

Deryaguin, B.V.,*Pure Appl. Chem.*, *10*, p.375, 1965.

Desai, D., Kumar, R., *Chem. Eng. Sci.*, *38* (19), p.1525, 1983.

Dinh, S., Ph.D Thesis, Massachusetts Institute of Technology, 1981.

Ferry, J.D., *Viscoelastic Properties of Polymers*, 2nd (3rd) ed., John Wiley & Sons, New York, 1970 (1982).

Hartland, S., Barber, A.D., *Trans. Instn. Chem. Engrs.*, *52*, p.43, 1974.

Hartland, S., Steiner, L., Hunkeler, R., *Trans. I ChemE.*, *55*, p.153, 1977.

Hiemenz, P.C., *Principles of Colloid and Surface Chemistry*, Dekker, New York, 1977.

Kitchener, J. A., Cooper, C.F., *Chem. Soc. London Quart. Rev.*, Vol. 13, p.71, 1959.

Kitchener, J.A., in *Recent Progress in Surface Science*, Vol.1, eds. Danielli, J.F., Pankhurst, K.G.A., Riddiford, A.C., AP, New York, 1964.

Kraynik, A., 54th Ann. Meet. Soc. Rheol., Illinois, 1982.

Kraynik, A., private communications, Sandia National Laboratories, 1984.

Kumar, R., Desai, D., Chem. Eng. Sci., 33 (9), p.1361, 1982.

Lemlich, R., ed., Adsorptive Bubble and Separation Techniques, AP, New York, 1972.

Lemlich, R., Ind. Eng. Chem. Fundam., 17 (2), p.89, 1978.

Matijevic, E., ed., Surface and Colloid Science, Vol. 3, 1971.

Matzke, E.B., Am. J. Botany, 33, p.58, 1946.

Matzke, E.B., Nestler, J., Am. J. Botany, 33, p.130, 1946.

Mitchell, B.J., Oil and Gas J., p.96, 1971.

Mooney, M., J. Rheol., p.210, 1931.

New, G.E., Proc. Int. Congr. Surf. Active Substances, 4th, Brussels, 2, p.1167, 1967.

Patton, J.T., Patton Jr., Kuntamukkula, M., Holbrook, S., Polymer Preprints, ACS, 22 (1), 1981.

Princen, H.M., Aronson, M.P., Moser, J.C., J. Coll. Int. Sci., 75 (1), p.246, 1980.

Princen, H.M., J. Coll. Int. Sci., 71, (1), p.55, 1979.

Princen, H.M., J. Coll. Int. Sci., 91, (1), p.160, 1983.

Princen, H.M., J. Coll. Int. Sci (submitted), 1984.

Prud'homme, R.K., Ph.D Thesis, University of Wisconsin, 1978.

Prud'homme, R.K., Bird, R.B., J. Non Newt. Fl. Mech., 3, p.261, 1978.

Prud'homme, R.K., 53rd Ann. Meet. Soc. Rheol., Kentucky, 1981.

Rand, P., personal communications, Sandia National Laboratories, 1982.

Rosen, M., Surfactants and Interfacial Phenomena, Wiley Interscience, New York, 1978.

Ross, S., J. Coll. Int. Sci., 95 (1), p.97, 1983.

Ross, S., Ind. Eng. Chem., 61 (10), p.48, 1969.

Ross, S., Nishioka, G., J. Coll. Int. Sci, 81 (1), p.1, 1981.

Ross, S., Nishioka, G.M., Witworth, M., J. Coll Int. Sci., 95 (2), 1983.

Shaw, D.J., Introduction to Colloid and Surface Chemistry, 2nd ed., Butterworth and Co. Ltd., 1970.

Surati, H.S., Mahalingam, R., Brink Jr., J.A., AIChE Symp. Ser.: Adv Int. Phenomena, 71 (150), p.52, 1975.

Teletzke, G.F., Ph.D dissertation, University of Minnesota, 1983.

Treolar, L.R.G., The Physics of Rubber Elasticity, 2nd ed., Oxford University Press, Oxford, 1967.

Wasan, D.T., personal communications, Illinois Institute of Technology, 1984.

Weaire, D., Kermode, J.P., Phil. Mag. B, 48 (3), p.245, 1983.

Weaire, D., Kermode, J.P., Phil. Mag. B, 50 (3), p.379, 1984.

Weinberg, M., Ph.D Thesis, Massachusetts Institute of Technology, 1981.

Wenzel, H.G., Brungraber, R.J., Stelson, T.E., ASCE: EM6, p.153, 1967.

Wenzel, H.G., Brungraber, R.J., Stelson, T.E., J. Matl., 5 (2), p.396, 1970.

Yoshimura, A., Ph.D Thesis in preparation, Princeton University, 1984; Prudhomme, R.K., personal comm., Princeton University, 1984.

APPENDIX A

Calculations for Dry Foam Model

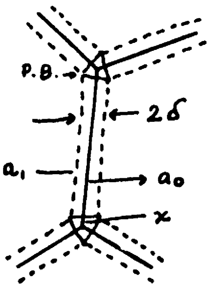

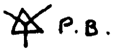

From the above figure, we get for zero strain:

$x_0 = \delta_0/\sqrt{3};$ $a_1 = \phi^{1/2}\, a_0$ $a_1 + 2x_0 = a_0$

This gives $\delta_0 = \sqrt{3}\, a_0\, (1 - \phi^{1/2})/2$ for zero strain.

As we strain, we can either set

$l_i\delta_i = a_0\delta_0 = a_0^2\, (1 - \phi^{1/2})\, \sqrt{3}/2$

or,

$l_i\delta_i = a_1\delta_0 = a_0^2\, (1 - \phi^{1/2})\, \phi^{1/2}\, \sqrt{3}/2$

Because we are dealing with dry foam (assuming $\phi = 0.99$) it makes very little difference, which expression we use. The second expression assumes that the Plateau border liquid volume is preserved in any deformation and is therefore a more rigorous one. We therefore used this to get $C(\phi)$ in the definition of N_{Ca}.

To get the final or critical strain, we use the criterion that at this γ the liquid film length is given by:

$2x + \sqrt{a_1\delta_0} = a_0\, (.707)$

A simpler approximation to use would to assume that

$a_0 \longrightarrow \sqrt{a_0\delta_0} = a_0\, (.06588)$ at the critical strain.

APPENDIX B

CALCULATIONS FOR CHAPTER IV

1. Explicit forms for l_1', l_2' and r' in Equation IV-8 for the $\delta=0$ case:

$l_1'+l_2'=3\ (A5/A1 + A6/A2)/8 + r'\ [(1/A1 + 1/A2)\ A4 - 2 \sin\beta + 4\ A3]$

$r' = -NUM1/(DENO1 + DENO2)$

$NUM1=3r \cos^2\beta\ [A6/A2 + A5/A1]/8 + 3 \sin\beta\ [A1.A6/A2 + A2.A5/A1]$

$DENO1=(A1 + A2)\ (\cos^2\beta + 4.A3.\sin\beta) + r \cos^2\beta\ A4\ [1/A1 + 1/A2]$

$DENO2= -2.A1.A2.A3/r - 2.r\ (2.A3.\sin^2\beta + \pi/4 \cos^2\beta)$

$\quad + A4.\sin\beta\ (A1/A2 + A2/A1)$

$A1 = [b_3{}^2 - r^2 \cos^2\beta]^{1/2}$ $\qquad A2 = [b_2{}^2 - r^2 \cos^2\beta]^{1/2}$

$A3 = \sin\beta - \pi/4$ $\qquad A4 = -r \cos^2\beta - 2.\sin\beta.r.A3$

$A5 = 2\gamma \cos^2(\theta+30) - \sin(2\theta+60)$

$A6 = 2\gamma \sin^2\theta + \sin(2\theta)$

2. Explicit form of r' for Regime I in the $\delta\neq0$ case (Equation IV-14)

$r' = -NUM2/DENO3$

$NUM2 = 0.75\ a.C1.C2.\gamma/C3$

$DENO3 = 2\sqrt{3}.r - C1^2/(C2x2\sqrt{3}) - \pi r + 0.25\ a.C1.C3/(C2^2)$

$C1 = (A/\sigma)^{1/3}$ $\qquad C2 = r^{1/3}$ $\qquad C3 = (\gamma^2+4)^{1/2}$